



Enhancement of Every Magneto-Optical Effect with All-Dielectric Guided-Mode Resonant Gratings Based on a Magnetic Sol-Gel Nanocomposite

Laure Bsawmaii

► To cite this version:

Laure Bsawmaii. Enhancement of Every Magneto-Optical Effect with All-Dielectric Guided-Mode Resonant Gratings Based on a Magnetic Sol-Gel Nanocomposite. Optics / Photonic. Université de Lyon, 2020. English. NNT : 2020LYSES028 . tel-03207393

HAL Id: tel-03207393

<https://theses.hal.science/tel-03207393>

Submitted on 24 Apr 2021

HAL is a multi-disciplinary open access archive for the deposit and dissemination of scientific research documents, whether they are published or not. The documents may come from teaching and research institutions in France or abroad, or from public or private research centers.

L'archive ouverte pluridisciplinaire **HAL**, est destinée au dépôt et à la diffusion de documents scientifiques de niveau recherche, publiés ou non, émanant des établissements d'enseignement et de recherche français ou étrangers, des laboratoires publics ou privés.



**UNIVERSITÉ
JEAN MONNET**
SAINT-ÉTIENNE

N° d'ordre NNT: 2020LYSES028

THÈSE de DOCTORAT de L'UNIVERSITÉ de LYON

opérée au sein du

Laboratoire Hubert Curien

École Doctorale N° 488

Science, Ingénierie et Santé

Discipline: Optique, Photonique, Hyperfréquences

Soutenue publiquement le 26/10/2020, par:

Laure BSAWMAII

Exaltation des Différents Effets Magnéto-Optiques à l'aide de Réseaux Résonants Diélectriques Basés sur un Nano-composite Magnétique Obtenu par Voie Sol-Gel

Devant le jury composé de:

Mme. DAGENS Béatrice	Directrice de Recherche, C2N, Palaiseau	Rapporteuse
Mr. MAGER Loïc	Chargé de Recherche HDR, IPCMS, Strasbourg	Rapporteur
Mr. BROQUIN Jean Emmanuel	Professeur, INP, Grenoble	Examineur
Mr. GHIBAUDO Olivier	Docteur-Ingénieur, Safran Tech, Saclay	Invité
Mr. VANWOLLEGHEN Mathias	Chargé de Recherche, IEMN, Lille	Invité
Mlle. GAMET Emilie	Maître de Conférence, UJM, Saint-Étienne	Co-encadrante
Mr. JAMON Damien	Ingénieur de Recherche, UJM, Saint-Étienne	Co-encadrant
Mr. ROYER François	Professeur, UJM, Saint-Étienne	Directeur



**UNIVERSITÉ
JEAN MONNET**
SAINT-ÉTIENNE

N° d'ordre NNT: 2020LYSES028

THÈSE de DOCTORAT de L'UNIVERSITÉ de LYON

opérée au sein du

Laboratoire Hubert Curien

École Doctorale N° 488

Science, Ingénierie et Santé

Discipline: Optique, Photonique, Hyperfréquences

Soutenue publiquement le 26/10/2020, par:

Laure BSAWMAII

Enhancement of Every Magneto-Optical Effect with All-Dielectric Guided-Mode Resonant Gratings Based on a Magnetic Sol-Gel Nanocomposite

Devant le jury composé de:

Mme. DAGENS Béatrice	Directrice de Recherche, C2N, Palaiseau	Rapporteuse
Mr. MAGER Loïc	Chargé de Recherche HDR, IPCMS, Strasbourg	Rapporteur
Mr. BROQUIN Jean Emmanuel	Professeur, INP, Grenoble	Examineur
Mr. GHIBAUDO Olivier	Docteur-Ingénieur, Safran Tech, Saclay	Invité
Mr. VANWOLLEGHEN Mathias	Chargé de Recherche, IEMN, Lille	Invité
Mlle. GAMET Emilie	Maître de Conférence, UJM, Saint-Étienne	Co-encadrante
Mr. JAMON Damien	Ingénieur de Recherche, UJM, Saint-Étienne	Co-encadrant
Mr. ROYER François	Professeur, UJM, Saint-Étienne	Directeur

"In the memory of my beloved mother. To my nieces and nephews."

Acknowledgements

A thesis is a real collaborative work. In fact, I could never have carried out this doctoral work without the support of a large number of people whose generosity, good humor and interest in my research have allowed me to progress in this delicate phase.

I would like to thank first Mrs. Béatrice DAGENS and Mr. Loïc MAGER for having accepted to be reporters of this research work. I would also like to thank Mr. Jean Emmanuel BROQUIN, Mr. Olivier GHIBAUDO and Mr. Mathias VANWOLLEGHEN for being part of the thesis committee. I deeply appreciated their time and their insightful comments and encouragements.

I would like to thank my thesis supervisor, Mr. François ROYER. His wise guidance, support, dynamism and vision have been invaluable throughout this work. I would also like to express my appreciation for his theoretical and practical expertise in the field, his communication skills and his availability each time I needed his help.

I would like to express my deep and sincere thanks to my co-supervisor, Mr. Damien JAMON, for his invaluable help in the different experimental measurements, and his various innovative ideas which played a key role in the running of this thesis work. I would also like to tell him how much I appreciated his availability each time I asked for his help, and his faith on me at every stage in this research, as well as his encouragements. He has taught me the methodology to carry out the research and to present the research works as clearly as possible. It was a great honor to work with him. Finally, I am extremely grateful for his human qualities of listening and understanding, as well as for his empathy and great sense of humor.

I am thankful also to my co-supervisor, Mrs. Emilie GAMET, for her invaluable attention to my work and to her precious help every time I have questions, especially concerning the numerical simulations. I appreciated her wise and constructive comments and advice.

I am extending my thanks to Mrs. Sophie NEVEU, for the fabrication of stable and homogeneous ferrofluids, which are at the base of the magneto-optical composite film elaborated in this work.

In addition to that, I would like to acknowledge all the current members of the Micro and Nano-structuring team for training me on the fabrication and characterizations tools of diffraction gratings, as well on the optical simulation software (MC Grating ©). In particular, my thanks go to all the members working in the Magneto-Optical research field for supporting me throughout this period.

Furthermore, I am deeply thankful to all my colleagues in the Hubert Curien laboratory, for the wonderful and cheerful moments spent together during this period.

I wholeheartedly thank my caring, loving and supportive fiancé. His encouragement when the times got rough is much appreciated. It was a great comfort and relief to know that he is beside me to manage every hard moment all over this period.

Finally, I am extremely grateful to my family, for their endless love, prayers, caring and sacrifices for educating and preparing me to this stage.

Contents

Acknowledgements	v
List of Abbreviations	xi
General Introduction	1
I Magneto-Optics: Introduction and Enhancement Processes	5
I.1 Magneto-Optics: an Introduction	5
I.1.1 Magneto-Optical Effects in Bulk Materials	5
I.1.1.1 Faraday Effect	5
I.1.1.2 Magneto-Optical Kerr Effects	11
I.1.2 Magneto-Optical Effects in Guided Configuration	14
I.1.2.1 Dielectric Planar Waveguides Modes	14
I.1.2.2 Plasmonic Modes	19
I.1.2.3 Modes Conversion in Magneto-Optical Waveguides	20
I.1.2.4 Phase Modulation in Magneto-Optical Waveguides	22
I.1.3 Magneto-Optical Materials	23
I.1.4 Magneto-Optical Devices	25
I.1.4.1 Magnetic Field Sensors	26
I.1.4.2 Biosensors	27
I.1.4.3 Non-Destructive Testing	29
I.2 Guided-Mode Resonance Gratings	31
I.2.1 Guided Mode Resonance: Principles	31
I.2.2 Phase Matching	33
I.3 Magneto-Optical Enhancement Achievements	34
I.3.1 All-Dielectric Structures	34
I.3.1.1 Enhancement of Polarization Rotation Effects	35
I.3.1.2 Enhancement of Magneto-Optical Phase Modulation Effects	39
I.3.2 Magneto-Plasmonic Structures	41
I.3.2.1 Enhancement of Polarization Rotation Effects	41
I.3.2.2 Enhancement of Magneto-Optical Phase Modulation Effects	46

I.4	Objectives	52
II	Materials and Devices: Properties and Fabrication Processes	55
II.1	Magnetic Nanoparticles of Cobalt Ferrite	55
II.1.1	Crystal Structure	56
II.1.2	Diameter Distribution	56
II.1.3	Stability and Homogeneity of the Ferrofluid	57
II.1.4	Magnetic Properties	58
II.1.4.1	Individual Magnetic State	58
II.1.4.2	Magnetization Behavior	59
II.1.5	Magneto-Optical Behavior	62
II.1.5.1	Individual Particle Permittivity	62
II.1.5.2	Composite Global Permittivity	63
II.1.5.3	Magneto-Induced Linear Anisotropy	64
II.1.5.4	Faraday Effect	66
II.1.6	Transmittance	69
II.2	Elaboration of Magneto-Optical Thin Films	70
II.2.1	Sol-Gel Technique	71
II.2.1.1	Basic Principles	71
II.2.1.2	Preparation of MO-Sol	73
II.2.2	Choice and Preparation of Substrates	73
II.2.3	Dip-Coating Process	74
II.2.3.1	Basic Principals	74
II.2.3.2	Magneto-Optical Films Deposition	75
II.2.3.3	Nano-Structuring: Deposition Under Magnetic Field	75
II.3	Characterization of Magneto-Optical Thin Films	77
II.3.1	Opto-Geometrical Properties	77
II.3.1.1	Ellipsometry: Basic Principles	77
II.3.1.2	Dielectric Function	79
II.3.1.3	Thickness	80
II.3.1.4	Transmittance	81
II.3.2	Magneto-Optical Properties	82
II.3.2.1	Description of the Traditional Magneto-Optical Setup	82
II.3.2.2	Faraday Effect Measurements on Thin Films	85
II.3.3	Estimation of Nanoparticles Concentration	86
II.3.4	Measurements of Nanoparticle Refractive Index	88
II.3.5	Magneto-Induced Anisotropies	90
II.4	Elaboration of Guided-Mode Resonant Gratings	92
II.4.1	Photoresist Gratings	92
II.4.1.1	Work Environment and Description of the Used Photoresist	92
II.4.1.2	Spin Coating Process and AFM	93
II.4.1.3	Fabricated Structures	94
II.4.2	Silicon Nitride Gratings	97
II.5	Conclusion	99

III Magneto-Optical Effects Enhancement:	
Numerical and Experimental Evidence	101
III.1 Numerical Simulations of Optical and Magneto-Optical Behavior	101
III.1.1 Calculations Method	101
III.1.2 Optical Behavior of PR-MO Structure	103
III.1.3 Magneto-Optical Behavior of PR-MO structure	107
III.1.3.1 Polarization Rotation Effects	107
III.1.3.2 TMOKE	110
III.2 Description of Magneto-Optical Setups for Resonant Structures	114
III.2.1 Polarization Rotation Measurements Setup	115
III.2.2 TMOKE Measurements Setup	117
III.3 Enhancement of Polarization Rotation Effects	118
III.3.1 Enhancement of Faraday Effect	119
III.3.1.1 Photoresist Grating	119
III.3.1.2 Comparison with Silicon Nitride Grating	123
III.3.2 Enhancement of LMOKE in Transmission	126
III.3.2.1 Photoresist Grating	126
III.3.2.2 Comparison with Silicon Nitride Grating	130
III.4 Enhancement of TMOKE	131
III.4.1 Transmission Geometry	131
III.4.2 Reflexion Geometry	133
III.4.3 Comparison with Silicon Nitride Grating	134
III.5 Reciprocal Effects	136
III.5.1 Faraday Configuration	138
III.5.2 Longitudinal Configuration	139
III.5.3 Transverse Configuration	140
III.6 Conclusion	145
Conclusion and Future Works	147
Bibliography	166
Abstract	167
Résumé	169

List of Abbreviations

AOI	A ngle O f I ncident
AFM	A tom i c F orce M icroscopy
ASE	A mplified S pontaneous E mission
BIG	B ismuth substituted I ron G arnet
Bi:YIG	B ismuth substituted Y ttrium I ron G arnet
Ce:YIG	C erium substituted Y ttrium I ron G arnet
EC	E ddy C urrents
EOT	E xtraordinary O ptical T ransmission
EIA	E lectromagnetically I nduced A bsorption
EMA	E ffective M edium A pproximation
Exp	E xperimental work
FR	F araday R otation
FE	F araday E llipticity
FRE	F araday R eciprocal E ffect
FWHM	F ull W idth at H alf M aximum
FoM	F igure of M erit
GGG	G adolinium G allium G arnet
GMR	G uided- M ode R esonance
LCV	L eft C ircular V ibrations
LMOKE	L ongitudinal M agneto- O ptical K err E ffect
LMPIE	L ongitudinal M agneto- P hotonic I ntensity E ffect
LRE	L ongitudinal R eciprocal E ffect
LSP	L ocalized S urface P lasmon
LIA	L ock- I n A mplifier
LabHC	H ubert C urien L aboratory
MO	M agneto- O ptics
MP	M agneto- P lasmonic
NPs	N ano P articles
NDT	N on- D estructive T esting
Num	N umerical work

PMOKE	Polar Magneto-Optical Kerr Effect
PR	PhotoResist
PBG	Photonic Band Gap
RCV	Right Circular Vibrations
RCWA	Rigorous Coupled Wave Analysis
SPPs	Surface Plasmon Polaritons
SPR	Surface Plasmon Resonance
SEM	Scannig Electron Microscopy
TEM	Transverse Electron Microscopy
TE	Transverse Electric
TM	Transverse Magnetic
TMOKE	Transverse Magneto-Optical Kerr Effect
TRE	Transverse Reciprocal Effect
TEOS	TetraEthyl OrthoSilicate
WPPs	Waveguide Plasmon Polaritons
YIG	Yttrium Iron Garnet

General Introduction

The Magneto-Optical (MO) effects [ZK97] are described as a rotation of the polarization plane or a modulation of the intensity, of the reflected or transmitted light through a magnetized material. These effects originate from energy coupling between the electric field components of TE and TM polarizations, under the influence of a magnetic field which creates off-diagonal elements in the permittivity tensor of the MO material. Depending on the magnetic field orientation with respect to the incident and sample planes, different MO effects can be defined: Faraday (or Polar for oblique incidence), Longitudinal and Transverse effects.

Due to their sensitivity to the magnetic field, the MO effects are currently highly desirable in non-destructive testing for defects characterization [NSM04; BFL16] or in magnetic field sensing [Sep+06; Reg+11]. However, the MO activity is generally weak: for example the relative change in the reflected light intensity, due to the Transverse MO effect in ferromagnets such as nickel or cobalt is of the order of 0.1% [Poh+13]. Thus, it is relevant to enhance the MO effects, in order to improve further the sensitivity of the MO devices.

From several years, the enhancement of the MO effects is taking lots of attention and different structures have been simulated or fabricated for this purpose. In the case of planar devices, the MO enhancement is based on the increase of the light/MO material interaction, generally through the excitation of plasmonic [CGMC15] or dielectric guided-modes [Vor+20] in the structure, named hence resonant structure.

To reach the maximum TE-TM mode conversion, in other words MO polarization rotation effects, a phase matching condition is required. This phase matching is satisfied when the TE and TM guided-modes are excited with the same propagation constant in the structure, through optimized opto-geometric parameters of this latter [Ala+11].

Most of the resonant structures are magneto-plasmonic structures (combination of metal and MO materials) due to the beneficial combination of the MO activity and the plasmon oscillations [Poh+13; Flo+17]. These latter are described by coupled oscillations of the TM electromagnetic field and the electron plasma in a metal, which are localized or guided along a metal/dielectric interface [Mai07]. Different magneto-plasmonic structures

have been implemented to enhance the MO effects, such as Au/Co heterostructures [Arm+09; Man+14; Ign+16; CGMC16] or perforated Au layer deposited on top of a dielectric magnetic film (generally Bismuth Iron Garnet) [Bel+11; Poh+13; Kre+13; DV+17]. High MO effects were reached experimentally and numerically through the magneto-plasmonic structures but accompanied mostly with low optical response due to the large absorption of the metal, limiting hence their practical applications.

A possible way to decrease the optical losses is to work with all-dielectric structures. Recently, theoretical enhancements of the MO effects were demonstrated through magnetic nanorods [Mar+14] or nanodisks [Chr+18; Che+20] arrays. However, the most practical in terms of fabrication is 1D all-dielectric guided-mode resonance gratings [Vor+20; MBK14]: combination of dielectric grating and MO waveguide.

The presented work is part of this evolution. It was conducted within the Micro and Nano structuring team in the Hubert Curien laboratory (UMR CNRS 5516), Jean Monnet University, Saint-Étienne, France. It is dedicated to the development of an innovative MO device, capable to enhance the MO effects in different configurations, in order to measure small and large magnetic field in three directions, applicable in sensing technology or in non-destructive testing.

The resonant structures under study in this work are 1D all-dielectric guided-mode resonance gratings. Due to its simplicity of fabrication, the adapted structure consists of a photoresist grating deposited on top of a MO film which is deposited on a glass substrate. A more complex all-dielectric structure was studied in this work, as a reference. It consists of alternating Silicon Nitride and MO material, deposited on a BK7 substrate.

The MO material is a composite, formed by cobalt ferrite nanoparticles embedded in a solid silica matrix by sol-gel process. This MO composite was developed in the research team more than 15 years ago [Roy04], and it was used in previous works [Var17; AD+16] for enhancing the MO effects in resonant structures. Therefore, the presented work is part of their continuity, taking into account the development of main lines of research presented in this manuscript.

Therefore, the manuscript is organized as follows:

- Chapter I is dedicated to introduce firstly the MO effects in free space and in guided configuration. In addition to that, the different existing MO materials will be presented and the advantages of the used MO composite will be highlighted. Moreover, the different MO devices, especially used in sensing and non-destructive testing, will be described.

In the second part of this chapter, the basic principles of 1D-all dielectric guided mode resonance gratings will be detailed. Finally, the MO enhancements achieved in the literature through magneto-plasmonic and all-dielectric structures will be compared.

- Chapter II is mainly dedicated to the MO composite material in terms of elaboration and

characterizations (opto-geometrical and MO properties). Therefore, a special study will be presented in order to deduce the whole permittivity tensor of the MO material and to hence expect the MO composite film characteristics before elaboration which is useful for a structure design.

The fabrication and the opto-geometric characterizations of the different all-dielectric structures will be detailed in the last part of this chapter.

- Chapter III is dedicated to present the experimental and numerical evidence of the MO effects enhancement in different magnetic field configurations, through the 1D all-dielectric guided-mode resonance gratings. The experimental measurements were done with homemade MO setups developed in the presented work.
- The final part of this manuscript is dedicated to present our suggestions for future works.

CHAPTER I

Magneto-Optics: Introduction and Enhancement Processes

I.1 Magneto-Optics: an Introduction

The intensity, phase and polarization of light reflected or transmitted through a MO material can be modulated by the medium's magnetization [ZK97] [Liu+09]. These effects, named MO effects, are promising tools for controlling light in optical devices such as optical isolators [Sha+13] [Onb+16], which are essential elements in laser systems. They can be used also in magnetic field sensors [SJM10], [DRD90], MO data storage [ZK97] or biosensors [Reg+11].

The presence of a magnetic field leads to the emergence or the variation of a non-reciprocal optical anisotropy in the MO material. Most of the MO effects are the direct or indirect results of the division of the electron's energy levels (Zeeman effect) of the magnetized system [Liu+09]. The MO effects can be classified, according to the relative orientation of the wave vector of the light \vec{k} and the magnetic field \vec{B} , into two distinguished groups:

- Polarization rotation effects [ZK97]: results in a rotation of the polarization's plane if the wave vector (\vec{k}) of the incident polarized light is parallel to the direction of the magnetic field (\vec{B}).
- Phase and intensity modulation effects [ZK97]: results in an intensity and phase modulation of the light (initially polarized) propagating perpendicularly to the direction of the magnetic field.

The description of the different MO effects, will be presented in details in the next sections, first in bulk materials then in guided configuration.

I.1.1 Magneto-Optical Effects in Bulk Materials

I.1.1.1 Faraday Effect

The Faraday effect [ZK97] belongs to the polarization rotation effects in transmission.

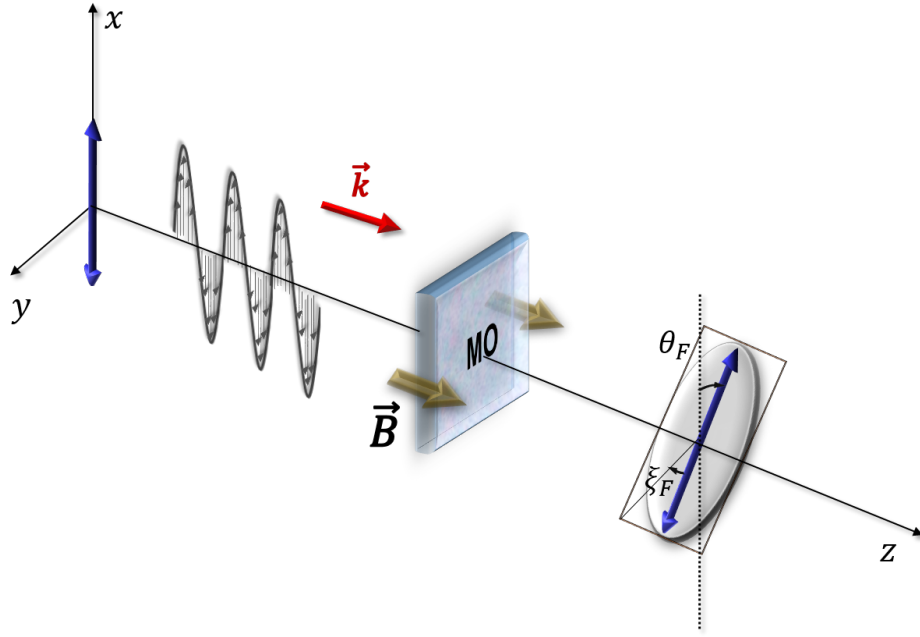


FIGURE I.1: Schematic illustration of the Faraday effect

To simply understand this effect, let's consider an applied magnetic field (\vec{B}) directed along z direction (see Fig.I.1), and an electromagnetic wave linearly polarized in x direction passing through the MO material along z axis. Hence, the electrons of the material, under the influence of the incident wave, oscillate in x direction with a velocity v . Due to the Lorentz force ($\vec{F} = q\vec{v} \times \vec{B}$) where q is the electron charge, a coupling between x and y directions occurs resulting in an elliptical movement of the electrons oscillations. Therefore, the transmitted waves have a component following y direction in addition to the initial one following x axis. This behavior leads to a rotation of the polarization plane of the wave, this is the Faraday rotation (FR) phenomenon.

To go further than the simple explanation described above for the Faraday effect and in order to understand well the physical origin of this effect, the Maxwell's equations will be implemented. The electric field of the monochromatic electromagnetic wave of Fig.I.1 can be expressed as follows:

$$\vec{E} = \vec{E}_0 e^{i(kz - \omega t)} \quad (I.1)$$

Where E_0 is the amplitude, k is the wavenumber, ω is the angular frequency and t is the time.

This wave should verify the equation:

$$k^2 \vec{E} - (\vec{k} \cdot \vec{E}) \vec{k} = \frac{\omega^2}{c^2} \epsilon_0 \epsilon \vec{E} \quad (I.2)$$

where, ϵ_0 is the permittivity of the vacuum and c is the celerity of the light in vacuum. ϵ is the permittivity tensor of the MO material:

- In the absence of a magnetic field, the MO material is generally isotropic ($\epsilon_{xx} = \epsilon_{yy} = \epsilon_{zz}$). The corresponding tensor is then diagonal [ZK97]:

$$\begin{pmatrix} \epsilon_{xx} & 0 & 0 \\ 0 & \epsilon_{xx} & 0 \\ 0 & 0 & \epsilon_{xx} \end{pmatrix} \quad (\text{I.3})$$

where $\epsilon_{xx} = N^2$, with $N = n - i\kappa$ (complex refractive index of the material).

- If a magnetic field is applied in z direction (referring to Fig.I.1), antisymmetric off-diagonal elements will appear in the tensor permittivity:

$$\begin{pmatrix} \epsilon_{xx} & i\epsilon_{xy} & 0 \\ -i\epsilon_{xy} & \epsilon_{xx} & 0 \\ 0 & 0 & \epsilon_{xx} \end{pmatrix} \quad (\text{I.4})$$

where, ϵ_{xy} is a dispersive term, in other words, it depends on the wavelength (see Fig.I.2).

This expression illustrates the coupling between x and y components under the influence of the magnetic field resulting in the Faraday effect.

The resolution of the Eq.(I.2), in a material owing a permittivity tensor with off-diagonal elements (as Eq.(I.4)), shows that only two states of polarization can propagate [ZK97]:

- The right circular vibrations (RCV) characterized by a propagation index:

$$N_+ = n_+ + i\kappa_+ = \sqrt{\epsilon_{xx} + \epsilon_{xy}} \quad (\text{I.5})$$

- The left circular vibrations (LCV) characterized by a propagation index:

$$N_- = n_- + i\kappa_- = \sqrt{\epsilon_{xx} - \epsilon_{xy}} \quad (\text{I.6})$$

Therefore, the Faraday effect can be then explained as follows: when a polarized light propagates in a direction parallel to that of the magnetic field, it can be decomposed into RCV and LCV inside the MO material. Each propagates at different velocities (c/n_+ and c/n_-) and have different absorption coefficients (κ_+ and κ_-) due to the applied magnetic field. Therefore, when they recombine at the exit of the material, an elliptical polarization is obtained. Its large axis is rotated by an angle θ_F (with respect to the direction of the initial polarization) and an ellipticity ζ_F appears.

The FR is a cumulative effect, proportional to the RCV and LCV phase shift and is expressed as follows [ZK97]:

$$\theta_F = \frac{\pi L}{\lambda_0}(n_+ - n_-) = \frac{\pi L}{\lambda_0} \text{Re}(N_+ - N_-) = \frac{\pi L}{\lambda_0} \text{Re}(\sqrt{\epsilon_{xx} + \epsilon_{xy}} - \sqrt{\epsilon_{xx} - \epsilon_{xy}}) \quad (\text{I.7})$$

The Faraday ellipticity (FE) is also a cumulative effect, proportional to the RCV and LCV absorption shift and is given as follows [ZK97]:

$$\zeta_F = \frac{\pi L}{\lambda_0}(\kappa_+ - \kappa_-) = \frac{\pi L}{\lambda_0} \text{Im}(N_+ - N_-) = \frac{\pi L}{\lambda_0} \text{Im}(\sqrt{\epsilon_{xx} + \epsilon_{xy}} - \sqrt{\epsilon_{xx} - \epsilon_{xy}}) \quad (\text{I.8})$$

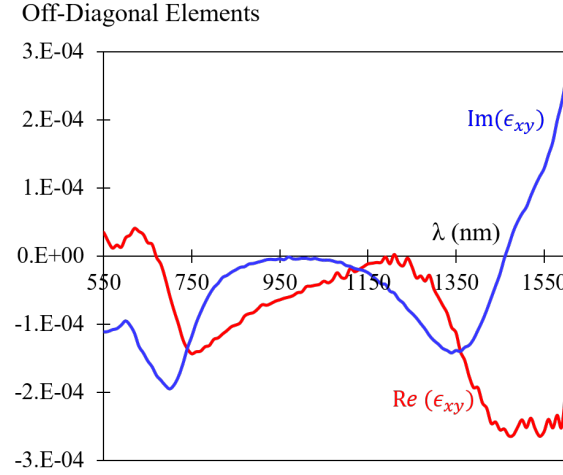


FIGURE I.2: Real and imaginary part of the off-diagonal term of the permittivity tensor, for a ferrofluid containing cobalt ferrite nanoparticles with a volume fraction of 1%.

Knowing that the off-diagonal term ϵ_{xy} is very weak as compared to the diagonal term ϵ_{xx} , with the help of the Taylor series we can write:

$$N_+ - N_- = \sqrt{\epsilon_{xx} + \epsilon_{xy}} - \sqrt{\epsilon_{xx} - \epsilon_{xy}} \approx \frac{\epsilon_{xy}}{\sqrt{\epsilon_{xx}}} \quad (\text{I.9})$$

Thus, the FR and FE can be simplified to:

$$\theta_F \approx \frac{\pi L}{\lambda_0} \text{Re}\left(\frac{\epsilon_{xy}}{\sqrt{\epsilon_{xx}}}\right) \quad (\text{I.10})$$

$$\zeta_F \approx \frac{\pi L}{\lambda_0} \text{Im}\left(\frac{\epsilon_{xy}}{\sqrt{\epsilon_{xx}}}\right) \quad (\text{I.11})$$

In the case of diamagnetic materials, ϵ_{xy} is proportional to the amplitude of the magnetic field [ZK97] and so the FR. This is illustrated on Fig.I.3a, where the normalized FR as a function of the magnetic field is plotted for a glass substrate. Hence the FR of diamagnetic materials can be expressed by the following equation:

$$\theta_F = V.B.L \quad (\text{I.12})$$

The constant V , called the Verdet constant, is defined as the rotation per unit of length and per unit of field ($^{\circ}.cm^{-1}.mT^{-1}$). It depends on the medium properties such as the refractive index dispersion, the light wavelength and the temperature. An example of the glass' Verdet constant is given in Fig.I.3b as function of the wavelength. As seen in this figure, V is inversely proportional to the wavelength and its value is weak, of the order of $0.0001^{\circ}.cm^{-1}.mT^{-1}$ around $\lambda = 1550$ nm.

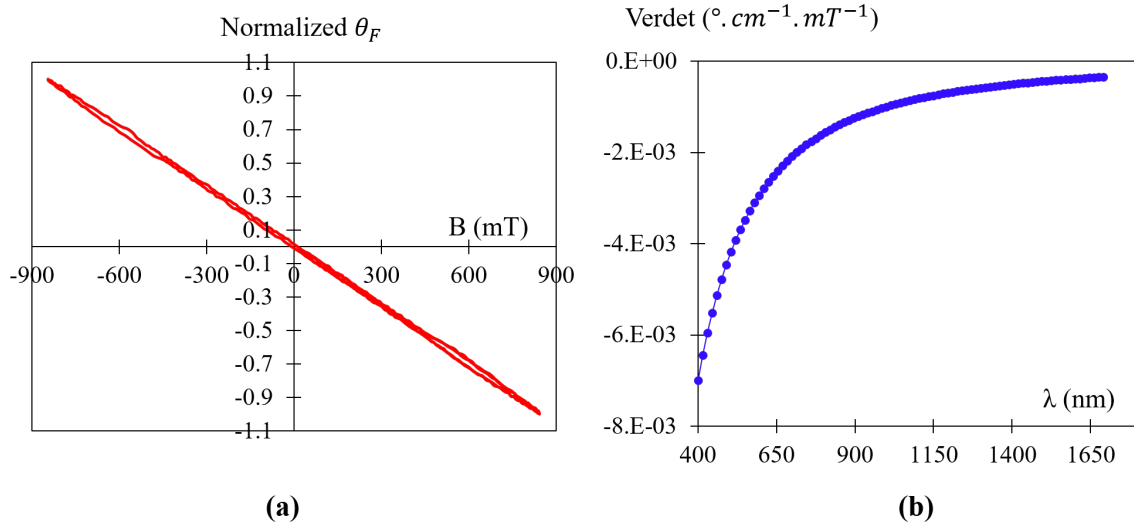


FIGURE I.3: Measurements of: (a) normalized Faraday rotation as a function of the magnetic field at $\lambda = 400$ nm; (b) Verdet constant as a function of the wavelength, for a 0.1-cm-thick glass substrate.

In the case of ferro or ferrimagnetic materials, ϵ_{xy} is proportional to the magnetization M [ZK97] and the Eq.I.10 becomes:

$$\theta_F \approx \frac{\pi L}{\lambda_0} \text{Re}\left(\frac{\epsilon_{xy}}{\sqrt{\epsilon_{xx}}}\right) \approx \frac{\pi L}{\lambda_0} \text{Re}\left(\frac{\mathcal{C}M}{\sqrt{\epsilon_{xx}}}\right) \quad (\text{I.13})$$

where, \mathcal{C} is a dispersive constant. This is illustrated on Fig.I.4a for ferrite material by the FR hysteresis loop, where a remanent rotation is observed insuring the proportionality of the FR to the medium magnetization rather than the applied magnetic field.

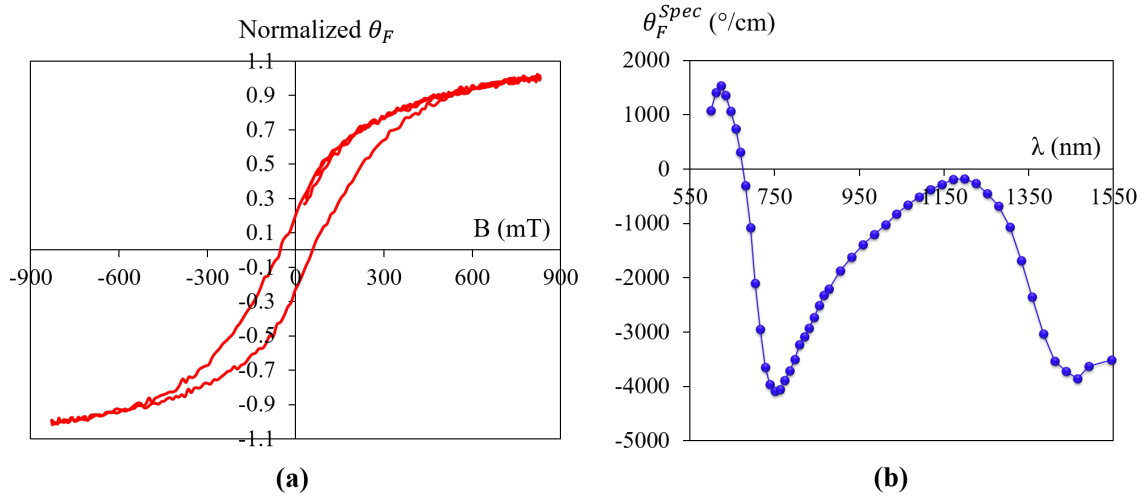


FIGURE I.4: Measurements of: (a) normalized FR hysteresis loop at $\lambda = 820$ nm; (b) specific FR at saturation as a function of the wavelength, for a film made by cobalt ferrite nanoparticles with a volume fraction of 26%, embedded in a silica matrix.

The FR is measured in degrees ($^\circ$), however to quantify the specific rotation of the medium,

the saturated FR should be divided by the propagation length L . Hence, the expression of the specific Faraday rotation expressed in $(^\circ)/cm$ is defined as below:

$$\theta_F^{spec} = \frac{\theta_F(^{\circ})}{L(cm)} \quad (I.14)$$

An example of the specific FR spectrum is giving in Fig.I.4b. The spectrum behavior is related to that of the real part of ϵ_{xy} presented in Fig.I.2 since it is the same MO material (cobalt ferrite nanoparticles).

An important feature of the Faraday effect is its non-reciprocity. As explained before, the FR is the result of a coupling between two electric field components under the influence of the Lorentz force. The direction of this latter, in other words the direction of the FR, depends on the direction of the magnetic field and of the electron oscillations, but not on the direction of the light propagation. Therefore, a polarized wave going back and forth in the material undergoes a polarization rotation equal to $2\theta_F$: the effect is doubled rather than canceled, as seen in Fig.I.5.

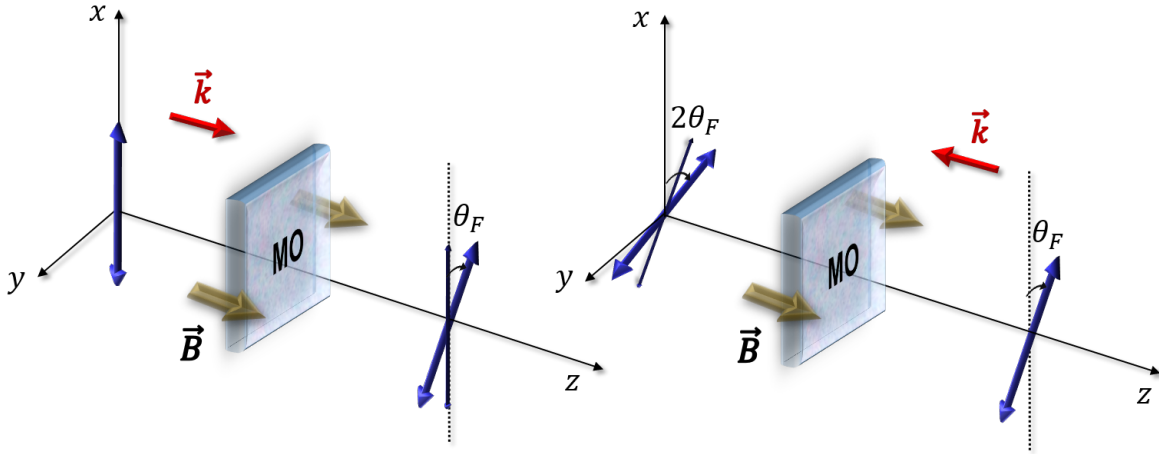


FIGURE I.5: Schematic description of the the non-reciprocal character of the Faraday effect.

I.1.1.2 Magneto-Optical Kerr Effects

In 1877, John Kerr discovered MO effects in reflection geometry, whose a part of these effects are similar to the Faraday effect and the other part belongs to the phase and intensity modulation effects.

Depending on the orientation of the applied magnetic field \vec{B} with respect to the sample surface and the incidence plane, three types of MO Kerr effects can be defined: the polar, longitudinal and transverse Kerr effects.

Since the Kerr effects are often observed in reflection with an angle of incidence (AOI) different from zero, two eigenstates of the light are defined with respect to the plane of incidence. These are two linearly polarizations, perpendicular to each other, noted s (senkrecht or perpendicular) and p (parallel) and defined as follows:

- p -polarization: where the direction of the electric field \vec{E} of the wave is in the incidence plane.
- s -polarization: where the direction of the electric field \vec{E} of the wave is transverse to the incidence plane.

In a semi-infinite MO material, the MO Kerr are interface and non-propagating effects contrary to the Faraday effect. Hence, the polarization rotation and the ellipticity can result from a shift of the complex Fresnel coefficient in reflection of the RCV (r_+) and LCV (r_-), due to the shift of the RCV and LCV complex refractive indices (N_+ and N_-) under the influence of a magnetic field as explained before. Hence, if the incident light is p -polarized the reflected light will have p and s -polarized light with an ellipticity.

However, through thin devices, the MO Kerr effects are interface and propagating effects. The schematic geometry of the different MO Kerr effects are illustrated on Fig.I.6 for a semi-infinite MO material. The description of each effect will be detailed in the following paragraphs.

Polar Magneto-Optical Kerr Effect (PMOKE): This effect occurs when the polarized light is reflected by a sample magnetized perpendicularly to its reflecting surface (see Fig.I.6a). Hence, the polar effect has the same magnetic field configuration than the Faraday effect and the corresponding permittivity tensor of the MO material is the same than Eq.I.4:

$$\begin{pmatrix} \epsilon_{xx} & i\epsilon_{xy} & 0 \\ -i\epsilon_{xy} & \epsilon_{xx} & 0 \\ 0 & 0 & \epsilon_{xx} \end{pmatrix} \quad (\text{I.15})$$

The reflected light undergoes both a rotation of the plane of polarization and an ellipticity. The polarization rotation (θ_{PMOKE}) and the ellipticity (ζ_{PMOKE}) in a semi-infinite MO material, are given as follows [ZK97]:

$$\theta_{\text{PMOKE}}^{s,p} = \text{Re}\left(\frac{r_{ps}(r_{sp})}{r_{ss}(r_{pp})}\right) = \text{Im}\left\{\frac{\eta^2[(\eta^2 - \sin^2(\theta_{\text{inc}}))^{1/2} \mp \sin(\theta_{\text{inc}})\tan(\theta_{\text{inc}})]}{(\eta^2 - 1)(\eta^2 - \tan^2(\theta_{\text{inc}}))}\left(\frac{\epsilon_{xy}}{\epsilon_{xx}}\right)\right\} \quad (\text{I.16})$$

$$\zeta_{\text{PMOKE}}^{s,p} = \text{Im}\left(\frac{r_{ps}(r_{sp})}{r_{ss}(r_{pp})}\right) = \text{Re}\left\{\frac{\eta^2[(\eta^2 - \sin^2(\theta_{\text{inc}}))^{1/2} \mp \sin(\theta_{\text{inc}})\tan(\theta_{\text{inc}})]}{(\eta^2 - 1)(\eta^2 - \tan^2(\theta_{\text{inc}}))}\left(\frac{\epsilon_{xy}}{\epsilon_{xx}}\right)\right\} \quad (\text{I.17})$$

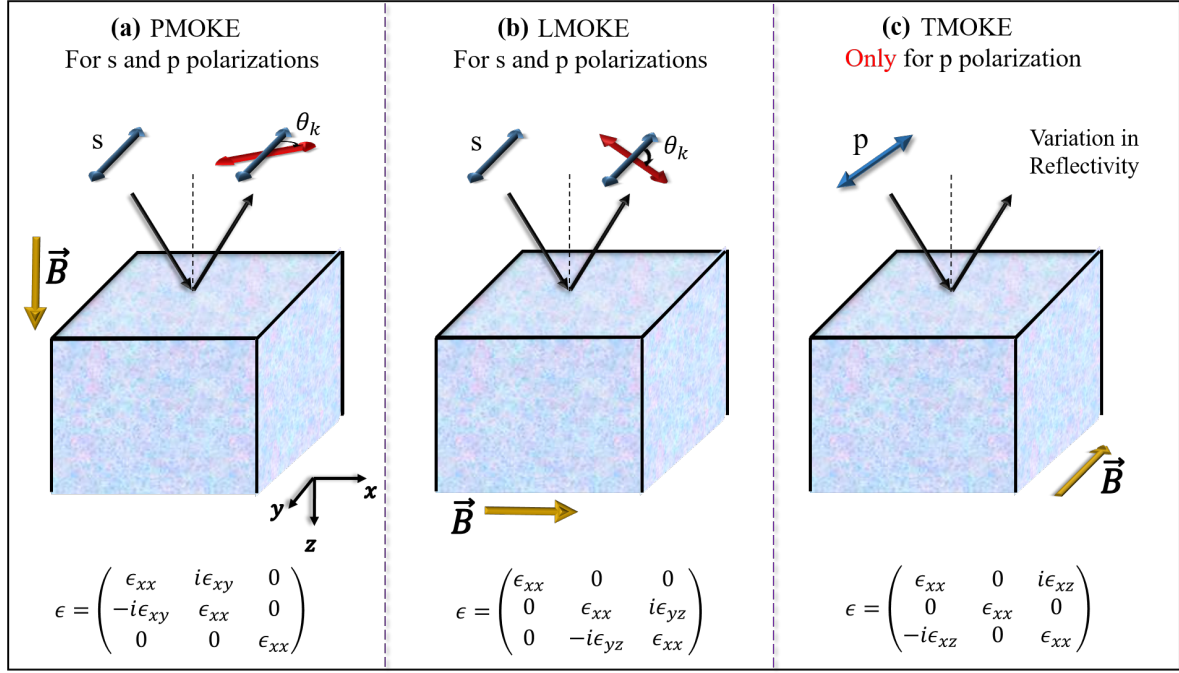


FIGURE I.6: Schematic illustration of the different configurations of the magneto-optical Kerr effects with the corresponding permittivity tensor.

where, θ_{inc} is the incident angle, $\eta = N_{MO}/N_{inc}$ is the ratio of the complex indices of the MO material and the incident medium. r_{ps} is the reflection component of the p -polarization generated from the s -polarized incident light and vice-versa. r_{ss} (or r_{pp}) is the reflection component of the s -polarization (or p -polarization) generated from the s -polarization (or p -polarization).

The upper sign corresponds to s -polarization and the lower sign to p -polarization of light.

Longitudinal Magneto-Optical Kerr Effect (LMOKE): This effect manifests in a rotation of the polarization plane and in the emergence of the ellipticity when a polarized light is reflected on the surface of a sample. This latter is subjected to a magnetic field lying in the incidence and the interface planes (see Fig.I.6b).

In this effect, there is a coupling between s -polarization (following y direction) and the z component of p -polarization, hence the permittivity of the MO material is now defined as:

$$\epsilon = \begin{pmatrix} \epsilon_{xx} & 0 & 0 \\ 0 & \epsilon_{xx} & i\epsilon_{yz} \\ 0 & -i\epsilon_{yz} & \epsilon_{xx} \end{pmatrix} \quad (I.18)$$

The polarization rotation and the ellipticity, in a semi-infinite MO material, are expressed as follows [ZK97]:

$$\theta_{LMOKE}^{s,p} = \text{Re}\left(\frac{r_{ps}(r_{sp})}{r_{pp}(r_{ss})}\right) = \text{Im}\left\{\frac{\sin(\theta_{inc})\eta^2[\sin(\theta_{inc})\tan(\theta_{inc}) \pm \sqrt{\eta^2 - \sin^2(\theta_{inc})}]}{(\eta^2 - 1)(\eta^2 - \tan^2(\theta_{inc}))[\eta^2 - \sin^2(\theta_{inc})]^{1/2}}\left(\frac{\epsilon_{xy}}{\epsilon_{xx}}\right)\right\} \quad (I.19)$$

$$\xi_{LMOKE}^{s,p} = \text{Im}\left(\frac{r_{ps}(r_{sp})}{r_{pp}(r_{ss})}\right) = \text{Re}\left\{\frac{\sin(\theta_{inc})\eta^2[\sin(\theta_{inc})\tan(\theta_{inc}) \pm \sqrt{\eta^2 - \sin^2(\theta_{inc})}]}{(\eta^2 - 1)(\eta^2 - \tan^2(\theta_{inc}))[\eta^2 - \sin^2(\theta_{inc})]^{1/2}}\left(\frac{\epsilon_{xy}}{\epsilon_{xx}}\right)\right\} \quad (\text{I.20})$$

The PMOKE and LMOKE mainly belong to the group of polarization rotation effects. However, under certain conditions, variations in intensity and phase of the polarized light can be observed since the wave vector \vec{k} can have a component perpendicular to the direction of the magnetic field, in case of oblique incidence [ZK97].

Fig.I.7 illustrates the polarization rotation calculated for the PMOKE and LMOKE as a function of the AOI using Eq.I.16 and Eq.I.19 respectively, for s-polarization and for a bulk of BIG with $\epsilon_{xx} = 6.7 + i0.053$ and $\epsilon_{xy} = 0.016 - i0.0092$ [YC+13]. It can be noted that the PMOKE (Fig.I.7a) decreases with AOI increasing, and that the LMOKE (Fig.I.7b) is zero at the normal incidence then it increases with the incident angle until a maximum value and then decreases. We can see also that these two effects are very small, of the order of 0.01° . Hence, for practical applications these effects should be enhanced and this will be one of the objectives of the presented work.

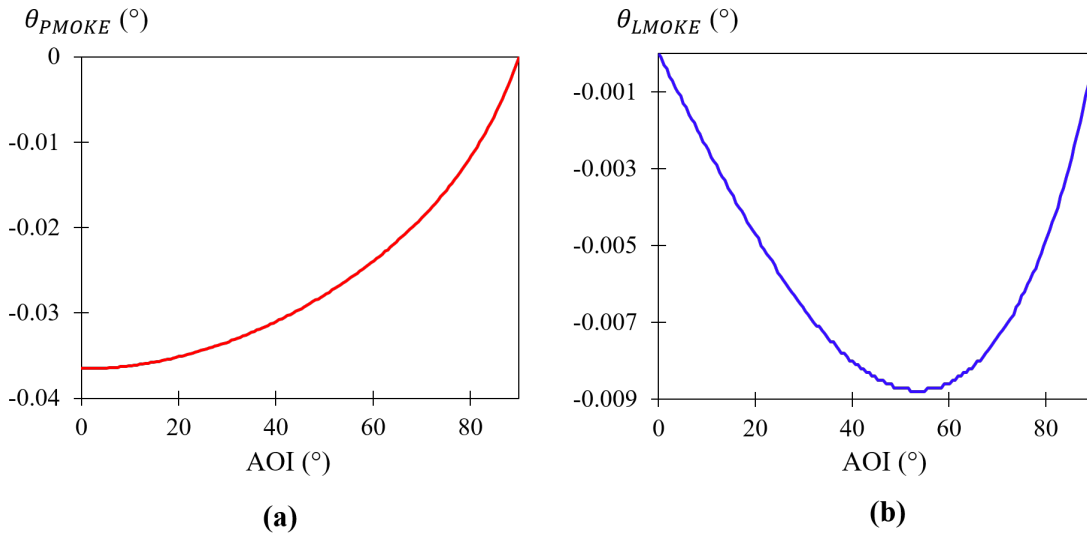


FIGURE I.7: Theoretical values of the (a) longitudinal and (b) polar magneto-optical Kerr effects as functions of the incident angle, for s-polarization and for a bulk of BIG ($\epsilon_{xx} = 6.7 + i0.053$ and $\epsilon_{xy} = 0.016 - i0.0092$ [YC+13]).

Transverse Magneto-Optical Kerr Effect (TMOKE): This effect is called transverse effect since the projection of the wave vector \vec{k} on the magnetization direction \vec{B} is zero. Hence, the magnetization lies in the interface plane and is perpendicular to incidence plane (see Fig.I.6c). This means that the magnetic field is parallel to s-polarization, that's why this effect exists only for p-polarized light. Therefore, a coupling between the components of the p-polarization (following x and z directions) is obtained, generating a variation in the intensity of the reflection coefficient or the phase, of the polarized light upon magnetization reversal

rather than polarization rotation. The permittivity of the MO material is defined here as:

$$\begin{pmatrix} \epsilon_{xx} & 0 & i\epsilon_{xz} \\ 0 & \epsilon_{xx} & 0 \\ -i\epsilon_{xz} & 0 & \epsilon_{xx} \end{pmatrix} \quad (\text{I.21})$$

Generally the TMOKE is defined as the relative change of the intensity I under a magnetization reversal M [ZK97]:

$$\delta = \frac{I(M) - I(-M)}{I(0)} = -\text{Im}\left\{ \frac{4\tan(\theta_{inc})\eta^2}{(\eta^2 - 1)(\eta^2 - \tan^2(\theta_{inc}))} \left(\frac{\epsilon_{xy}}{\epsilon_{xx}} \right) \right\} \quad (\text{I.22})$$

The TMOKE signal for bulk Cobalt or Nickel is of order of 0.1% [Poh+13], hence its detection is challenging, limiting its application. Therefore, the enhancement of this effect is fundamental and will be one of the objectives of this work.

In this section, the different MO effects (Faraday and Kerr) and their physical origin have been detaily described in bulk materials. However, in this work we will be interested to thin devices (MO film deposited on a substrate) and the MO effects will be studied in free space and in guided configuration. In free space, the Faraday effect is propagating and interface effects, but these latter are very weak compared to the propagation effects leading to a Faraday definition as in bulk materials. The Kerr effects for thin devices are also interface and propagating effects and it can be studied in reflection and in transmission geometries, which is not the case of semi-infinite MO material (here the Kerr effect is interface and only in reflection).

The next section will be dedicated to MO effects in guided configuration. To understand well this latter, a presentation of TE and TM guided-modes in a dielectric planar waveguide, as well as a presentation of plasmonic guided-modes at metallic/dielectric half space interface, should be introduced. This will be the aim of the next section.

I.1.2 Magneto-Optical Effects in Guided Configuration

I.1.2.1 Dielectric Planar Waveguides Modes

The basic structure of a dielectric waveguide is generally presented by a slab, strip or cylinder of a dielectric material embedded in other dielectric materials of lower refractive index (see Fig.I.8). The light is confined in the inner medium and transported by multiple total internal reflections at the boundaries.

The slab optical waveguide (Fig.I.8a) consists of a longitudinally extended medium (called the film) of thickness d and refractive index n_f which is surrounded by a substrate and a cover material (generally air) with lower indices: n_s and n_c respectively. The cross section of the slab waveguide in the xz plane (referring to Fig.I.8) is illustrated on Fig.I.9. The underlying principle of optical confinement is simple. In the guiding film, if the light propagation direction is oriented with an angle greater than the corresponding critical angles, the wave undergoes successive total internal reflections, and the rays propagate inside the film with a longitudinal

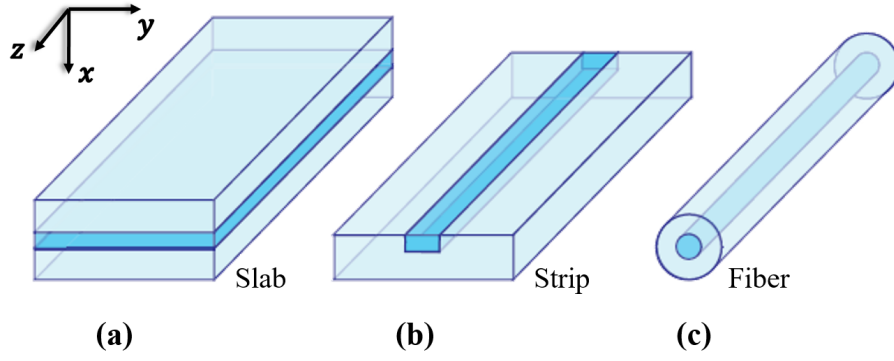


FIGURE I.8: Schematic geometries of the different optical waveguides: (a) slab, (b) strip and (c) fiber. This figure is taken from [MCB01].

propagation constant called β and expressed as follows:

$$\beta = k_0 n_f \cos(\Omega) = k_0 N_{eff} \quad (I.23)$$

where, k_0 is the wavenumber in the vacuum, Ω is the angle between \vec{k} ($k = n_f k_0$) and z axis, and N_{eff} is the effective index of the guided-mode.

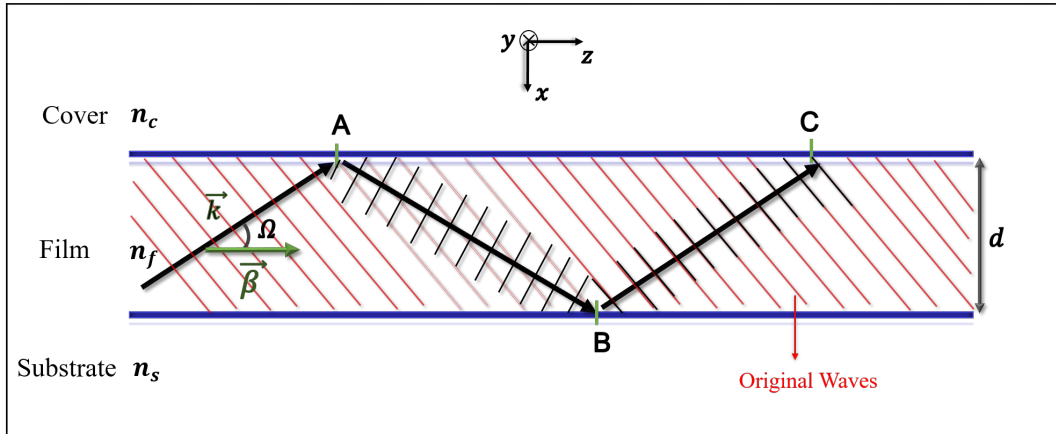


FIGURE I.9: Cross section of a planar dielectric waveguide, where the light is trapped inside by total reflections and propagates with a propagation constant β .

Field Profile Distribution

The confined light wave is named guided-mode and it is described by an electromagnetic field (\vec{E}, \vec{H}) . In the case of a planar waveguide, the wave propagating in z direction doesn't undergo variations in y direction. Hence, the electric and magnetic fields of a mode can be expressed as follows:

$$E_m(r, t) = \mathcal{E}_m(x) e^{j(\beta_m z - \omega t)} \quad (I.24)$$

$$H_m(r, t) = \mathcal{H}_m(x) e^{j(\beta_m z - \omega t)} \quad (I.25)$$

where m is the guided-mode index, $\mathcal{E}_m(x)$ and $\mathcal{H}_m(x)$ are the mode field profiles and β_m is the mode propagation constant.

By resolving the Maxwell's equations, only two types of electromagnetic waves can be presented inside a dielectric planar waveguide [Liu05]:

- The TE (Transverse Electric) mode which has three non-zero components: \mathcal{E}_y , \mathcal{H}_z and \mathcal{H}_x . The wave equation is expressed as follows [Liu05]:

$$\frac{\partial^2 \mathcal{E}_{my}}{\partial x^2} + (k_i^2 - \beta_m^2) \mathcal{E}_{my} = 0 \quad (\text{I.26})$$

where, k_i corresponds to the wave number of the medium (air, substrate or film).

And the equations of \mathcal{H}_x and \mathcal{H}_z are expressed respectively as [Liu05]:

$$\mathcal{H}_{mx} = \frac{-\beta_m}{w\mu_0} \mathcal{E}_{my} \quad (\text{I.27})$$

$$\mathcal{H}_{mz} = \frac{1}{jw\mu_0} \frac{\partial \mathcal{E}_{my}}{\partial x} \quad (\text{I.28})$$

- The TM (Transverse Magnetic) mode which has three non-zero components: \mathcal{H}_y , \mathcal{E}_x and \mathcal{E}_z . The wave equation and the expressions of \mathcal{E}_x and \mathcal{E}_z are given as follows [Liu05]:

$$\frac{\partial^2 \mathcal{H}_{my}}{\partial x^2} + (k_i^2 - \beta_m^2) \mathcal{H}_{my} = 0 \quad (\text{I.29})$$

$$\mathcal{E}_{mx} = \frac{\beta_m}{w\epsilon_i} \mathcal{H}_{my} \quad (\text{I.30})$$

$$\mathcal{E}_{mz} = \frac{-1}{jw\epsilon_i} \frac{\partial \mathcal{H}_{my}}{\partial x} \quad (\text{I.31})$$

where ϵ_i is the dielectric function of each medium.

Fig.I.10a-b illustrates the TE electric (\mathcal{E}_{0y}) and the TM magnetic (\mathcal{H}_{0y}) field distribution, calculated from the solutions of Eq.I.26 and Eq.I.29 respectively, for the fundamental modes. Here, the used waveguide is asymmetric with thickness equal to 600 nm, and with: $n_f = 1.64$, $n_s = 1.51$ and $n_c = 1$ at $\lambda = 1550$ nm. As seen in Fig.I.10a-b, the magnitude of the electric field \mathcal{E}_{0y} or magnetic field \mathcal{H}_{0y} is maximum close to the substrate-film interface due to refractive index asymmetry of the structure, and an important part of the field is present in the substrate.

From Eq.I.31 and Eq.I.30, the electric field components (\mathcal{E}_{0x} and \mathcal{E}_{0z}) of TM fundamental mode were calculated and plotted on Fig.I.10c-d. As seen in this figure, the magnitude of the longitudinal component (\mathcal{E}_{0z}) is smaller than the transverse one (\mathcal{E}_{0x}). In addition to that, \mathcal{E}_{0z} is maximum at the air-film boundaries, for this reason this TM field component is sensitive to any changes in the cover medium. The discontinuity of \mathcal{E}_{0x} at the waveguide boundaries is linked to ϵ_i in Eq.I.30, which is not the same for the three regions.

In the presented thesis, the film will be surrounded on top by a grating with effective index of $n_c = 1.4$ at $\lambda = 1550$ nm, rather than only air. Hence, the field distributions will be slightly

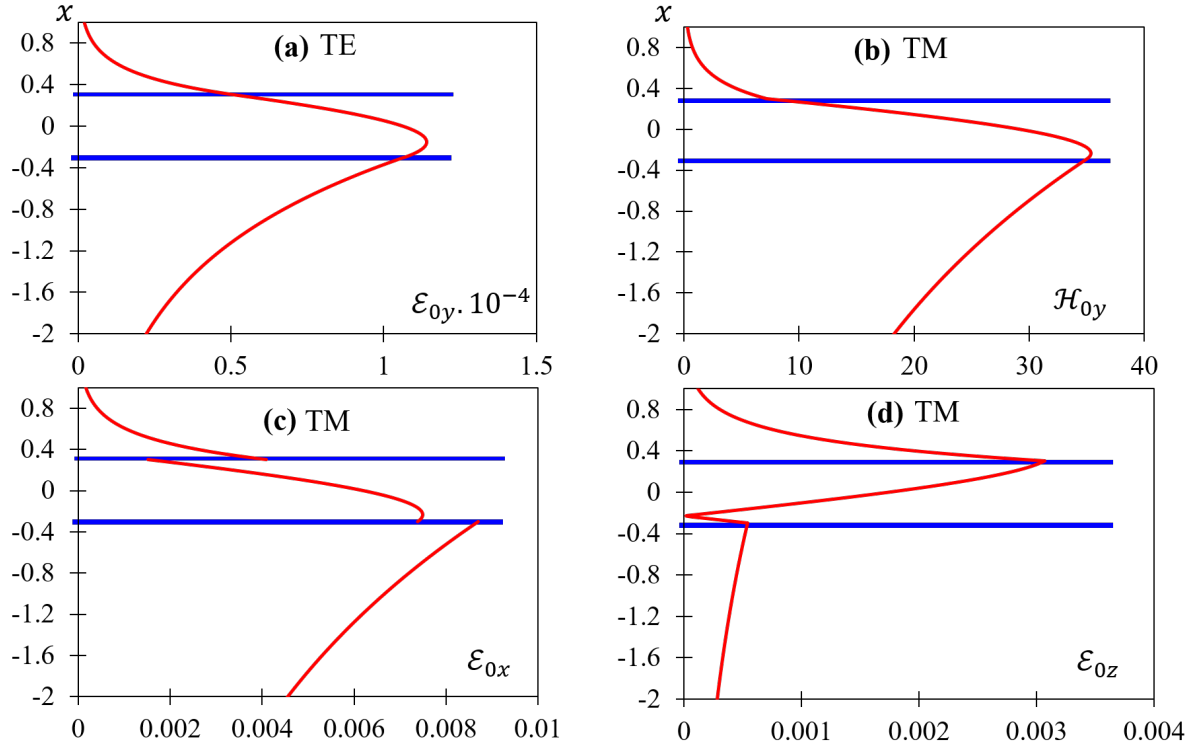


FIGURE I.10: Field Distribution of: (a) \mathcal{E}_y for TE mode; (b) \mathcal{H}_y , (c) \mathcal{E}_x , and (d) \mathcal{E}_z for TM mode, in a 600 nm-thick waveguide with $n_c = 1$, $n_f = 1.64$ and $n_s = 1.51$ at $\lambda = 1550$ nm.

modified with a maximum amplitude of \mathcal{E}_{0y} , \mathcal{H}_{0y} and \mathcal{E}_{0x} at the center of the film. However, \mathcal{E}_{0z} will be minimum in this region and maximum at the waveguide boundaries.

The underlying of the field distribution of the different components of the guided-modes, especially the TM mode, will be very helpful to understand some phenomena that will be presented later in this manuscript.

As a summary, the planar dielectric waveguide can only support TE and TM guided-modes. The TE mode has one electric field component, whereas the TM mode has two electric field components where the transverse one is more important than the longitudinal one. Moreover, the magnitude of this latter is maximum at the waveguide boundaries and minimum at the center.

The next section will be dedicated to the description of the propagation equations of the TE and TM guided-modes in a planar dielectric waveguide.

Modes Propagation Equations

Inside the waveguide the reflected light interferes with the original waves, and the guided-modes originate from constructive interferences. Hence, according to Fig.I.9, the phase shift between the original waves and the twice reflected wave (ABC) should be $2\pi m$ at point C.

The total phase shift accumulated by the twice reflected light is:

$$\varphi = \varphi_{cf} + \varphi_{sf} + \varphi_{\delta} = 2\pi m \quad (\text{I.32})$$

φ_{δ} is the phase shift due to the optical path difference (ABC) and it expressed as follows [Liu05]:

$$\varphi_{\delta} = 2d\sqrt{k_0^2 n_f^2 - \beta_m^2} \quad (\text{I.33})$$

φ_{cf} and φ_{sf} are the phase shifts accumulated due to the reflection on the interfaces cover-film and substrate-film respectively. These phase shift are not the same for TE and TM modes [Liu05]:

- For TE-mode:

$$\varphi_{cf} = -2 \arctan \left[\sqrt{\frac{\beta_m^2 - k_0^2 n_c^2}{k_0^2 n_f^2 - \beta_m^2}} \right] \quad (\text{I.34})$$

- For TM-mode:

$$\varphi_{cf} = -2 \arctan \left[\left(\frac{n_f^2}{n_c^2} \right) \sqrt{\frac{\beta_m^2 a^2 - k_0^2 n_c^2}{k_0^2 n_f^2 - \beta_m^2}} \right] \quad (\text{I.35})$$

φ_{sf} for TE and TM modes are defined in the same way than Eq.I.34 and Eq.I.35 respectively, provided that n_c is replaced by n_s . By replacing in Eq.I.32 the expressions of φ_{cf} , φ_{sf} and φ_{δ} , one gets the propagation equations of each mode defined as:

For TE-mode:

$$d\sqrt{k_0^2 n_f^2 - \beta_m^2} - \arctan \left[\sqrt{\frac{\beta_m^2 - k_0^2 n_s^2}{k_0^2 n_f^2 - \beta_m^2}} \right] - \arctan \left[\sqrt{\frac{\beta_m^2 - k_0^2 n_c^2}{k_0^2 n_f^2 - \beta_m^2}} \right] = m\pi \quad (\text{I.36})$$

For TM-mode:

$$d\sqrt{k_0^2 n_f^2 - \beta_m^2} - \arctan \left[\left(\frac{n_f^2}{n_s^2} \right) \sqrt{\frac{\beta_m^2 - k_0^2 n_s^2}{k_0^2 n_f^2 - \beta_m^2}} \right] - \arctan \left[\left(\frac{n_f^2}{n_c^2} \right) \sqrt{\frac{\beta_m^2 - k_0^2 n_c^2}{k_0^2 n_f^2 - \beta_m^2}} \right] = m\pi \quad (\text{I.37})$$

The values of N_{eff} , solutions of Eq.I.36 and Eq.I.37, are plotted on Fig.I.11a as a function of the film thickness at $\lambda = 1550$ nm. The optical parameters of the used waveguide are: $n_f = 1.64$, $n_s = 1.51$ and $n_c = 1$. As seen in this figure, the number of the propagated modes depends on the film thickness. For example, if the thickness is equal to $1 \mu m$ only the pair (TE and TM) of fundamental modes can propagate: in this case the waveguide is called monomode. However, if the thickness is equal to $4 \mu m$, three pairs of TE and TM modes can propagate and the waveguide is named multimode. We can also see in Fig.I.11a, that the modes don't always exist: a sufficient thickness of guiding layer is necessary. The TE and TM dispersion curves for a fixed mode m are different. This difference is named phase shift $\Delta\beta$ or modal birefringence ΔN_{eff} :

$$\Delta\beta = \beta_{TE} - \beta_{TM} = k_0 \Delta N_{eff} \quad (\text{I.38})$$

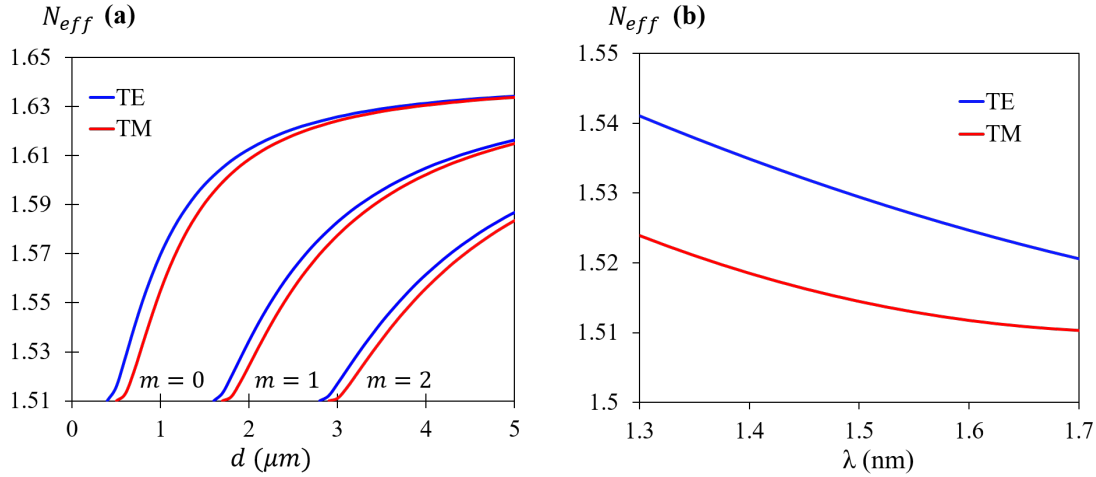


FIGURE I.11: Theoretical values of the effective index of TE and TM modes: (a) as a function of the thickness at $\lambda = 1550$ nm for different propagation modes m ; (b) as a function of the wavelength for a 600 nm-thick waveguide and for $m = 0$. The refractive indices of the film, substrate and cover are respectively: 1.64, 1.51 and 1.

This phase shift is mainly due to the geometric profile of the waveguide, and the intrinsic birefringence of the used material can modify this value.

Fig. I.11b illustrates the effective index as a function of the wavelength for $d = 600$ nm for TE and TM modes. As seen in this figure, the modal birefringence is varying with the wavelength.

After describing the optical properties of the TE and TM guided-modes in a planar dielectric waveguide, in the next section we will describe the fundamentals of an other type of guided-modes: the plasmonic modes that propagate at metal/dielectric interface.

I.1.2.2 Plasmonic Modes

The surface plasmon polaritons (SPPs) [Mai07] are described by coupled oscillations of the electromagnetic field and the electron plasma in a metal, which are guided along a metal/dielectric interface and evanescently confined in the perpendicular direction.

The simplest geometry sustaining SPPs is that of a single, flat interface (see Fig. I.12a) between a dielectric, non-absorbing half space ($x > 0$) described via a positive real dielectric constant ϵ_d , and an adjacent metal, conducting half space ($x < 0$) owing a dielectric function ($\epsilon_m(w)$) with $Re[\epsilon_m(w)] < 0$.

The dispersion relation of SPPs propagating at the metal/dielectric half space interface is given as follows [Mai07]:

$$\beta_{SPPs} = k_0 \sqrt{\frac{\epsilon_d \cdot \epsilon_m}{\epsilon_m + \epsilon_d}} \quad (I.39)$$

where k_0 is the wave number in the vacuum for the incident light. This expression is valid for both real and complex ϵ_d and ϵ_m . An example of the propagation constant of SPPs at an Au/air half space interface is illustrated on Fig. I.12b, as a function of the wavelength.

The resolution of Maxwell's equations [Mai07], implies that the SPPs cannot be excited by TE polarization. Hence, surface modes only exist for TM polarization.

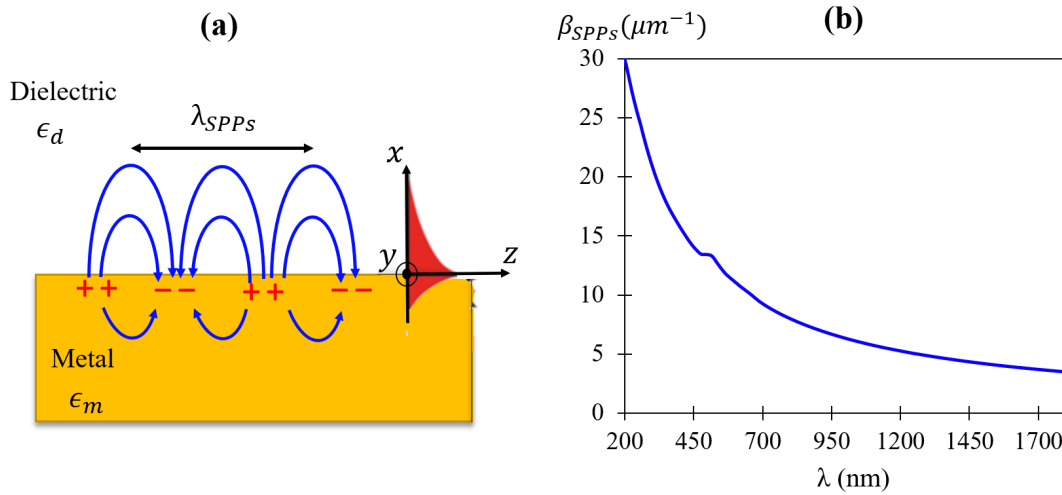


FIGURE I.12: (a) Schematic representation of SPPs guided at metal/dielectric half space interface. (b) SPPs propagation constant dispersion at an Au/air half space interface.

An important feature of the SPPs is that they are highly sensitive to any small changes in the dielectric medium properties, such as the refractive index. This feature allows the SPPs to be used in the biosensors for detecting or identifying dielectric media [Sep+06; RPH18; Reg+11; Man+17], more details on this application will be presented later.

After describing the different guided-modes: TE and TM modes in a planar dielectric waveguide and SPPs modes at a dielectric/metallic interface, now it is the time to present the MO effects in guided configuration. The polarization rotation effects described by modes conversion, will be presented in the next section followed by a description of the phase modulation effects.

I.1.2.3 Modes Conversion in Magneto-Optical Waveguides

It was described in section I.1.1.1, that for the polarization rotation effects ($\vec{k} \parallel \vec{B}$) in free space, the polarization rotation is explained by a phase shift between the eigenmodes of polarization states (RCV and LCV) inside the MO material. Now, if we consider a dielectric planar waveguide made by a MO material and subjected to a magnetic field in the xz plane (Fig.I.13a), this description is still valid when the phase shift $\Delta\beta$ between TE and TM modes is zero. However, as explained before the TE and TM modes generally have different propagation constants ($\Delta\beta \neq 0$). In this case, neither the circular polarization, nor the linearly polarization states can be the eigenmodes of the propagation. The MO effects then, are described as an inter-modes conversion energy (between TE and TM modes) under the influence of a longitudinal magnetic field, which is described by the theory of coupled modes [Yar73].

To quantify the TE-TM coupling, a simple case is considered: a TM mode light is injected, then propagates in the MO waveguide over a distance z . The conversion efficiency $R(z)$ is defined as the ratio of the intensity of TE mode at a distance z on the initial intensity of TM

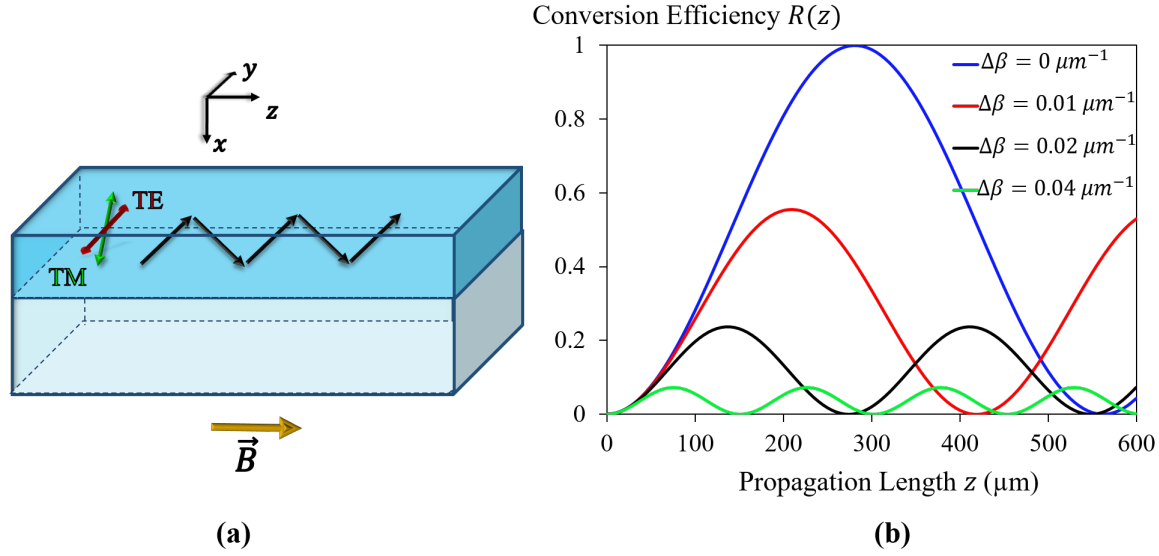


FIGURE I.13: (a) Schematic illustration of TE and TM guided-modes and the magnetic field configuration under study. (b) Calculated values of the TE-TM conversion efficiency as a function of the propagation length for different values of TE-TM phase shift ($\Delta\beta$), with $K = 3200^\circ/\text{cm}$ at $\lambda = 1550 \text{ nm}$.

mode:

$$R(z) = \frac{I_{TE}(z)}{I_{TM}(0)} \quad (\text{I.40})$$

Hence, an efficiency equal to unity means that all the TM mode is converted to TE. Calculations done in Ref. [Yar73], give an expression of $R(z)$ as follows:

$$R(z) = R_M \sin^2[\sqrt{K^2 + (\Delta\beta/2)^2}z] = \frac{K^2}{K^2 + (\Delta\beta/2)^2} \sin^2[\sqrt{K^2 + (\Delta\beta/2)^2}z] \quad (\text{I.41})$$

where, K is the coupling coefficient between TE and TM modes (it corresponds to θ_F^{spec} in free space, expressed in $^\circ/\text{cm}$).

Let's consider the first case where the phase shift is equal to zero. The Eq.I.41 is transformed to:

$$R(z) = \sin^2(Kz) \quad (\text{I.42})$$

As seen in Eq.I.42, $R(z)$ corresponds to the polarization rotation in free space. At a propagation distance $z_c = \pi/2K$, the efficiency is equal to unity: the initial TM mode is totally converted to TE. After a double distance ($z = 2z_c$), the efficiency is zero: the polarization state is returned to its initial state (TM). This behavior is periodical with a period equal to $z_0 = \frac{2z_c}{\sqrt{1 + (\frac{\Delta\beta^2}{2K^2})}} = \frac{\pi}{K}$.

The second case is when TE-TM propagation constants are considered to be different ($\Delta\beta \neq 0$). Here, there is a partial TE-TM conversion where the amplitude (R_M) of the conversion efficiency could not achieve the unity.

Fig.I.13b illustrates the conversion efficiency for different phase shifts as a function of the propagation length. As seen in this figure, R_M and the period z_0 decrease with the increase of $\Delta\beta$ which is consistent with their expressions defined above. One can see also on Fig.I.13b, that for small propagation lengths all the curves are overlapped: the MO effects are described

as in free space.

Therefore, to reach the maximum MO conversion efficiency, the TE-TM phase matching condition should be satisfied.

As a summary, the polarization rotation in guided configuration, is generally explained by modes conversion between TE and TM guided-modes. To achieve a maximum conversion efficiency, the TE-TM phase matching condition ($\Delta\beta=0$) should be satisfied. Nevertheless, for MO effects in transverse configuration (the projection of \vec{k} on the direction of \vec{B} is zero), the phase matching condition is not required since these effects are only for TM polarization (as only for p -polarization in bulk materials). The description of these effects will be introduced in the next section.

I.1.2.4 Phase Modulation in Magneto-Optical Waveguides

As explained in section I.1.1.2, the TMOKE are described by intensity modulation of the reflection coefficient, due to a coupling between the electric field components of p -polarized light.

Now, we will consider a MO waveguide or a MO metal/dielectric half space, subjected to a magnetic field in y direction (referring to Fig.I.8 or Fig.I.12a). Here, the TMOKE induces a phase shift of the guided-wave upon magnetization reversal, due to an intra-modes coupling (between electric field components of the same mode). This phase shift can be interpreted as a difference in the propagation constants and in the absorption coefficients of the TM or SPPs modes. As a result, an intensity modulation of the guided-waves can be produced upon magnetization reversal.

TM mode: Eq.I.43 [Fuj+99] describes the propagation constant of the fundamental TM mode in transverse configuration ($\vec{k} \perp \vec{B}$ and \vec{B} lies in the sample plane). This expression is the same than that of Eq.I.37, taking into account the off-diagonal elements ϵ_{xz} of the MO material's permittivity tensor. One can obviously notice from Eq.I.43 that by modifying the sign of ϵ_{xz} , in other words the magnetization direction ($+\vec{M}$; $-\vec{M}$) since the MO term is odd in magnetization, the propagation constant β of the TM mode is modified. This modification results from the coupling of the TM electric field components: \mathcal{E}_x and \mathcal{E}_z under the influence of a transverse magnetic field.

$$d\sqrt{k_0^2\epsilon_{eff} - \beta^2} = \arctan\left[\frac{\epsilon_{eff}}{\sqrt{k_0^2\epsilon_{eff} - \beta^2}}\left(\frac{\sqrt{\beta^2 - k_0^2\epsilon_s}}{\epsilon_s} + \frac{\beta\epsilon_{xz}}{\epsilon_{xx}\epsilon_{eff}}\right)\right] + \arctan\left[\frac{\epsilon_{eff}}{\sqrt{k_0^2\epsilon_{eff} - \beta^2}}\left(\frac{\sqrt{\beta^2 - k_0^2\epsilon_c}}{\epsilon_c} - \frac{\beta\epsilon_{xz}}{\epsilon_{xx}\epsilon_{eff}}\right)\right] \quad (I.43)$$

With $\epsilon_{eff} = \epsilon_{xx} - \epsilon_{xz}^2/\epsilon_{xx}$

Fig.I.14 illustrates the propagation constant (left axis) of TM mode for two opposite magnetic field directions: $+\vec{M}$ and $-\vec{M}$, and their shift $\Delta\beta_{\pm M}$ (right axis), as a function of the thickness for $\epsilon_{xx} = 2.69$ (Fig.I.14a) and as a function of ϵ_{xx} for $d = 600$ nm (Fig.I.14b). The

studied MO waveguide has the following parameters: $\epsilon_{xz} = 0.0064$, $\epsilon_c = 1$, $\epsilon_s = 2.28$ at $\lambda = 1550$ nm.

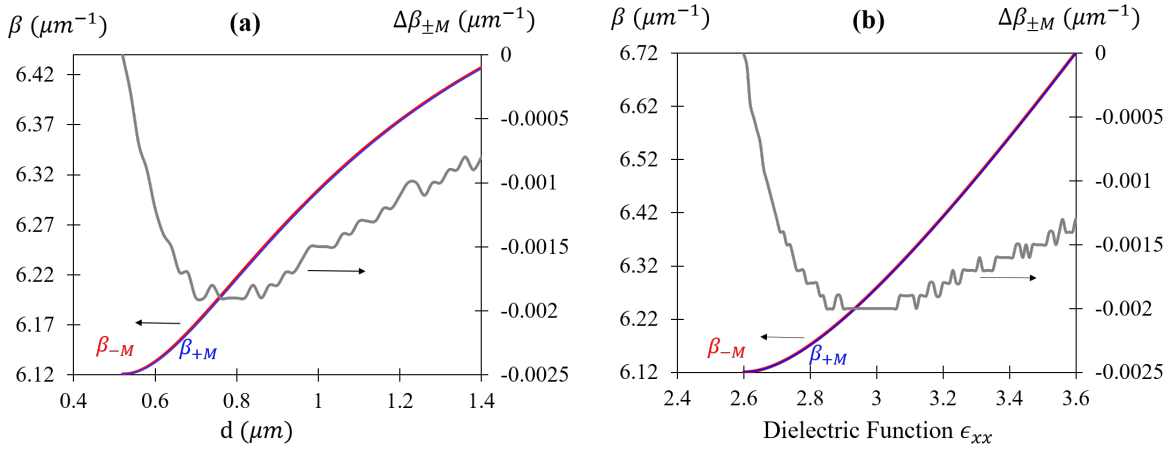


FIGURE I.14: Calculated values of TM propagation constants for opposite magnetization ($\pm M$, red and blue curves) and their phase shift $\Delta\beta_{\pm M}$ at $\lambda = 1550$ nm: (a) as a function of the thickness for $\epsilon_{xx} = 2.69$; (b) as a function of the dielectric function ϵ_{xx} for a 600 nm-thick film. The studied MO waveguide has the following parameters: $\epsilon_{xz} = 0.0064$, $\epsilon_c = 1$, $\epsilon_s = 2.28$ at $\lambda = 1550$ nm.

As seen in Fig. I.14, there is an optimized thickness (d around 780 nm) and dielectric functions (ϵ_{xx} around 2.98) for whose $\Delta\beta$ is maximum and equal to $-0.002 \mu\text{m}^{-1}$.

SPPs modes: In the case of SPPs guided at a metallic/dielectric interface with one of the two media owing MO properties and subjected to transverse magnetic field (\vec{B} following y direction in Fig. I.12), the SPPs propagation constant depends on the magnetic field direction following the equation [Bel+11]:

$$\beta_{SPPs} = k_0 \sqrt{\frac{\epsilon_d \cdot \epsilon_m}{\epsilon_d + \epsilon_m}} \left(1 + \frac{\epsilon_{xz}}{\varrho}\right) \quad (\text{I.44})$$

where,

$$\varrho = \sqrt{-\epsilon_m \epsilon_d} \left(1 - \frac{\epsilon_d^2}{\epsilon_m^2}\right)$$

It is evident that when ϵ_{xz} is zero, Eq. I.44 collapses to Eq. I.39. However, when $\epsilon_{xz} \neq 0$, the SPPs propagation constant is modified when the magnetic field is flipped.

In sections I.1.1 and I.1.2, the different MO effects and their physical origin were described in details, in bulk materials and in guided configuration. These descriptions will serve as a basis to explain the MO effects studied in this work on 1D MO grating. The following section will be dedicated to MO materials.

I.1.3 Magneto-Optical Materials

The different MO materials can be mainly divided into two groups [ZK97]. The first group consists of metals and alloys such as ferromagnetic metals (Co, Ni, Fe, etc.), alloys based on simple metals (CoCr, FeAl, etc.), binary intermetallics (CoPt, MnBi, etc.) or rare earth transition

TABLE I.1: Specific Faraday rotation, specific absorption and figure of merit for different MO materials at different wavelengths, at temperatures less than 10K for Europium compounds and equal to 300K for the others. The properties of the Bi:YIG or Ce:YIG vary with Bi or Ce concentrations.

MO Material	λ (nm)	θ_F^{spec} ($^\circ/cm$)	α (dB/cm)	FoM ($^\circ/dB$)
Fe [Fre68]	546	3.5×10^5	3.3×10^6	0.11
Co [Fre68]	546	3.6×10^5	3.7×10^6	0.10
Ni [Fre68]	400	7.2×10^5	9.1×10^5	0.79
EuO [Alb71]	1000	9×10^4	2.2×10^4	4
EuS [Alb71]	750	7×10^5	1.2×10^4	60
EuSe [Alb71]	750	1.8×10^5	180	1000
YIG [Sek+99; Zha01]	1064	280	65	4.3
	1200	240	50	4.8
	1550	216	23.8	9.1
Bi:YIG [Sek+99]	1550	-1250	2.7	463
Ce:YIG [Sek+99]	1310	-2510	9.8	256
	1550	-1310	2.7	486
CoFe ₂ O ₄ NPs [This work] with $\phi = 1\%$	750	-225	600	0.37
	1490	-220	61	3.5

metals compounds (NdCo, ErFe, etc.). These latter were widely used in MO disk memory systems.

The second group includes dielectric materials such as ferrimagnetic garnets like Yttrium Iron Garnet: YIG ($Y_3Fe_5O_{12}$), Bismuth or Cerium substituted Yttrium Iron Garnet: Bi:YIG ($Bi_xY_{3-x}Fe_5O_{12}$) or Ce:YIG ($Ce_xY_{3-x}Fe_5O_{12}$). The dielectric group contains also orthoferrite, spinel ferrites (like cobalt ferrite $CoFe_2O_4$) or europium compounds (EuO, EuS, EuSe, etc.). The dielectric materials are promising for applications in integrated non-reciprocal devices such as optical isolator, since they present generally low absorption compared to the metals.

For practical applications, the ideal material presents high specific FR (θ_F^{spec} in $^\circ/cm$) and low specific absorption (α in dB/cm). To quantify these two properties of a MO material, a parameter called Figure of Merit (FoM) is defined and expressed as follows [Liu05]:

$$FoM(^\circ/dB) = \frac{\theta_F^{spec}(^\circ/cm)}{\alpha(dB/cm)} \quad (I.45)$$

Table I.1 illustrates the specific FR, absorption and the FoM for different MO materials at different wavelengths. As seen in this table, the ferromagnetic metals such as Fe, Co and Ni present the largest specific FR compared to the other materials. However, the absorption of these metals is very high, leading to the smallest FoM. In the Europium compounds family, EuSe have the largest MO response and transmittance giving a very high FoM of $1000^\circ/dB$ at $\lambda = 750$ nm. But, the disadvantage of this material is that it presents MO activity at very low temperatures (below 20 K).

The ferrimagnet garnet family exhibits in the near IR region high values of FoM, while the values of the specific FR are weak in this region compared to the ferromagnetic metals and europium compounds. Nevertheless, they are the most preferred MO material since they are

highly transparent in the near IR region. However, they present some drawbacks preventing their incorporation in opto-electronic devices and integrated photonic circuits. First, due to the high crystallization temperature of the ferrimagnet garnet (higher than 700°C) and due to a lattice parameter mismatch, they cannot be grown easily on common photonic substrates such as glass, silicon, GaAs, and require substrates as gadolinium gallium garnet (GGG). Good quality iron garnet films require complex fabrication methods such as pulsed laser deposition [Lux+06; Weh+11; Lei+08], sputtering [GTA85; Yan+07; Vas+09; Vas+11], liquid phase epitaxy [Aic+03], etc. To solve this problem, some current works deal with the hybrid integration of YIG films on glass or semiconductor substrates by molecular bonding [MS09; Jou+08]. Another promising approach suitable to realize MO fiber sensors consists to grow directly a YIG nanocrystal on the edge of an optical fiber, using a localized photopolymerisation of YIG precursors through the fiber [Nad19; Nad+19].

The MO material developed in this work, is a composite MO material made of a sol-gel silica matrix doped with cobalt ferrite (CoFe_2O_4) magnetic nanoparticles (NPs). The development and the characterization of the MO sol-gel will be detailed in Chap. II. The specific FR for the NPs are at they maximum values: around $-220^\circ/\text{cm}$ at $\lambda=750\text{ nm}$ and $\lambda=1490\text{ nm}$, for NPs volume fraction (ϕ) equal to 1%. These values are very promising when compared to those of the YIG (see Tab. I.1). In term of FoM, the MO composite yields maximum FoM equal to $3.5^\circ/\text{dB}$ at 1490 nm which is quiet lower than those of the YIG. But a major advantage of the MO composite is its ability to be deposited as uniform thin layers on large scale conventional substrates (glass, silicon, etc.), with simple coating processes (spin, dip-coating, etc.), and with a 100°C thermal treatment.

The different MO materials presented in this section are employed in different applications, whose description will be detailed in the next section.

I.1.4 Magneto-Optical Devices

The important feature of the MO effects as light control under the influence of a magnetic field, allows them to be promising tools for several applications. Some common applications based on the MO effects are listed as bellow:

- MO modulators [ZK97]: devices that control the intensity of optical radiation in optical communication and data-processing systems through an applied magnetic field.
- MO isolators [Sha+13; Onb+16]: core elements in communication and laser systems. They are based on the non-reciprocity feature of the MO effect in order to prevent unwanted reflected light into an optical oscillator, such as laser cavity. The reflected light in the laser cavity can cause amplitude modulation or frequency shift of the emitted wave or can eventually damage the laser in the case of high power sources.
- MO circulators [ZK97; Šmi+10; WF05]: they are used in communication, detection and measurement equipment. The function of a circulator is to physically separate the two directions of propagation of a wave.
- MO imaging [NSM04; Rad+01; Den+06; JP06]: mainly used for the non-destructive control in order to detect, locate and measure discontinuities and imperfections of wide

variety of materials. An example of the MO imaging application is detecting, through eddy currents, fatigue cracks and hidden corrosion zones on an aircraft surface.

- MO sensors: can be used to measure the electric current [NCJ91; DF08], the magnetic field [SSH90; Ami+18] as well as to identify a dielectric media [Sep+06; Reg+11].

The next paragraph will be dedicated to such sensors.

I.1.4.1 Magnetic Field Sensors

The MO magnetic field sensors are based on the Faraday effect, where the measurement of the light polarization rotation leads directly to the amplitude of the magnetic field. Fig.I.15 illustrates a magnetic field sensor based on a planar waveguide formed by Gd, Ga-substituted YIG material synthesized on GGG substrate [SS91], the thickness of the YIG can be in the range of 5-10 μm . One or two optical fibers are attached to the front of the sensing element and the

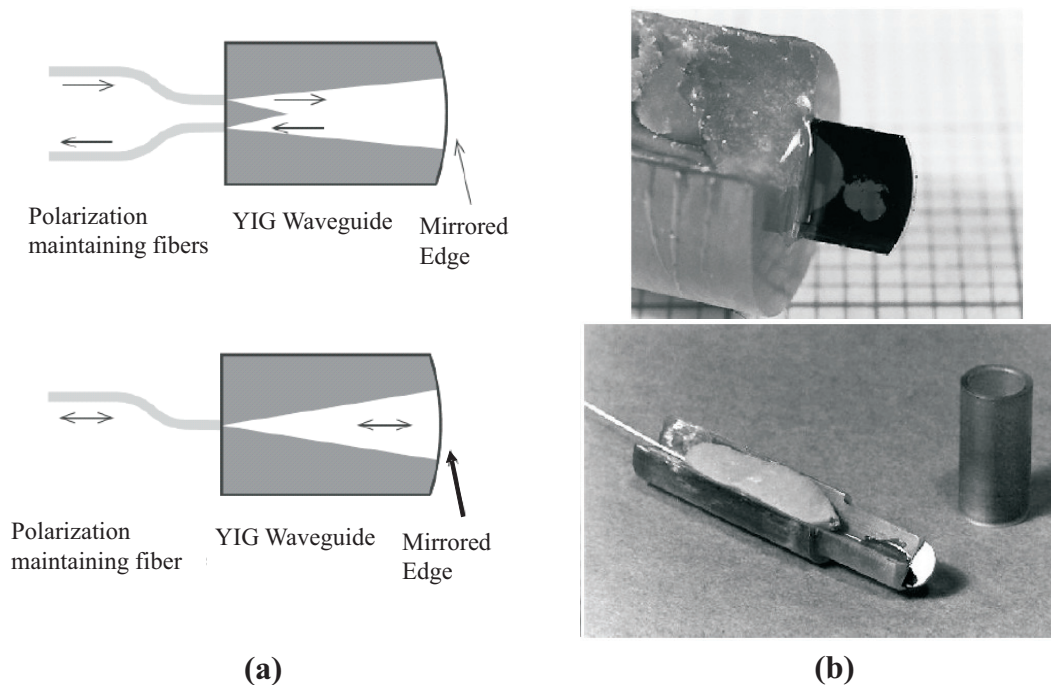


FIGURE I.15: (a) Basic principle of the magnetic field sensors based on YIG waveguide. (b) The fabricated sensors. Figures are adapted from [Nad19; SS91].

back is coated with a thin gold film to increase the back reflection (see Fig.I.15a,b), in order to double the Faraday effect and then improve the measurements sensitivity. The use of two optical fibers makes the system insensitive to power and loss fluctuations. The measurements range of this sensors is at least several mT with an equivalent magnetic field noise level of less than $8 \text{ nT}/\sqrt{\text{Hz}}$.

Amirsolaimani et al [Ami+18], have developed a new nanocomposite-based system for miniaturized magnetic field sensing. The sensor is based on Dy^{3+} -doped magnetite and cobalt ferrite NPs dispersed in a polymer matrix. Its geometry is illustrated on Fig.I.16. A compact fiber-optic interferometer is used to measure the magnetic field. For a thickness of the MO material around 500 μm , the measured noise floor is 20 fT without using a Lock-In Amplifier.

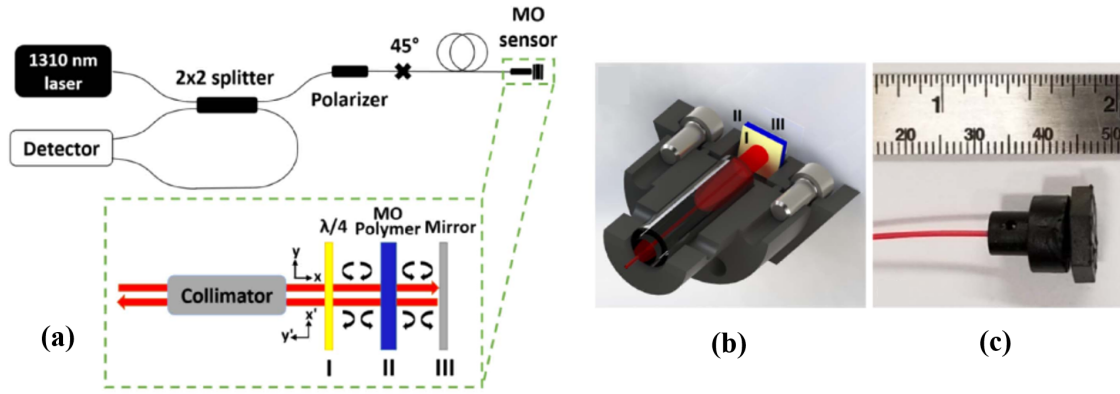


FIGURE I.16: (a) Schematic diagram of the designed in-line Sagnac interferometer magnetic field sensor based on MO polymer. (b) Cross section of the sensor prototype. (c) The fabricated sensor. The figures are adapted from [Ami+18].

I.1.4.2 Biosensors

The surface plasmon resonance (SPR) sensors are used to detect and identify dielectric media such as gas (air, Helium, etc.) or fluids (in particular bio-samples: water, urine, proteins, etc.) [Sep+06]. These sensors are based on the resonant excitation of the SPPs which wave vector depends on the optical properties of the metal and the dielectric media. Hence, a variation in the physical properties, such as the refractive index, of the dielectric medium being probed will induce a shift in the SPPs resonance (see Fig.I.17a). Hence, the measurement of the reflectivity spectrum (R_p) shift is the principle of operation of the SPR-sensors.

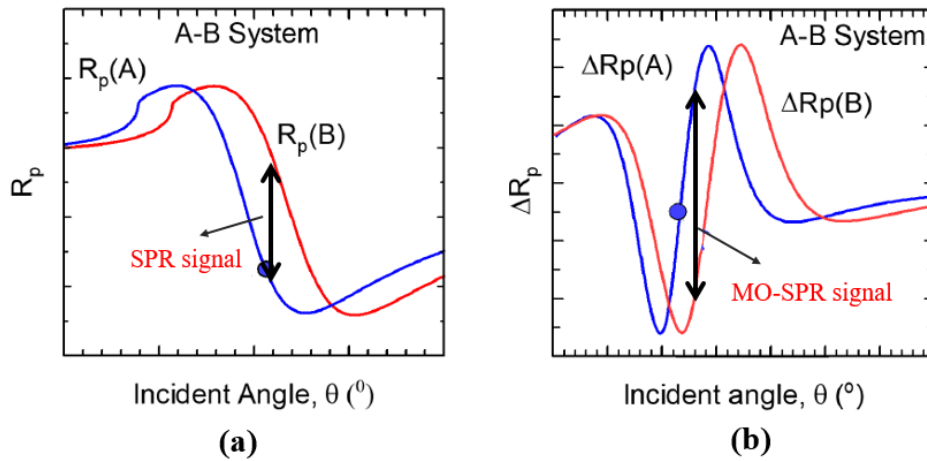


FIGURE I.17: Comparison of the SPR and MO-SPR sensitivities for two systems denoted A and B. The figures are adapted from [Riz+19].

SPR-sensors already exist but they have reached their detection limit [Riz+19]. The next candidate for biosensor is MO-SPR sensors.

The MO-SPR sensors are based on the TMOKE signal shift, rather than reflectivity shift for SPR sensors, when the optical property of the dielectric media changes (see Fig.I.17b). As explained in section I.1.1.2, the TMOKE response is defined as the relative change in the reflected intensity when the magnetic field is flipped (ΔR_p). The presence of the MO activity,

highly improves the sensitivity of the MO-SPR sensors compared to the SPR sensors. This enhancement is related to the fact that the TMOKE spectrum (ΔR_p) is narrower than the reflectance spectrum (R_p). Hence, a small shift of a narrow curve gives rise to the sensor signal than the same shift of a broad curve.

Most of the MO-SPR are bimetallic systems consisting of noble and ferromagnetic metals, with either smooth or perforated surface. Fig.I.18a illustrates the geometry of a MO-SPR sensor with the corresponding experimental signal compared to that of a standard SPR sensor [Reg+11]. The experimental signal to noise ratio of the DNA immobilization is increased by a factor of 4 as compared to a conventional SPR whose sensing surface is Au.

Fig.I.18b illustrates the measurements of the normalized signal of a MO-SPR sensor, for different refractive indices shifts of the dielectric media [Sep+06]. The MO-SPR sample is consisting of multilayers of Co/Au. As seen in Fig.I.18b, the normalized MO-SPR signal is higher than that obtained by the SPR sensor.

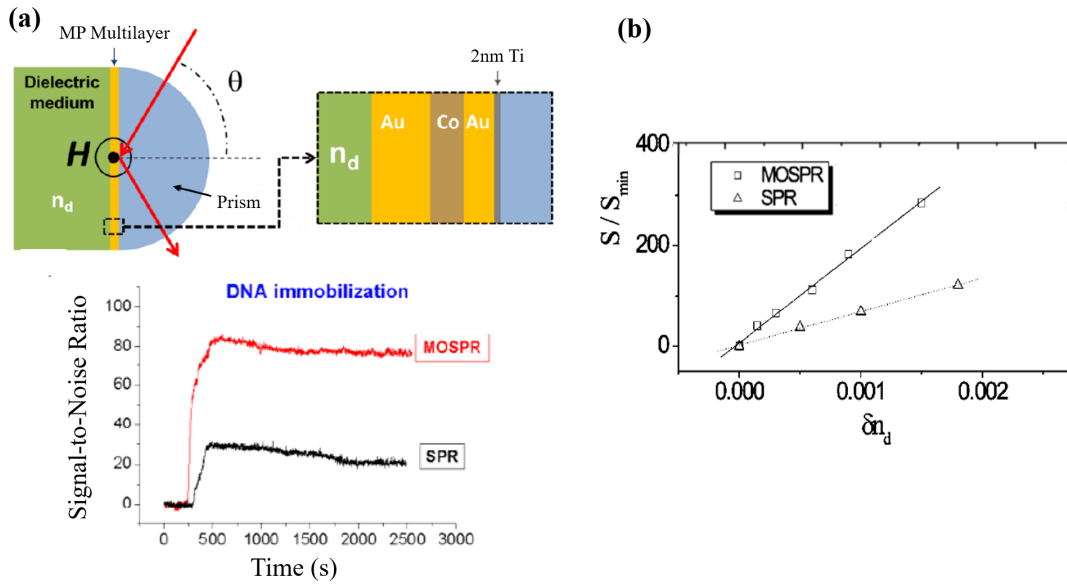


FIGURE I.18: (a) Schematic geometries of MO-SPR transducer with the corresponding measured signal to noise ratio [Reg+11]. This latter was compared with that of a SPR device (Au). (b) Normalized measured signal of MO-SPR and SPR sensors, for different refractive indices shifts of the dielectric media (δn_d).

The MO-SPR sample is consisting of multilayers of Co/Au [Sep+06].

I.1.4.3 Non-Destructive Testing

Non-destructive testing (NDT) [GMGGVS11] is a wide group of testing and analyzing techniques used to evaluate the properties of a material, component, structure or system, in order to characterize defects or discontinuities without causing damage to the inspected object. NDT is widely used in the industrial areas for controlling any stage in the production or life cycle of many components. The mainstream applications are in aerospace, power generation, railway, petrochemical and pipeline markets. Some of the common NDT methods are: electromagnetic, ultrasonic and liquid penetrant testing [Kuh13]. One of the conventional electromagnetic methods used for the inspection of conductive materials is eddy currents (EC) NDT [GMGGVS11].

The principle of EC technique is based on the electromagnetic induction law. When a coil supplied by an alternating electric current approaches to a conductive material, the primary alternating magnetic field (considered as excitation field \vec{B}_e , see Fig.I.19a) penetrates into the material and generates EC. This latter, prevailing within the conductor, will create a secondary magnetic field (called the reaction field \vec{B}_r) which tends to cancel the primary magnetic field resulting in a total magnetic field equal to zero in the absence of losses ($\vec{B}_t = \vec{B}_e + \vec{B}_r = \vec{0}$).

Now, in the case of a default presented in the conductor, a deviation in the magnetic reaction field is created, as a result \vec{B}_t is not anymore zero. The characterization of this latter gives an information about the defect.

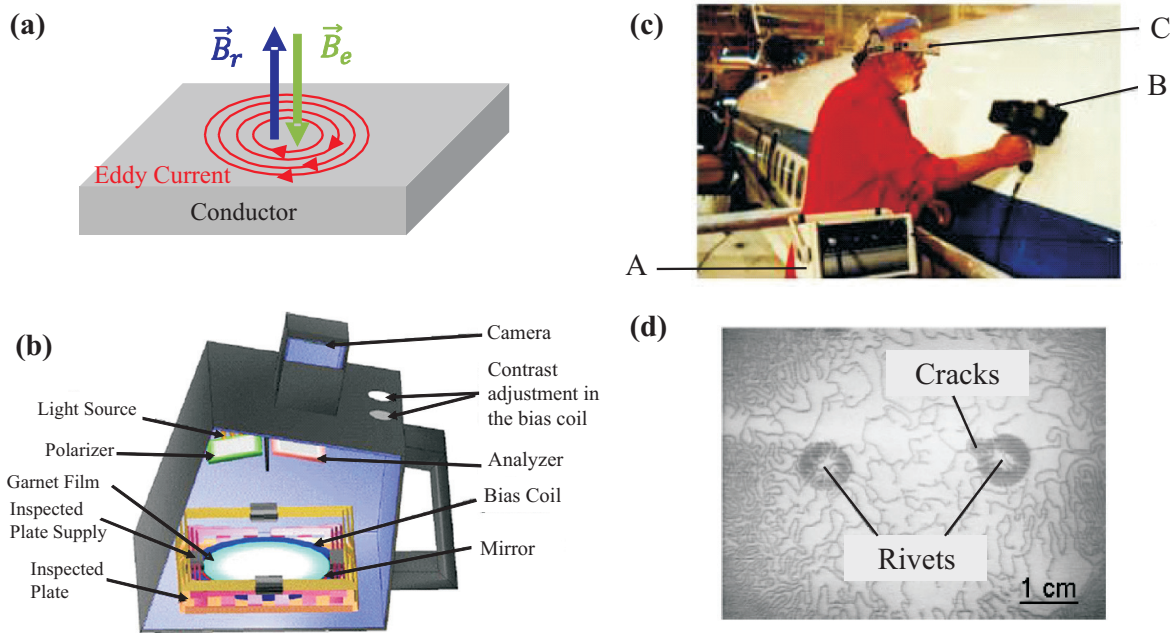


FIGURE I.19: (a) Schematic illustration of the Eddy currents prevailing within a conductor. (b) Schematic representation of the MO imager. (c) Presentation of the commercial device. (d) Example of image of rivets with and without cracks, provided by the EC/MO imager. (b), (c) and (d) are taken from [Dir08].

To detect the magnetic field \vec{B}_t , several sensors can be used, such as magneto-resistive and magneto-impedance sensors, inductive sensors, or MO devices [Dir08]. The advantage of these latter is their potentiality to describe a spatial distribution of the three components of the magnetic field due to the polarization rotation and intensity variation measurements (Faraday

and Kerr effects). The MO devices produce real-time images with shapes and sizes correlated to the actual defects [NSM04; BFL16]. The MO devices accelerate the inspection by several time compared to the other sensors. In addition to that, it has a good sensitivity to small and large defects and a quick coverage of the inspected area [Den+06].

A first high-performance EC/MO system was developed and marketed in the 1980s by the American company PRI (Physical Research Incorporated), for the control of riveted joints in aeronautics [Fit+93; Fit+96]. This device is based on the FR of the transmitted and reflected (due to the mirror) light, when the garnet film is magnetized (see Fig.I.19b). The used garnet film presents a switch mode: FR can take only two values: $\pm\theta_F^s$, where s means saturated value. The commercial device is consisting of (see Fig.I.19c): (A) a control unit to create \vec{B}_e , (B) the MO imager and (C) a real-time visualization headset. Fig.I.19d illustrates example of images provided by EC/MO imager device.

Although the EC/MO device allows a relatively quick inspection of the structures under study, the fabricated EC/MO device has a certain number of disadvantages and limitations. First, the sensitivity to defaults remains fairly low, especially when they are localized beyond 1 mm in depth. As well as, the quality of the images provided is highly dependent on the temperature.

In order to improve the performance of the EC/MO devices, several works have been developed [NSM04; Rad+01; Den+06]. In order to implement a quantitative characterization of the defects, J.M. Decitre [Dec03], has proposed a new approach based on measurements of the complex magnetic field with an integrated device based on garnet film, using EC with an optically modulated FR process. The relevance of the estimation methods associated with EC/MO imaging has led to a patent in 2006. With this approach, Y. Le Diraison [Dir08] demonstrated excellent performance in terms of spatial resolution of the image ($100 \mu m^2$) and speed of acquisition (typically equal to 26 s to obtain a useful image of 49 mm in diameter), as well as they proved a visualization of cracks up to 6-8 mm of depth.

All the presented works are based on the detection of the magnetic field normal to the inspected surface, hence a full characterization of the defect is still challenging. To solve this problem, a device that can measure different components of the magnetic field should be implemented.

As a summary, the variety of MO materials which defines the sensitivity range of the MO sensors, and the controllable size of the sensing system makes the MO devices very competitive in sensing technology and in NDT.

Therefore, the aim of this work is to implement a high performance MO device for sensing applications or for NDT, capable to detect small and large magnetic field in the three directions, by measuring the polarization rotation (Faraday at normal incidence, LMOKE at oblique incidence) and the intensity modulation (TMOKE). However, as explained before, these effects (especially the Kerr effects) are weak, thus it is relevant to enhance them in order to obtain a high sensitive device. Such enhancement can be achieved by several structures like magneto-phonic crystals [Ino+06], noble and ferromagnetic metals heterostructures [CGMC16], and guided-mode resonance gratings [MBK14]. These latter will be detailed in the next section.

I.2 Guided-Mode Resonance Gratings

In its simplest form, the guided-mode resonance grating consists of a subwavelength dielectric grating deposited on top of a waveguide itself deposited on a substrate [RSF97]. For a metallic grating, additional phenomena will be highlighted, they will be presented in section I.3.2.

I.2.1 Guided Mode Resonance: Principles

A dielectric grating is a structure having a periodic spatial variation in refractive indices defined as high (n_H) and low (n_L) indices.

Now, if the grating is deposited on a guiding layer (or if the grating is a guiding layer), the structure is named guided-mode resonance (GMR) grating. When such a structure is illuminated with an incident light beam, one part of the beam is directly transmitted through the structure and the other part is diffracted. If the diffracted mode in transmission have a propagation constant equal to that of a guided-mode, the diffracted light is then trapped in the waveguide (see Fig.I.20). The coupling condition can be written as:

$$\frac{2\pi}{\lambda_0} n_c \sin \theta_{inc} + \frac{2\pi q}{\Lambda} = \beta \quad (\text{I.46})$$

where, n_c is the refractive index of the incident medium and β is the propagation constant of the guided-mode. θ_{inc} is the incident angle, q is the diffraction order, λ_0 is the vacuum wavelength and Λ is the grating's period.

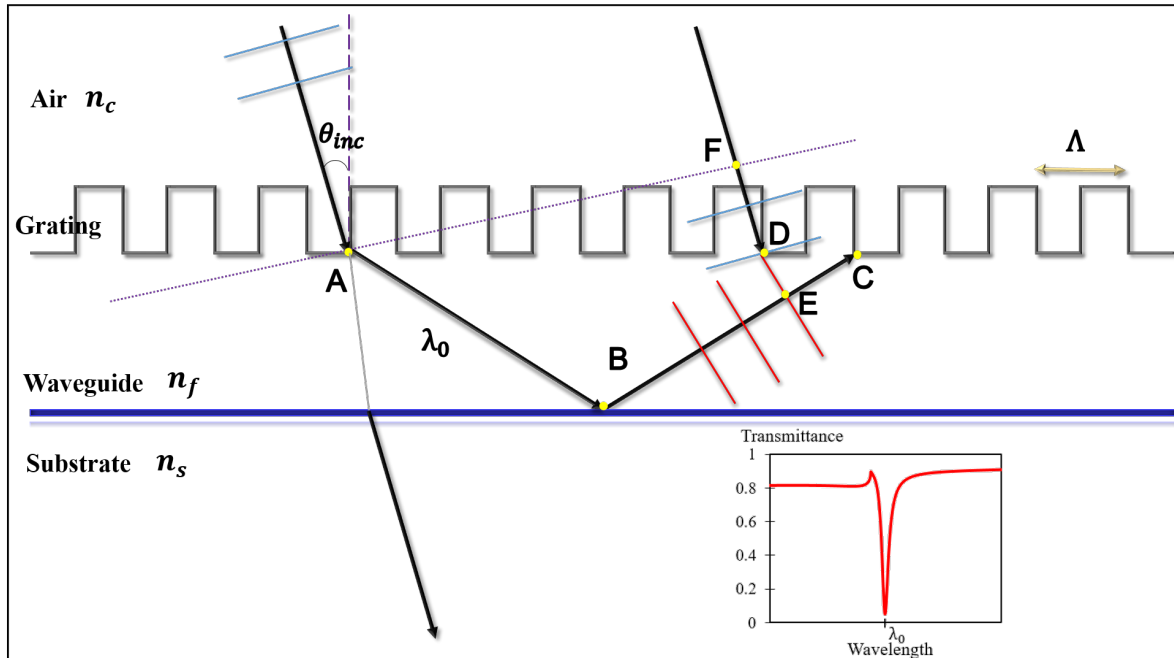


FIGURE I.20: Schematic illustration of the guided-mode resonance grating: basic geometry and resonance phenomenon.

Some of the confined light is then coupled out by the re-diffraction and the corresponding plane waves interfere destructively with the transmitted plane waves, resulting in a dip in the transmittance spectrum and consequently a peak in reflectance [RSF97; San+06; SRF97].

Hence, at specific wavelength and AOI, the structure resonates. This phenomenon is called guided-mode resonance. The structure is a subwavelength grating: only the 0th diffraction order exists in the substrate and the upper air cover, the ± 1 st diffracted orders exist in the waveguide [San+06].

The key feature is the relative phase shift (φ) between the incident and the re-diffracted plane waves (point D in Fig.I.20). The grating diffracts a small fraction of the incident plane waves which travel the path (ABC)-(CE) and re-diffracts, while the plane waves of the incident light just travels the path FD. Hence, the phase shift at point D is given as follows:

$$\varphi = \varphi_\delta + \varphi_{sf} + 2\varphi_d \quad (\text{I.47})$$

where φ_δ is the phase shift accumulated by the length (ABC)-(CE)-(DF) and expressed as Eq.I.33. φ_d is the phase accumulated by the diffraction and it is determined by:

$$2\varphi_d = \varphi_{cf} - \pi \quad (\text{I.48})$$

φ_{sf} and φ_{cf} are the phase accumulated by the reflections at the interface substrate-film and cover-film respectively, and is not the same for TE and TM as explained in section I.1.2.1.

It is necessary that the waves trapped inside the waveguide interferes constructively with each other to have a guided-mode. Hence, as mentioned in section I.1.2.1, the condition of a guided-wave should be:

$$\varphi_\delta + \varphi_{cf} + \varphi_{sf} = 2\pi m \quad (\text{I.49})$$

Combining Eq.I.49 and Eq.I.47, we find that the total phase φ is equal to $(2m - 1)\pi$.

Hence, at resonance the total phase difference between transmitted and diffracted wave fronts is π and total destructive interferences occur. Therefore, as seen in Fig.I.20 a dip in transmittance spectrum at the resonant wavelength, and consequently a peak in reflectance spectrum, are obtained.

Fig.I.21 illustrates the TE reflectance spectrum for different AOI with $\Lambda = 1000$ nm (Fig.I.21a) and different grating periods for AOI=0° (Fig.I.21b), for a GMR grating. The calculations were done with the MC Grating © software, which will be explained in Chap.III. The TE or TM polarization are defined with electric field parallel or perpendicular to the grating's grooves respectively. One can see on Fig.I.21a, that for the normal incidence one resonance in the reflectance spectrum is observed, whereas for oblique incidence two resonances appear, corresponding to the +1st and -1st diffraction orders in the waveguide. By increasing the AOI and the grating period, the resonance wavelength increases which is consistent with the coupling equation (Eq.I.46).

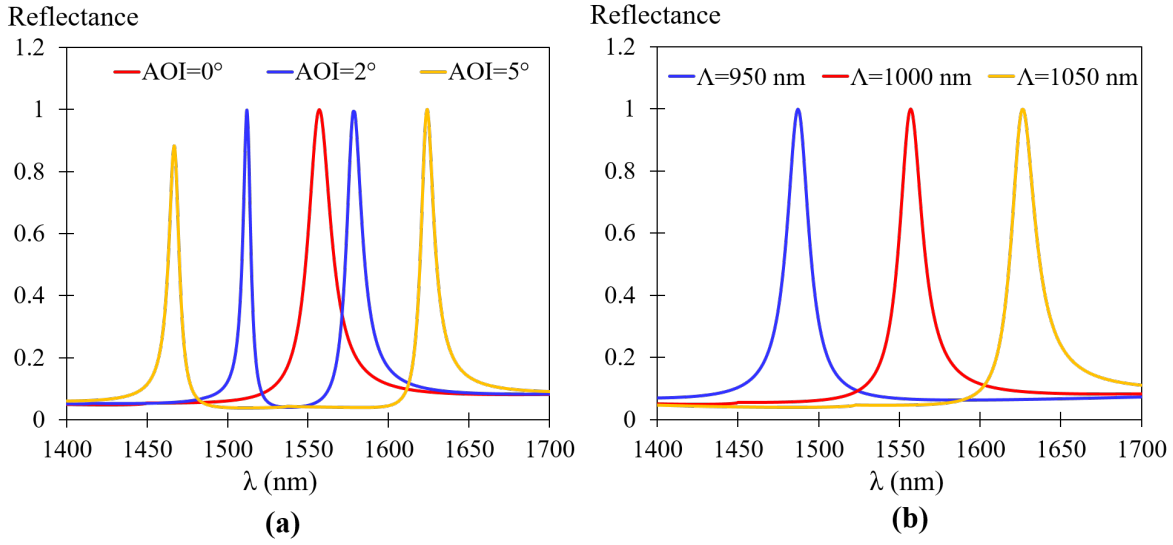


FIGURE I.21: Numerical simulations of the reflectance done with MC Grating© of a GMR structure, for TE-polarized incident light, as a function of the wavelength for (a) different AOI (for $\Lambda = 1000$ nm) and (b) different grating periods at normal incidence.

I.2.2 Phase Matching

Dispersion equations being different for guided TE and TM modes, the spectral position of the resonance is most of the time different for these two polarizations. But, as explained before in section I.1.2.3, for an efficient MO conversion a phase matching condition is required ($\beta_{TE} = \beta_{TM}$). It can be obtained with a GMR device with a periodic structuring with optimized opto-geometric parameters [Ala+11].

Fig.I.22b shows the numerical simulations of the reflectance peak for TE and TM modes, as a function of the grating height (h) and the line width (w) of a structure formed by a titanium dioxide (TiO_2) grating deposited on a silica substrate (see Fig.I.22a). Here, the guiding layer is the grating itself.

As seen in Fig.I.22b, the two dispersion curves overlapped for $h = 147$ nm and $w = 280$ nm and this is confirmed by Fig.I.22c, where the reflectance as a function of the wavelength is plotted for TE and TM modes at the intersection parameters of Fig.I.22b. Referring to Eq.I.46, equal resonance wavelengths means equal propagation constants for TE and TM modes. Hence, the phase matching condition can be satisfied through GMR gratings with optimized opto-geometric parameters.

An important information to know is that to have a MO enhancement, the light/matter interaction should be increased and the TE-TM phase matching condition should be reached. The GMR structure plays a twofold role. On one hand, it increases the light/matter interaction due to the trapped light in the waveguide. On the other hand, the periodic nanostructuring with optimized opto-geometric parameters engenders the phase matching condition. An advantage also of the GMR is that enhancement of MO effects can be accompanied with high reflectivity.

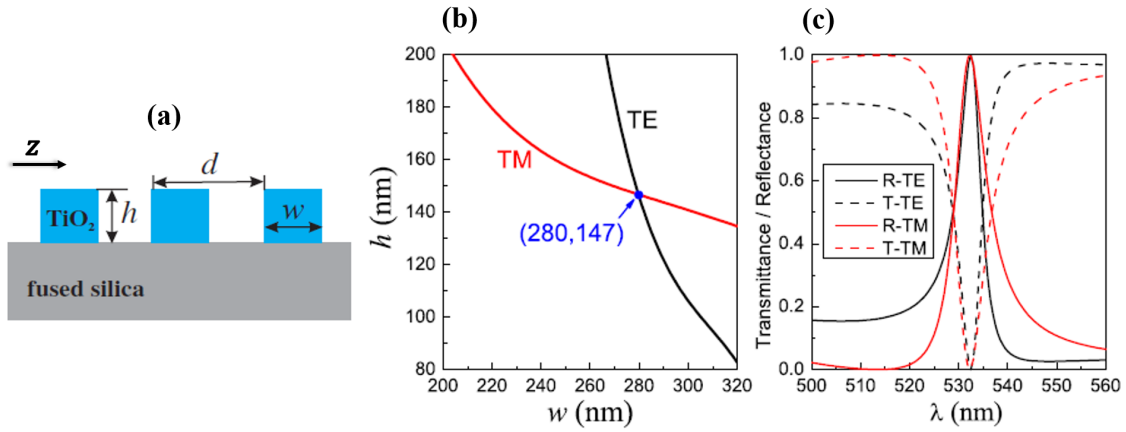


FIGURE I.22: (a) Schematic geometry of the GMR structure under study. (b) Numerical simulations of TE and TM resonances for the GMR structure with period $d = 340$ nm, as a function of the grating height h and the line width w , at $\lambda = 532$ nm. (c) TE and TM transmittance T and reflectance R spectra for $h=147$ nm and $w=280$ nm (intersection point on (b)). The figures are taken from [Ala+11].

The description of selected structures in the literature, dedicated for MO enhancement, will be detailed in the next section.

I.3 Magneto-Optical Enhancement Achievements

The different structures cited in the literature can be mainly divided into two groups: all-dielectric structures and magneto-plasmonic structures.

Let's start first by explaining the all-dielectric structures and the MO enhancement achievements through these types of structures. After that the magneto-plasmonic structures will be presented.

I.3.1 All-Dielectric Structures

Such structures are made only with dielectric materials. Example of these structures are GMR gratings [MBK14], metasurfaces [Chr+18], and magneto-photonic crystals [Ino+06]. These latter are a combination of a MO dielectric material and photonic-crystals. The photonic crystals are materials with a periodic spatial variation in their dielectric constant and the light propagates along this periodicity. They can demonstrate Photonic Band Gap (PBG): by analogy with the band gap of semi-conductors, a PBG corresponds to a range of wavelengths for which the wave propagation is forbidden inside a crystal, which results in a dip in the transmittance spectrum. This behavior is related to the appearance of standing waves resulting from constructive interference in reflection at these wavelengths. Hence, at the edges of the transmittance dip (PBG), the group velocity of the waves inside the structure is zero, increasing the interaction between the material and the light. As a result, giving to the photonic-crystals MO properties, enhances resonantly the MO effects at the edges of the PBG.

The enhancement of the MO effects through the different all-dielectric structures will be described in the next paragraphs and will be divided into two groups: enhancement of the polarization rotation effects and enhancement of the phase modulation effects.

I.3.1.1 Enhancement of Polarization Rotation Effects

Fedyanin et al. [Fed+04], has demonstrated an experimental enhancement of Faraday effect, through a 1D magneto-photonic crystal (see Fig.I.23a) consisting of four alternating layers of MO material (Bi:YIG) and non-magnetic dielectric (SiO_2). The measurements spectra of the transmittance and the FR are illustrated on Fig.I.23b. As seen in this figure, a broad dip

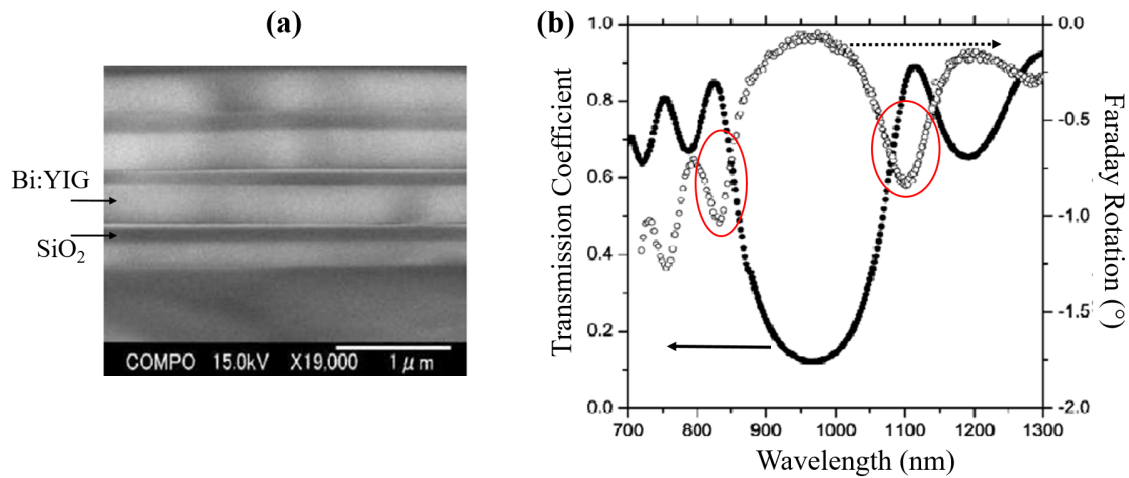


FIGURE I.23: (a) Field-emission SEM image of a 1D magneto-photonic crystal consisting of $(\text{Bi:YIG}/\text{SiO}_2)_4$ deposited on a fused quartz substrate. (b) Measurements of the transmission coefficient and the FR spectra. The figures are taken from [Fed+04].

in the transmittance spectrum is observed revealing the presence of a PBG beginning. As a result, an enhancement of the Faraday effect is reached at the PBG's edges. The FR reaches a value up to 0.8° at $\lambda = 1100$ nm, that is approximately eight times larger than the off-MO resonance at this wavelength.

With the same type of structure but using Ce:YIG as the magnetic layer, Yoshimoto et al. [Yos+16] demonstrated an experimental enhancement by a factor of 30 for the FR at around $\lambda = 1550$ nm.

Moreover, enhancement of Faraday effect was demonstrated experimentally in the Hubert Curien Laboratory (LabHC), by Abou Diwan et al. [AD+16] through a 3D magneto-photonic crystals formed by periodic arrangement of air balls in a silica matrix doped with cobalt ferrite NPs. A Scanning Electron Microscopy (SEM) image of the fabricated structure is given in Fig.I.24a. The experimental measurements of the transmittance and the FR are illustrated on Fig.I.24b. One can see a dip in the transmittance spectra centred at $\lambda = 720$ nm, revealing the PBG. The PBG central wavelength can be tuned by changing the air holes diameters and the volume fraction of the magnetic NPs embedded in the silica matrix [Kek+13]. Enhancement of the FR by a factor around 2 was achieved as compared to the single layer of the MO composite (dashed line in Fig.I.24b) at the edges of the PBG.

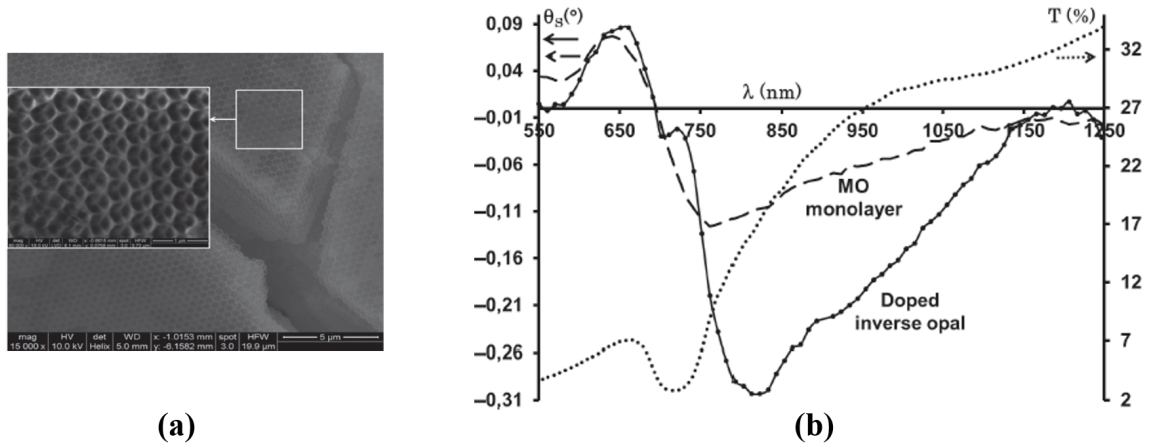


FIGURE I.24: (a) SEM image of a 3D magneto-photonic crystals formed by periodic arrangement of air balls in a silica matrix doped with cobalt ferrite nanoparticles. (b) Transmittance and Faraday rotation ($\theta_s(^{\circ})$) measurements spectra for the magneto-photonic crystals. The measurements of FR for a single layer of MO composite is illustrated in dashed curve. The figures are adapted from [AD+16].

Based on their ability to largely enhance the Faraday effect, the magneto-photonic crystals are promising for applications such as optical isolators [YWF07; Fan+11], and spatial light modulators [Cha+09].

Enhancement of Faraday effect was theoretically demonstrated by Christofi et al. [Chr+18], through a highly transmissive all dielectric MO metasurface. The structure is illustrated on Fig.I.25a and it is formed by BIG nanodisks array embedded into a low-index silica matrix and magnetized along the z direction. The transmittance and the FR are illustrated on Fig.I.25b as a function of the wavelength. As seen in this figure, large values of FR are achieved with a highest value equal to -7.5° at $\lambda = 1393$ nm. Indeed, the FR of a single BIG film is around -0.75° , hence an enhancement of one order of magnitude was achieved with an all-dielectric metasurface. More importantly, the large FR is accompanied with very high transmission (96%). This high transmittance is related to the fact that the structure was optimized in such a way that the magnetic and electric dipoles resonances overlap spectrally, resulting in constructive interferences.

Giant values of rotations and ellipticity in Faraday and PMOKE configurations have been theoretically demonstrated by Bai et al. [BTT06] through a 2D-all dielectric GMR structure with optimized parameters. The structure consists of a Bi:YIG grating embedded in a dielectric material (the cross section of the structure is illustrated on Fig.I.26a). The use of a symmetric 2D grating allows to fully degenerate the polarization at normal incidence: in such a case TE and TM resonances will always match ($\Delta\beta = 0$). Hence, as explained before, due to the MO activity, the Faraday effect and PMOKE can be explained by the lifting of the degeneracy of the RCV and LCV propagating in the structure, which leads to a splitting of the resonance peak into two (see Fig.I.26b). The calculated FR can reach a value of 50° with a transmittance around $T=40\%$, as seen in Fig.I.26b. As well as, a value of PMOKE equal to 90° was theoretically demonstrated with a reflectivity of 24%. However, the disadvantage is that the MO resonance occurs at a wavelength with 0.1 nm of precision. Otherwise, if the incidence wavelength is

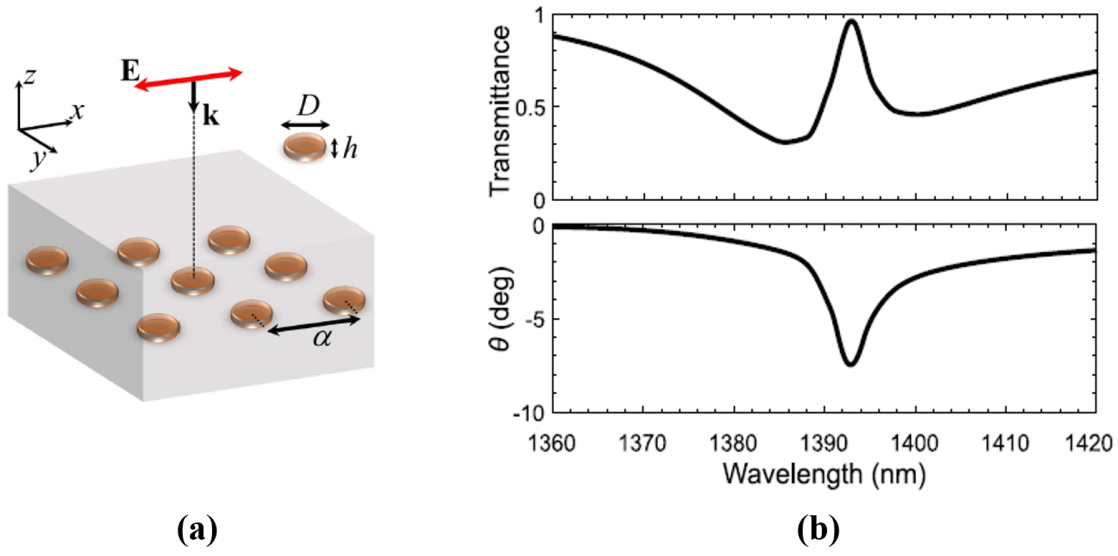


FIGURE I.25: (a) Structure under consideration formed by BIG nanodisks array embedded into a low-index silica matrix with: $\alpha = 850$ nm, $D = 620$ nm and $h = 260$ nm. (b) Numerical simulations of the transmittance and the FR (θ) spectra. The figures are adapted from [Chr+18].

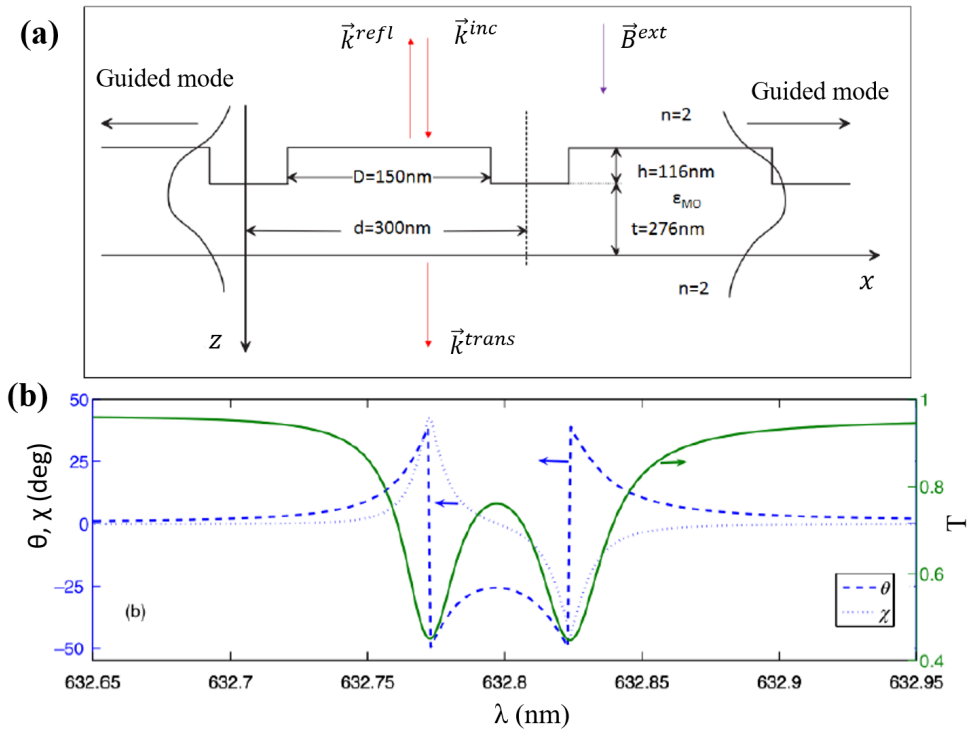


FIGURE I.26: (a) Cross section of the structure under consideration in the work of [BTT06]. Example of the structure parameters: $n = 2$, $d = 300$ nm, $D = 150$ nm, $t = 276$ nm, and $h = 116$ nm. (b) Calculated FR (θ , dashed line), Faraday ellipticity (χ , dot line) and transmittance.

632.7 instead of 632.8 the giant value of FR is lost.

In the LabHC, an all-dielectric GMR grating was developed [Var17]. The structure is consisting of a subwavelength grating made by an alternating MO material and silicon nitride (Si_3N_4) and deposited on a BK7 substrate (see Fig.I.27a). The MO material is made of cobalt ferrite NPs embedded in a silica matrix as described in section I.1.3.

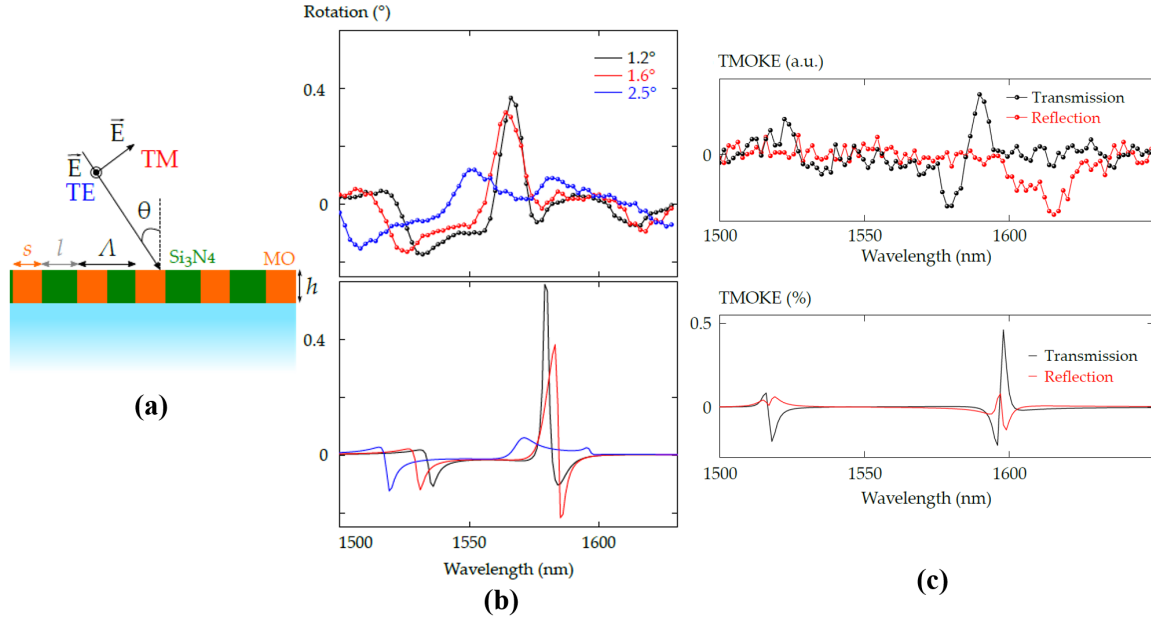


FIGURE I.27: (a) GMR structure consisting of a grating layer, formed by alternating MO composite and Si_3N_4 , deposited on BK7 substrate. The geometric parameters of the structure are: $l = 608$ nm, $h = 623$ nm and $\Lambda = 966$ nm. Measured (upper panels) and calculated (lower panels) of: (b) LMOKE in transmission spectra for different AOI and for TM polarization; (c) TMOKE in transmission and in reflection spectra at AOI= 2.6° . The figures are adapted from [Var17].

With this structure, experimental enhancements of the FR (magnetic field perpendicular to the sample plane) by a factor of 3.5 and 2 as compared to the continuous film, were achieved for TE and TM-polarized incident light respectively, at $\lambda = 1579$ nm. Moreover, experimental enhancements of the LMOKE in transmission was achieved. Here, the applied magnetic field is parallel to the incident and sample planes. Upper panel of Fig.I.27b illustrates the experimental measurements of the longitudinal Kerr rotation in transmission as a function of the wavelength, for TM polarization and different AOI. As seen in this figure, highest values of LMOKE in transmission around 0.4° at $\lambda = 1565$ nm were achieved at AOI= 1.2° and 1.6° . We have to mention that the LMOKE in transmission for the continuous MO composite film is around 0.001° , hence a large enhancement of this effect was achieved through an all-dielectric resonant grating. In addition to that, the numerical simulations are in good agreement with the experimental measurements (see lower panel of Fig.I.27b).

I.3.1.2 Enhancement of Magneto-Optical Phase Modulation Effects

As explained before, the phase modulation effects are described by a modulation of the propagation constant ($\Delta\beta_{\pm M}$) or the extinction coefficient ($\Delta\kappa_{\pm M}$) of the guided-mode, for two different magnetic field directions. In the resonant structures, this phase modulation is translated by a spectral shift (due to $\Delta\beta_{\pm M}$) or amplitude variation (due $\Delta\kappa_{\pm M}$) of the transmittance or reflectance resonance, resulting in an intensity modulation of the transmitted or reflected light. The TMOKE is generally characterized by the term δ and defined as the relative change of the intensity I of the transmitted or reflected light upon to magnetization M reversal [Kre+13]:

$$\delta(\%) = 100 \times \frac{I(+M) - I(-M)}{(I(+M) + I(-M))/2} \quad (\text{I.50})$$

The intensity of the transmitted or reflected light can be replaced by the transmittance or the reflectance.

With the same structure illustrated on Fig.I.27a, TMOKE signal enhancement was experimentally and numerically demonstrated in reflection for AOI= 2.6° as seen in Fig.I.27c. Therefore, GMR-MO devices can enhance different MO effects.

Maksymov et al. [MBK14], have demonstrated theoretically an enhancement of the TMOKE signal through a GMR formed by a subwavelength dielectric grating, consisting of alternating MO material (Bi:YIG) and nonmagnetic dielectric (Si) nanostripes on a GGG substrate (see Fig.I.28a). Here, the alternating Bi:YIG/Si is the guiding layer and a transverse magnetic field is applied in z direction. The TMOKE signal and the reflectivity spectra for different AOI ($\theta = 35^\circ, 25^\circ, 15^\circ$ and 10°) were studied and the results are illustrated in Fig.I.28b. One can see that by decreasing the AOI, the width of the reflectivity peak gets thinner resulting in a higher TMOKE signal. This behavior is linked to the fact that a spectral shift of a narrow reflectance peak gives rise to a higher TMOKE response than the same spectral shift of a broad peak. The TMOKE reaches a highest value of 4% for AOI=10° at a wavelength around 680 nm. Hence, an enhancement of two orders of magnitude was achieved for the TMOKE signal as compared to the continuous magnetic film. The advantage here is that the TMOKE resonance coincides with high reflectivity (larger than 50% for the different AOI). This structure is promising for applications in MO data storage [ZK97], magnonics [KDG10; SCH10], and 3D imaging [Aos+10].

Voronov et al. [Vor+20] demonstrated an experimental enhancement of the TMOKE signal through a 1D all-dielectric GMR grating. The structure consists of a perforated Bi:YIG film deposited on top of a GGG substrate (see Fig.I.29a). Fig.I.29b illustrates the TMOKE signal in transmission as a function of the wavelength and the AOI. One can notice, the presence of two TMOKE resonances for a fixed AOI, which are linked to the ± 1 st diffraction order ($q = \pm 1$ referring to Eq.I.46). TMOKE signal with highest value equal to 0.9% is reached as seen in Fig.I.29b, accompanied with a high transmittance of 60%. For a comparison, the continuous Bi:YIG film provides a TMOKE signal about $\delta = 0.004\%$. Hence, large enhancement of the TMOKE signal in transmission was experimentally achieved through 1D-all dielectric GMR structure, but with a complex fabrication process (see [Vor+20]).

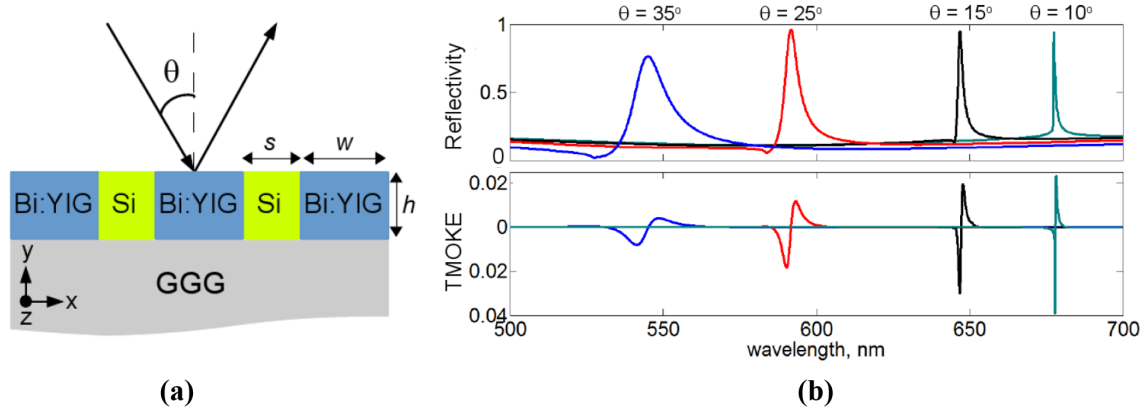


FIGURE I.28: (a) Structure under consideration formed by a grating layer, consisting of alternating Bi:YIG and Si on GGG substrate. The geometric parameters of the GMR structure are: $w = 264$ nm, $h = 100$ nm and $s = 113$ nm. (b) Calculated reflectivity and TMOKE spectra for different AOI (θ). The figures are taken from [MBK14].

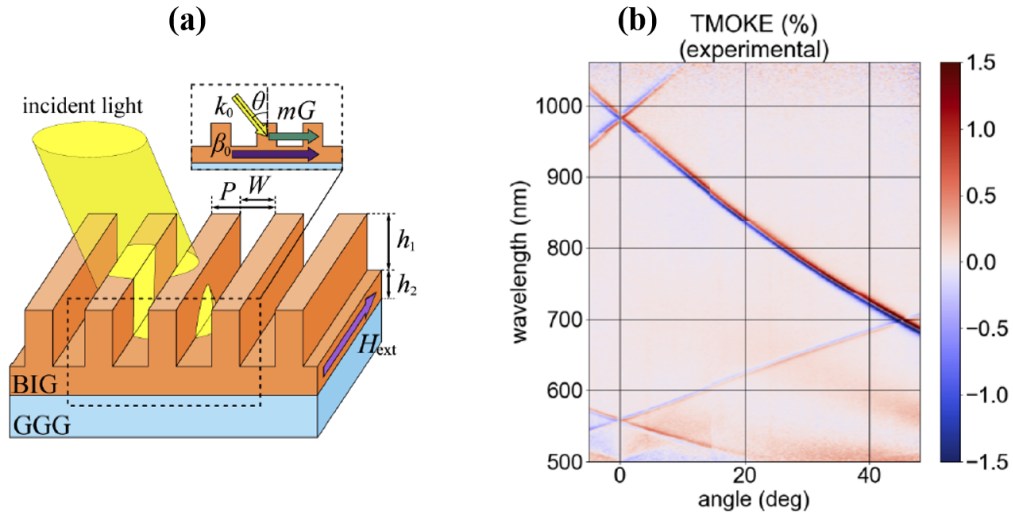


FIGURE I.29: (a) Structure under consideration: perforated Bi:YIG film on GGG substrate. The geometric parameters of the GMR structure are: $h_1 = 225$ nm, $h_2 = 75$ nm, $W = 200$ nm and $P = 500$ nm. (b) Measured TMOKE signal as a function of the wavelength and the AOI. The figures are taken from [Vor+20].

As a summary, all-dielectric resonant structures were used to enhance experimentally and numerically the polarization rotation and phase modulation effects. These latter were not widely explored by all-dielectric structures and to our knowledge few experimental evidence of the TMOKE were demonstrated.

The next section will be dedicated to the enhancement of the MO effects through magneto-plasmonic structures.

I.3.2 Magneto-Plasmonic Structures

Several works [FSW77; AB78; Gru+10; Gru+12; GD+10; GD+07; Arm+08; New+08] studied the beneficial combination between the MO activity of a magnetic material and the plasmon oscillations [Mai07]: the resulting structure is named magneto-plasmonic (MP). As explained before, the plasmon oscillations are described by coupling oscillations of the electromagnetic field (TM polarization) and the electron plasma in a metal. These oscillations can propagate at the metal/dielectric surface and are known as SPPs, or can be localized and known as localized surface plasmon (LSP). These latter can be found in the case of metallic NPs or metallic grating with small width. The LSP are independent on the grating period contrary to the SPPs. However, they are highly sensitive to the grating width.

The MP structures can achieve a resonant enhancement of the MO response. On one hand, the excitation of the plasmonic oscillations (SPPs or LSP) increases the interaction between the MO material and the light. On the other hand, the SPPs wave vector is modified under the influence of a magnetic field (Eq.I.44).

In the following paragraphs, the enhancement achievements of the polarization rotation effects and the phase modulation effects, with the different MP structures will be presented.

I.3.2.1 Enhancement of Polarization Rotation Effects

Rowan-Robinson et al.[RR+19] demonstrated experimental enhancement of the PMOKE in Co hexagonal antidot arrays fabricated on a Si substrate. A SEM image of the structure is illustrated on Fig.I.30a. Experimental measurements of the reflectivity and the polar rotation spectra (θ_{Kerr}) of the antidot sample are illustrated on Fig.I.30b-c respectively, at AOI=4° and with different thickness of Co (20, 60 and 100 nm).

As seen in Fig.I.30b, for 60 nm and 100 nm of thicknesses, a dip in the reflectivity spectrum is observed at 2.81 eV ($\lambda = 441$ nm) and 2.69 eV ($\lambda = 461$ nm) respectively, revealing the excitation of SPPs at Co/Air interface. As a result, enhancement of the PMOKE is detected at these positions and it is more obvious for 100 nm (0.66°) than for 60 nm as seen in Fig.I.30c. Moreover, for the case of 100 nm of thickness, the dramatic enhancement of θ_{Kerr} , peaking around 3.75 eV ($\lambda = 330$ nm), do not have plasmonic origin: it is exacerbated by the near-zero reflectivity associated to the large absorption of Si substrate around 3.75 eV ($\lambda = 330$ nm).

With the same type of structure, experimental evidence of LMOKE enhancement was achieved by [Che+12] through a 2D MP structure made by 2D array of nickel nanodisks arranged into hexagonal lattice and placed on 500 μm -thick nickel foil. The LMOKE is enhanced up to 0.13° at AOI=45° for TM-polarization.

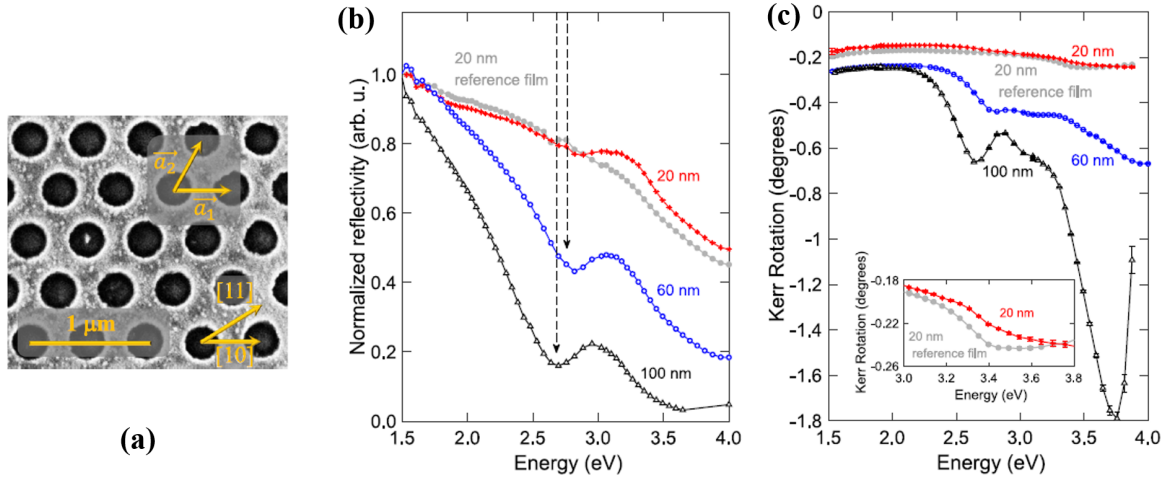


FIGURE I.30: (a) SEM image for the Co hexagonal arrays fabricated on Si-substrate. The structure has a periodicity of 470 nm and a hole diameter of 260 nm. Experimental measurements at AOI=4° of (b) normalized reflectivity and (c) polar Kerr rotation spectra of the MP structure, for different Co thicknesses and for TM polarization. Inset (c): polar Kerr rotation spectra for the MP structure (red curve) and Co single layer (gray curve), for a 20 nm-thick of Co. The figures are taken from [RR+19].

Caballero et al. [CGMC15] demonstrated theoretically FR enhancement through Au-Co-Au films perforated with a periodic array of subwavelength holes (see Fig. I.31). Numerical simulations of FR and transmittance for the MP structure, as a function of the wavelength and the thickness d of the upper Au film are illustrated on Fig. I.31b-c, for TM-polarization. The presence of a peak in the transmittance spectrum (Fig. I.31b) is obvious, which stems from the resonant excitation of SPPs at the interfaces of the perforated membranes. This phenomenon is named Extraordinary Optical Transmission (EOT) which was presented for the first time by Ebbesen et al. [Ebb+98], where an unusual high transmission spectra was observed through a metallic film perforated with subwavelength hole arrays. As seen in Fig. I.31c, the highest values of FR are achieved by placing the Co layer close to the upper (Au/Air) or lower (Au/substrate) interfaces. Indeed, SPPs enhance the electromagnetic field at the interfaces and by placing the Co layer close to one of the two interfaces, an amplification of the electromagnetic field in the ferromagnetic layer is achieved, which leads to an increase in the MO activity. The best trade off between the FR and the transmittance is: 0.25° with 3% at $\lambda = 710$ nm.

Belotelov et al. [BDZ07] have demonstrated theoretically a simultaneous enhancement of FR and an EOT with a MP structure illustrated in inset Fig. I.32. The structure consists of a 2D gold grating perforated by holes and deposited on a thin layer of Bi:YIG magnetized perpendicularly to its plane. As seen in Fig. I.32, a high value of FR equal to 0.78° with T=35% at $\lambda = 963$ nm was reached for TM-polarized incident light. In addition to that, a polar Kerr rotation of a value of 0.63° was also demonstrated (not shown here). Therefore, an enhancement by a factor of 9 of the FR and the PMOKE, was demonstrated in comparison to a thin film of Bi:YIG.

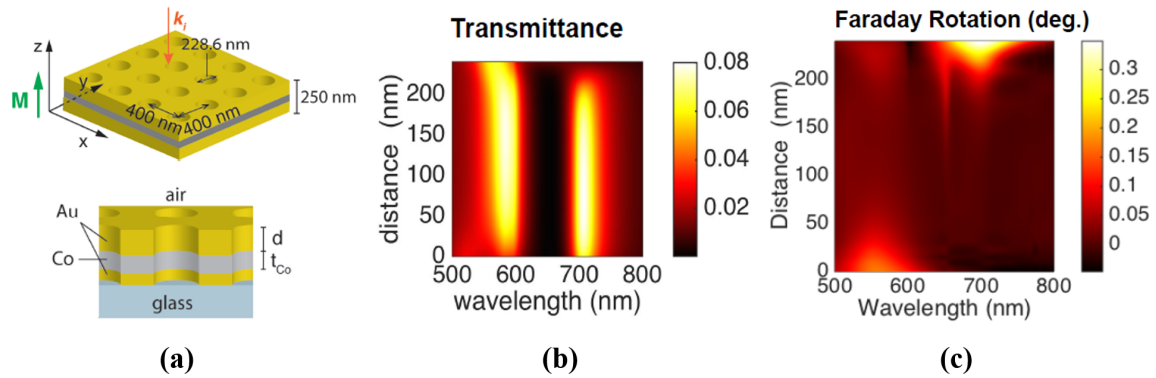


FIGURE I.31: (a) Schematic representation of the structure under study: Au-Co-Au films perforated with a periodic array of subwavelength holes and deposited on a glass substrate. Numerical simulations of the (b) transmittance and (c) FR, as a function of the wavelength and the distance d (thickness of the upper Au film) with $t_{Co} = 10$ nm, for TM-polarization. The figures are adapted from [CGMC15].

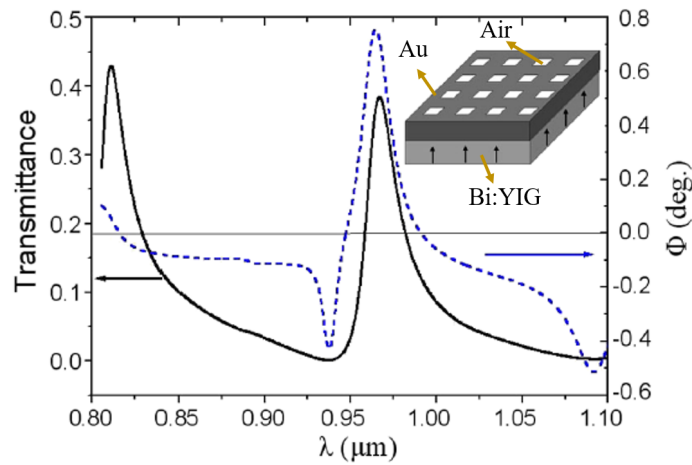


FIGURE I.32: Calculated transmittance and FR (Φ) spectra, for a bilayer system (illustrated in inset) and for TM-polarization. The structure is formed by perforated 68 nm-thick Au film deposited on a uniform 118 nm-thick Bi:YIG film. The grating period is 750 nm and the holes' size is $r = 395$ nm. The figures are adapted from [BDZ07].

Li et al. [Li+16] have demonstrated by numerical simulations an EOT with a bilayer metal/dielectric structure, consisting of a silver (Ag) film perforated with circle annular arrays deposited on top of a uniform Bi:YIG film as seen in Fig.I.33a. The transmittance and the FR spectra for different grating periods (P) are plotted in Fig.I.33b. One can see peaks of FR up to 3.2° , 3.5° and 2.9° for the different grating periods. The disadvantage is that these FR coincide with very low transmittance. Nevertheless, a good trade off can be found, as an example: -1° of FR with $T=50\%$ for $P = 400$ nm. We have to mention that in this work, the FR for a single layer of Bi:YIG is only about -0.022° (dashed line in lower panel of Fig.I.33b), hence a significant enhancement was achieved with the proposed 2D MP structure.

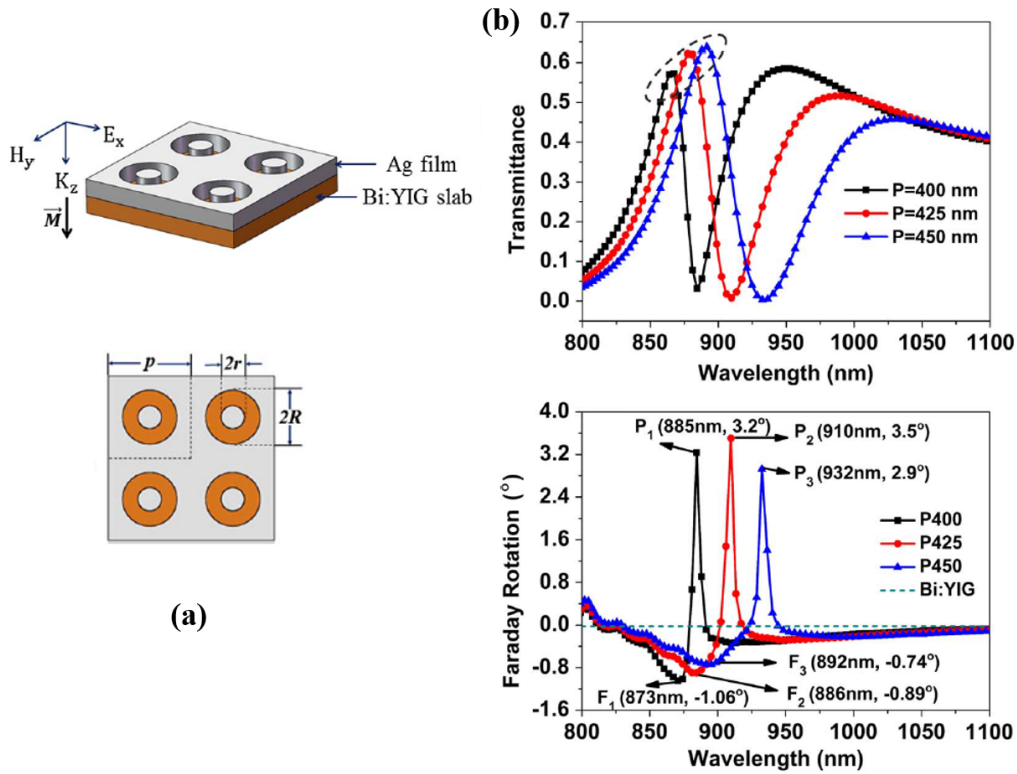


FIGURE I.33: (a) Schematic illustration of the bilayer nanostructure under study: $r = 75$ nm, $R = 150$ nm, the Au and Bi:YIG thicknesses are both 100 nm. (b) Simulated spectra of the transmittance (upper graphs) and the FR (lower graphs) for different grating period (P) and for TM polarization (following x direction).

The figures are taken from [Li+16].

With the same structure, Li et al. [Li+16] demonstrated numerically enhancement of the PMOKE at normal incident, where values around 0.85° were reached.

Numerical and experimental evidence of the FR enhancement was achieved by Floess et al. [Flo+15] with a 1D MP structure. This latter is illustrated on Fig.I.34a and formed by a gold grating deposited on a thin film of EuSe, itself deposited on a glass substrate. Fig.I.34 illustrates the simulated absorbance (upper panels) and FR (lower panels) for TE and TM polarization as a function of the wavelength and the grating period. The black and white dashed lines trace the TE and TM mode dispersion respectively, whereas the red dashed line represents the Rayleigh anomaly. This latter results from diffracted plasmonic waves propagating tangentially to the grating surface. For small wavelengths, the TM mode absorbance curve is broad and

barely moves with the period, revealing the presence of waveguide plasmon polaritons (WPPs): LSP coupled with TM guided-mode. However, for larger wavelengths, the TM hybrid-mode dispersion becomes more waveguide-like and converges toward sharp and purely waveguide mode resonance. Since the LSP can be only excited for TM-polarization, the TE mode dispersion (Fig.I.34b.II) shows a behavior of a pure waveguide resonance. As seen in Fig.I.34b.I-II, the WPPs and the TE absorbance curves are overlapped for a period equal to 340 nm, insuring the phase matching condition explained in section I.2.2. As a result, the largest values of FR are reached around 340 nm, as seen in Fig.I.34b.III-IV. The numerical simulations were accompanied with experimental measurements for TM polarization, and a maximum value of 4.2° for a period of 360 nm was measured with $T=30\%$, giving an enhancement by a factor of 4 as compared to a single layer of EuSe. The disadvantage here is that the measurements were done at 20 K because the EuSe becomes magneto-optic at very low temperature as mentioned in section I.1.3.

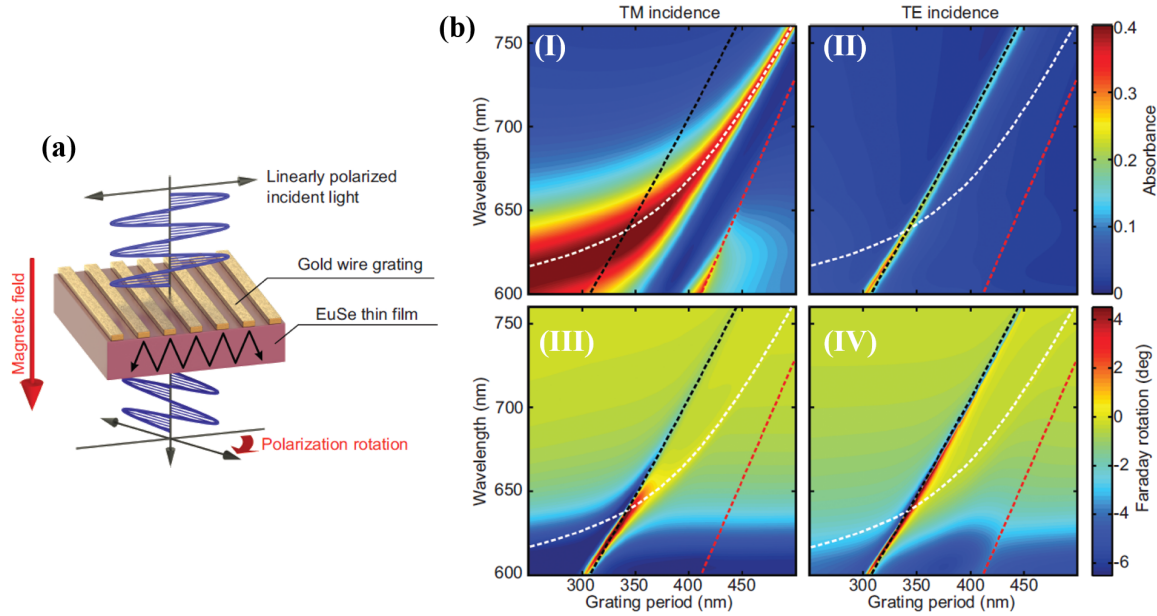


FIGURE I.34: (a) Schematic representation of the structure under study consisting of a gold grating of 70 nm thick and 70 nm wide deposited on 150 nm thick of EuSe slab. (b) Simulated diagrams of the absorbance (upper panels) and the Faraday rotation (lower panels) for TM (I-III) and TE (II-IV) polarized incident light, as a function of the wavelength and the grating period. The black and white dashed lines indicate the calculated TE and TM resonance modes respectively. The red dashed line indicates the Rayleigh anomaly. The figures are taken from [Flo+15].

With the same type of structure, Kalish and Belotelov [KB16] have demonstrated numerically an enhancement of the LMOKE. The structure consists of Au grating deposited on top of a Bi:YIG film. Highest values of 8° and 3° were achieved in transmission and in reflection respectively, at $\lambda = 957$ nm and for AOI= 10° .

Another experimental enhancement of the FR was achieved by Floess et al [Flo+17], for TE and TM polarized incident light with a 1D MP structure formed by an embedded Au nanowires grating in a thin film of EuS, the structure is illustrated on Fig.I.35a. In this work, a new phenomenon was introduced to enhance the MO effect: the electromagnetically induced

absorption (EIA). This latter is related to a weak coupling (with a certain phase shift) between strongly damped plasmonic oscillations and a TM guided-mode. As a result, a highly absorbed hybrid mode is created which manifests in a dip in the transmittance spectrum. By changing the parameter b (distance between the lower surface of the gold grating and the substrate, see Fig.I.35a), the phase shift can be tuned and for certain values of b a high absorptive TM hybrid mode is obtained. As seen in Fig.I.35b, significant values of FR were measured for TM mode and for $b = 33$ nm, with a maximum value equal to 8° for $p = 490$ nm. For this period, the sharp EIA feature is best centered with respect to the broad (mainly plasmonic feature) transmittance dip. The best FR enhancement (FR= 14° for $p = 505$ nm, see Fig.I.35c) is obtained with optimized parameters which leads to a phase matched situation between TM hybrid mode and TE guided-mode. As a result, an enhancement by a factor of 5.3 and 9.3 were demonstrated for TM and TE polarized incident light respectively as compared to a single layer of EuS. The numerical simulations are in a good agreement with the measurements (not shown here). However, one should not forget that the measurements were performed at 20 K.

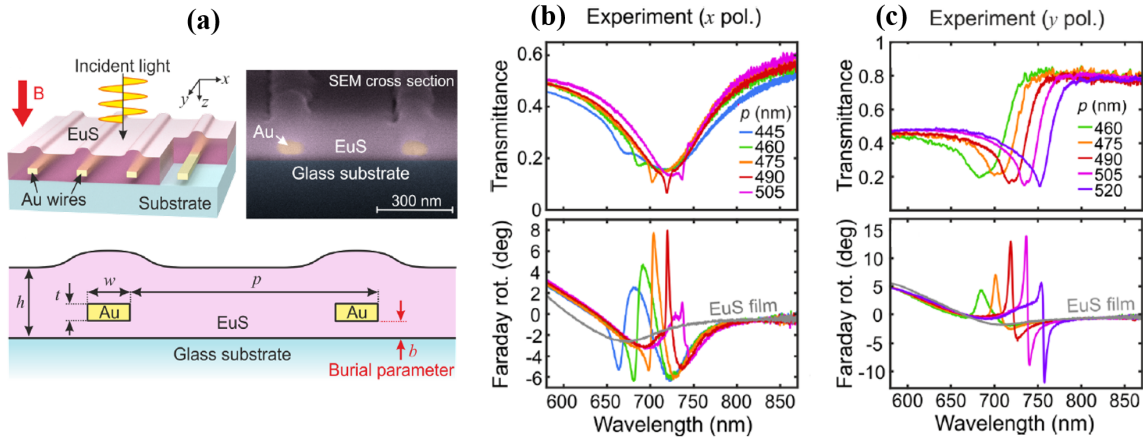


FIGURE I.35: (a) Schematic geometry and SEM image of the structure under consideration. The geometry parameters of the structures are: $w = 85$ nm, $t = 33$ nm and $h = 139$ nm, $b = 33$ nm. Measured transmittance (upper panels) and FR (lower panels) spectra for different period p , for (b) TM and (c) TE polarizations. The figures are adapted from [Flo+17].

Other demonstrations of the polarization rotation effects enhancement are cited in the ref [Kha+07; SH18; DSN18; Lei+16; Li+18].

After describing the different structures developed for polarization rotation enhancement, the next section will be dedicated to describe the different enhancement achievements for MO phase modulation effects.

I.3.2.2 Enhancement of Magneto-Optical Phase Modulation Effects

Grunin et al. [Gru+10] demonstrated an experimental evidence of the TMOKE enhancement through a 1D MP structure consisting of subwavelength nanostructuring of nickel film. The schematic illustration and the atomic force microscopy (AFM) measurements of the structure are illustrated on Fig.I.36a. The measurements of the reflectance and the TMOKE signal

of the structure, as a function of the wavelength are illustrated on Fig.I.36b, for an AOI=68°. As seen in Fig.I.36b, the TMOKE is enhanced by a one order of magnitude compared to the Ni

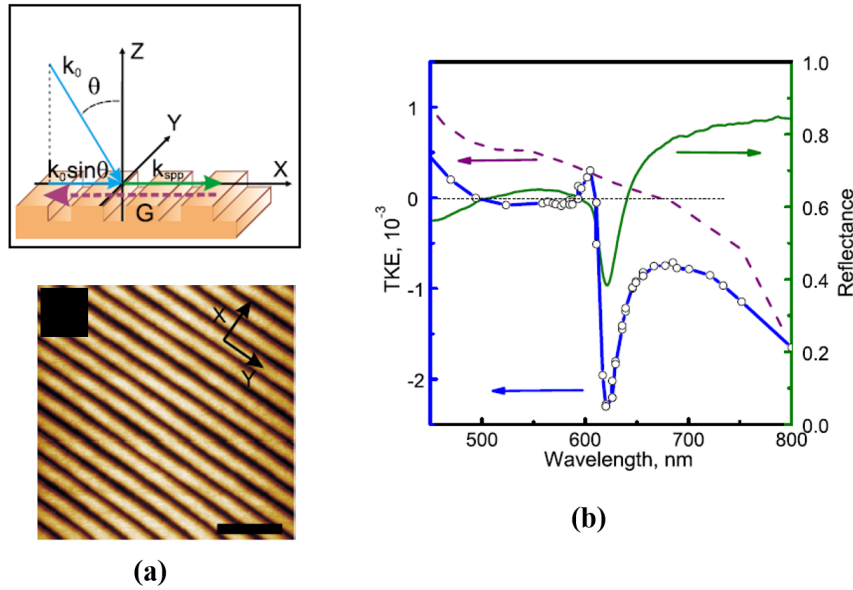


FIGURE I.36: (a) Schematic illustration and AFM measurements of the MP structure. It is formed by a nickel film with 100 nm of thickness deposited on a polymeric substrate and having 1D spatial profile with a modulation period of 320 nm and depth of 50 nm. (b) Experimental measurements of the TMOKE (denoted here TKE) and reflectance spectra of the MP structure at AOI=68° and for TM polarization (x direction). The purple dashed line illustrates the TMOKE spectrum for Ni continuous film. The figures are adapted from [Gru+10].

continuous film (dashed purple curve), at the excitation wavelength of the SPPs ($\lambda = 625$ nm).

Caballero et al.[CGMC16] demonstrated theoretically with the same type of structure of Fig.I.31, a significant TMOKE signal of values up to 8% for an AOI=45°, but with a very small reflectance (near to zero).

Frolov et al. [FSF20] demonstrated an enhancement of the TMOKE signal by experimental measurements and numerical simulations. The work was done by a 1D MP structure consisting of multilayer Au/Ni/Au nanowires. The schematic illustration and the SEM image of the structure are illustrated on Fig.I.37a. Fig.I.37b illustrates the measurements of the transmittance and the TMOKE signal at AOI=15° for the 1D MP structure. The transmittance spectrum shows two peaks related to the coupling between LSP with different diffraction orders at Au/Al₂O₃ interface, through the periodic structure. As seen in Fig.I.37b, the TMOKE signal reaches a maximum value of -0.25% with T=35%.

Significant value of the TMOKE signal was experimentally achieved by Phol et al. [Poh+13] through the standard MP structure: gold grating deposited on top of BIG film. Fig.I.38b illustrates a measured 2D diagram of the TMOKE response in transmission as a function of the incident angle and the photon energy. One can notice on Fig.I.38b, the presence of two opposite TMOKE resonances for a fixed AOI, which is related to the ± 2 nd diffraction order of SPPs propagating at the Au/BIG interface. One can see also that for AOI higher than 4°, remarkable values of $\delta = 13\%$ were reached. However, these values are accompanied with low transmittance of 6%.

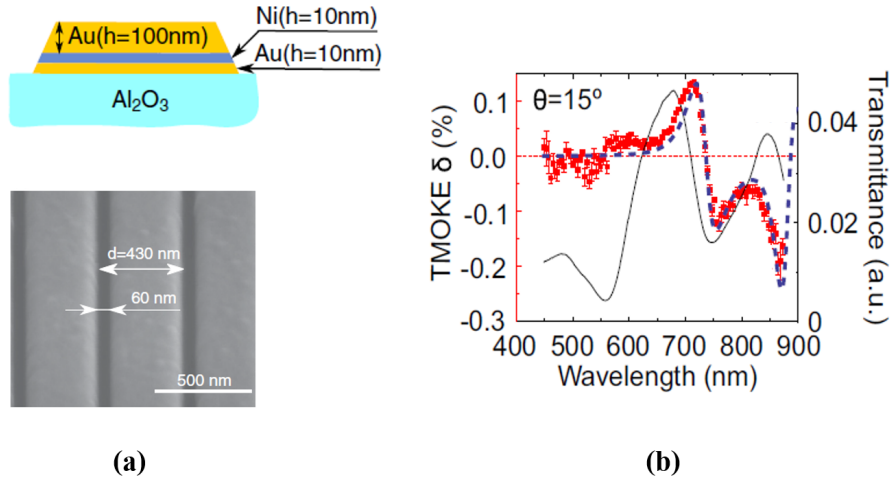


FIGURE I.37: (a) Schematic geometry and SEM image of the resonant structure under study. (b) Experimental measurements of the TMOKE (red curve) and transmittance (black curve) spectra for the MP structure at $\text{AOI}=15^\circ$. The dashed blue curve illustrates the calculated TMOKE. The figures are adapted from [FSF20].

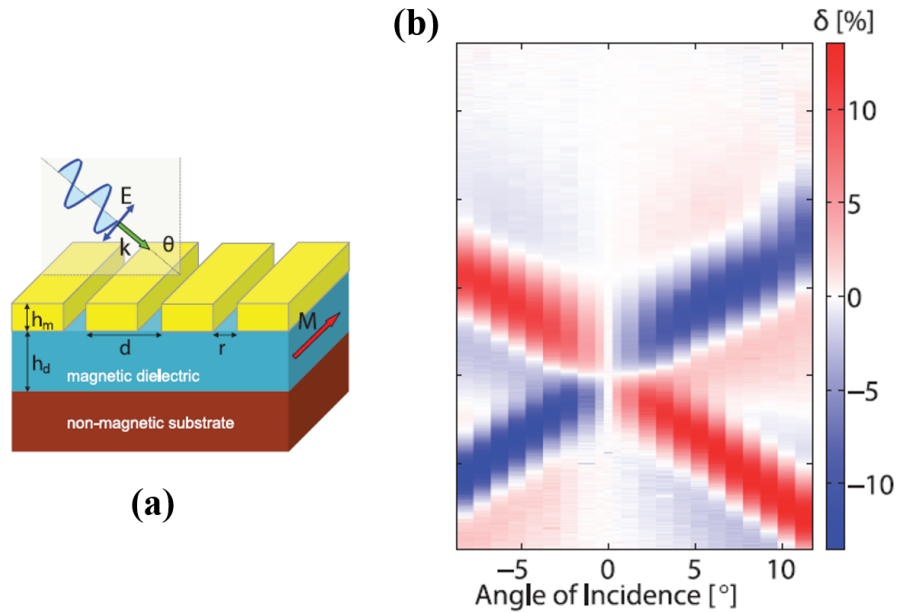


FIGURE I.38: (a) Scheme of the magneto-plasmonic structure: $h_m=125\text{ nm}$, $h_d=905\text{ nm}$, $d=605\text{ nm}$, $r=160\text{ nm}$. (b) Measured angle dependence of the TMOKE signal. The figures are adapted from [Poh+13]

With the same type of structure, Kreilkamp et al. [Kre+13] have demonstrated by numerical simulations and experimental measurements a TMOKE signal enhancement in transmission, where δ reaches a value of 1.5% for an AOI= 9° with $T=45\%$. The TMOKE enhancement in this structure is related to the excitation of WPPs.

Moreover, with similar structures, Halagacka et al. [Hal+13; Hal+18], have demonstrated that the TMOKE signal can be enhanced in case of hybridization of SPPs excited at air/Bi:YIG interface and cavity modes excited in the air slits. The cavity modes can be presented when the air slit is very small compared to the metallic width.

TMOKE enhancement achievements were reached also through structures formed by noble/ferromagnetic multilayers (for example: MO-SPR structures described in section I.1.4.2). TMOKE values up to 15% were experimentally and theoretically achieved with these type of structures owing a high sensitivity to the surrounding medium [Reg+11; Sep+06; RPH18].

More TMOKE enhancements can be found in the references [Dya+19; BKB16; Ign+16; Bar+17; Khr+19; Kal+18; Kos+13; Man+14].

With the same type of structure illustrated on Fig.I.38a, Belotelov et al. [Bel+13], have experimentally demonstrated a variation of the intensity of the transmitted light in the longitudinal configuration, where the Bi:YIG is magnetized perpendicularly to the grating slits. This effect is named Longitudinal Magneto-Photonic Intensity Effect (LMPIE), its origin is explained as follows: due to the longitudinal applied magnetic field, the guided-modes (TE or TM) excited in the MO layer transform into quasi-modes. It means that beside the TM components, the quasi-TM mode also contains TE components due to the MO conversion and vice-versa. The mode wave number of the quasi-modes changes quadratically with respect to the MO term ϵ_{xy} , resulting in a reciprocal spectral shift or shape modification of the transmittance spectrum. Therefore, the LMPIE signal is defined as the relative change of the transmitted intensity I between the magnetized ($I(M)$) and demagnetized ($I(0)$) structure.

Fig.I.39a-b illustrates the experimental measurements of the LMPIE signal with the transmittance spectra at normal incidence and for TM-polarized incident light. As seen in Fig.I.39b, the transmittance spectrum of the MP structure, has three resonances related to the excitation of three quasi TM-modes in the MO waveguide. The black and red arrows illustrate the calculated spectral position of the quasi TE-modes and quasi-TM modes. The presence of opposite peaks in the LMPIE spectra for every mode number, is linked to the quasi-TM and quasi-TE modes resonances. When the quasi TE-mode and quasi TM-mode are spectrally very close, the LMPIE reaches its maximum value (24% at $\lambda=840$ nm). An important remark is that for a bare magnetic film, there is no LMPIE signal (green curve in Fig.I.39b), hence a new effect has appeared with the MP structure at normal incidence.

The numerical simulations (blue curve in Fig.I.39b) are in good agreement with the measurements (red curve).

Recently, the LMPIE in a MP was used for magnetometry [Kny+18]. The experimental study revealed that such an approach allows to reach the nT sensitivity level, which was limited by the noise of the laser. Moreover, the sensitivity can be improved up to $fT/Hz^{1/2}$ and micrometer spatial resolution can be reached.

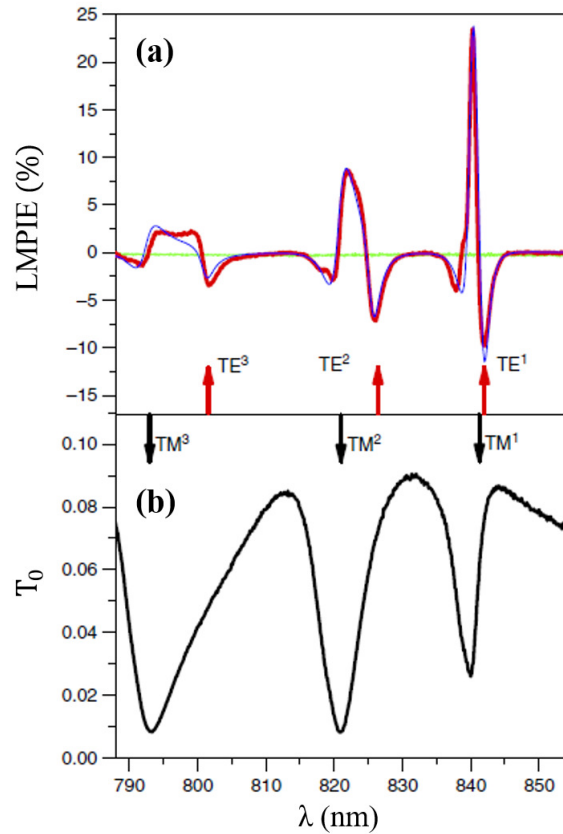


FIGURE I.39: (a) Measurements (red curve) and simulations (blue curve) of LMPIE signal as a function of the wavelength for TM polarization and at normal incident. Green curve indicates the calculated LMPIE signal for a bare magnetic film, which is equal to zero. (b) Spectrum of the optical transmittance for the demagnetized resonant structure. Black and red arrows indicate calculated spectral positions of the quasi-TM and quasi-TE resonances, respectively. The figures are adapted from [Bel+13].

This section was dedicated to present the works mainly done in the literature for enhancing the MO effects. The results of these works are mainly summarized in Tab.I.2 and Tab.I.3. They show that the best MO enhancements are obtained through simulations, underlying the difficulty to process efficient MO materials. Furthermore, MO enhancements are generally accompanied with higher signal level for all-dielectric devices compared to plasmonic ones. Finally, it should be noticed that the devices given in this table generally produce enhancement for only one type of MO effects.

TABLE I.2: Comparison between the different results of enhancing the polarization rotation MO effects. Exp and Num are abbreviations for Experimental and Numerical works respectively.

	Structure	Work Type	MO Effect	Rotation Value	Optical Response	Reference
All-Dielectric	$(Bi : YIG / SiO_2)_4$	Exp	Faraday	-0.8°	T=80%	[Fed+04]
	$(Ta_2O_5 / SiO_2)_{10} / Bi : YIG$	Exp & Num	Faraday	-0.63°	T=63%	[Ino+06]
	3D inverse opal of MO composite	Exp	Faraday	-0.31°	T=3%	[AD+16]
	BIG nanodisks in SiO_2	Num	Faraday	-7.5°	T=96%	[Chr+18]
	1D-(MO composite; Si_3N_4)	Num & Exp	Faraday	0.49°	T=50%	[Roy+20]
		Num & Exp	LMOKE	0.4°	T=25%	[Roy+20]
	2D-Bi:YIG	Num	Faraday	50°	T=40%	[BTT06]
		Num	PMOKE	90°	R=24%	[BTT06]
Magneto-Plasmonic	Co Hexagonal	Exp & Num	PMOKE	-0.66°	R=—	[RR+19]
	Ni Hexagonal	Exp	LMOKE	0.13°	R=2%	[Che+12]
	Au/Co/Au array	Num	Faraday	0.25°	T=3%	[CGMC15]
	2D-Au/Bi:YIG	Num	Faraday	0.78°	T=35%	[BDZ07]
		Num	PMOKE	0.63°	R=—	[BDZ07]
	2D-Ag/Bi:YIG	Num	Faraday	-1°	T=50%	[Li+16]
		Num	PMOKE	-0.85°	R=24%	[Li+16]
	1D-Au/BIG	Exp & Num	Faraday	0.8°	T=36%	[YC+13]
	1D-Au/Bi:YIG	Num	LMOKE	8°	T=10%	[KB16]
		Num	LMOKE	3°	R=—	[KB16]
	1D-Au/EuSe	Exp & Num	Faraday	4.2°	T=30%	[Flo+15]
	1D-Au in EuS	Exp & Num	Faraday	14°	T=20%	[Flo+17]

TABLE I.3: Comparison between the different results of enhancing the phase modulation MO effects. Exp and Num are abbreviations for Experimental and Numerical works respectively. Di and MP are abbreviations for all-Dielectric and Magneto-Plasmonic structures respectively.

	Structure	Work Type	MO Effect	MO Response	Optical Response	Reference
Di	1D- $(Bi : YIG ; SiO_2)$	Num	TMOKE	4%	R=97%	[MBK14]
	1D-(MO composite; Si_3N_4)	Num	TMOKE	0.5%	T=25%	[Roy+20]
	1D-Bi:YIG	Exp& Num	TMOKE	0.9%	T=60%	[Vor+20]
	1D-Ni	Exp	TMOKE	0.23%	R=40%	[Gru+10]
MP	Au/Co/Au	Exp & Num	TMOKE	15%	R ~ 0%	[Reg+11]
	Co/Au	Exp & Num	TMOKE	10%	R=10%	[Ign+16]
	1D-(Au/Ni/Au)	Exp & Num	TMOKE	0.25%	T=35%	[FSF20]
	(Ni ; a-Si:H) nanodisks	Exp & Num	TMOKE	0.6%	T=42%	[Bar+17]
	1D-Au/Bi:GIG	Exp& Num	TMOKE	1.5%	R=20%	[Hal+18]
	1D-Au/BIG	Exp	TMOKE	13%	T=6%	[Poh+13]
	1D-Au/Bi:YIG	Exp & Num	TMOKE	1.5%	T=4%	[Bel+11]
		Exp & Num	LMPIE	24%	T=30%	[Bel+13]
		Num	LMPIE	50%	T=10%	[KB16]

I.4 Objectives

From several years, the enhancement of the MO effects is taking lots of attention due to the wide applications of the MO activity in controlling light and sensing technology. Different structures have been simulated or fabricated to reach this objective, using different MO materials. Most of these structures are magneto-plasmonic, due to the beneficial combination of the MO activity and the SPPs. Bimetallic systems consisting of noble and ferromagnetic metals with smooth or perforated surface [CGMC15; Ign+16], have been studied to enhance the MO effects. These structures have a high sensitivity to the surrounding medium (biosensing applications), but they present large optical losses limiting their practical applications. To decrease the optical losses, a magneto-plasmonic structure formed by perforated noble metal deposited on a dielectric magnetic film was implemented [Poh+13; Flo+15]. As explained in the previous sections, these latter structures have been recently the interest of lots of papers, where different MO effects have been improved, through 1D and 2D systems.

Another way to decrease the optical losses is working with all-dielectric structures where also different MO effects were enhanced with high reflectance or transmittance, through multilayers, metasurfaces or GMR gratings.

Therefore, the enhancement of the MO effects will be the interest of this presented work, in order to obtain a high sensitive device for the detection of different magnetic field components, applicable in non destructive techniques. The structure will be all-dielectric: first, to avoid the formation of EC in the structure which limits the measurements precision, second to decrease the optical losses. The target structure is 1D-GMR grating, consisting of a photoresist grating deposited on top of a MO composite waveguide which is deposited on a glass substrate (see Fig.I.40). Hence, the guided-mode resonance will be the only phenomenon contributing in the MO enhancement. This structure was chosen for its simplicity of fabrication even at large scale, which leads to low costs MO devices.

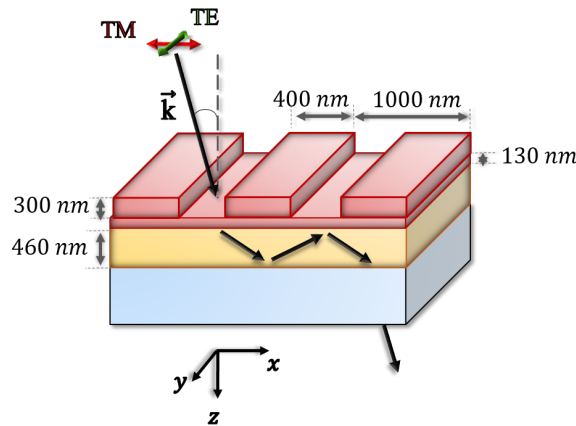


FIGURE I.40: Schematic illustration of the structure under study in this work: photoresist grating deposited on MO composite waveguide itself deposited on a glass substrate.

Section I.1.3 has shown that, different magnetic films were used in the literature. Some of them are difficult to fabricate, present large optical losses or work in difficult environment condition (such low temperature). From several years, a MO material has been developed in the LabHC, made of cobalt ferrite NPs embedded in a silica matrix by the sol-gel process

resulting in a MO composite. With this latter, it is possible to deposit uniform thin layers on large scale substrates, with a 100°C thermal treatment and with standard deposition processes (dip or spin coating). An important feature of this MO sol-gel is that by modifying the volume fraction of the NPs inside the MO composite, the whole permittivity tensor of this latter can be tuned.

This MO material was employed during previous works to impregnate all-dielectric 1D, 2D [Var17] and 3D [AD+16] micro/nano-structured templates for enhancing the MO effects. These works have led to promising MO enhancements, but the fabrication process was too long or difficult which is not suitable for applications or industrial use. For example, fabricating a 1D- Si_3N_4 grating needs expensive process.

Thus, the main objective of this work is to study and optimize the ability of the simple adapted 1D-GMR structure to enhance several MO effects: polarization rotation and intensity modulation through every orientation of the magnetic field. Such work will be based on a structure design and optimization through numerical simulations, followed by fabrication and MO characterizations. Comparison between simulations and measurements, and fine analysis of the results will lead to a good understanding of the physical mechanisms inducing MO enhancement. Finally, a suitable configuration of sensing will be defined to measure every component of a magnetic field.

Secondary objectives are also the interest of this work:

- A broader study on the whole permittivity tensor of the MO composite, in order to master well the optical and MO properties of this latter.
- Development of different homemade MO setups in order to have a precise MO resonances measurements, in different magnetic field configurations.

Therefore, the rest of this thesis manuscript is as follows:

- Chapter II is dedicated to present the evolution of the optical, MO and geometrical properties of the MO composite films, with the NPs concentration. As a result, the estimated volume fraction and refractive index of the NPs in the final MO composite will be presented. All this study aims to identify the whole permittivity tensor of the MO composite and to expect the MO composite film characteristics before elaboration for the structure design.
- Chapter III is dedicated to present the numerical and experimental evidence of the MO enhancement effects through the 1D all-dielectric structures, preceded by the description of the different MO homemade developed setups.

CHAPTER II

Materials and Devices: Properties and Fabrication Processes

This chapter is mainly dedicated to the composite material in terms of optical or magneto-optical properties, but also in terms of elaboration. Indeed, a special study has been carried out to deduce the whole permittivity tensor of this material. This latter consists of cobalt ferrite NPs embedded in a silica matrix, employing a sol-gel approach.

Hence, an introduction of the cobalt ferrite NPs is presented firstly. Then, the MO composite and films elaboration is detailed before a presentation of their geometrical, optical and MO properties. As a result, the NPs concentration and their refractive index are determined. This will be helpful to forecast all the MO composite characteristics before elaboration.

The last part of the chapter finally relates to the fabrication and the opto-geometric characterizations of the different all-dielectric GMR structures.

II.1 Magnetic Nanoparticles of Cobalt Ferrite

Magnetic NPs are magnetic materials formed by particles with diameter smaller than 1 micrometer (typically 1-100 nm) containing from a few hundred to about 10^5 atoms. Different materials have been synthesized in this form: magnetite (Fe_3O_4), copper ferrite ($CuFe_2O_4$), maghemite (γFe_2O_3), cobalt ferrite ($CoFe_2O_4$) [Woh86], etc.

The NPs can be manipulated by a magnetic field and can be dispersed in different media: liquid, gel and solid. When they are stabilized in a carrier liquid (for example water), the resulting solution is called ferrofluid or magnetic liquid [BB96].

The NPs can be widely used for biomedical applications such as drug-targeting, cancer therapy, lymph node imaging, or hyperthermia [BC03; Tar+03; And+07]. They can also be used in magnetic data storage [Bed+13], as well as in defect sensors [Bai+20].

Cobalt ferrite NPs with ellipsoidal shapes will be the interest of the presented work. Indeed, even if their shape is quite random (rock-like [Has+98]), NPs often have a greater spatial extension in one direction, they are then represented by ellipsoids (see Fig.II.3). Therefore,

their crystal structure, diameter distribution, as well as their magnetic, optical and MO properties, will be detailed in the following sections.

II.1.1 Crystal Structure

The spinel ferrite [Tat+17; MJ07] is a class of compounds with cubic crystallisation. It has the formula of $M^{2+}Fe_2^{3+}O_4^{2-}$, where M^{2+} is a divalent metal like Ag^{2+} , Mn^{2+} , Fe^{2+} , Co^{2+} , etc. The ferrite cobalt ($CoFe_2O_4$) belongs to the spinels ferrite and its crystal structure is similar to that of the mineral spinels [Bra15; Nis15]: gemstone magnesium aluminate ($MgAl_2O_4$, see Fig.II.1).

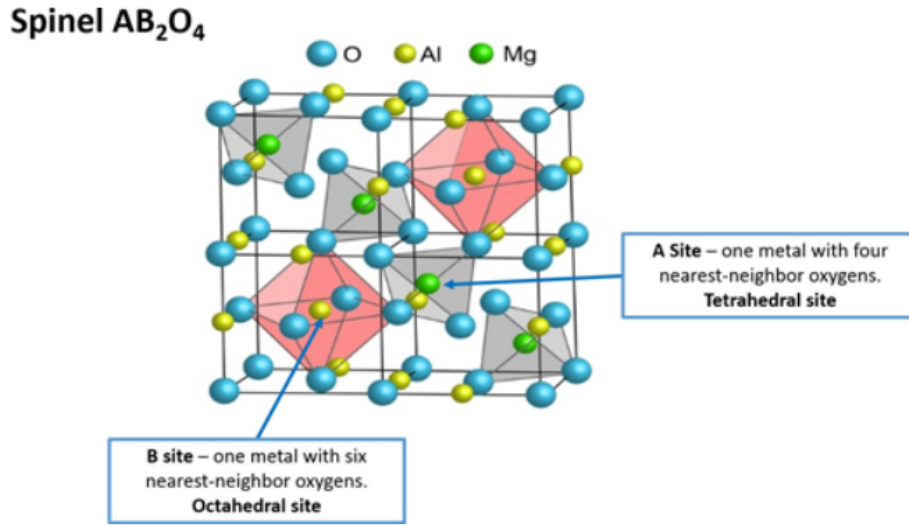


FIGURE II.1: Representation of the ions distribution in the gemstone magnesium aluminum spinel, $MgAl_2O_4$. The O^{2-} anions constitute a cubic network with centered faces. The divalent Mg^{2+} cations occupy tetrahedral sites, and the trivalent Al^{3+} cations occupy octahedral sites. The figure is adapted from [Nan16].

The unit cell of the mineral spinel is formed by 8 molecules of $Mg^{2+}Al_2^{3+}O_4^{2-}$:

- 32 anions of O^{2-} are distributed in a cubic face centered (cfc) arrangement and they define 64 tetrahedral sites (noted A) and 32 octahedral sites (noted B)
- 8 divalent cations Mg^{2+} are arranged in the tetrahedral sites.
- and 16 trivalent cations Al^{3+} are arranged in the octahedral sites.

The structure of cobalt ferrite NP is a mixture between a direct and an inverse spinel structures [VKP80]. Hence, it consists of 8 divalent cations of Co^{2+} and 16 trivalent cations of Fe^{3+} distributed between tetrahedral and octahedral sites.

II.1.2 Diameter Distribution

The cobalt ferrite NPs employed in the presented work, have variable diameters D . The log normal law $P(D)$ is the most frequently used model to describe the distribution of NPs:

$$P(D) = \frac{1}{\sqrt{2\pi}\sigma D} \exp\left(-\frac{1}{2\sigma^2} \ln^2\left(\frac{D}{D_0}\right)\right) \quad (II.1)$$

With $\int_0^\infty P(D) dD = 1$. D_0 is the median diameter and σ is the standard deviation of the distribution.

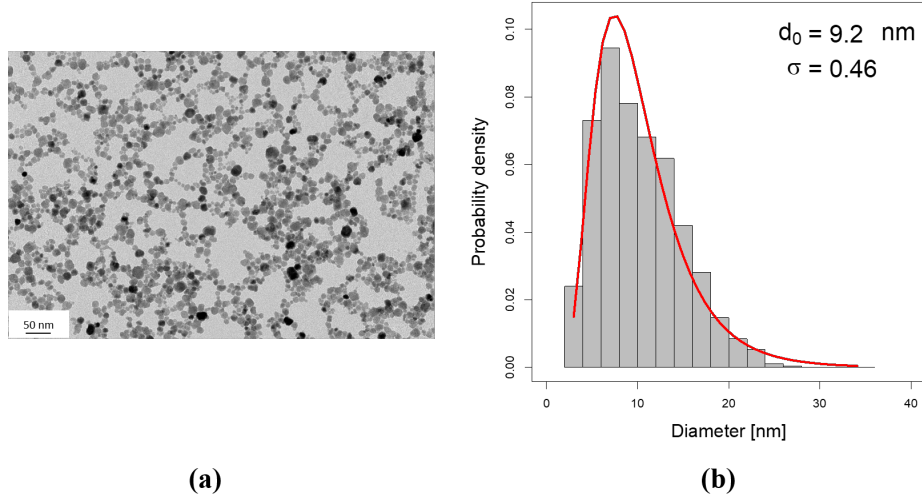


FIGURE II.2: (a) TEM image of CoFe_2O_4 NPs initially dispersed in water. (b) Histogram representing the diameter distribution of the NPs. The red curve represents the adjusted log normal distribution $P(D)$ with $D_0 = 9.2 \text{ nm}$ and $\sigma = 0.46 \text{ nm}$. The measurements are done in PHENIX laboratory, UMPC.

To determine the parameters of $P(D)$, one solution consists of observing the magnetic liquid with the transmission electron microscopy (TEM, see Fig. II.2a), and performing a statistical count of the diameters. This process is shown on Fig. II.2b, with parameters of the log normal distribution fitting the best with the counting histogram.

II.1.3 Stability and Homogeneity of the Ferrofluid

It is necessary to have a stable and homogeneous ferrofluid to avoid the formation of aggregates and precipitates of NPs, which affect the good dispersion of these latter in the final MO composite and their behavior under a magnetic field. For this reason, the production of the magnetic liquid requires special attention. The thermal energy promotes the homogeneity and the stability of the NPs inside the liquid. Hence, the diameter of the particles must be sufficiently small for the gravitational energy to be weaker than the thermal energy, which justifies nanometer sizes [Lac99]. The interaction forces between magnetic and electric dipoles of the NPs can create aggregates in the ferrofluid, hence repulsive forces are needed. These latter can be reached by coating the NPs with surfactant or by giving the NPs same electrical charges [Mas81].

The different ferrofluids used in this work were all prepared by Sophie Neveu, in the PHENIX laboratory of Sorbonne university, Paris. They consist of cobalt ferrite NPs dispersed in water. Their elaboration process is explained as follows: cobalt ferrite NPs result from the co-precipitation of hydroxides of iron (Fe^{3+}) and cobalt (Co^{2+}) in stoichiometric proportions [Nev+02]. The NPs are thermally treated at 100°C for two hours. Then, they are treated with a solution of ferric nitrate at boiling point in order to complex them with a layer of amorphous iron hydroxide which makes it possible to obtain stable particles of cobalt ferrite in an acid

medium. After various washes with acetone and ether, the complexed NPs are dispersed in distilled water to obtain the magnetic liquid [Nev+02].

The initial NPs concentration of the ferrofluid is 7.8%. For decreasing this latter, water was added to the ferrofluid with specific quantities, depending on the desired final concentration.

II.1.4 Magnetic Properties

II.1.4.1 Individual Magnetic State

The magnetic particles consist of individual magnetic moments carried by the magnetic ions (such as Fe^{2+} , Fe^{3+} and Co^{2+}). The exchange interaction between these moments tends to orient them all in the same direction in the case of NPs of diameter smaller than 20 nm. The particle is then called monodomain and bears a macro-moment $\vec{\mu}$ whose magnitude depends on its volume V by the relation: $|\vec{\mu}| = m_s V$. m_s is the saturated magnetization (for cobalt ferrite, $m_s = 3.5 \times 10^5 A.m^{-1}$ [Has+01]). Due to a magnetic anisotropy coming from an anisotropy of the material or from a particular form of the particle, the orientation of the magnetic macro-moment in the particle is not random. There is always a privileged orientation called easy axis of magnetization represented by the vector \vec{n} in Fig.II.3. The anisotropy energy E_a is the energy required to change the direction of the magnetic moment away from its easy axis of magnetization.

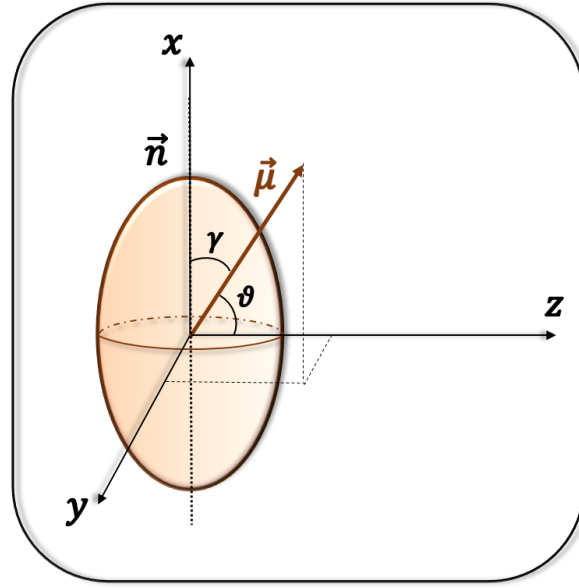


FIGURE II.3: Schematic representation of a magnetic nanoparticle having a uniaxial optical anisotropy (\vec{n}) and a macro-moment ($\vec{\mu}$), which is the case of cobalt ferrite nanoparticle.

In the case of cobalt ferrite, the origin of the magnetic anisotropy is due to a magneto-crystalline volume anisotropy with a cubic symmetry, which is linked to the presence of the Co^{2+} ions in the octahedral sites [Nan16]. This anisotropy is characterized by an energy expressed as follows:

$$E_a = K_a V \sin^2 \gamma \quad (II.2)$$

where K_a is a characteristic constant of the material and it is equal to $5 \times 10^5 \text{ J.m}^{-3}$ for cobalt ferrite NPs [Has+01], V is the volume of the NP and γ is the angle between the magnetic moment and the axis of easy magnetization. According to Eq.II.2, this energy is minimal when γ is zero or 180° (the magnetic moment is aligned with its easy axis of magnetization) and it is maximum when γ is 90° .

Due to their ellipsoidal shape or to their crystalline structure, the ferrite cobalt NP has also a uniaxial optical anisotropy, with an optical axis overlapped with the direction of \vec{n} ($n_x > n_y = n_z$).

The behavior of the magnetic moments depends on the anisotropic (E_a) and thermal energies ($k_B T$). For cobalt ferrite NPs with diameters larger than 10 nm, the anisotropy energy is dominant: it is a rigid dipole. In this case, the magnetic moments are strongly attached to the axis of easy magnetization and they are barely sensitive to thermal fluctuations. Otherwise, for diameter less than 10 nm, the thermal and anisotropic energy are in equilibrium. Hence, the magnetic moment direction can fluctuate: it is a soft dipole.

Now, if a magnetic field \vec{B} is applied in z direction referring to Fig.II.3, the magnetic moment tends to align in its direction, with a magnetic energy given as:

$$E_B = -\vec{\mu} \cdot \vec{B} = -|\vec{\mu}|B \cos \vartheta \quad (\text{II.3})$$

where ϑ is the angle between $\vec{\mu}$ and z axis (see Fig.II.3).

The magnetic energy increases with the volume of the NPs ($|\vec{\mu}| = m_s V$). Hence, larger magnetic fields are needed to orient the magnetic moments of small NPs.

After describing the magnetic properties of an individual particle, the next section will be dedicated to the magnetic behavior of assembly of NPs, either dispersed in water or blocked in a matrix.

II.1.4.2 Magnetization Behavior

In this section, we will consider an applied magnetic field in z direction (referring to Fig.II.3) and we will study the behavior of the magnetization of the different systems.

Magnetic Liquid:

The behavior of the ferrofluid magnetization under an applied magnetic field is illustrated on Fig.II.4. In the absence of an external applied magnetic field, the axes of easy magnetization of the NPs dispersed in a liquid, are disorderly oriented in the liquid due to the thermal energy. Hence, the magnetic moments have random directions and the total magnetization M of the liquid is zero (see Fig.II.4a). Whereas, if a magnetic field is applied, the magnetic moments and the NPs tend to align in the direction of the field. Hence, the oriented moments create a certain magnetization. This latter increases with the magnitude of the applied magnetic field (linear behavior for small field values) before attaining a saturated value M_s (see Fig.II.4b-c). Once the magnetic field is cutted-off, the magnetic moments return to their disorder state and the NPs to their random directions in the liquid because of the

thermal energy (Fig.II.4d). The magnetization is zero again and the curve doesn't present any hysteresis.

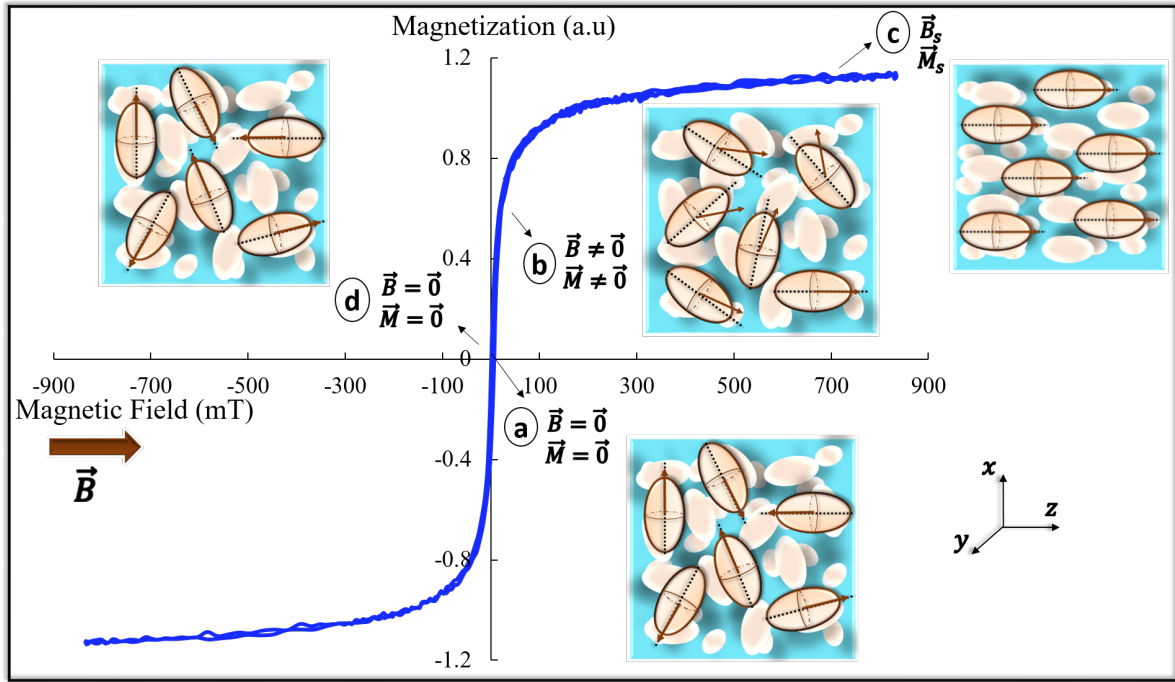


FIGURE II.4: Representation of the magnetization loop for cobalt ferrite nanoparticles dispersed in a liquid.

The magnetization produced by the oriented NPs magnetic moments in a magnetic liquid is the sum of the magnetization of oriented NPs magnetic moments with the same diameter D . It is described by the Langevin's law [Lan05] and expressed as follows:

$$M(B) = \int_0^\infty M(B, D) dD = \int_0^\infty m_s \phi(D) L(\mathfrak{L}) dD \quad (\text{II.4})$$

where L is the Langevin function and it is given by:

$$L(\mathfrak{L}) = \coth(\mathfrak{L}) - \frac{1}{\mathfrak{L}}$$

and \mathfrak{L} is the Langevin parameter and it is expressed as follows:

$$\mathfrak{L} = \frac{\mu_0 \mu B}{k_B T} = \frac{\mu_0 m_s \pi D^3 B}{6 k_B T}$$

The Langevin parameter describes the competition between the orientation of NPs along the magnetic field and the desorientation due to the thermal agitation.

μ_0 is the vacuum permeability, k_B is the Boltzmann constant, T is the absolute temperature of the ferrofluid, B is the applied magnetic field and $\phi(D)$ is the NPs volume fraction with diameter D .

For high magnetic field, the Langevin function tends to the unity and the expression of the magnetization tends to its saturated value:

$$M(B \rightarrow \infty) = m_s \phi \quad (\text{II.5})$$

For low magnetic field, $L(\mathcal{L}) \simeq \frac{\mathcal{L}}{3}$ hence the expression of the magnetization is transformed to:

$$M(B) = \frac{m_s^2 \mu_0 \pi}{18 k_B T} B \int_0^\infty D^3 \phi(D) dD \quad (\text{II.6})$$

Thus, for low magnetic field amplitudes, the magnetization follows a linear evolution (see Fig.II.4) with a slope proportional to the average volume of the NPs (according to Eq.II.6). Whereas, for high magnetic field the magnetization reaches a saturated value (see Fig.II.4) which depends on the concentration of NPs (referring to Eq.II.5).

Blocked Nanoparticles:

Now, let's consider cobalt ferrite NPs embedded in a sol-gel solid matrix (the description of this system will be detailed later in this chapter). The magnetization behavior of the system is illustrated on Fig.II.5. In the absence of a magnetic field the NPs are frozen in the sol-gel matrix in a disorder way. Hence, the magnetic moments have random directions in the film and the total magnetization is zero (Fig.II.5a). Once, a magnetic field is applied only the magnetic momentum tends to align in the direction of the magnetic field creating a certain M until saturation (see first magnetization curve). The NPs and their easy axis of magnetization cannot follow the movement of the moments since they are blocked in the matrix (Fig.II.5b-c).

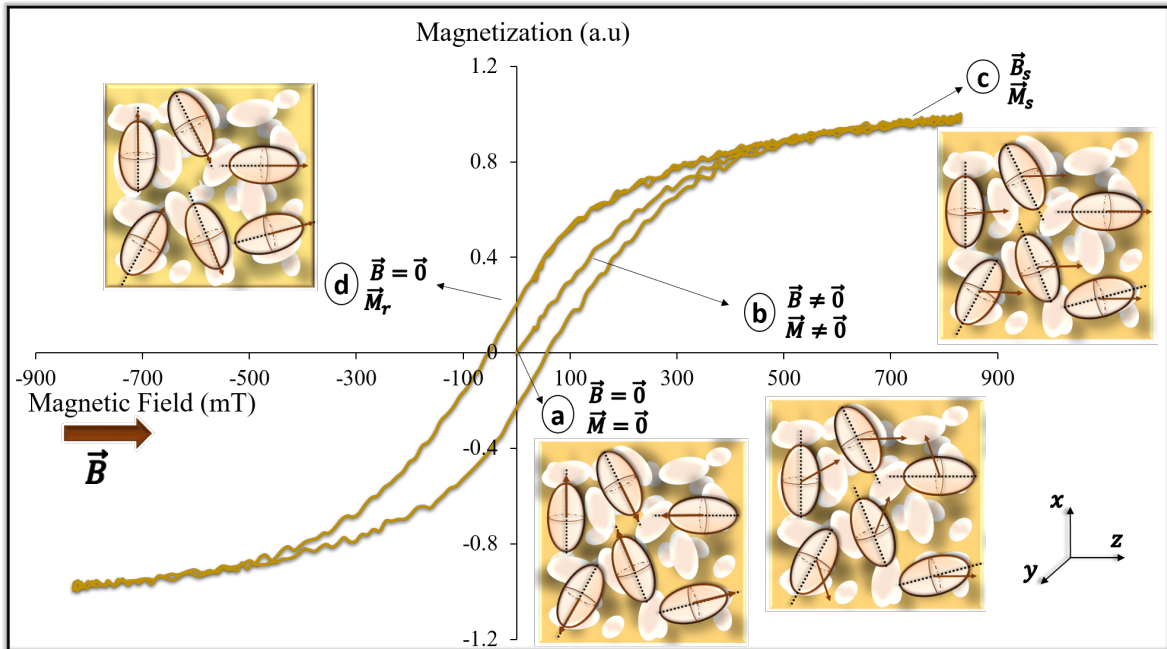


FIGURE II.5: Magnetization loop of a thin film formed by cobalt ferrite nanoparticles embedded in a sol-gel matrix.

Now if the magnetic field is cutted-off, the moments go back in the easy axis direction which makes the weakest angle with the direction of the applied field. Hence, a remanent magnetization (M_r) is obtained (Fig. II.5d). Therefore, contrary to the M of a magnetic liquid, a hysteresis loop is observed with a remanence M_r and a coercive field B_c . This latter describes the field needed to cancel the remanent magnetization.

The hysteresis loop disappears in the case of superparamagnetic materials: anisotropic energy \ll thermal fluctuations [Jam+09]. In this case, the thermal fluctuations prevent having a remanent M_r (similar to magnetic liquid).

After describing the magnetic behavior of a magnetic liquid and blocked NPs, the next section will be dedicated to the MO behavior.

II.1.5 Magneto-Optical Behavior

The MO behavior of an assembly of individual magnetic NP depends on two different anisotropies:

- The reciprocal linear anisotropy that relates to the orientation of the intrinsic anisotropy core of the NP.
- The non-reciprocal circular anisotropy or MO activity (leading to Faraday effect) which is due to the orientation of the magnetic moment of the NP. Its magnetic field induced behavior is thus identical to that of the magnetization [Jam+09].

Hence, the MO properties of such an assembly will depend on both the anisotropies of the individual NP, and also on the whole orientation of their cores and magnetic moments. Of course, they also depend on the volume fraction of NPs (ϕ).

II.1.5.1 Individual Particle Permittivity

The reciprocal linear anisotropy originates from the ellispoidal shape of the NP or from the crystalline structure of cobalt ferrite core. In both cases, the optical axis can be considered identical to the easy axis of magnetization (\vec{n} on Fig. II.3). In the NP coordinate system (x, y, z axes on Fig. II.3), the permittivity tensor corresponding to this anisotropy can be written as:

$$\epsilon_L = \begin{pmatrix} \epsilon_{xx}^{NP} & 0 & 0 \\ 0 & \epsilon_{yy}^{NP} & 0 \\ 0 & 0 & \epsilon_{yy}^{NP} \end{pmatrix} \quad (\text{II.7})$$

ϵ_{xx}^{NP} and ϵ_{yy}^{NP} are both complex. Their imaginary part gives rise to the light absorption and their difference is the origin of the linear anisotropy.

The circular anisotropy is linked to the magnetic moment of the NP, which induces a coupling between polarized waves whose direction are perpendicular to this moment. If we consider that the moment is aligned along z direction, the permittivity tensor related to this

effect contains off-diagonal antisymmetric terms and can be written as:

$$\epsilon_C = \begin{pmatrix} 0 & i\epsilon_{MO} & 0 \\ -i\epsilon_{MO} & 0 & 0 \\ 0 & 0 & 0 \end{pmatrix} \quad (\text{II.8})$$

For all other directions of the moment $\vec{\mu}$, this permittivity is written as:

$$\epsilon_C = \begin{pmatrix} 0 & i\epsilon_{MO}\cos(\vec{\mu};z) & i\epsilon_{MO}\cos(\vec{\mu};y) \\ -i\epsilon_{MO}\cos(\vec{\mu};z) & 0 & i\epsilon_{MO}\cos(\vec{\mu};x) \\ -i\epsilon_{MO}\cos(\vec{\mu};y) & -i\epsilon_{MO}\cos(\vec{\mu};x) & 0 \end{pmatrix} \quad (\text{II.9})$$

Finally, the permittivity of the NP is the sum of both contributions ϵ_L and ϵ_C , and its expression depends on the orientation of NP's core and magnetic moment.

II.1.5.2 Composite Global Permittivity

Instead of one particle, we consider now an assembly of NPs dispersed in a liquid (water), or embedded in a sol-gel solid matrix. This mixture is called a composite material. The permittivity tensor of such material can be obtained using an Effective Medium Approximation (EMA) [Cho15], which combines the permittivity of the host material (ϵ^H) and that of the NP (ϵ^{NP}) taking into account the volume fraction ϕ of NPs in the matrix. Concerning the matrix, the permittivity is isotropic:

$$\epsilon_H = \begin{pmatrix} \epsilon_{xx}^H & 0 & 0 \\ 0 & \epsilon_{xx}^H & 0 \\ 0 & 0 & \epsilon_{xx}^H \end{pmatrix} \quad (\text{II.10})$$

The contribution of the NPs to the whole matrix is more complex, because it depends on the orientation of the core and moment of every NP. To obtain this contribution, it is necessary to sum each individual contribution with a statistical approach based on Boltzmann Low, which gives N the number of NPs possessing an energy U through: $N \propto \exp(\frac{-U}{k_B T})$ [KJL01]. For the NP, the energy U derives from the Zeeman and anisotropy energies: $U = -\vec{\mu} \cdot \vec{B} - E_a \vec{\mu} \cdot \vec{n}$.

In the case of random orientations of the NPs, the whole tensor remains isotropic:

$$\begin{pmatrix} \epsilon_{xx} & 0 & 0 \\ 0 & \epsilon_{xx} & 0 \\ 0 & 0 & \epsilon_{xx} \end{pmatrix} \quad (\text{II.11})$$

with ϵ_{xx} is linked to ϵ_{xx}^H , the mean value of ϵ_{xx}^{NP} and ϵ_{yy}^{NP} , and to ϕ .

In the other cases, the statistical sum has to be done properly for each term, and can lead to simple expressions in special cases. This statistical analysis is based mainly on the following physical mechanism:

- A magnetic field applied to the material tends to align the magnetic moments in its direction through Zeeman energy: $\vec{\mu} \cdot \vec{B}$.
- Whether the matrix is solid or liquid, the NP core will orientate in order to align its easy axis of magnetization \vec{n} with the moment $\vec{\mu}$.

Based on these assumptions, we will now describe the linear and circular anisotropy in both liquid and solid matrices.

II.1.5.3 Magneto-Induced Linear Anisotropy

Magnetic Liquid:

As mentioned before, the application of a magnetic field to a magnetic liquid, tends to align the moments $\vec{\mu}$ following its direction and thus the NPs core too (in other words the axis \vec{n}). Hence, an optical anisotropy of the system is created whose optical axis is parallel to the direction of the applied magnetic field (considered to be following z direction). The permittivity tensor of the system at saturation is then defined as:

$$\begin{pmatrix} \epsilon_{xx} & 0 & 0 \\ 0 & \epsilon_{xx} & 0 \\ 0 & 0 & \epsilon_{zz} \end{pmatrix} \quad (\text{II.12})$$

Once the magnetic field is cutted-off, the anisotropy is canceled due to the thermal fluctuations and the whole tensor will take again the expression of Eq.II.11.

Fig.II.6 illustrates the calculated optical linear anisotropy (Δn) in a magnetic liquid, as a function of the magnetic field. The statistical sum of individual NP anisotropies gives a difference between ϵ_{xx} and ϵ_{zz} , which follows a second order Langevin function. The final birefringence of the fluids is thus given by:

$$\Delta n \propto 1 - \frac{3L(\mathcal{L})}{\mathcal{L}} \quad (\text{II.13})$$

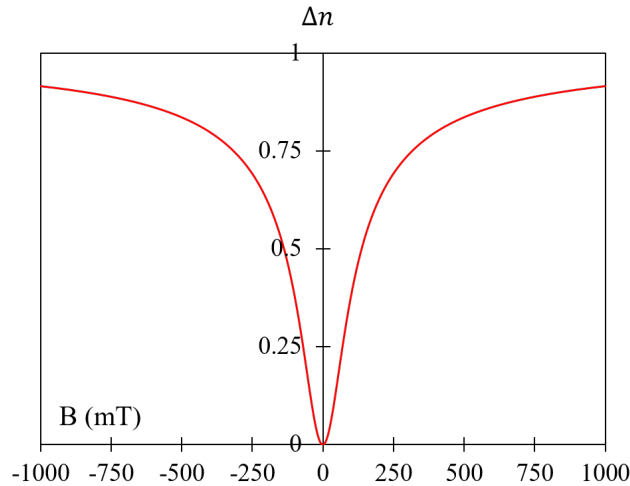


FIGURE II.6: Calculated optical linear anisotropy as a function of the magnetic field amplitude at 300K, in case of CoFe_2O_4 NPs dispersed in magnetic liquid. The average diameter of the NPs is $D_0 = 9.2$ nm.

Therefore, for small magnetic field the evolution of the linear anisotropy is quadratic and attains the saturation for large field values (see Fig.II.6).

One can see on Fig.II.6, that the linear optical anisotropy is a reciprocal effect because it has identical value for opposite magnetic field directions, contrary to the circular anisotropy (see Fig.II.4 and explained more in Chap.I).

Blocked Nanoparticles:

In case of NPs embedded in a matrix, the NPs cannot follow the direction of the applied magnetic field since they are blocked in the matrix. However, if a magnetic field was applied to the NPs before the gelation of the matrix, a permanent linear optical anisotropy can be created. Indeed, the NPs and their momentum follow initially the direction of the applied magnetic field (named gelation field). Once the matrix is gelified, the magnetic field is cutted-off and the direction of the NPs is then blocked, creating a permanent anisotropy of the system with optical axis parallel to the direction of the gelation field. Therefore, the tensor permittivity of the final composite is the same than Eq.II.12.

This permanent anisotropy has been demonstrated by Jamon et al. [Jam+01]. The results of the created optical anisotropy (Δn) are illustrated on Fig.II.7, as a function of the volume fraction of NPs and for two different gelation magnetic field magnitudes. As seen in this figure, Δn is proportional to the concentration of NPs and depends on the magnitude of the gelation magnetic field.

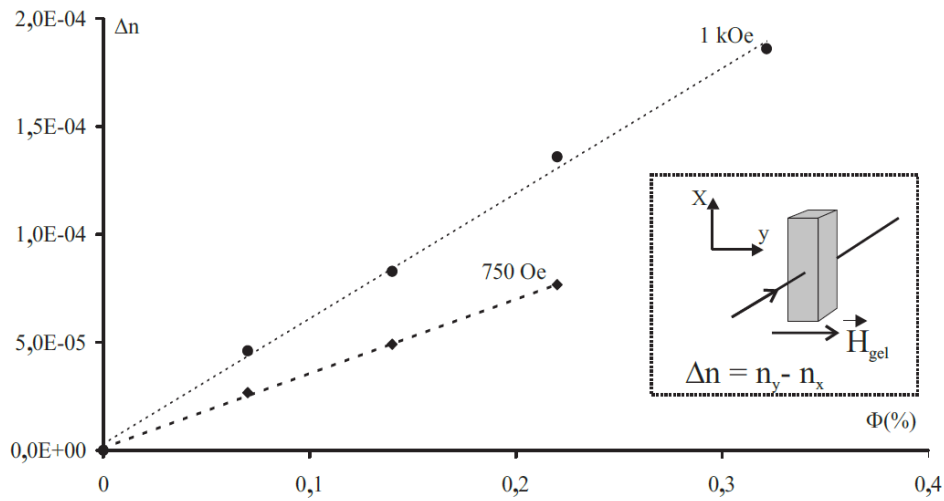


FIGURE II.7: Measurements of the created in-plane optical anisotropy ($\Delta n = n_y - n_x$) for MO composite, as a function of the NPs concentration and for two different gelation magnetic field magnitudes. Inset: schematic illustration of the sample under study with the gelation magnetic field orientation (\vec{H}_{gel}). The MO composite is consisting of NPs of Maghemite embedded in a silica matrix.

The figures are adapted from [Jam+01]

Similar work was done by Royer et al. [Roy+04] in order to decrease the fundamental mode birefringence $\Delta N_0 = N_{effTE} - N_{effTM}$ in a MO waveguide for higher MO effects. For this reason, MO films were deposited under magnetic field with different orientations with respect to the waveguide plane (in-plane or out of-plane, see Fig.II.8a). The measurement results of ΔN_0 for the different orientations and for two different NPs concentrations (1/30 and 4/30) are illustrated on Fig.II.8b. One can see, that ΔN_0 is increased in the case of a

in-plane field (\vec{B}_{in}) while it is decreased in the case of out of-plane field (\vec{B}_{out}) as compared to the case of zero applied magnetic field. This behavior is related to the orientation of the gelation magnetic field with respect to the direction of the electromagnetic field components of TE and TM modes in the waveguide, which will be explained in detail in Chap.III. As seen in Fig.II.8b, the shift of ΔN_0 between the cases of perpendicular and zero field for $\phi = 4/30$ and $\phi = 1/30$ are: 8.10^{-4} and 2.10^{-4} respectively, which are in the concentration ratios.

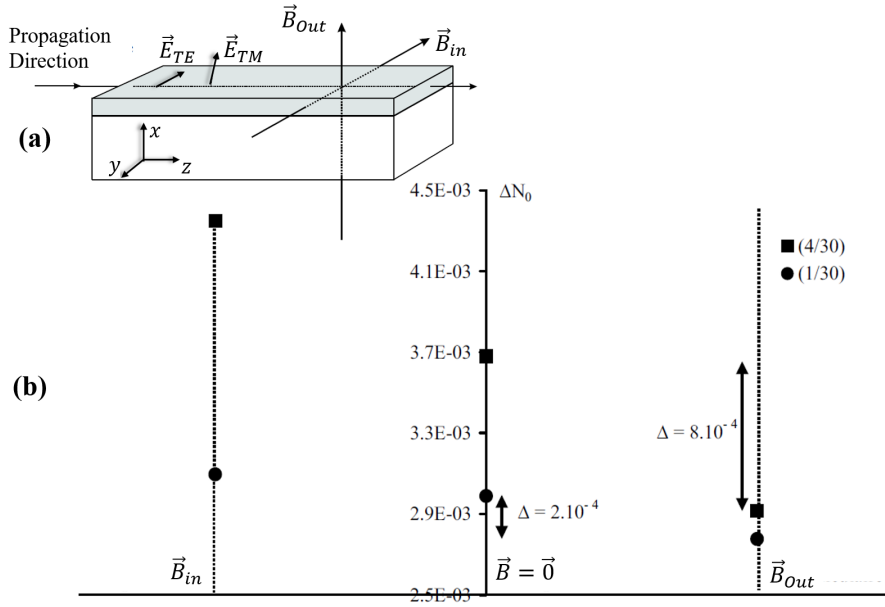


FIGURE II.8: (a) Schematic illustration of the sample under study with the gelation magnetic field orientations. (b) Fundamental modal birefringence measurements ΔN_0 at $\lambda = 633$ nm for two NPs concentrations (1/30 and 4/30), as a function of the gelation field direction. The MO films are formed by Maghemite NPs embedded in SiO_2/TiO_2 matrix. The figures are taken from [Roy+04].

In this section, the linear anisotropy under the influence of a magnetic field was described in case of a magnetic liquid and blocked NPs. In the next section, we will focus on the circular anisotropy especially the Faraday effect.

II.1.5.4 Faraday Effect

The Faraday effect, or circular anisotropy, is linked to the orientation of the magnetic moments $\vec{\mu}$ following the direction of an external magnetic field (considered to be z direction). The physical mechanism is identical to that of the magnetization and thus the whole permittivity tensor has off-diagonal elements as follows:

$$\begin{pmatrix} \epsilon_{xx} & j\epsilon_{xy} & 0 \\ -j\epsilon_{xy} & \epsilon_{xx} & 0 \\ 0 & 0 & \epsilon_{zz} \end{pmatrix} \quad (II.14)$$

where, $\epsilon_{xy} = \phi \times \epsilon_{MO} \times M_z$, with M_z the normalized magnetization in z direction.

Thus, the FR is proportional to the magnetization and the FR loops for a magnetic liquid and blocked NPs are similar to that of the magnetization illustrated on Fig.II.4 and Fig.II.5, respectively. Hence, for a solid matrix there is a remanent FR and consequently a hysteresis loop (see Fig.II.9), which is not the case for a magnetic liquid.

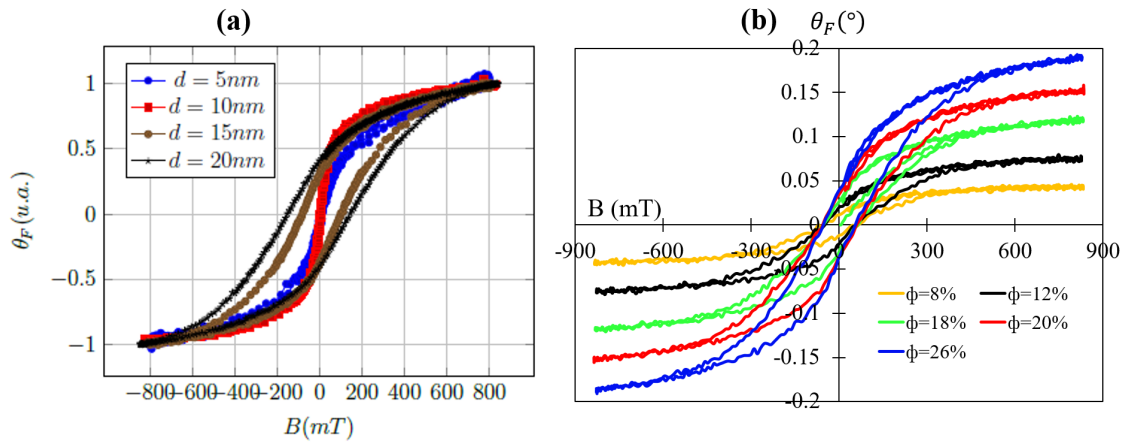


FIGURE II.9: (a) Normalized FR loops for different average diameter of cobalt ferrite NPs embedded in a silica matrix. Figure is taken from [Nan16; Gar17]. (b) FR loops for different NPs concentrations at $\lambda = 820\text{ nm}$.

L. Nandiguim [Nan16], demonstrated that the width of the hysteresis loop of CoFe_2O_4 NPs embedded in a sol-gel matrix can be controlled by the NPs diameters. Fig.II.9a illustrates the normalized FR loops for different NPs sizes. As seen in this figure, by increasing the size of the NPs, their magnetic behavior is modified, going from superparamagnetic to ferromagnetic. In addition to that, as for the magnetization, the saturated FR of blocked NPs depends on the volume fraction of these latter (see Fig.II.9b).

Spectral Behavior:

Fig.II.10 represents the specific FR ($^\circ/\text{cm}/\%$) at saturation as a function of the wavelength. As seen in this figure, three maxima were obtained at the wavelengths: 630 nm, 750 nm and 1490 nm respectively. These peaks are linked to the dispersion of ϵ_{MO} of CoFe_2O_4 NPs, described in Chap.I and illustrated on inset Fig.II.10. According to a quantum point of view, the Faraday effect takes place at wavelengths close to electron transitions (Zeeman effect [ZK97]). Therefore, the specific Faraday spectrum peaks (in other words the peaks of $\text{Re}(\epsilon_{xy})$ spectrum) can be explained as follows [Nan16]:

- Dip at $\lambda = 1490\text{ nm}$ is linked to electron diamagnetic transition of Co^{2+} in tetrahedral site.
- Dip at $\lambda = 750\text{ nm}$ is related to electron paramagnetic transition of Co^{2+} in tetrahedral site.
- Peak at $\lambda = 630\text{ nm}$ is related to electron paramagnetic transition of Co^{2+} and Fe^{3+} in octahedral sites.

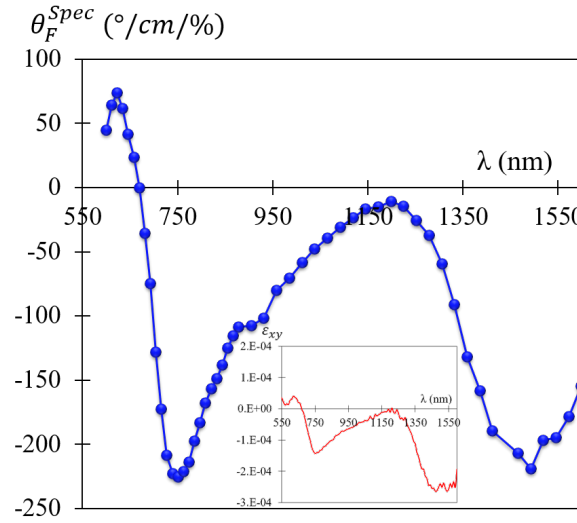


FIGURE II.10: Specific FR as a function of the wavelength. Inset: real part of the off-diagonal term of the permittivity tensor, at saturation. The used ferrofluid consists of cobalt ferrite NPs dispersed in water with a volume fraction of 1%.

The diamagnetic or paramagnetic transitions are described respectively by electrons transition to or from the degenerated levels (created under magnetic field as explained in section I.1).

The spectral behavior is the same for magnetic liquid and blocked NPs in terms of peaks, however a slightly difference in the specific FR amplitude can be found due to the refractive index difference between a ferrofluid ($n \simeq 1.33$ at $\lambda = 1550$ nm) and a MO film formed by NPs embedded in a matrix (in silica matrix: $n > 1.43$ at $\lambda = 1550$ nm).

As a summary, when a magnetic field is applied to a system of NPs, two main phenomena can exist: linear and circular anisotropies. Hence, the global permittivity tensor of the composite at saturation can be generally defined as follows (case of magnetic field in z direction):

$$\begin{pmatrix} \epsilon_{xx} & j\epsilon_{xy} & 0 \\ -j\epsilon_{xy} & \epsilon_{xx} & 0 \\ 0 & 0 & \epsilon_{zz} \end{pmatrix} \quad (\text{II.15})$$

The diagonal elements define the complex refractive index of the composite: $\epsilon_{xx} = (n_x - i\kappa_x)^2$ and $\epsilon_{zz} = (n_z - i\kappa_z)^2$. However, the off-diagonal elements define the FR and FE:

$$\theta_F^{spec} = \frac{\pi}{\lambda_0} \text{Re}\left(\frac{\epsilon_{xy}}{\sqrt{\epsilon_{xx}}}\right) = \frac{\pi\phi}{\lambda_0} \text{Re}\left(\frac{\epsilon_{MO}M_z}{\sqrt{\epsilon_{xx}}}\right) \quad (\text{II.16})$$

$$\zeta_F^{spec} = \frac{\pi}{\lambda_0} \text{Im}\left(\frac{\epsilon_{xy}}{\sqrt{\epsilon_{xx}}}\right) = \frac{\pi\phi}{\lambda_0} \text{Im}\left(\frac{\epsilon_{MO}M_z}{\sqrt{\epsilon_{xx}}}\right) \quad (\text{II.17})$$

In case of a magnetic liquid, the two anisotropies are observed. However, for blocked NPs the linear anisotropy is zero unless if the NPs optical axes are pre-oriented in the solid matrix, what will be performed in this work employing a magnetic field before the gelation of the matrix.

In the next section, the transmittance of the NPs will be presented.

II.1.6 Transmittance

The transmittance (T) measurements were done with Cary 5000 UV-Vis-NIR spectrophotometer (Agilent) at normal incidence, where the transmitted light of a 1 mm-thick cell filled with ferrofluid (cobalt ferrite NPs dispersed in water) were measured for different NPs concentrations (0.05%, 0.14% and 1%). In order to have only the effect of the NPs, the transmittance curve has been referred to a cell filled with water and the results are plotted on Fig.II.11. As seen in this figure, the transmittance decreases with the increment of the NPs concentration. This behavior is linked to the fact that by increasing the concentration of NPs, the absorption (α) of these NPs assembly increases, decreasing the transmittance:

$$T = \exp(-\alpha x) \quad (\text{II.18})$$

where x is the propagation length.

Indeed, the expression of α can be written as follows:

$$\alpha = \frac{4\pi\kappa}{\lambda} \quad (\text{II.19})$$

κ is the extinction coefficient. If the matrix is a transparent medium, Eq.II.19 transforms to :

$$\alpha = \frac{4\pi\phi\kappa^{NP}}{\lambda} \quad (\text{II.20})$$

It is obvious from Eq.II.20, that the absorption is proportional to the NPs concentration.

One can see also on Fig.II.11 that, when the concentration is low (0.05%), the transparency window of the NPs starts beyond $\lambda=700$ nm. Hence, around $\lambda = 1550$ nm the NPs are more or less transparent, which is can be beneficial for practical applications, especially that the FR is maximum in this region.

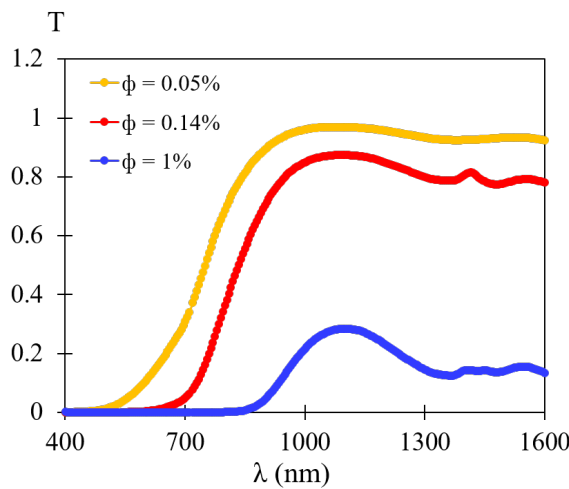


FIGURE II.11: Measurements of transmittance spectra of cobalt ferrite nanoparticles, for different concentrations.

In this section, an introduction of cobalt ferrite NPs was presented, where their geometrical, magnetic, optical and MO properties were described. The next section will be dedicated to describe the elaboration of MO thin films formed by ferrite cobalt NPs embedded in a silica matrix.

II.2 Elaboration of Magneto-Optical Thin Films

The different steps of elaboration of MO thin films are illustrated on Fig.II.12, whose are divided into two main stages: preparation of the MO composite by sol-gel process and MO film coating. The next section will be dedicated to present the basic principles of the sol-gel technique followed by the MO-sol preparation.

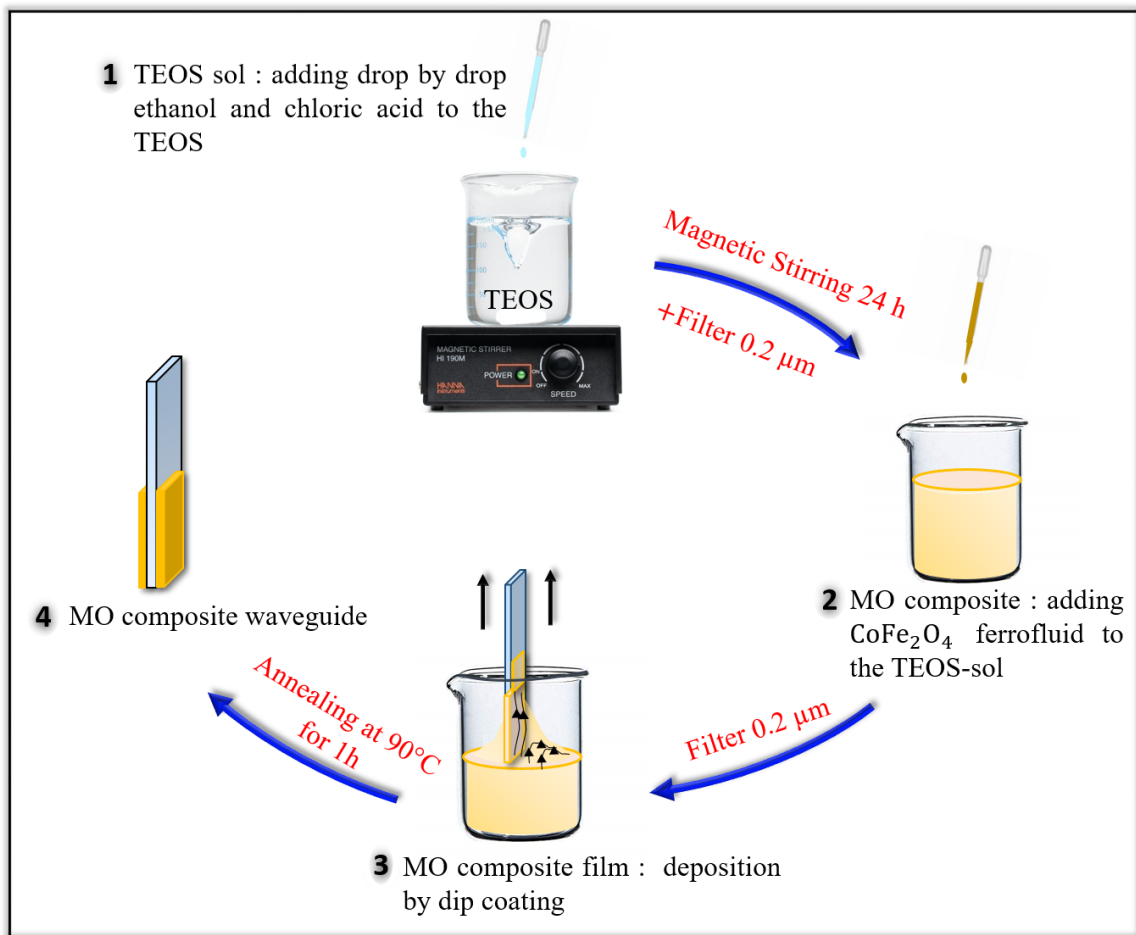


FIGURE II.12: Illustration of the steps of elaboration of the magneto-optical thin films.

II.2.1 Sol-Gel Technique

II.2.1.1 Basic Principles

The sol-gel process [Pet08; BS13] is a method for preparing a wide variety of composites mostly metal oxides (SiO_2 , TiO_2 , ZrO_2 , etc.) by hydrolyzing chemical precursors that pass from a solution to a gel state before being dehydrated to glass or ceramic. Sol-gel technology can be used to prepare monoliths, fibers, porous or dense materials, powders and thin films with better homogeneity and purity than high temperature conventional processes [Sch03].

The precursors are generally metal alkoxides of formula $M(\text{OR})_n$: M being the metal: silicon, zirconium, titanium, etc. And R denotes a $\text{C}_n\text{H}_{2n+1}$ alkyl group. In the presented work, the Tetraethyl orthosilicate (TEOS) is considered as a precursor with the formula $\text{Si}(\text{OC}_2\text{H}_5)_4$.

The synthesis process is divided into two main stages which are hydrolysis (action of water) and condensation (formation of a covalent network) of organo-metallic compounds or salts.

- Hydrolysis (Fig. II.13): it is favored under acid catalysis conditions. This is the activation reaction in which a molecule of water reacts with the alkoxide to form a hydrolyzed precursor molecule and an alcohol molecule:

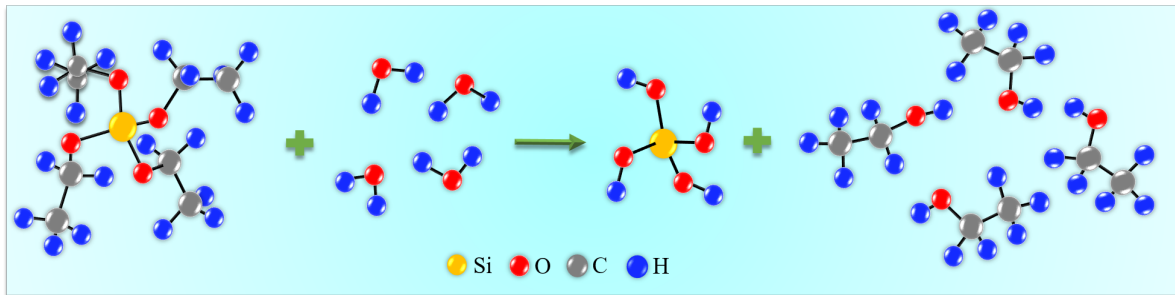
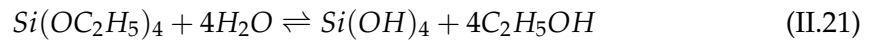
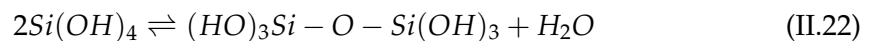


FIGURE II.13: Schematic illustration of the hydrolysis phenomenon for TEOS precursor [Pet08; BS13].

- Condensation (Fig. II.14): it is favored under basic catalysis conditions. It should be preceded by at least partial hydrolysis of the precursors. Therefore, a siloxane (Si-O-Si) bridge is formed from the condensation of two partially hydrolyzed alkoxides groups, leaving a molecule of water:



The condensation can occur also between two metal alkoxides of which only one has been partially hydrolysed.

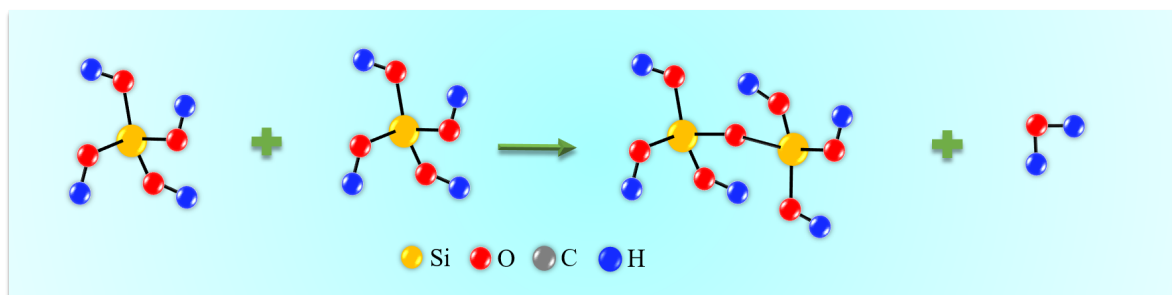


FIGURE II.14: Schematic illustration of the condensation phenomenon for partially hydrolyzed TEOS precursor [Pet08; BS13].

The resulting siloxane bridge continues to react with each other and form a polymeric clusters (see Fig. II.15a). These latter gradually occupy an increasing volume fraction. When one of these clusters reaches an infinite size (ie practically the size of the beaker, see Fig. II.15b), the viscosity of the medium then becomes important: this is the sol-gel transition. From this moment, the infinite cluster called gel fraction continues to grow by incorporating the smaller polymeric groups. When all the reactions have been used the gel is formed and it consists only by Si-O-Si network (see Fig. II.15c). This final step should be accompanied with a thermal treatment in order to evaporate the produced molecules of water.

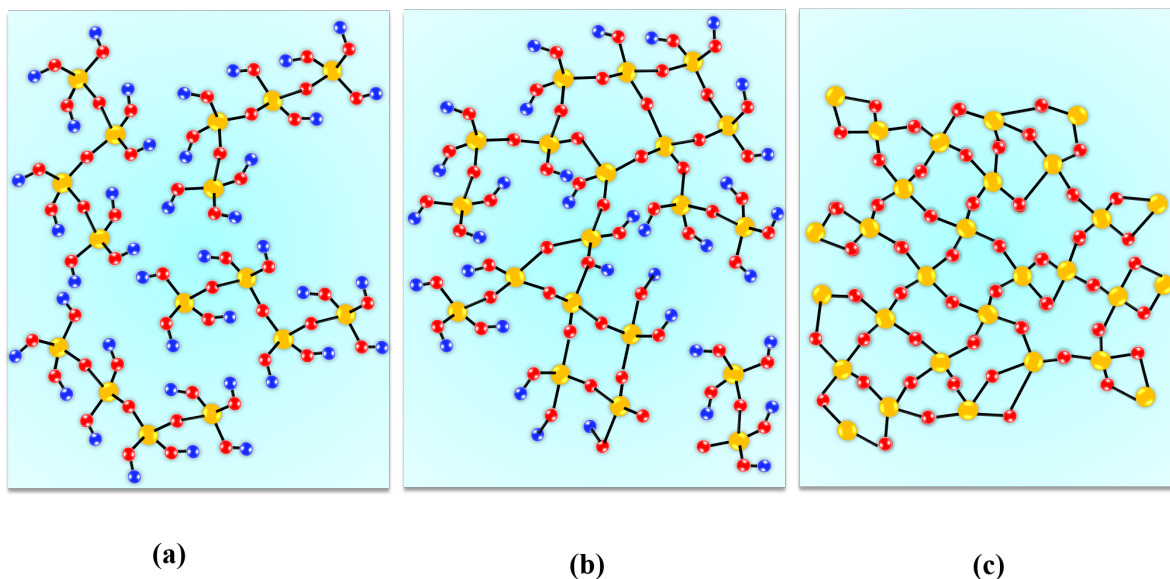


FIGURE II.15: (a) Polymeric clusters, (b) cluster with infinite size: sol-gel transition, (c) network Si-O-Si: formation of the gel [Pet08; BS13].

The competition between hydrolysis and condensation defines the geometry of the structures. This competition is controllable by the pH of the solutions, which modifies in particular the speed of the reactions. In acidic medium, the hydrolysis is faster than the condensation, which causes a quick formation of particles with diameter smaller than 1 nm. As a result, a branched polymer is formed. However, in basic medium, the condensation is faster than hydrolysis hence, the polymer is gradually fed with monomers. Therefore, dense particles larger than 100 nm are formed and the resulting structure is called colloidal.

II.2.1.2 Preparation of MO-Sol

- First of all, a sol of TEOS is prepared by adding drop by drop ethanol and then chloric acid under magnetic stirring to the TEOS (see Fig. II.12). After keeping the resulting sol under magnetic stirring for 24 hours, the sol is filtered with a $0.2 \mu\text{m}$ filter to remove the unwanted dust particles.

The pH of the prepared TEOS solution is around $\text{pH} = 2$ and this is linked to the chloric acid. Hence, the resulting sol is in an acidic medium and it is consisting therefore, of small particles rather than dense ones, which allows the doping with NPs.

- After that, acidic ferrofluid containing NPs of cobalt ferrite is added drop by drop to the TEOS sol (see Fig. II.12). Each drop set is followed by one minute of mechanical stirring to ensure its good dispersion. In order to obtain a good stability of the NPs in the sol, distilled water is added to this latter before doping. One should mention that the prepared ferrofluids are very compatible with the TEOS-sol: there are no precipitates of NPs. The resulting doped solution is filtered again by a filter of $0.2 \mu\text{m}$ to avoid aggregated NPs in the resulting MO-sol.

The MO-sol is then deposited on a substrate, followed by a thermal treatment at 90°C for one hour in order to eliminate the persistent solvents and ensure the densification of the MO composite. Here, the condensation reactions are not totally finished and no gel with only Si-O-Si network is formed since the thermal treatment is not very high.

To control well the optical and MO properties of the MO composite, different MO-sol were prepared with different volume fraction of ferrofluid. Tab. II.1 summarizes the different prepared MO composite with the corresponding quantities. As seen in this table, five MO-sol were prepared in which the quantity of the TEOS sol is fixed to 10 mL while that of the mixture ferrofluid and water is fixed to 5 mL, resulting in a total volume of 15 mL of the MO-sol. We should know that the viscosity of the different MO sol-gel is not the same and it seems to increase with the volume fraction of NPs.

TABLE II.1: The fabricated MO-sol with the corresponding materials quantities.

MO Sol-Gel	TEOS	Ferrofluid	Distilled Water
MO-SOL 1	10 mL	2.5mL	2.5mL
MO-SOL 2	10 mL	2mL	3mL
MO-SOL 3	10 mL	1.5mL	3.5mL
MO-SOL 4	10 mL	1mL	4mL
MO-SOL 5	10 mL	0.5mL	4.5mL

The different MO-sol mentioned in Tab. II.1 were deposited on different types of substrate, hence MO films with different concentrations of NPs were obtained. These concentrations cannot be deduced directly from the sol constituents, because of the chemical reactions in the sol and the evaporation of the solvent. Therefore, the adapted estimation method is based on specific FR measurements and it will be presented later in this chapter.

II.2.2 Choice and Preparation of Substrates

Depending on the applications, two types of substrates were used in this work:

- Glass, pyrex and BK7 substrates: owing a maximum refractive index around 1.51 at $\lambda = 1550$ nm, which is suitable for the guiding condition of the light inside the MO film. In addition, these substrates have a good transmission in Visible-IR wavelength range allowing the MO measurements.
- Silicon substrate: owning a high refractive index, which is convenient for ellipsometry measurements (for thickness and refractive indices characterizations), since these latter require a high refractive index contrast for high measurements precision. Before film deposition, these substrates were treated thermally at 1000°C for 1 hour to create a layer of silica on top, insuring a good adhesion of the MO film.

Cleaning the substrates is an essential step in the fabrication of the MO thin film. The surface of the substrate must be very clean to avoid inhomogeneity in the film thickness, originating from the dusts particles or any default on the substrate surface. For this reason, the substrates were first washed with a detergent, then rinsed with demineralised water and dried with nitrogen. After that, they were cleaned with ethanol and finally dried with lens paper.

In the next section, the deposition of the MO films will be detailed starting from the description of the coating method (basic principles of dip-coating and the used dip-coater in this work), to the different fabricated MO films coated with or without applied magnetic field.

II.2.3 Dip-Coating Process

II.2.3.1 Basic Principals

Dip-coating [Scr88] is a simple method to produce large scale uniform thin films. Basically, the process can be divided into four essential technical steps (illustrated on Fig.II.16a) [Scr88]:

- Immersion: the substrate is immersed in the coating solution with a constant velocity.
- Dwelling: the substrate is remained in the solution for a giving time.
- Withdrawal: the substrate is pulled up with a constant withdrawal velocity v_0 and a wet film of the solution is remained on the surface of the substrate.
- Drying: the evaporation of the solvent in the film occurs during and after coating. Over time, most of the solvent will be removed and a dry (gel-like) film is formed on the surface of the substrate.

All the steps mentioned above are important but the last two (withdrawal and drying) are critical for determining the property of the deposited thin film. The withdrawal stage can be described as the interaction of the draining and entraining forces. The entraining forces work to maintain the liquid on the substrate, however the draining forces work to pull back the fluid into the bath. The balance between these forces (stagnation point S on Fig.II.16b) defines the thickness of the wet film remained on the surface of the substrate.

Different coating regimes are defined depending on which forces are dominated, but the thickness of the wet film evolves with the withdrawal speed and the solution viscosity in most of this regimes [SSW74; MMH04; Bri+92].

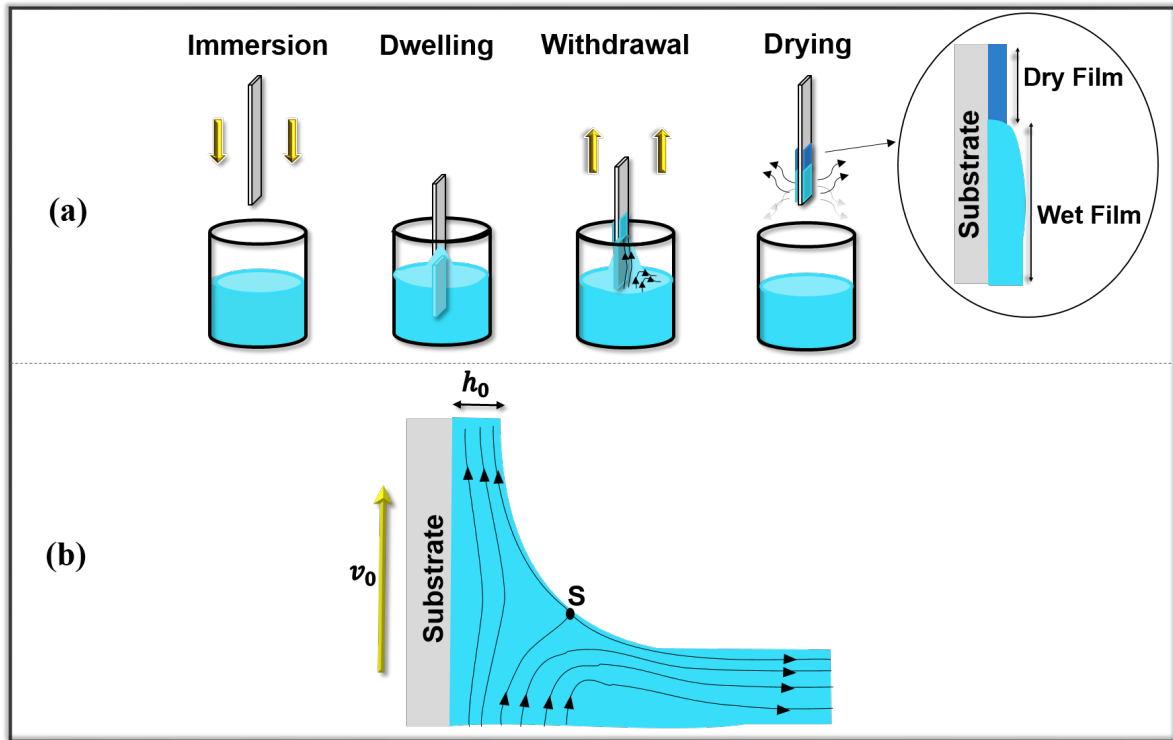


FIGURE II.16: (a) Schematic illustration of the different steps of the dip-coating process [Scr88]. (b) Illustration of the withdrawal stage [SSW74]. The balance between the entraining and draining forces at the stagnation point S, defines the thickness of the wet film remained on the surface of the substrate.

II.2.3.2 Magneto-Optical Films Deposition

In this work, the coating of MO films was done by a dip-coater illustrated on Fig. II.17a. The substrate was fixed tightly on a holder and instead of moving it, a Teflon beaker filled with the MO-sol, is allowed to move vertically. The beaker is standing on a holder connected to an electric motor and its movement speed (in other word the withdrawal speed) can be controlled by changing the position of the potentiometer. The withdrawal speeds can be modified from 2.3 cm/min to 8.2 cm/min.

The different MO-sol described in Tab. II.1 were deposited on different types of substrates (Pyrex, glass and silicon) with three different withdrawal velocities. The obtained MO films are very homogeneous with low optical diffusion and high uniformity of thickness.

Fig. II.17b illustrates the measurements of the MO film thickness (t_{MO}) of MO-SOL 1 as a function of the withdrawal speeds. The measurements were done by an ellipsometer (HORIBA Jobin Yvon UVISEL). This figure shows that the thickness of the dry films increases with the withdrawal velocity. This behavior is explained by the fact that the thickness of the wet film evolves with the withdrawal speed, as explained in the previous section.

II.2.3.3 Nano-Structuring: Deposition Under Magnetic Field

In order to control the effective indices of TE and TM modes, different MO films (MO-SOL1 in Tab. II.1) were deposited under magnetic field (denoted \vec{B}_{gel}) with different magnitudes and different orientations with respect to the substrate plane (in-plane and out of-plane). The

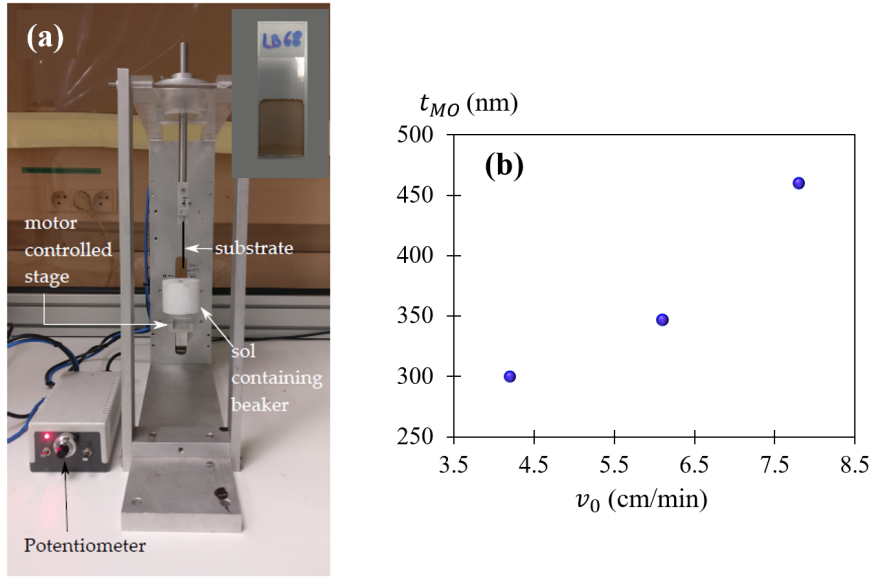


FIGURE II.17: (a) Snapshot of the dip-coater used to deposit thin films of MO composite. The figure is adapted from [Var17]. Inset: MO thin film coated on a glass substrate. (b) Measurements of MO films thicknesses for different withdrawal speeds.

application of a magnetic field, during the MO films coating, tends to align the moments ($\vec{\mu}$) of the magnetic NPs following its direction and thus the NPs too. Once the film is dried, the magnetic field is cutted-off and the NPs are frozen, creating permanent anisotropies (linear optical and magnetic) in the MO film.

For this purpose, the dip-coater is coupled with an electromagnet (see Fig.II.18): the beaker containing the MO-sol is placed in the center of the air gap of the electromagnet and the deposited layer should remain entirely under the influence of the magnetic field. The amplitude of this latter can reach a maximum value of 300 mT. In order to have the two gelation field configurations (in-plane and out-of-plane), the sample holder can be rotated.

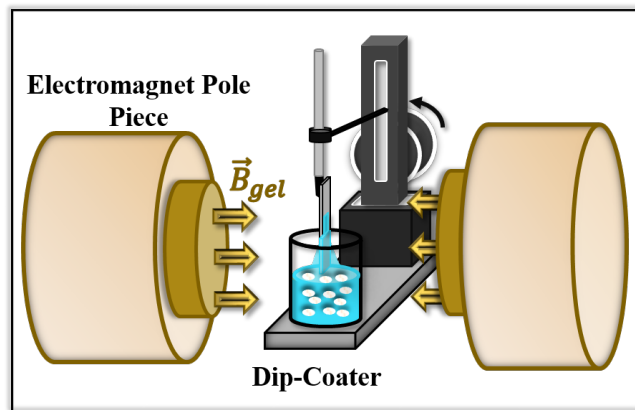


FIGURE II.18: Schematic illustration of the MO composite coating under a magnetic field.

The magnetic field is applied during the film coating on a glass substrate and once the substrate is totally out of the solution, the field is cutted-off.

As a summary, different MO films were fabricated with different NPs concentrations in order to study extensively the MO composite and to be able after that to control well this latter. In addition to that, MO films were coated under magnetic field in order to create a permanent optical anisotropy which can be helpful to decrease the modal birefringence for higher MO effects. Hence, the optical and MO characterizations of the different MO films will be presented in the next section.

II.3 Characterization of Magneto-Optical Thin Films

This section is dedicated to define the whole permittivity tensor of the MO composite (Eq. II.15). Hence, the dielectric function (ϵ_{xx}), the thicknesses and the transmission will be presented as a function of the ferrofluid volume fractions. These opto-geometrical properties were measured by ellipsometry. In addition to that, the Faraday effect (θ_F and ζ_F , Eq. II.16 and Eq. II.17) will be studied. The MO properties were measured by a homemade MO setup. Therefore, the NPs concentration (ϕ) and refractive index (ϵ^{NP}) will be deduced.

Finally, the optical permanent anisotropy ($\epsilon_{xx}-\epsilon_{zz}$) will be studied in MO films deposited under gelation magnetic field and the intrinsic anisotropy ($\epsilon_{xx}^{NP}-\epsilon_{zz}^{NP}$) of the NP will be estimated.

II.3.1 Opto-Geometrical Properties

II.3.1.1 Ellipsometry: Basic Principles

An ellipsometer is employed to obtain the opto-geometric properties of materials (such as film thickness d , refractive index n , extinction coefficient κ , etc.) for a large wavelength range of [280-2100 nm], by measuring the change of polarization state of the incident light after reflection on the sample surface. The inspected materials can be in solid phase (bulk or multi-layer thin films), liquid or even gaseous phase. They can be as well isotropic or anisotropic.

The ellipsometer used in this work is a UVISEL from HORIBA Jobin Yvon (Fig. II.19). It consists of three blocks: the first one named polarization state generator is formed by light source followed by a linear polarizer. The second block is the structure holder with vertical axis to optimize the position of the incident spot on the inspected sample. This holder can be changed for ellipsometry measurements in transmission. The third one named polarization state analyzer is formed by a photoelastic modulator followed by an analyzer and a photodetector.

Measurement Principles of Ellipsometry Let's consider a 45° -linearly polarized light, incident onto the surface of an isotropic material (see Fig. II.19b). The polarization state of the reflected light transforms into an elliptical polarization where the large axis have two components following p- and s-polarization with a certain phase shift. The parameter ρ is defined as the ratio of the Fresnel complex reflection coefficients for p- and s-polarized light and it is expressed as follows:

$$\rho = \frac{r_p}{r_s} = \tan(\psi)e^{i\Delta} \quad (\text{II.23})$$

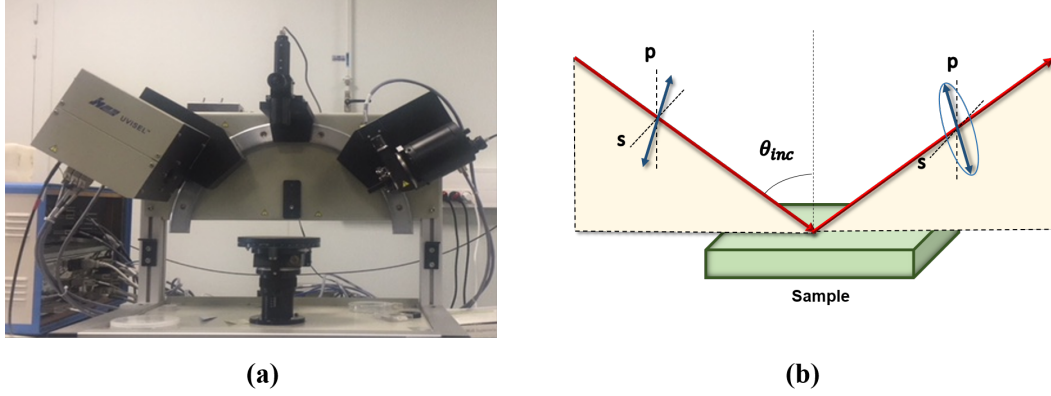


FIGURE II.19: (a) Snapshot, (b) schematic illustration of the ellipsometer UVISSEL from HORIBA Jobin Yvon.

Where, $\tan \psi$ is the ratio of the amplitude of the reflection coefficients and Δ is the phase shift between p and s-polarized reflected light. $\tan \psi$ and Δ are called ellipsometry parameters and they are measured for a large wavelength range [280-2100 nm].

To obtain the opto-geometrical parameters (n , κ , d , etc.) by ellipsometry, a model should be built for the inspected structure. After that, the theoretical values of ψ and Δ are compared with the measured values. The parameters can be then extracted once the best fitting is reached.

The precision of the obtained optical parameters by ellipsometry depends on two factors:

- The measurement accuracy of ψ and Δ , which can be high by working with surfaces with high reflectivity.
- The right model, which is related to our primitive knowledge about the inspected structure.

Effective Medium Approximation The effective medium approximation is a method to describe a composite or a mixed material medium. There are various effective medium methods in the ellipsometry but the most used are two:

- The Maxwell-Garnett EMA: assuming small spherical inclusions of material B well separated from each others within a host material A. It is mathematically described as:

$$\frac{\epsilon - \epsilon_A}{\epsilon + 2\epsilon_A} = f_B \frac{\epsilon_B - \epsilon_A}{\epsilon_B + 2\epsilon_A} \quad (\text{II.24})$$

Where, ϵ , ϵ_A , and ϵ_B are the dielectric functions of the whole system, of the host material A and the spherical inclusions B, respectively. f_B is the volume fraction of B.

Volume fractions of less than 30% and diameter of less than one fifth of the wavelength can be described by this Maxwell Garnett EMA. In other way, it applies to a system with non-interacting spherical NPs.

- The Bruggeman EMA: does not assume a host material, but rather equally weights the constituent materials according to their volume fractions and dielectric functions. It is described by:

$$f_A \frac{\epsilon_A - \epsilon}{\epsilon_A + 2\epsilon} + f_B \frac{\epsilon_B - \epsilon}{\epsilon_B + 2\epsilon} = 0 \quad (\text{II.25})$$

Ellipsometer in Transmission This can be beneficial to measure the planar anisotropy of a material. In this case, the phase shift Δ and the ratio of the amplitude transmission coefficients $\tan(\psi)$ can be measured in transmission by ellipsometry for large wavelength range [280-2100 nm]. The birefringence for different wavelength can be then deduced by the relation given as follows:

$$\Delta n = \frac{\lambda}{2\pi d} \Delta \quad (\text{II.26})$$

This method was used to measure the in-plane anisotropy for the MO films deposited under magnetic field.

II.3.1.2 Dielectric Function

The dielectric function (ϵ_{xx}) of the MO films with different volume fractions of NPs (described in Tab.II.1) were measured by ellipsometry. To increase the accuracy of the ellipsometry measurements, these latter were done with MO films deposited on silicon substrates owing higher reflectivity than the glass. Here, the diagonal elements of the MO composite permittivity tensor are supposed to be equal ($\epsilon_{xx} = \epsilon_{yy} = \epsilon_{zz}$), since the studied MO films were deposited without gelation magnetic field. However, some differences could be obtained due to the stress, resulting for example from the thermal treatment of the films.

The real and imaginary parts of the dielectric function of the MO film resulting from MO-SOL1 (see Tab.II.1) are illustrated on Fig.II.20, as a function of the wavelength. As seen in this figure, $\text{Re}(\epsilon_{xx})$ and $\text{Im}(\epsilon_{xx})$ are higher in the UV-visible than in the near IR wavelength range, which is related to the NP dispersion. One can see that $\text{Im}(\epsilon_{xx})$ is very low in the near IR region, linked to the fact that the NPs are transparent here comparing to the visible range (see Fig.II.11). We should say that the ellipsometry precision decreases when $\text{Im}(\epsilon_{xx})$ is very small explaining the zero values for this latter, illustrated on Fig.II.20 for the near IR region.

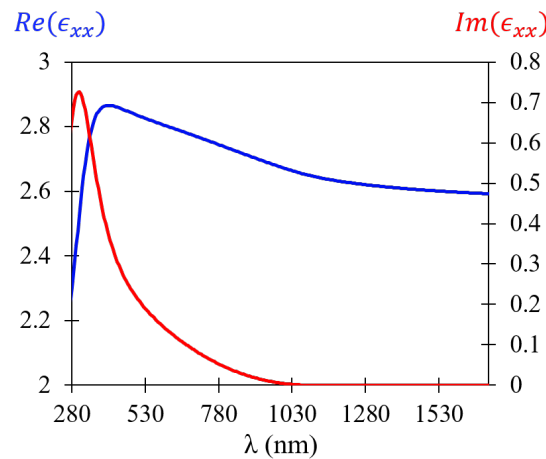


FIGURE II.20: Measurements of the refractive index of MO composite film coated from MO-SOL1 (Tab.II.1) as a function of the wavelength.

Fig. II.21a-b illustrates the refractive index (n_{MO}) and the dielectric function $\epsilon_{xx} = (n_{MO} - i\kappa_{MO})^2$ of the MO films as a function of the dopant volume fraction. This latter is defined as the rate of the volume of the ferrofluid (column 3 in Tab. II.1) and the total volume of the MO-sol (15 mL). Here, the values of $\text{Im}(\epsilon_{xx})$ were estimated by the transmittance measurements of the ferrofluid using Eq. II.18 and Eq. II.20.

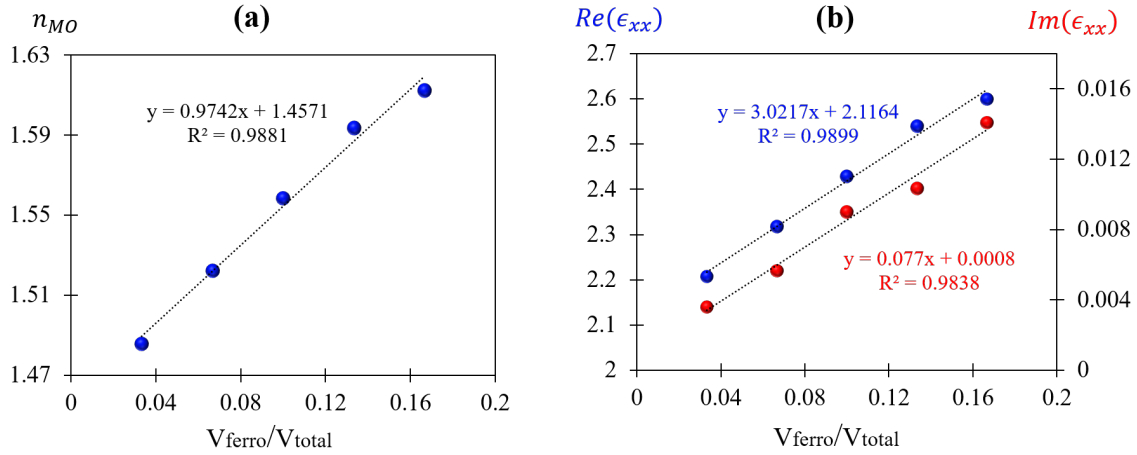


FIGURE II.21: Measurements of (a) refractive index and (b) dielectric function of MO films at $\lambda = 1550$ nm, as a function of the dopant volume fraction. This latter is defined as the ratio of the ferrofluid volume in the MO-sol and the total volume of this latter (15 mL).

As seen in Fig. II.21a-b, the refractive index or the dielectric function depends highly on the dopant volume fraction with a linear behavior. n_{MO} evolves from a value of 1.45 for $V_{\text{ferro}}/V_{\text{total}} = 0$ to a value of 1.61 for $V_{\text{ferro}}/V_{\text{total}} = 0.167$. Hence, a variation around 0.17 in dopant volume fraction undergoes a variation around 0.16 in the refractive index. Thus, one can deduce that the refractive index of the NPs is high.

The small deviations from the linear curve in Fig. II.21a-b, are linked first to the measurements precision of the ellipsometer which can be in order of 10^{-2} , second to the reliability of the chosen ellipsometry model.

II.3.1.3 Thickness

The thicknesses of the MO films with different dopant volume fractions are illustrated on Fig. II.22, for a withdrawal speed equal to 4.2 cm/min. One can see that by increasing the dopant volume fraction, the thickness of the MO layer is increased. This behavior is linked to the fact that by increasing the dopant volume fraction in the MO-sol, this latter becomes more viscous. Hence, as explained in section II.2.3.1, the thickness of the wet film evolves with the solution viscosity resulting in thicker dry film.

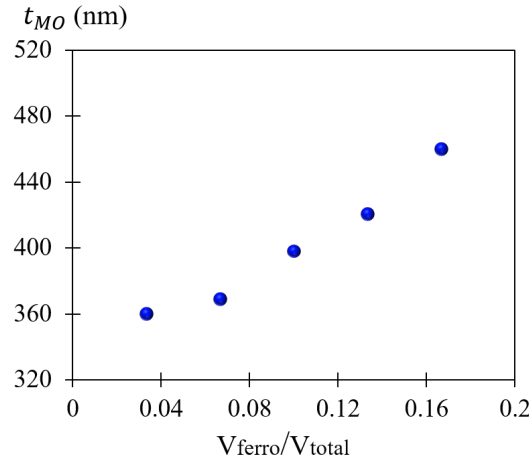


FIGURE II.22: Measurements of MO films thicknesses for a withdrawal speed equal to 4.2 cm/min, as a function of the ferrofluid fractions.

II.3.1.4 Transmittance

Fig. II.23 illustrates the transmittance measurements of the MO films as a function of the dopant volume fraction. The transmittance was measured by a photodetector at $\lambda = 820$ nm and it is defined as the ratio of the transmitted and initial intensities. As seen in this figure, the transmittance decreases with the dopant volume fraction in a linear way. This behavior is explained by the fact that $\text{Im}(\epsilon_{xx})$, in other words the absorption of the MO composite, increases with the dopant volume fraction (see Eq. II.20 and Fig. II.21b). Moreover, as demonstrated above, n_{MO} increases with the dopant volume fraction, thus the reflection too. For $V_{ferro}/V_{total} = 0$, the transmittance is around 92% which is related to the twice reflection on the air/(MO film; glass) interfaces (for each reflection, the transmittance loses around 4%).

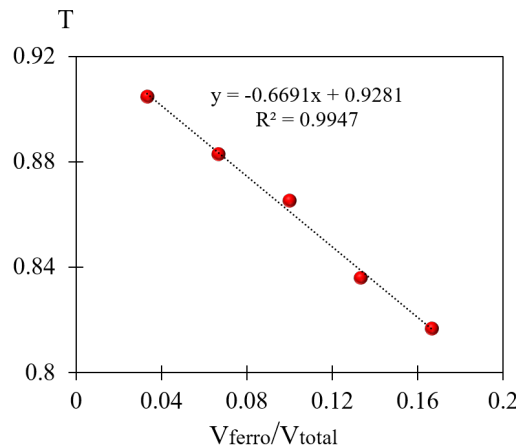


FIGURE II.23: Transmittance measurements at $\lambda = 820$ nm as a function of the dopant volume fractions for MO films deposited on glass substrates.

After describing the opto-geometrical properties of the different MO films, the next section will be dedicated to present the MO properties.

II.3.2 Magneto-Optical Properties

II.3.2.1 Description of the Traditional Magneto-Optical Setup

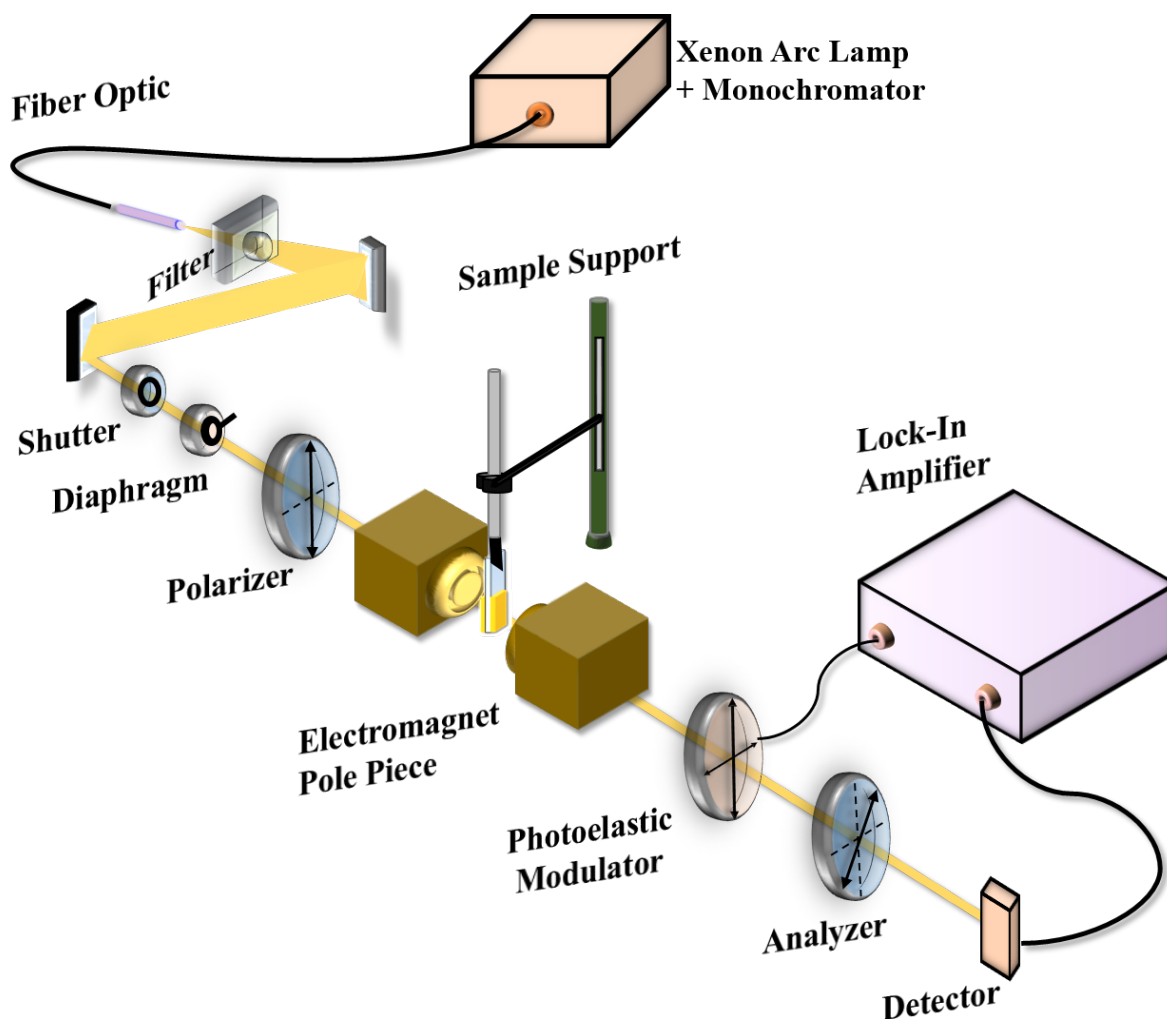


FIGURE II.24: Representation of the essential elements of the MO polarization rotation homemade setup.

The traditional Faraday setup is illustrated on Fig. II.24 and it consists mainly of: a 450 W Xenon Arc light source associated to a motorized TRIAX180 monochromator, a linear polarizer mounted on a rotating support with 0.001° of resolution, an electromagnet, a photoelastic modulator, an analyzer inclined at -45° referring to the proper axes of the modulator and a photodiode. The detected signal is analyzed by a Lock-In Amplifier (LIA).

The monochromator covers the spectral range [330 nm - 1700 nm]. It is used to select the desired wavelength of the light beam going out from the Xenon Arc source. The spectral resolution of the light can be adjustable by modifying the width of the input and output slits of the monochromator.

After the monochromator, the light is transported by an optical fiber and at the output of this latter, a high pass optical filter is placed in order to transmit only the first diffraction order of the monochromator's grating.

The light beam leaving the optical fiber is divergent, hence spherical mirrors are used to image the fiber output on the sample. The opening of the light beam can be controlled by a diaphragm placed before the polarizer.

Then, the polarized light passes through the magnetized sample and undergoes a rotation of polarization and an ellipticity. The sample is fixed on a support ensuring a wide sweep (longitudinal and vertical) on its surface and placed between two poles of an electromagnet generating a magnetic field of an amplitude varied in the range of $[-800 \text{ mT} ; +800 \text{ mT}]$. A Hall probe is inserted close to the sample, in the air gap of the electromagnet, in order to measure the magnetic field in real-time.

After passing through the MO system, the light crosses a photoelastic modulator which periodically modulates the state of polarization of the light. The photoelastic modulator consists of a slab of silica subjected to a constraint produced by a piezoelectric transducer oscillating at its mechanical resonant frequency: $F = 50 \text{ kHz}$. The constraint in the bar creates a periodical phase shift with an amplitude Δ_m (see Eq. II.27), between the linear polarization components following the modulator axes.

$$\Delta(t, \lambda) = \delta_0(\lambda) + \Delta_m(\lambda) \sin(2\pi Ft) \quad (\text{II.27})$$

δ_0 is the residual stress and Δ_m depends on the given voltage to the piezoelectric transducer and on the wavelength.

After crossing the analyzer, the two phase shifted components of the light polarization interfere resulting in a linear polarization with a direction parallel to the analyzer's axe.

The LIA, referenced to the frequency F of the photoelastic modulator, enables the acquisition of the DC and AC components of the signal at frequencies F and $2F$. The information is processed by the computer. A program allows to control the various elements constituting the MO setup and to display the measurement results.

Measurements Method of Polarization Rotation and Ellipticity

The light intensity reaching the photodetector can be mathematically determined by a product of individual Jones matrix for every optical element and for the initially linearly polarized light.

After the polarizer, the light initially unpolarized, is linearly polarized in the direction of the polarizer axis. This latter is oriented along one of the two axes of the photoelastic modulator. After passing through the MO system, the linearly polarized light undergoes FR θ_F and FE ζ_F and its Jones matrix relative to the axes of the modulator is expressed as below:

$$\begin{pmatrix} \cos \theta_F & \sin \theta_F \\ -\sin \theta_F & \cos \theta_F \end{pmatrix} \begin{pmatrix} \cos \zeta_F \\ i \sin \zeta_F \end{pmatrix} \quad (\text{II.28})$$

The Jones matrix of the modulator relative to the axes of the analyzer is as follows:

$$\begin{pmatrix} \cos \beta & -\sin \beta \\ \sin \beta & \cos \beta \end{pmatrix} \begin{pmatrix} e^{i\Delta(t, \lambda)} & 0 \\ 0 & 1 \end{pmatrix} \quad (\text{II.29})$$

Where the analyzer is oriented with an angle $\beta = -45^\circ$ with respect to the modulator axes and its Jones matrix is:

$$\begin{pmatrix} 1 & 0 \\ 0 & 0 \end{pmatrix} \quad (\text{II.30})$$

Hence, the light at the exit of the analyzer can be expressed as follows:

$$\begin{pmatrix} 1 & 0 \\ 0 & 0 \end{pmatrix} \begin{pmatrix} \cos \beta & -\sin \beta \\ \sin \beta & \cos \beta \end{pmatrix} \begin{pmatrix} e^{i\Delta(t,\lambda)} & 0 \\ 0 & 1 \end{pmatrix} \begin{pmatrix} \cos \theta_F & \sin \theta_F \\ -\sin \theta_F & \cos \theta_F \end{pmatrix} \begin{pmatrix} \cos \xi_F \\ i \sin \xi_F \end{pmatrix} \quad (\text{II.31})$$

By calculating this product of matrices, the intensity of the transmitted light can be expressed as below:

$$I(t, \lambda) = [1 + I_s \sin(\Delta(t, \lambda)) + I_c \cos(\Delta(t, \lambda))] \frac{I_0(\lambda)}{2} \quad (\text{II.32})$$

where $I_s = \sin(2\xi_F)$, $I_c = -\sin(2\theta_F) \cos(2\xi_F)$ and $\Delta(t, \lambda) = \delta_0(\lambda) + \Delta_m(\lambda) \sin(2\pi Ft)$.

The standard expansions in terms of Bessel functions (J) give the expression of the continuous and the first 2 harmonics terms contained in $I(t, \lambda)$:

$$I(t, \lambda) = I_{0F} + I_{1F} \sin(2\pi Ft) - I_{2F} \sin(4\pi Ft) \quad (\text{II.33})$$

$$I_{0F} = \frac{I_0}{2} + \frac{I_0}{2} J_0(\Delta_m) [I_s \sin(\delta_0) + I_c \cos(\delta_0)] \quad (\text{II.34})$$

$$I_{1F} = I_0 J_1(\Delta_m) [I_s \cos(\delta_0) - I_c \sin(\delta_0)] \quad (\text{II.35})$$

$$I_{2F} = I_0 J_2(\Delta_m) [I_s \sin(\delta_0) + I_c \cos(\delta_0)] \quad (\text{II.36})$$

I_{0F} , I_{1F} and I_{2F} are measured by the LIA. Δ_m and δ_0 are calculated by an automatic calibration described in the work of Abou Diwan [AD+16]. Hence, the FR (θ_F) and the FE (ξ_F) can be calculated using the Eq. II.35 and Eq. II.36, with a precision of the order of one thousandth degree.

An example of Faraday measurements at a fixed wavelength ($\lambda = 820$ nm) for a cell filled with ferrofluid of cobalt ferrite and for a thin layer of MO composite deposited on a glass substrate are illustrated in Fig. II.25a-b, respectively. As seen in this figure, for a fixed wavelength the magnetic field is varied from -800 mT to 800 mT and the polarization rotation is measured.

As explained before, the rotation spectrum of the ferrofluid has no remanent rotation since the NPs and their momentum return to a random orientation once the magnetic field is cutted-off giving a zero magnetization, however it is not the case for NPs in thin films. One can see also that at the saturation, the rotation loops are curved which is related to the Verdet constant of the cell plus water in case of ferrofluid or to the Verdet of the glass substrate in case of MO film. Once the effect of the Verdet has been removed, the graph of the FR of the NPs has the form of Fig. II.25c-d. The saturated polarization rotations are then plotted as a function of the wavelength, in case of a spectral study.

After describing the traditional homemade MO setup, the next paragraphs will be dedicated to present the MO characterizations for the different fabricated MO films.

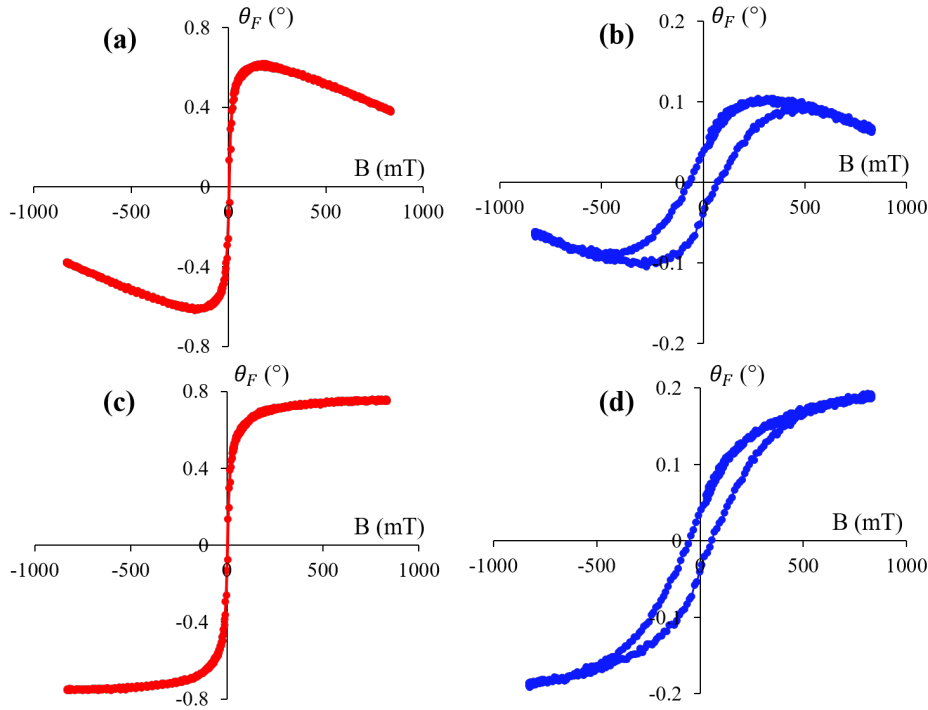


FIGURE II.25: Measurements of FR for a (a) cell filled with ferrofluid, (b) MO composite film, at $\lambda = 820$ nm. Hysteresis loops after removing the Verdet of the (c) cell plus water and (d) glass substrate.

II.3.2.2 Faraday Effect Measurements on Thin Films

The different FR and FE presented in this section, were measured at $\lambda = 820$ nm with the homemade MO setup described in the previous section.

Fig.II.26 illustrates the measurement of the saturated FR and FE, as a function of the ferrofluid fraction of NPs. One can see, that FR and FE are proportional to the ferrofluid volume. This dependency is related to the fact that by increasing the ferrofluid volume, the concentration of NPs (ϕ) in the MO-sol is higher, increasing the MO activity (see Eq.II.16 and Eq.II.17).

In addition to that, the thickness of the MO layer evolves with V_{ferro}/V_{total} as explained in section II.3.1.3, hence the propagation length of the light inside the MO film is higher, increasing the Faraday effect.

The small deviation of the experimental measurements from the linear behavior can be related to the accuracy of the components quantities during the MO-sol preparation, other words to the fabrication imperfections.

Normalized hysteresis loops of the FR for the different MO films with different ferrofluid fractions are plotted on Fig.II.27. A superposition of the different loops was obtained insuring that the NPs are well dispersed in the MO composite for the different values of V_{ferro}/V_{total} . Indeed, for high dopant volume fraction, an aggregation of NPs could be obtained. In this case, the coercive field and the remanent FR will not be the same as for low dopant volume fraction. Therefore, the homogeneity of the different MO sol-gel and the stability of the NPs for different dopant volume fractions can be deduced from Fig.II.27.

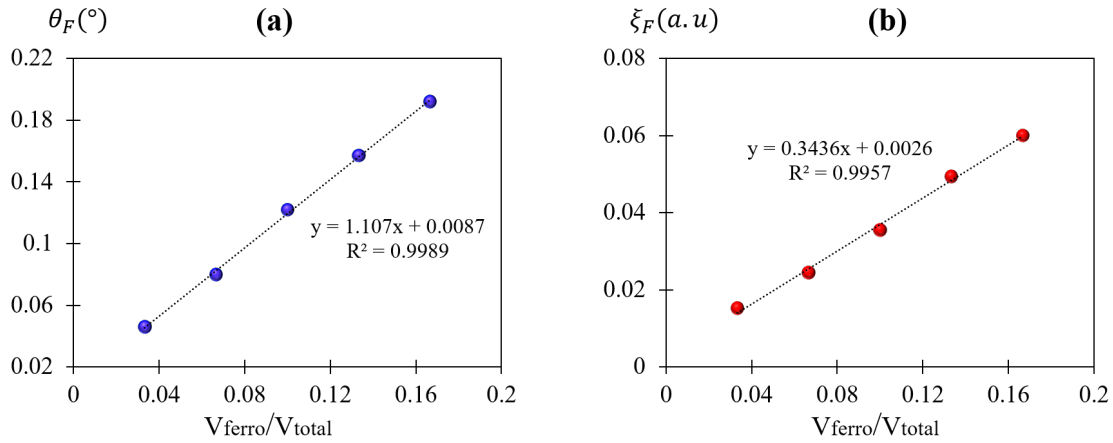


FIGURE II.26: Measurements of MO films (a) Faraday Rotation and (b) Faraday Ellipticity, as a function of the ferrofluid fraction at $\lambda = 820$ nm.

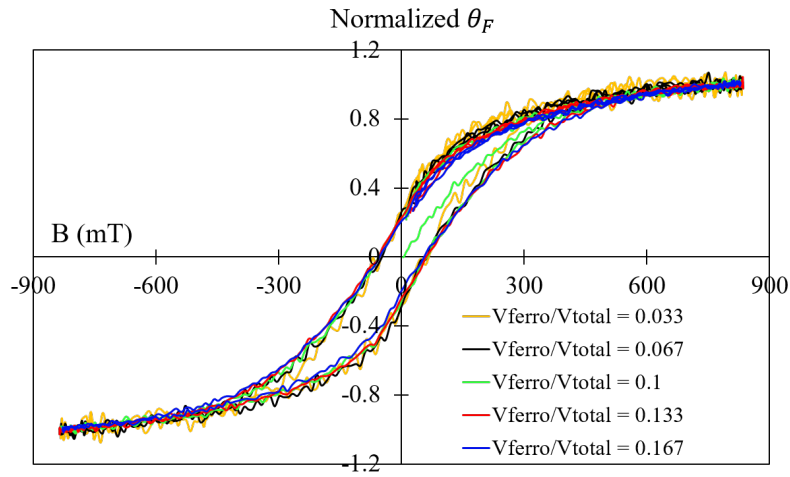


FIGURE II.27: Normalized FR as a function of the applied magnetic field for the MO films with different dopant volume fractions.

After presenting the geometrical, optical and MO properties evolution as a function of the ferrofluid volume fraction in the MO-sol, the NPs concentration ϕ in the final MO composite can be finally estimated. The estimation method and the results will be described in the next section.

II.3.3 Estimation of Nanoparticles Concentration

The volume fraction of NPs for the different MO films summarized in Tab. II.1 can be deduced from specific FR measurements. Indeed, in the case of MO composite, the FR is proportional to NPs concentration as demonstrated in Eq. II.16. By comparing the specific FR ($^{\circ}/cm$) at $\lambda = 820$ nm of the different MO thin films (θ_{film}) to that of a ferrofluid sample (θ_{ferro}), the concentrations of the different MO films can be deduced from the following equation:

$$\phi = \frac{\theta_{film}}{\theta_{ferro}} \times \frac{n_{film}}{n_{ferro}} \times \phi_{ferro} \quad (II.37)$$

where n_{film} and n_{ferro} are the refractive indices of the film and the ferrofluid respectively.

Knowing all the parameters of Eq.II.37: $n_{ferro} = 1.33$, $\theta_{ferro}/\phi_{ferro}$ is measured (see Fig.II.10) and it is equal to: $157^\circ/cm/\%$ at $\lambda = 820$ nm. From the values of n_{film} and θ_{film} given in section II.3.1.2 and II.3.2.2 respectively, the concentration ϕ of each MO film can be deduced.

Fig.II.28 illustrates the estimated values of the volume fraction of NPs as a function of the fraction of the dopant. As seen in this figure, the behavior is linear with a correlation coefficient close to one. One can notice that the volume fraction of NPs can be expected for a desired quantity of ferrofluid.

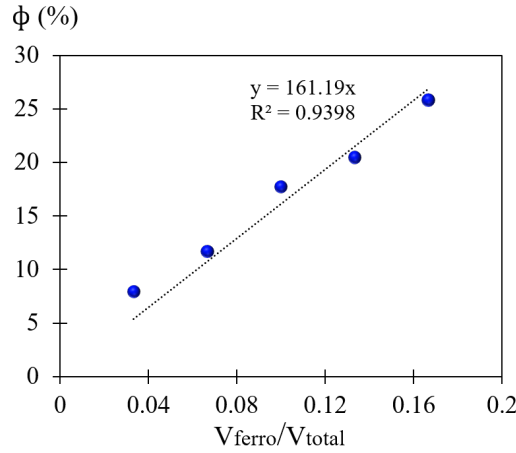


FIGURE II.28: Calculated values of the NPs volume fractions as a function of the dopant volume fractions.

The deviation of the experimental measurements from the linear behavior can be linked mainly to the uncertainty of the thickness values at small ferrofluid volume fraction, which creates an uncertainty on θ_{film} . Indeed, the refractive index shift between the MO thin film and the substrate decreases with the NPs concentration decreasing hence the ellispometry measurements precision. In addition to that, this deviation can be related to the precision of V_{ferro}/V_{total} .

A parametric study of the MO films as a function of the NPs concentrations was presented in this section. As a result, for a certain NPs concentration in the MO sol-gel, the whole characteristics of the MO film such as FR, FE, refractive index and thickness are well known in the whole spectral range [280-1700 nm]. Therefore, the off diagonal term ϵ_{MO} can be deduced for every NPs concentration from Eq.II.16 and Eq.II.17.

An example of this study, Fig.II.29 illustrates the dielectric function of the MO film (ϵ_{xx}) as a function of the NPs concentrations. Moreover, this large study allows us to measure the refractive index of the NP, in other words ϵ^{NP} . The NP refractive index measurements method will be described in the next section.

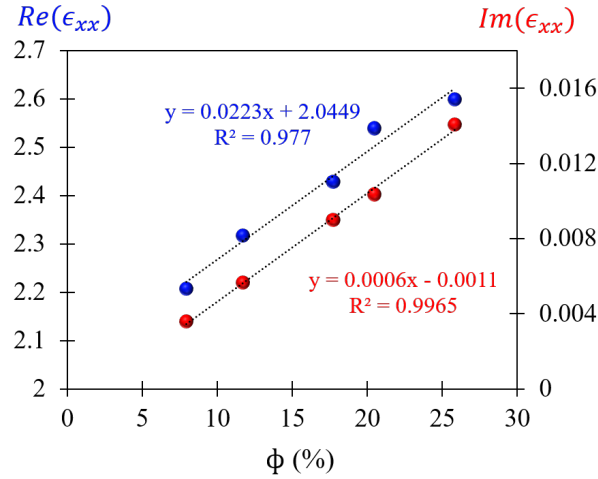


FIGURE II.29: Measurements of the real and imaginary parts of the MO films dielectric function at $\lambda = 1550$ nm, as a function of the NPs volume fraction.

II.3.4 Measurements of Nanoparticle Refractive Index

A multi-model fitting method was applied to ellipsometric measurements, in which models of the MO samples with different volume fraction of NPs are gathered and fitted all together. The objective of the multi-model is to find the refractive index of the cobalt ferrite NPs, by taking in account the whole study done before.

The opto-geometric model was defined as a layer of MO composite deposited on the top of a silicon substrate, as seen in Fig. II.30. This latter has on top a small layer (60 nm) of thermal oxide (SiO_2) created after heating the substrate at a temperature of 1000°C (see section II.2.2). This layer thickness was measured before MO composite deposition.

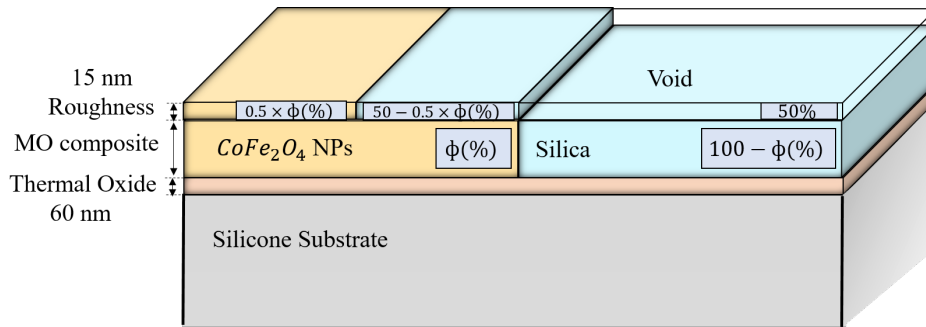


FIGURE II.30: Example of MO composite film model.

The MO composite was defined, according to the Maxwell-Garnett EMA, as a homogeneous medium formed by NPs embedded in a silica matrix. As explained before, the Maxwell Garnett EMA assumed small spherical inclusions well separated from each other within a host matrix, which is very close to our case. On top of the MO composite we defined a thin layer (around 15 nm) of roughness formed by 50% of MO composite and 50% of void.

The dispersion law of the silica matrix is chosen to be classical. This latter is defined as follows:

$$\epsilon_{CI}(E) = \epsilon_{\infty} + \frac{(\epsilon_s - \epsilon_{\infty})E_t^2}{E_t^2 - E^2 + i\Gamma_0 E} \quad (\text{II.38})$$

where $\epsilon_\infty = 1$ is the high frequency dielectric constant, $\epsilon_s = 2$ gives the value of the static dielectric function at a zero frequency, $E_t = 12$ eV is the resonant frequency of the absorption peak, Γ_0 is related to the Full Width at Half Maximum (FWHM) of the absorption peak, and it is chosen to be zero.

The chosen dispersion law of the NPs is a Tauc Lorentz model. This latter works particularly well for amorphous materials exhibiting an absorption in the far UV or in the visible range, which is the case of cobalt ferrite NPs. The Tauc-Lorentz dispersion law is defined with one absorption peak. Its imaginary part is expressed as follows:

$$Im(\epsilon_{TL}(E)) = \begin{cases} \frac{1}{E} \frac{AE_0C(E-E_g)^2}{(E^2-E_0^2)^2+C^2E^2} & E > E_g \\ 0 & E \leq E_g \end{cases} \quad (II.39)$$

And, its real part is derived from Eq.II.39 using the Kramers-Kronig integration:

$$Re(\epsilon_{TL}(E)) = \epsilon_\infty + \frac{2}{\pi} P \int_{E_g}^{\infty} \frac{\Xi Im(\epsilon_{TL}(\Xi))}{\Xi^2 - E^2} d\Xi \quad (II.40)$$

The terms A and C are related respectively to the amplitude and the FWHM of the absorption peak, E_0 is the peak central energy, E_g is the optical band gap energy and P is the Cauchy principal value.

The volumes fraction of NPs are those estimated from specific Faraday measurements and illustrated on Tab.II.1. The experimental values are those measured by ellipsometry for each MO film.

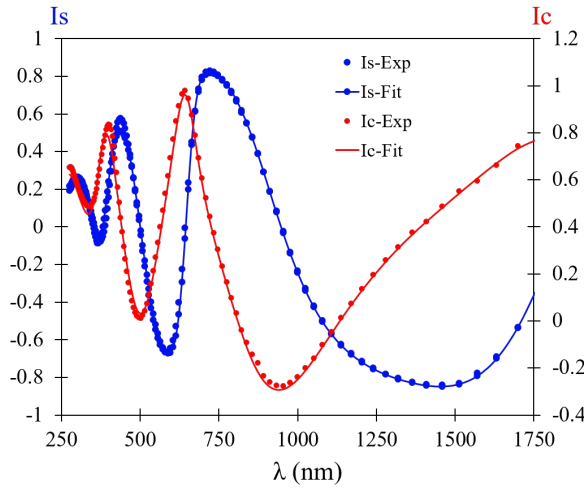


FIGURE II.31: Example of the experimental measurements (Exp) and the multi-model fitting (Fit) of I_s and I_c , as a function of the wavelength.

$$I_s = \sin(2\psi) \sin(\Delta) \text{ and } I_c = \sin(2\psi) \cos(\Delta).$$

In every MO opto-geometric model, the MO film and roughness layer thicknesses and the NPs dispersion were chosen to be fitted. Fig.II.31 illustrates an example of the experimental measurements and the multi-model fitting, as a function of the wavelength. As seen in this figure, the fitting and the measurements are in good agreement.

As a result, the MO film thicknesses and refractive indices of the multi-model fit are very close to those presented on Fig.II.22 and Fig.II.21, respectively. Moreover, the dielectric

function of the ferrite cobalt NPs is obtained and it is illustrated on Fig.II.32. The resulting parameters of the Tauc-Lorentz model are: $\epsilon_\infty = 3$, $E_g = 1.36$ eV, $A = 59.3$, $C = 4.95$ eV, and $E_0 = 3.45$ eV.

As seen in Fig.II.32, the dispersion of the NPs dielectric function is similar to that of the MO film (see Fig.II.20). Hence, $\text{Re}(\epsilon^{NP})$ is maximum in the visible wavelength range, resulting in a refractive index n^{NP} equal to 2.8 at $\lambda = 580$ nm and around 2.45 at $\lambda = 1550$ nm. These values are coherent with the literature for bulk [Sti94; Yan+15] and NPs [Len96] cobalt ferrite.

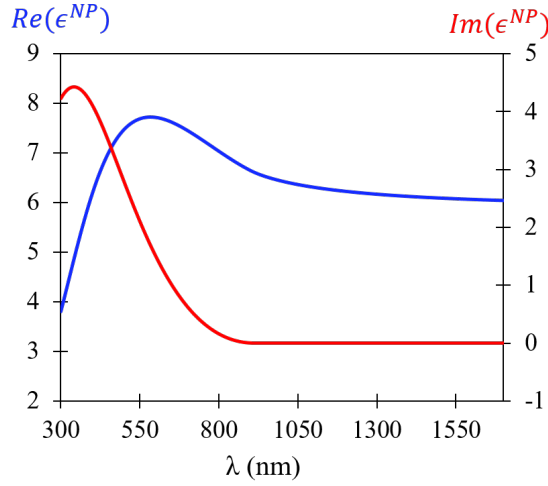


FIGURE II.32: Dielectric function of cobalt ferrite NPs resulting from the ellipsometry multi-model, as a function of the wavelength.

Until now, the diagonal elements of the MO films permittivity tensor are supposed to be equal ($\epsilon_{xx} = \epsilon_{yy} = \epsilon_{zz}$), since the NPs are blocked randomly in the silica matrix resulting in non permanent anisotropy. The next section will be dedicated to the MO films deposited under gelation magnetic field. Hence, the optical permanent anisotropy will be studied and the intrinsic anisotropy of the NP will be estimated.

II.3.5 Magneto-Induced Anisotropies

As described in section II.2.3.3, some MO films were deposited under gelation magnetic field, creating a permanent linear optical anisotropy in the film due to the fact that the NPs optical axis is blocked following the direction of the magnetic field applied during the gelation. Hence, the diagonal elements of the tensor permittivity of the MO composite are not equal anymore.

The measurements of the in-plane anisotropy ($\Delta n = n_z - n_y$) for the MO films with $\phi = 26\%$, deposited under gelation magnetic field are plotted on Fig.II.33a as a function of the wavelength, for different magnetic field magnitudes and orientations. The measurements were done by ellipsometry in transmission. As seen in Fig.II.33a, the amplitude of the anisotropy is more important in the visible region than in the near IR, which is related to the refractive index dispersion of the NP. The anisotropy reaches a value of $\Delta n = 10^{-2}$ around $\lambda = 1550$ nm for in-plane gelation field sample.

Therefore, the intrinsic anisotropy of the cobalt ferrite NP ($\Delta n^{NP} = n_z^{NP} - n_y^{NP}$) which relates to its ellipsoidal shape or its crystalline structure, can be approximately deduced by taking into account a linear EMA. Hence, $\Delta n^{NP} = \Delta n / \phi = 10^{-2} / 0.26 = 0.038$. This value corresponds to NP embedded in a silica matrix and it may varies with the matrix refractive index.

For the out of-plane \vec{B}_{gel} sample, the anisotropy cannot be measured by ellipsometry but it can be detected by the hysteresis loops of the FR.

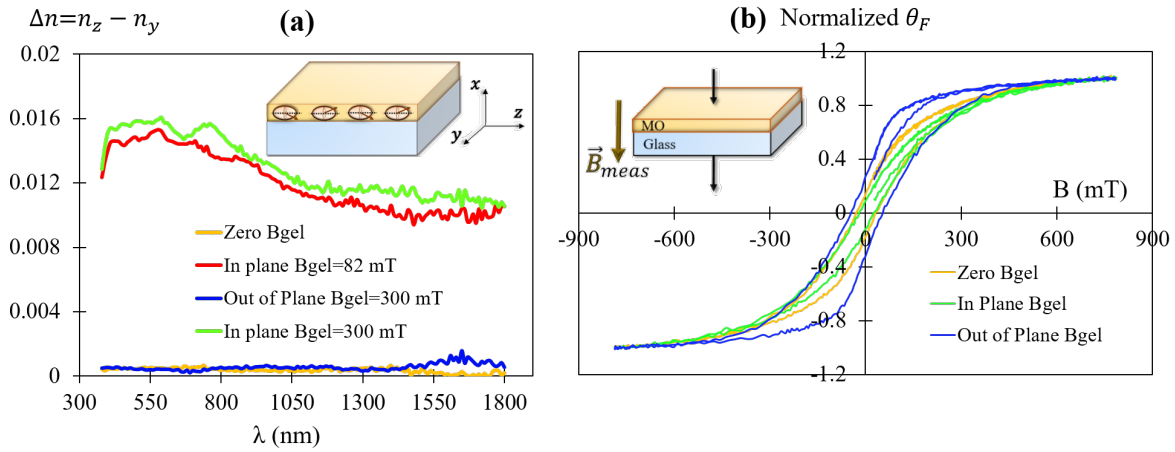


FIGURE II.33: (a) In-plane anisotropy ($\Delta n = n_z - n_y$) as a function of the wavelength for different magnitudes and directions of the gelation field \vec{B}_{gel} . (b) Normalized Faraday loop at $\lambda = 820$ nm for different \vec{B}_{gel} orientations with 300 mT of amplitude. The MO films result from MO-SOL1 (see Tab.II.1).

The normalized FR for the different samples under magnetic field at a fixed wavelength are plotted in Fig.II.33b. It is clear from this figure that the hysteresis loops are not overlapped, which proves that a permanent magnetic anisotropy is created during the gelation under magnetic field. One can see that the hysteresis loop of the out of-plane field sample is the largest one and that of the parallel field is the thinner. In the case of out of-plane \vec{B}_{gel} , the NPs easy axis of magnetization is oriented in a direction parallel to that of the measurement field \vec{B}_{meas} (the measurement configuration of the Faraday effect is illustrated in inset Fig.II.33b), resulting in higher FR remanence compared to that of the zero field. While, in the case of the in-plane field, the NPs easy axis of magnetization is oriented perpendicularly to the direction of \vec{B}_{meas} resulting in lower polarization rotation remanence. For the case of zero field the NPs are randomly oriented and the behavior is in the middle. Same analysis can be applied to the coercive field values.

After the large parametric study of the MO composite, the whole permittivity tensor of this latter (ϵ_{xx} , ϵ_{zz} , ϵ^{NP} , ϕ and ϵ_{MO}), is well defined now. In addition to that, for a certain ferrofluid quantity, all the MO characteristics are well known before elaboration, and can be used therefore in the simulations for the structure design.

The next section will be dedicated to the elaboration of the all-dielectric GMR structures.

II.4 Elaboration of Guided-Mode Resonant Gratings

As explained in Chap.I, the main objective of this thesis is to fabricate a simple GMR structure capable to demonstrate an enhancement of the MO effects. For the simplicity of fabrication which leads to low cost devices, the first proposed structure is a photoresist (PR) grating structured on top of the MO composite waveguide which is deposited on a glass substrate. The second all-dielectric proposed structure consists of an alternating Si_3N_4 and MO composite grating, deposited on a BK7 substrate. The elaboration of the different structures will be described in details in the next sections.

II.4.1 Photoresist Gratings

II.4.1.1 Work Environment and Description of the Used Photoresist

The fabricated structures are in nanometric dimensions, thus any dust or surface pollution represents a critical defect in the structure. Therefore, the cleanliness is essential during the fabrication process. For this reason, all the fabrication steps of the GMR structure were done in a clean room. Before the fabrication of the PR grating on top of the MO film, this latter was cleaned by a wet bench.

The used PR is the S1805©. It is a positive resin. It means that the exposed areas to the light are dissolved during the development stage. The PR has been chosen for several reasons: first, this resin has a good adhesion to the MO film. In addition to that, it is possible to dilute the S1805© in ethyl-lactate in order to change its viscosity and thus modify the thickness of the deposited layer. This important feature allows us to control the grating height and width. Moreover, the PR requires a low annealing (60°).

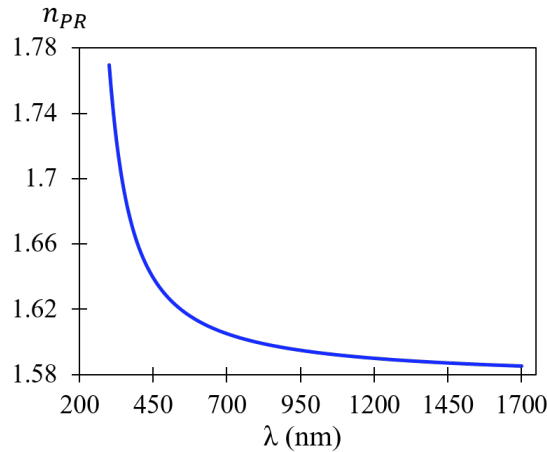


FIGURE II.34: Refractive index of a PR film as a function of the wavelength.

The refractive index of a thin film of the used PR (n_{PR}) was measured by ellispometry and illustrated on Fig.II.34. As seen in this figure, $n_{PR} = 1.59$ around $\lambda = 1550$ nm. The refractive index measurements were done for an non-insolated and insolated PR film with UV lamp ($\lambda = 360$ nm), and the results are the same.

The elaboration of the different PR gratings on top of the MO films will be detailed in the following paragraphs, preceded by an introduction to spin coating process and to AFM.

II.4.1.2 Spin Coating Process and AFM

Spin Coating Process The spin coating is a technique used to create uniform thin films (a few nm to a few μm) on the surface of flat substrates. The process is described as follows (see Fig.II.35):

- First, the solution is deposited on the center of the substrate with a pipette.
- Then, the substrate is rotated at high speed (typically around 3000rpm). A thin layer of the coated solution is formed on the substrate surface due to the centrifugal force and the surface tension. The higher the rotation speed, the thinner the film.
- While the rotation is continued, the airflow evaporates the majority of the solvent leaving a dry film. Hence, the longer the time of rotation, the thinner the film.

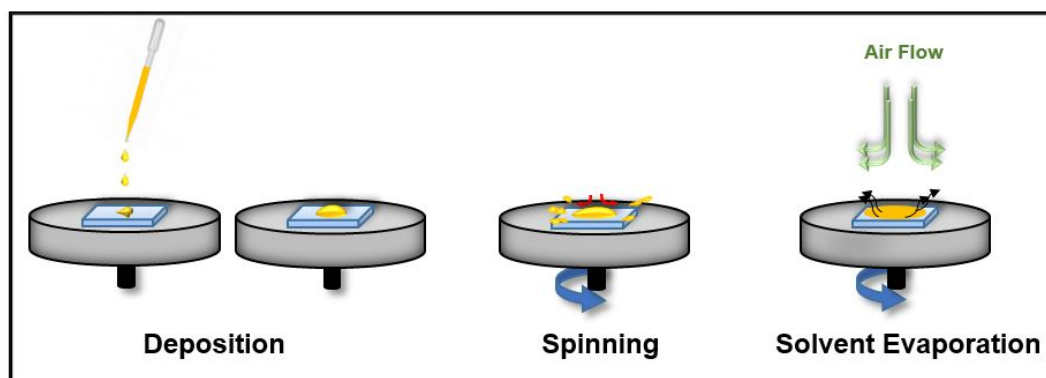


FIGURE II.35: Schematic representation of the different steps of spin coating process.

Final film thickness depends on one hand on the properties of the coated solution (viscosity, surface tension, etc.), and on the other hand on the spin coating parameters (rotation speed, spinning time, etc.).

Atomic Force Microscopy The fabricated GMR gratings were characterized by AFM in order to obtain the grating profile and measure the grating height and width.

AFM [BQG86] is a powerful tool to analyze and observe surface of a sample in a very small scale (micrometer and nanometer) in two and three dimensional images and study the topography. The examination of the samples can be done in ambient conditions, in vacuum, as well as in liquids. The scanning is done by a probe consisting of a nanometric tip attached to the free end of a cantilever and placed very close to the surface (see Fig.II.36). The repulsive or attractive interactions between the atoms constituting the tip and the surface atoms of a sample will cause a bending of the cantilever. The analysis of the cantilever deviation gives images of the surface sample. The deflection is detected by a laser beam, which is reflected from the surface of the cantilever and detected by a photodiode.

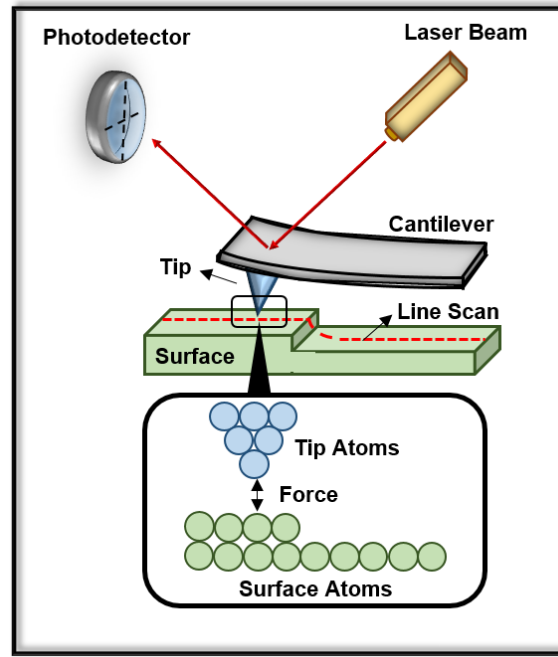


FIGURE II.36: Schematic representation of the working principle of the AFM.

II.4.1.3 Fabricated Structures

The essential fabrication steps of the PR grating are illustrated in Fig. II.37 and summarized as follows:

- First, thin layers of diluted S1805 (60%, 80% and 100%) were deposited on top of MO thin films by spin coating process.
- Second, the deposited PR was heated at 60°C for 60 seconds, to evaporate the persistent solvent, ensuring its mechanical strength and its adhesion to the MO film.
- After that, the PR film was structured by classical photolithographic process using a Mercury vapour lamp ($\lambda = 360$ nm) and a periodic quartz-supported chromium amplitude mask with a period of 1000 nm.
- Finally, the samples were immersed in MF319 developer for a certain time depending on the UV exposure time, in order to remove the exposed PR. After this step, the GMR structure is obtained.

During the exposure of the PR with the UV lamp, the reflection of the light at the PR/MO film interface is limited due to their small index difference ($n_{PR} = 1.68$ and $n_{MO} = 1.69$ for $\phi = 26\%$, at $\lambda = 360$ nm), insuring a good grating profile. In addition to that, the reflection of the light at the MO film/substrate interface is attenuated due to the large absorption of the cobalt ferrite NPs at $\lambda = 360$ nm (see Fig. II.11).

The parameters of the different fabricated PR gratings are summarized in Tab. II.2. The fill factor is defined as the ratio of the PR width and the grating period. The initial PR thicknesses were measured by ellipsometry, while the grating height and the fill-factor by AFM.

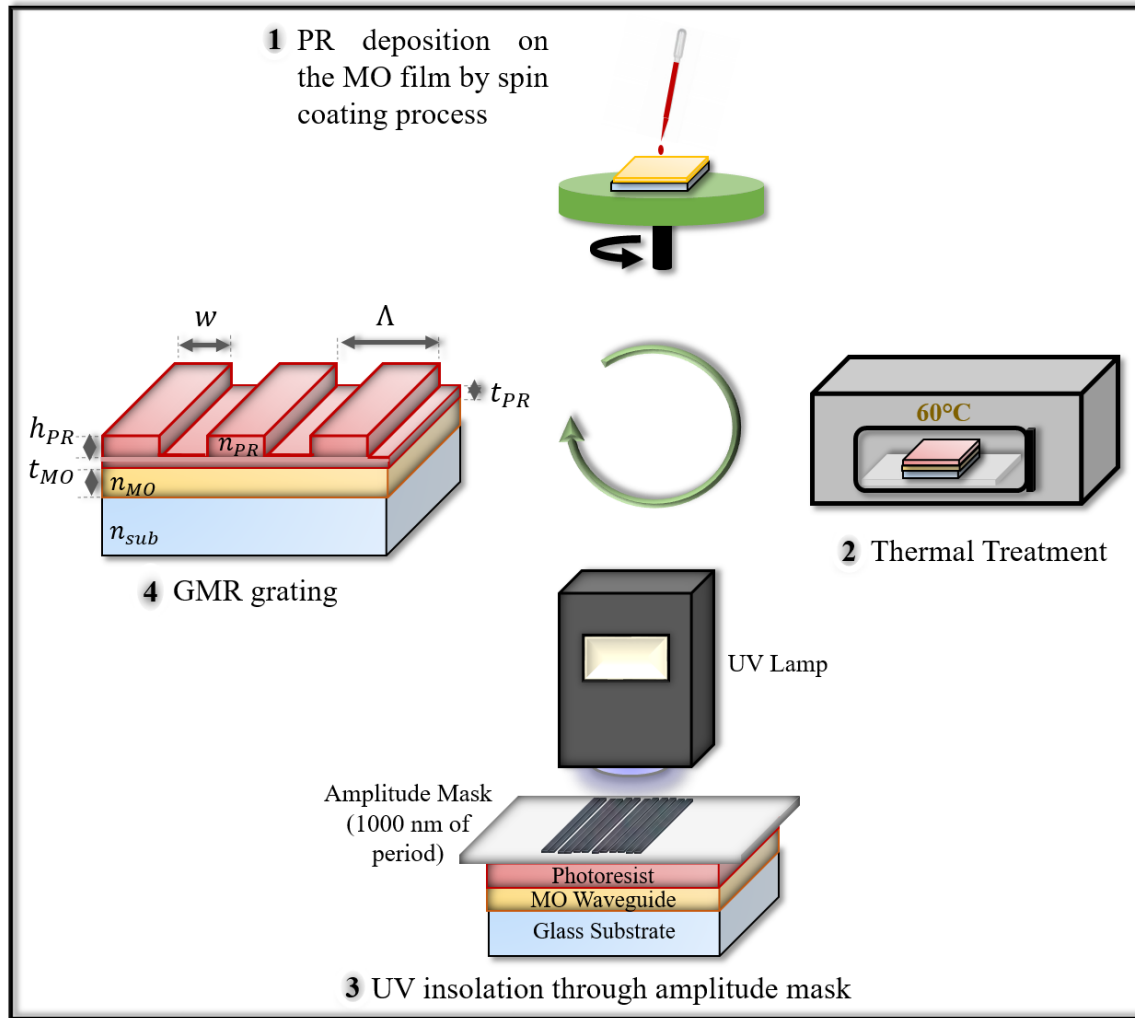


FIGURE II.37: Schematic illustration of the elaboration steps of a GMR structure based on photoresist grating.

The grating period ($\Lambda = 1000$ nm, the choice of this period will be explained in Chap. III) was verified by using Littrow mounting.

In order to control the parameters of the PR gratings, different initial PR thicknesses were deposited (in other words different concentrations of S1805 were used) and different exposure and development times were applied to the PR films (see Tab. II.2).

As seen in Tab. II.2, for the exposure and development time of 12s and 15s respectively, the grating height is around 300 nm and the fill factor is around 0.4. However, for the 8 s and 10 s of exposure and development times respectively, the grating height and the fill factor are 225 nm and 0.5, respectively. These values can be varied depending on the conditions of fabrication like temperature, humidity, power of the UV lamp, age of the PR, etc.

One can say that for PR1 we should increase the exposure time to have deeper gratings, but the PR width will decrease hence the fill-factor. For this reason, the time couple (12 s, 15 s) is a good choice to have a compromise between the height and the fill-factor.

One can notice from Tab. II.2, that the grating is not dug to the bottom and a thin layer of PR is kept. This latter has a refractive index close to that of the MO film at $\lambda = 1550$ nm, as

TABLE II.2: The different fabricated PR gratings with the corresponding elaboration and geometrical parameters.

Sample Name	S1805 Concentration	Initial PR thickness	Exposure Time	Development Time	Grating Height	Fill Factor
PR 1	100%	690 nm	12 s	15 s	300 nm	0.4
PR 2	80%	500 nm	12 s	15 s	300 nm	0.4
PR 3	60%	380 nm	12 s	15 s	300 nm	0.4
PR 4	60%	380 nm	8 s	10 s	225 nm	0.5

demonstrated in Fig.II.34. This persistent PR film can be beneficial to have the two guided-modes (TE and TM) in the structure, when the MO film cannot be perfectly a guided-film (low index contrast of the MO film with the substrate or low thickness, as in the case of the prepared MO film in this work). But, the thickness of the persistent PR should not be high compared to that of the MO film to avoid having a big part of the modes energy in the PR layer.

Therefore, the sample PR 3, 60% of diluted PR with the time couple (12 s, 15 s), is the best choice. Fig.II.38 illustrates example of AFM measurements for a PR 3 structure. We see the topography (Fig.II.38a), a 3D (Fig.II.38b) and a 2D profile (Fig.II.38c). From these figures we can deduce the uniformity and the rectangular profile of the grating. As well as, we can deduce the grating parameters: the height ($h_{PR} = 300$ nm) and the PR width ($w = 400$ nm).

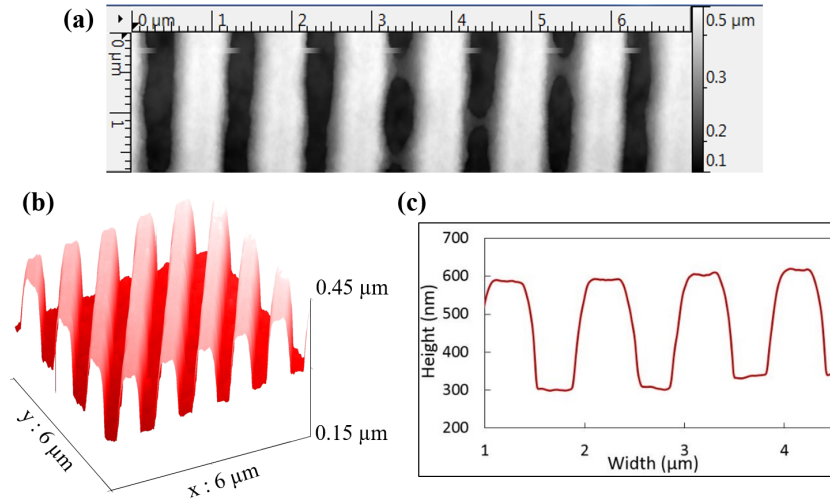


FIGURE II.38: Example of measurements done by AFM for a GMR structure based on PR grating: (a) topography image, (b) 3D and (c) 2D grating profile.

Hence, with the same fabrication parameters of PR 3, around thirty PR gratings were structured on top of MO composite films either coated with or without applied magnetic field \vec{B}_{gel} . Thus, the different fabricated PR-MO structures can be summarized according to four types and illustrated on Tab.II.3.

The purpose of fabricating PR grating on top of MO film with oriented NPs, is to control the effective indices of TE and TM modes, in other words the phase shift $\Delta\beta$. Due to fabrication imperfections, the geometrical parameters may be slightly different from a sample to another.

TABLE II.3: The fabricated PR-MO structures with the corresponding NPs orientation in the MO films. The elaboration parameters correspond to those of PR 3 (Tab.II.2).

PR-MO structures	Magnetic field (\vec{B}_{gel}) orientation
Type 1	Zero field
Type 2	Out of-plane
Type 3	In-plane with grating grooves perpendicular to the field direction
Type 4	In-plane with grating grooves parallel to the field direction

After describing the elaboration process of PR gratings on top of MO films, the next section will be dedicated to describe the fabrication process of GMR structures based on Si_3N_4 grating.

II.4.2 Silicon Nitride Gratings

In previous work in the LabHC, an all-dielectric grating was studied by numerical simulations and experimental measurements in order to enhance also the MO effects. The structure was presented in Fig.I.27. It is formed by alternating Si_3N_4 and MO composite grating deposited on a BK7 substrate. This structure was optimized by numerical simulations in order to achieve the TE-TM phase matching condition. The grating height and width, and the MO composite refractive index are very critical to satisfy this condition. Therefore, the optimized parameters were: $h = 560$ nm, $w = 719$ nm and $n_{MO} = 1.61$ at $\lambda = 1550$ nm. To obtain resonances around $\lambda = 1550$ nm at normal incidence, the grating period was chosen to be $\Lambda = 950$ nm.

Due to manufacturing tolerances, the desired structural parameters of the Si_3N_4 grating were difficult to achieve, therefore the phase matching condition was lost, for the chosen MO refractive index (1.61). Nevertheless, enhancement of the MO effects were reached through the Si_3N_4 -MO structure, as described in Chap.I.

In this work, this type of structure has been employed to compare its performance to that of the PR-MO one. Furthermore, following the work led before [Var17], we will try to improve the phase matching condition with the persistent fabricated Si_3N_4 gratings, by finding the suitable MO composite refractive index. Therefore, due to the large study of the MO composite presented previously in this chapter, we will be able to predict the precise ferrofluid quantity in the MO-sol, for the desired MO composite refractive index.

The structure was fabricated as follows (see Fig.II.39):

- First, a film of Si_3N_4 was deposited on a BK7-substrate. Then, the grating was structured through electron beam lithography and reactive ion etching [Var17]. This method of fabrication is more complex and expensive than the classic photolithography (fabrication method of the PR gratings). This work was done by the University of Joensuu (Finland).
- After that, the Si_3N_4 grating was impregnated in the MO composite by dip coating, followed by a thermal treatment at 90°C for one hour.

Fig.II.40 illustrates the AFM measurements for a Si_3N_4 grating before impregnation. As seen in Fig.II.40b the grating height and width are equal to 545 nm and 500 nm, respectively. The initial thickness of Si_3N_4 is 593 nm, hence the grating is not dug to the bottom and a

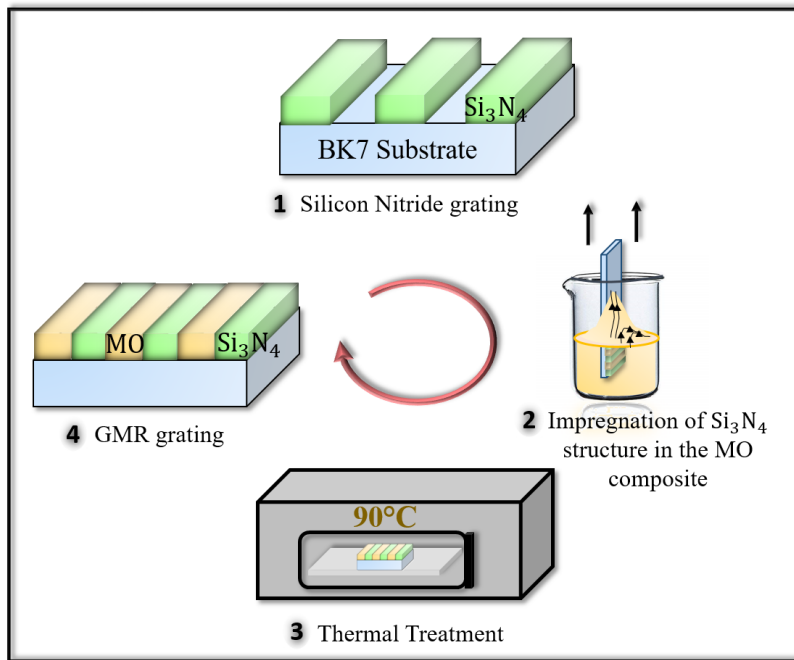


FIGURE II.39: Schematic illustration of the elaboration steps of a GMR structure based on Si_3N_4 grating.

thin layer of Si_3N_4 with 48 nm-thick is still present. The grating period is 966 nm and it was verified by the Littrow mounting. Therefore, for these grating parameters, the phase matching condition at normal incidence can be achieved with $n_{\text{MO}} = 1.49$. This value was found by rigorous coupled wave analysis simulations, which will be explained in the next chapter.

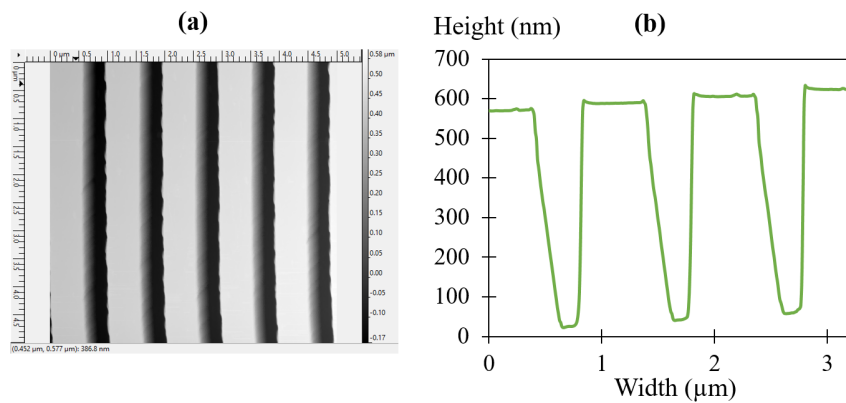


FIGURE II.40: Example of measurements done by AFM for a Si_3N_4 grating on a BK7 substrate: (a) topography image, (b) 2D grating profile.

II.5 Conclusion

In this chapter, the geometric, magnetic, optic and MO properties of the cobalt ferrite NPs were firstly described in an individual state then in a composite, with the corresponding permittivity tensors. After that, the MO films elaboration (TEOS-sol preparation, doping process and MO films coating) was presented with the used techniques and elaboration methods. MO films with different NPs concentrations were fabricated on different types of substrates. The obtained films present excellent optical quality with no optical diffusion and no cracks. In addition to that, different MO thin films were coated under magnetic field with different orientations. Hence, permanent optical and magnetic anisotropies were demonstrated by ellipsometry measurements in transmission and by the hysteresis loops of the FR, respectively.

The dependency of the MO films' characteristics (such as FR, refractive index and thickness, etc.) on the ferrofluid volume fraction was largely studied. The volume fraction and the refractive index of the NPs were deduced from this study. As a result, the whole MO composite permittivity tensor was defined for every NPs concentration. Hence, for a certain ferrofluid quantity in the MO-sol, the whole characteristics of the MO film can be identified before elaboration and used therefore in the simulations for the structure design.

Finally, the elaboration steps of the all-dielectric GMR structures were detailed. The numerical and experimental evidence of the MO enhancement through these structures will be detailed in the next chapter.

CHAPTER III

Magneto-Optical Effects Enhancement: Numerical and Experimental Evidence

This chapter is dedicated to present the experimental and numerical evidence of the MO effects enhancements, in order to demonstrate that the chosen all-dielectric structure can be used for magnetic field sensing or NDT.

Hence, numerical simulations of the GMR structure based on PR grating will be firstly presented, in order to study the optical and MO optical behavior for different structure opto-geometric parameters.

In the second part of the chapter, measured MO enhancements will be presented. The experimental measurements were done with homemade MO setups developed in the presented work.

Beside the PR-MO structure, a dielectric structure based on Silicon Nitride grating was also studied in this work. The experimental and numerical results will be presented and compared to those demonstrated through the PR-MO structures.

III.1 Numerical Simulations of Optical and Magneto-Optical Behavior

III.1.1 Calculations Method

Different methods can be used to model the optical response of diffraction gratings. The most common methods are Fourier-modal methods. These methods are based on the decomposition of the structure and the electromagnetic field in Fourier orders according to the periodicity direction. By resolving the Maxwell's equations in the system, the reflectance and the transmittance of every diffraction orders can be modeled.

The decomposition of the system differs according to the used method of calculation:

- The Rigorous Coupled Wave Analysis (RCWA) [MG81] method divides the structure into a succession of layers. Thus, a simple binary grating will be described by one layer

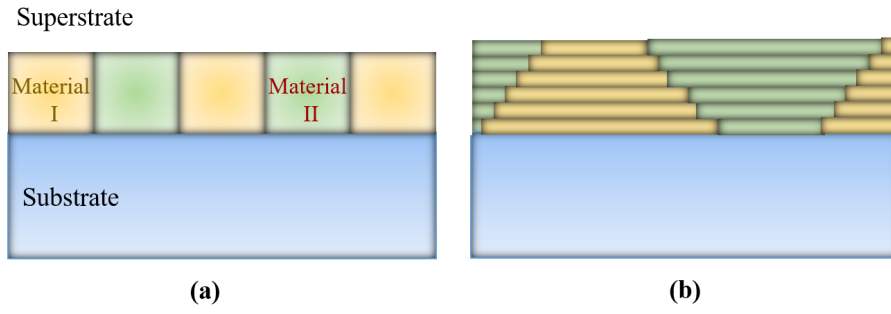


FIGURE III.1: Schematic illustration of the layer decomposition in case of (a) binary and (b) sinus grating through RCWA calculation methods.

decomposed into two cells filled with different materials (Fig. III.1a). The superstrate and the substrate are considered as semi-infinite media. Hence, the RCWA method is adapted to the modeling of the binary structures. However, the description of a sinus profile by the RCWA method will require the decomposition of the structure into a succession of layers with a variable fill-factor (as seen in Fig. III.1b). Hence, large number of layers is needed to describe this type of structure.

- The Chandezon method [Cha+82] describes every interface of the system as a Fourier series and uses a coordinate transformation to reduce it to a system possessing planar and/or curvilinear interfaces. Thus, this method is very adapted to the description of sinusoidal structures or structures with variable fill-factor (triangular profile for example). On the other hand, it is difficult to model binary profiles with this method because the description of a slot signal requires a large number of terms in the Fourier series.

These calculation methods are implemented in the commercial software MC Grating ©. This latter was used in this work with the RCWA calculation method since we are interested in rectangular profile gratings. However, this software is not adapted to materials owing permittivity tensor with anti-symmetric off-diagonal elements (like MO materials). Therefore, in order to calculate the MO response, a RCWA code has been developed within the team taking into account the whole permittivity tensor [Li98]. Hence, the study of optimized structures was done by MC Grating © (faster calculations) and then the MO simulations were done with the homemade RCWA code.

After describing the calculations method used in this work, numerical simulations for the all-dielectric GMR structure will be presented in the next section. As mentioned before, a simple GMR structure was adapted and consists of a PR grating deposited on top of a MO composite film. The optical and the MO response of this structure were largely studied for different grating and MO film opto-geometric parameters. In order to understand well the influence of these parameters on the MO effects we have to clarify that in resonant structures:

- The polarization rotation effects depend firstly on the TE-TM phase shift: for a maximum rotation the condition of phase matching ($\Delta\beta = 0$) is required. Second, the magnitude of these effects count on the transmittance or reflectance resonance amplitudes of TE

and TM polarizations, in other words on the coupling efficiency into the MO waveguide. Finally, if cavity modes are excited in this latter, the propagation length of the modes is increased enhancing more the MO effects compared to a structure without cavity modes. However, in case of PR-MO structure, the index difference between the MO layer and the PR grating is low ($\Delta n = 0.05$ for $\phi = 26\%$), preventing then the existing of cavity modes in this structure.

- The phase modulation effects don't require a phase matching condition since they are described by a coupling between the components of the same polarization which is TM. However, they depend on the amplitude of the transmittance resonance as for the rotation effects. And, the TMOKE is highly sensitive to the FWHM of the TM resonance since it is described by a spectral or amplitude shift of this resonance.

III.1.2 Optical Behavior of PR-MO Structure

The optical behavior of the PR-MO structure under consideration was studied firstly for different MO film thicknesses and indices. A schematic illustration of the structure is reported on Fig.III.2, which also illustrates a calculated 2D scan of the transmittance as a function of the wavelength and the MO film thickness t_{MO} (b, d) and MO film refractive index n_{MO} (c, e), for TE and TM polarizations. The grating height of the PR-MO structure is equal to $h_{PR} = 300$ nm and its fill-factor is equal to $f = 0.4$. These initial parameters were chosen to insure the coupling of the light into the MO waveguide for the two polarizations (TE and TM modes), depending of course on the MO film refractive index (1.64 for Fig.III.2b-c) and thickness (500 nm for Fig.III.2d-e). According to Eq.I.46 and in order to have at normal incidence an optical resonance at a wavelength around 1550 nm, the grating period is fixed at $\Lambda = 1000$ nm. Hence, the structure is a subwavelength structure, where only the zeroth diffraction order can exist in the substrate and the superstrate (here, the air) and the ± 1 orders in the MO waveguide. The refractive indices of the glass substrate and the PR were measured by ellipsometry and have values of: $n_s = 1.51$ and $n_{PR} = 1.59$ respectively, for the wavelength range of [1480-1630 nm].

The behavior of the resonance wavelength, or in other words β according to Eq.I.46, as a function of t_{MO} (Fig.III.2b-c) and n_{MO} (Fig.III.2d-e) is explained by the propagation equation of guided-modes in dielectric planar waveguide (Eq.I.36 and Eq.I.37 and Fig.I.11). Hence, as seen in Fig.III.2, the guided-modes don't always exist: a sufficient thickness and refractive index of guiding layer are necessary. In addition to that, the phase shift $\Delta\beta$ is varying with the waveguide properties, more obvious with n_{MO} (See Fig.III.2d-e) and no phase matching is achieved.

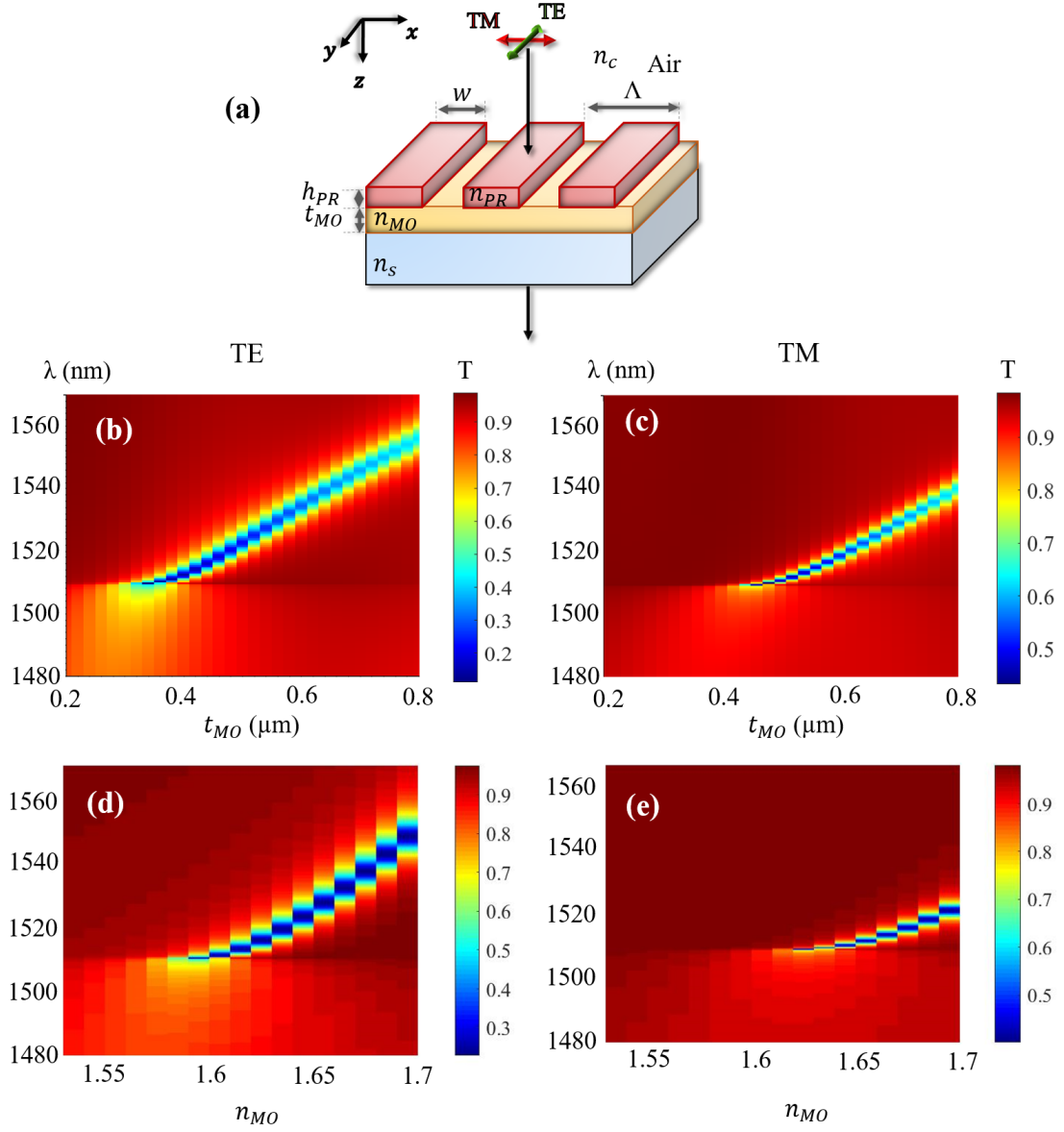


FIGURE III.2: (a) GMR structure under study: $w = 400$ nm, $\Lambda = 1000$ nm, $h_{PR} = 300$ nm, $n_c = 1$, $n_{PR} = 1.59$ and $n_s = 1.51$. Numerical simulations of TE and TM transmittance spectra at normal incidence of the GMR structure as a function of (b,c) the MO film thickness t_{MO} for $n_{MO} = 1.64$ and (d,e) the refractive index n_{MO} for $t_{MO} = 500$ nm.

Moreover, one can see on Fig.III.2 that by increasing the thickness and the refractive index, the FWHM of the transmittance resonance increases while its amplitude decreases (only with the thickness). Indeed, for the cut-off values of n_{MO} and t_{MO} , in other words the sufficient values to have a guided-mode, the FWHM of the transmittance resonance is very small (less than 1 nm).

The increment of FWHM and the decrement of the resonance amplitude are linked to the electromagnetic field distribution of TE and TM modes inside the MO waveguide. Fig.III.3 illustrates a 2D diagram of the distribution of the electric field intensity $|E_y|$ for TE mode and the magnetic field intensity $|H_y|$ for TM mode at the resonance wavelengths, for the same parameters structure of Fig.III.2 with $t_{MO} = 500$ nm and $n_{MO} = 1.64$. As seen in this figure, an

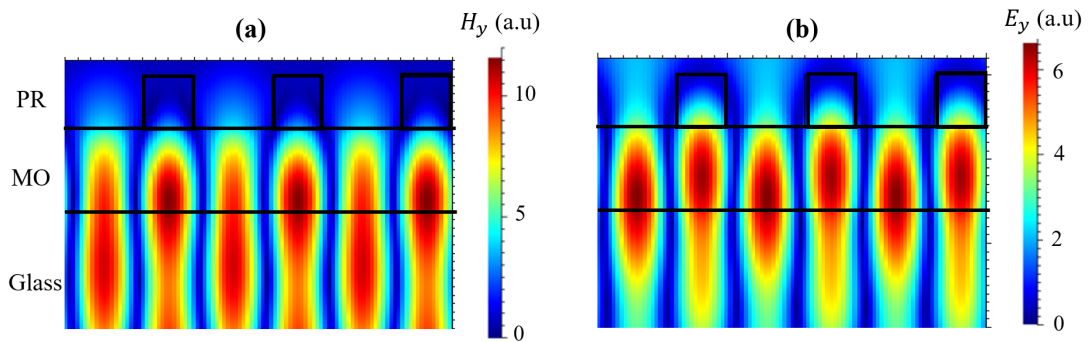


FIGURE III.3: Simulated distribution of the magnetic field intensity $|H_y|$ for TM mode (at $\lambda = 1511$ nm) and electric field intensity $|E_y|$ for TE mode (at $\lambda = 1523$ nm) at normal incidence, in the x-z plane. The considered PR-MO structure has the same parameters than Fig.III.2 with $n_{MO} = 1.64$ and $t_{MO} = 500$ nm.

important field amplitude is present in the substrate, which is close to what was presented in Fig.I.10 for a MO waveguide without grating.

Now, if t_{MO} or n_{MO} are higher, the guided-modes are more confined in the MO absorbing film, hence the field amplitude in this latter increases while it decreases in the substrate. Thus, the light absorption increases resulting in resonances with larger FWHM and weaker amplitudes.

Therefore, in order to reach higher TMOKE signal it is more favorable to work with n_{MO} and t_{MO} close to cut-off values. Indeed, a shift of a narrow transmittance resonance gives rise to a higher TMOKE response than the same shift of a broad resonance. However, for polarization rotation effects it is better to have guided-modes well confined in the MO film to have a good TE-TM conversion efficiency, since these effects are less sensitive to the resonance width. Therefore, a compromise of the MO properties is needed if we want to enhance the two types of MO effects with the same structure (for example $n_{MO} = 1.64$ and $t_{MO} = 500$ nm).

In the following paragraph we will study the effect of the fill-factor and grating height on the PR-MO optical responses. Indeed, we are searching also for grating parameters satisfying the TE/TM phase matching condition at normal incidence for higher rotation effects.

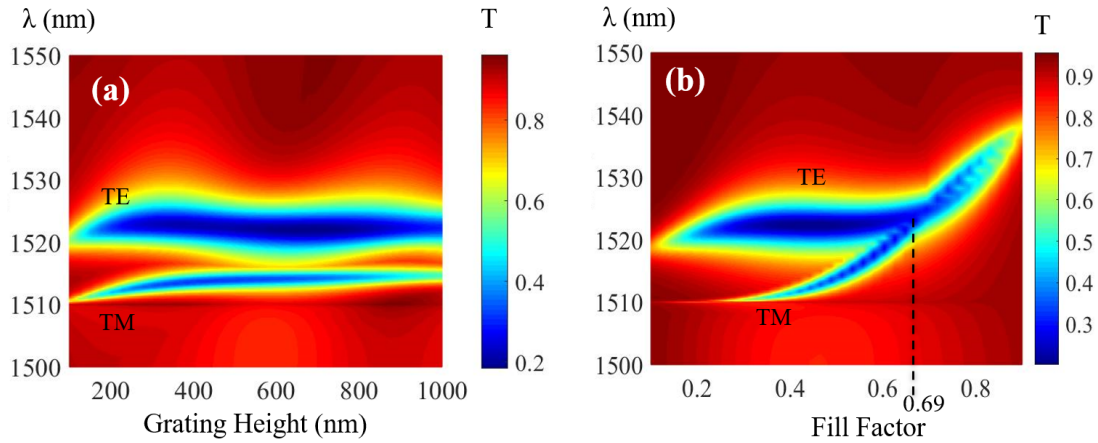


FIGURE III.4: Calculations of the transmittance of TE and TM modes at normal incidence as a function of the wavelength and (a) the grating height for $f = 0.4$ and (b) the fill factor for $h_{PR} = 500$ nm, $n_{MO} = 1.64$ and $t_{MO} = 500$ nm.

Fig. III.4a illustrates a 2D diagram of the transmittance as a function of the incident wavelength and the grating height with $f = 0.4$, for TE and TM-polarized incident light. The MO film parameters are: $n_{MO} = 1.64$ and $t_{MO} = 500$ nm. As seen in this figure, the resonance wavelengths for the two polarizations, in other words the propagation constants, are slightly modified as a function of the grating height resulting in a non-phase matching.

Fig. III.4b shows a 2D scan of the transmittance as a function of the wavelength and the fill-factor. Here, the grating height is fixed at a value of $h_{PR} = 500$ nm, where TE and TM resonances are closer spectrally compared to other values of h_{PR} as seen in Fig. III.4a. One can see that the TM mode starts to appear in the MO waveguide for values of fill-factor around 0.4. In addition to that, the resonant wavelength of the TE mode is slightly modified, while that of the TM mode highly increases with the fill-factor. This behavior is related to the change of the grating's effective index with the fill-factor. And, since the longitudinal component of the electric field of the TM mode is maximum near the MO waveguide boundaries, as explained in Fig. I.10, the TM mode is more sensitive to this variation than the TE mode. Therefore, as seen in Fig. III.4b a phase matching is reached for a fill-factor equal to $f = 0.69$ at $\lambda = 1525$ nm.

The angular behavior of the optical resonance was also studied and illustrated on Fig. III.5 for the structure parameters of phase matching ($h_{PR} = 500$ nm, $f = 0.69$, $n_{MO} = 1.64$ and $t_{MO} = 500$ nm). As demonstrated before at normal incidence ($\text{AOI} = 0^\circ$), the TE and TM modes are excited simultaneously. For non-zero incident angle, two dispersion curves appear for each polarization resulting from $q = \pm 1$ diffraction orders (according to Eq. I.46). As mentioned before, there are only the ± 1 diffraction orders in the waveguide.

One can notice on Fig. III.5a that for oblique incidence the phase matching disappears. This behavior is linked to the fact that the TE-TM effective index shift is not constant as a function of the wavelength (as explained in Fig. I.11b), in other words the AOI.

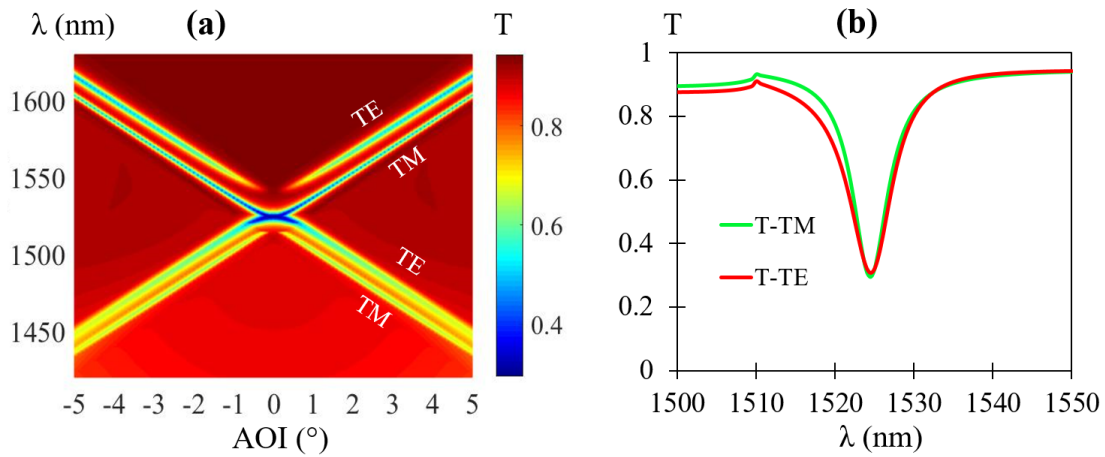


FIGURE III.5: (a) Calculated diagram of the transmittance for TE and TM polarizations as a function of the AOI and the wavelength. (b) Simulated transmittance spectra for TE and TM polarizations at AOI=0°. The considered PR-MO structure has the following parameters: $h_{PR} = 500$ nm, $f = 0.69$, $n_{MO} = 1.64$ and $t_{MO} = 500$ nm.

After studying the optical response of the PR-MO structure for different grating and waveguide opto-geometric parameters, the next section will be dedicated to the MO behavior. First, the Faraday effect will be studied at normal incidence for two conditions: phase matching ($f = 0.69$) and mismatching. Then, the LMOKE and TMOKE will be studied for different oblique incidence since these effects don't exist at normal incidence as mentioned in section I.1.1.2. Finally, the TMOKE will be plotted for different values of n_{MO} and t_{MO} , since it is highly sensitive to the resonance width.

III.1.3 Magneto-Optical Behavior of PR-MO structure

III.1.3.1 Polarization Rotation Effects

Faraday Effect: Fig.III.6b illustrates a simulated 2D scan of the FR as a function of the wavelength and the fill-factor. The structure parameters are illustrated on Fig.III.6a and the magnetic field is considered following z direction. The considered off-diagonal terms in the simulations are for $\phi = 26\%$. As seen in Fig.III.6b, at the phase matching condition ($f = 0.69$) the FR is maximum, reaching values of -0.7° and $+0.4^\circ$, while it is around -0.1° and $+0.35^\circ$ for a phase mismatch ($f = 0.5$ for example). Comparing the maximum FR values to that of a single MO film (θ_F around $+0.2^\circ$), an enhancement by a factor of 3.5 is demonstrated at the phase matching condition, accompanied with a FR sign change.

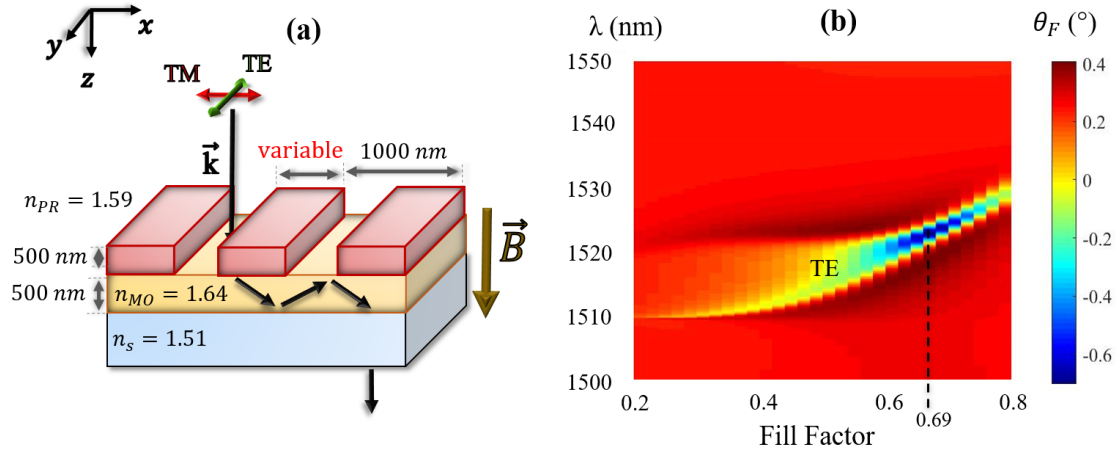


FIGURE III.6: (a) PR-MO structure under study with the corresponding opto-geometric parameters and magnetic field configuration. (b) Simulated 2D diagram of the FR at normal incidence for TE polarization.

For a reliable analyze, a compromise between intensity and polarization rotation should be taken into consideration, this is done by the study of the FoM defined in resonant structures as $\text{FoM}(^{\circ}) = \sqrt{T} \times |\theta(^{\circ})|$ [Kha+07]. The calculated FR, transmittance and the corresponding FoM are plotted on Fig.III.7a-b, for TE polarization. The parameters structure are the same than Fig.III.6a with $f = 0.69$. The peak of the FoM curves observed on Fig.III.7b corresponds to the MO resonance (Fig.III.7a). Highest FoM value of 0.36° is reached for TE polarization.

Same order of FoM magnitude was reached also numerically for TM polarization but not shown here.

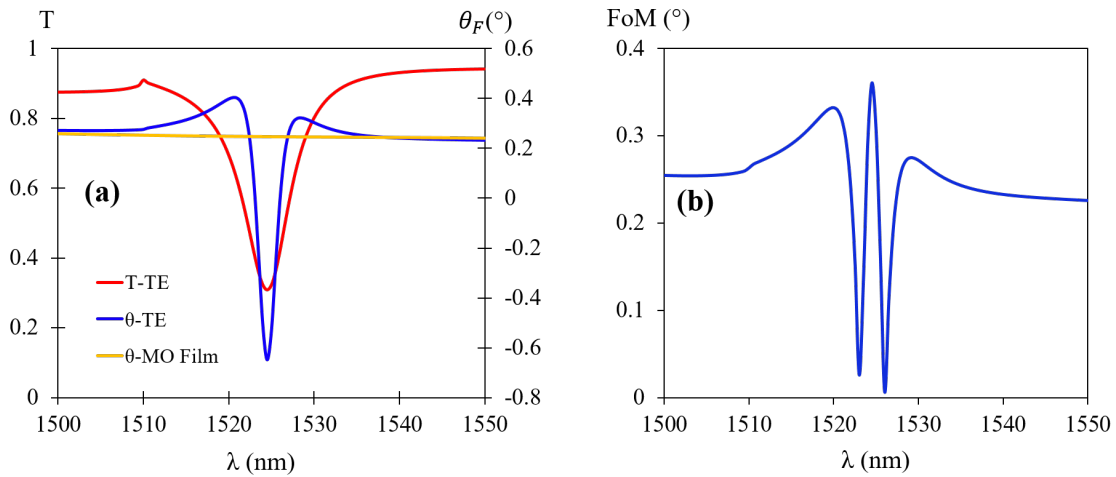


FIGURE III.7: Simulated (a) transmittance and FR and (b) corresponding figure of merit spectra for TE polarization, for the PR-MO structure of Fig.III.6 at the phase matching ($f = 0.69$). The yellow curve corresponds to FR spectrum for a MO thin film.

After studying the Faraday effect, the next paragraph will be dedicated to the LMOKE.

This latter is also maximum when TE-TM resonance overlap. However, this condition was achieved only at normal incidence (Fig.III.5) where the LMOKE is zero. Nevertheless, the LMOKE is studied for different AOI.

LMOKE: Fig.III.8b-c illustrates the LMOKE rotation in transmission for TE and TM polarized incident light respectively, where a longitudinal magnetic field is applied (x direction in Fig.III.8a). The AOI is varied from 0° to 5° .

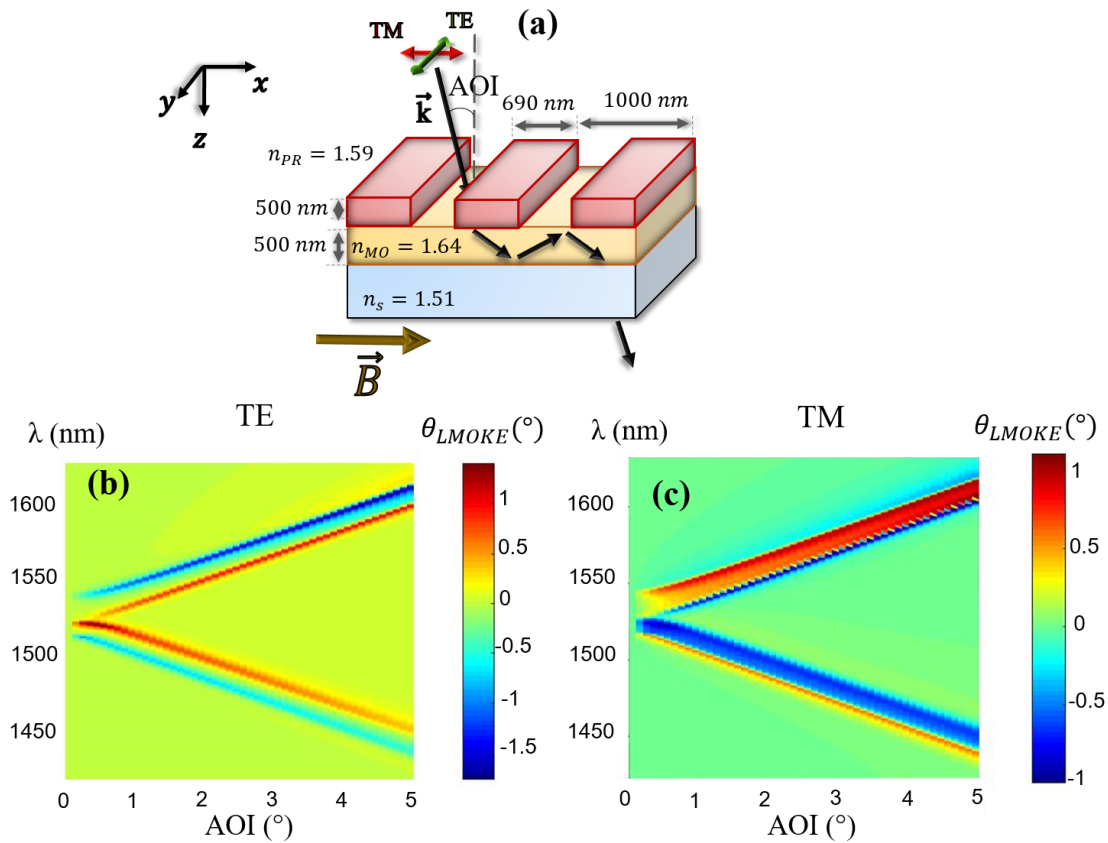


FIGURE III.8: (a) PR-MO structure under study with the corresponding opto-geometric parameters and magnetic field configuration. Simulated 2D diagram of the LMOKE polarization rotation in transmission, for (a) TE and (b) TM polarizations.

One can see on Fig.III.8b that the LMOKE rotation for TE polarization reaches maximum values around -1.7° . For a single MO layer these effects are in order of 0.001° . Hence, large enhancement of LMOKE in transmission can be achieved through the PR-MO structure.

The presence of large opposite rotation peaks on Fig.III.8b-c for a fixed AOI, is linked to the transmission resonances for both polarizations (see Fig.III.5). As seen in Fig.III.8b and for the up curves (red and blue), the rotation increases with the incident angle. This behavior is expected since the LMOKE rotation evolves with the AOI, as demonstrated in Fig.I.7b. However, for the down curves (red and blue) the effects decrease and this is related

to the decreasing of the coupling efficiency of this order (in other words, transmittance dip amplitude) as a function of the AOI (See Fig.III.5).

Same behavior for the polarization rotation spectrum of TM-polarized incident light is observed (see Fig.III.8c).

Fig.III.9 illustrates the calculated rotation, transmittance and the corresponding FoM values for LMOKE in transmission at an AOI=0.4°. At this AOI, the TE and TM transmittance re-

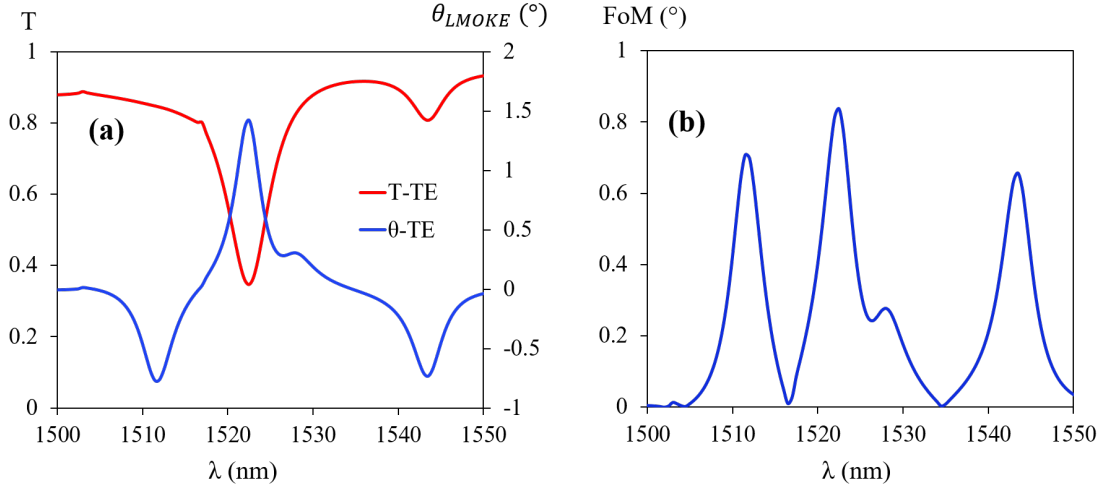


FIGURE III.9: Simulated (a) transmittance and LMOKE rotation and (b) corresponding figure of merit spectra for TE polarization at AOI=0.4°, for the PR-MO structure of Fig.III.8.

sonances resulting from different orders are spectrally close (see Fig.III.5). High values of FoM were reached and the highest value is equal to 0.84°.

According to the Lorentz force, the guided LMOKE originates from coupling between the electric fields of TE mode (y direction in Fig.III.10) and the larger (transverse) component of TM mode (z direction). The guided Faraday effect results from the coupling between electric fields of TE mode (y direction) and the smaller (longitudinal) component of TM (x direction). For this reason, the longitudinal effect reaches rotation values higher than that of the Faraday effect.

Thus, we have demonstrated that the PR-MO structure is promising to enhance the polarization rotation effects (Faraday and LMOKE in transmission). The second type of MO effects, phase modulation effects (TMOKE), will be studied in the next section.

III.1.3.2 TMOKE

As explained in section I.1.2.4, the guided TMOKE is described by a modulation of the propagation constant ($\Delta\beta_{\pm M}$) or the extinction coefficient ($\Delta k_{\pm M}$) of the TM guided-mode, for two different magnetic field directions. In the resonant structures, this effect manifests as a spectral shift (due to $\Delta\beta_{\pm M}$) or amplitude variation ($\Delta k_{\pm M}$) of the transmittance (reflectance) resonance, resulting in an intensity modulation of the transmitted (reflected) light.

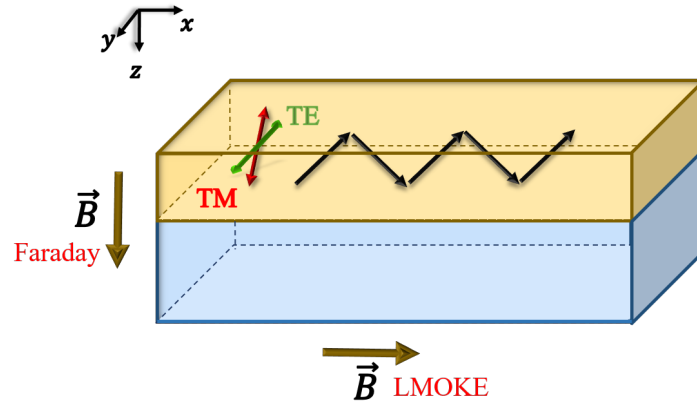


FIGURE III.10: Schematic illustration of TE and TM guided-modes and the magnetic field orientations for Faraday and LMOKE configurations, in case of GMR structures.

The calculated TMOKE is defined here as the relative difference of the transmittance (reflectance) upon magnetization M reversal:

$$\delta(T) = 100 \times \frac{T(+M) - T(-M)}{(T(+M) + T(-M))/2} \quad (\text{III.1})$$

Fig.III.11b illustrates the numerical simulations of the transmittance and the TMOKE signal of the PR-MO structure, for TM polarization and for different AOI going from 0.5° to 8° . The structure parameters and the magnetic field orientation are illustrated on Fig.III.11a.

As seen in Fig.III.11b, the TMOKE increases with the AOI and reaches a maximum value equal to 15% at $\lambda = 1650$ nm for AOI= 8° . Although, around $\lambda = 1650$ nm the real part of the MO term ($\text{Re}(\epsilon_{xz})$) is weak compared to smaller wavelength (Fig.III.11c, black curve). Hence, we can say that the imaginary part of ϵ_{xz} plays a role in the TMOKE signal since $\text{Im}(\epsilon_{xz})$ increases in this wavelength region (Fig.III.11d, black curve).

Therefore, the TMOKE response resulting only from the $\text{Re}(\epsilon_{xz})$ is described by a change in the propagation constant upon magnetization reversal (as explained in Eq.I.43), resulting in a shift in the resonance wavelength of the transmittance peak, giving a TMOKE signal with symmetric shape (Fig.III.11c).

However, the TMOKE signal resulting only from $\text{Im}(\epsilon_{xz})$ is described by a change in the absorption coefficient of the magnetic film upon magnetization reversal, resulting in a variation in the transmittance peak amplitude, giving a TMOKE signal with one peak (see Fig.III.11d).

As seen in Fig.III.11c-d, by increasing the AOI the TMOKE signal resulting only from $\text{Re}(\epsilon_{xz})$ decreases, however the TMOKE signal resulting only from $\text{Im}(\epsilon_{xz})$ increases. This behavior is related to the dispersion of the real and imaginary part of ϵ_{xz} (black curves).

As a result, the TMOKE signal is the sum of the two effects resulting from $\text{Im}(\epsilon_{xz})$ (Fig.III.11b) and $\text{Re}(\epsilon_{xz})$ (Fig.III.11a). For this reason, by increasing the AOI, the TMOKE signal increases and loses its symmetric shape as seen in Fig.III.11b.

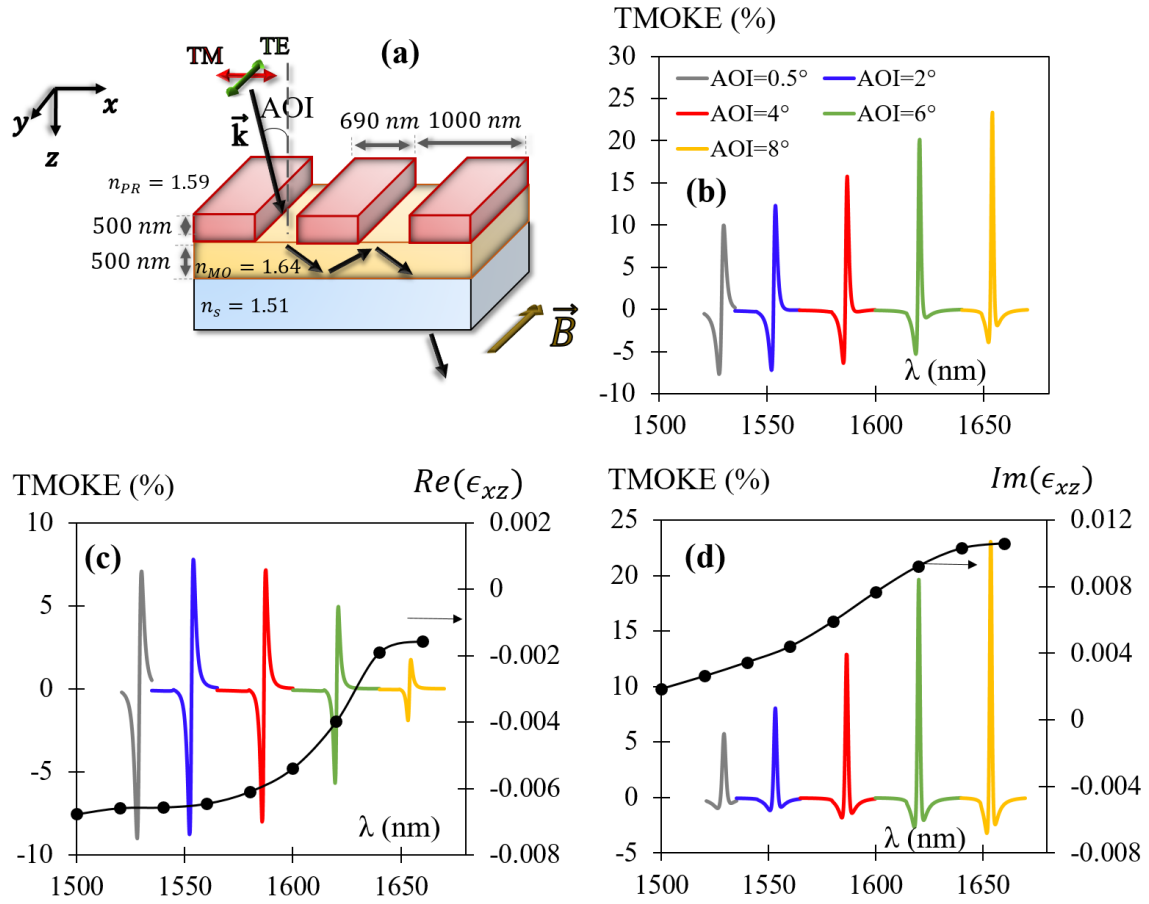


FIGURE III.11: (a) PR-MO structure under study with the corresponding opto-geometric parameters and magnetic field configuration. Calculated TMOKE in transmission for TM polarization and different AOI in case of: (b) $Re(\epsilon_{xz})$ and $Im(\epsilon_{xz})$ are different from zero, (c) $Im(\epsilon_{xz}) = 0$, (d) $Re(\epsilon_{xz}) = 0$. The black curves correspond to the (c) real and (d) imaginary parts of the MO term ϵ_{xz} at saturation for $\phi = 26\%$.

The effects of the MO waveguide thickness and refractive index on the TMOKE signal were studied in section I.1.2.4 for a simple guided-layer without grating (in other words without resonance). We observed that the TMOKE is optimized for a certain n_{MO} and t_{MO} (see Fig. I.14). Hence, in order to study the same effect in the resonant structures, Fig. III.12a-b illustrates the calculated transmittance and TMOKE in transmission spectra with different MO thicknesses (380 nm, 500 nm, 750 nm and 1000 nm), for TM polarization and at AOI=2°. The other structure parameters are the same than Fig. III.11a. The simulations were done with a constant value of ϵ_{xz} equal to $-0.0064+i0.0044$ (corresponding to $\phi = 26\%$), to study only the effect of the thickness and avoid any TMOKE variation due to the ϵ_{xz} dispersion.

One can see on Fig. III.12a, that by increasing the thickness, the FWHM of the transmittance resonance increases while its amplitude decreases. This behavior was observed also on Fig. III.2c and it was explained by the increase of the absorption due to the guided-mode confinement in the MO film, when the thickness of this latter is higher. As a confirmation, the calculated TMOKE (observed on Fig. III.12b) is maximum when the FWHM is minimum and

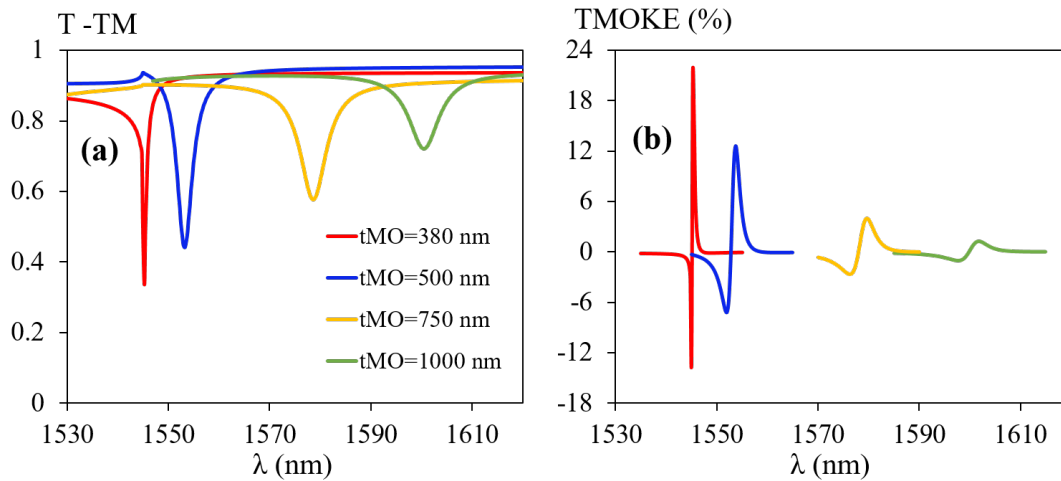


FIGURE III.12: Calculated (b) transmittance and (c) TMOKE in transmission spectra for different MO film's thicknesses, for TM polarization and at AOI=2°. The structure parameters are the same than Fig.III.11a. ϵ_{xz} was fixed to a value of -0.0064+i0.0044.

the resonance amplitude is maximum, in other words close to the cut-off thickness ($t_{MO} = 380$ nm). Hence, TMOKE values up to 22% was achieved with a transmittance of 33%.

Moreover, the transmittance and the TMOKE in transmission were also studied for different MO thicknesses (250 nm and 500 nm), but with higher MO refractive index $n_{MO} = 1.74$. The results are plotted on Fig.III.13. As seen in this latter, the TMOKE value for $n_{MO} = 1.74$ and $t_{MO} = 500$ nm (blue curve) is weaker than for $n_{MO} = 1.64$ and $t_{MO} = 500$ nm (blue curve, Fig.III.12b). This TMOKE decrement is linked to the fact that by increasing the MO index with a constant MO film, the light is more confined in the absorbing MO waveguide increasing hence the width of the transmittance resonance. However, if we optimize the MO film thickness for $n_{MO} = 1.74$, in other words work at the cut-off value (red curve, Fig.III.13), a significant TMOKE value ($\delta = 37\%$) can be achieved with $T=20\%$. This TMOKE value is higher than what was reached before ($\delta = 22\%$) for $n_{MO} = 1.64$ and $t_{MO} = 380$ nm. This behavior is linked to the resonance amplitude which is higher for higher index contrast between the MO waveguide and grating, and lower MO thickness (see red curve on Fig.III.12a and green curve on Fig.III.13).

As a summary of this part dedicated to numerical simulations, one can notice that the grating geometrical parameters were varied in order to achieve the phase matching condition at normal incidence and reach the highest FR value. Rotation values up to -0.7° and $+0.4^\circ$ were achieved, with the following grating parameters: $h_{PR} = 500$ nm and $f = 0.69$. Due to fabrication limits, these parameters are very difficult to achieve. However, as mentioned in section II.4.1.2, grating with: $h_{PR} = 300$ nm and $f = 0.4$ can be fabricated. These parameters are the closest to the simulations. Hence, the phase matching cannot be reached and the FR will decrease to a value around -0.1° and $+0.35^\circ$ (see Fig.III.6b). Nevertheless, due to the high resolution (0.001°) of the MO homemade setup, these FR values will be measured.

In addition to that, the LMOKE was studied numerically for different AOI and a rotation up to -1.7° was achieved in transmission. We mentioned that, for oblique incidence the phase

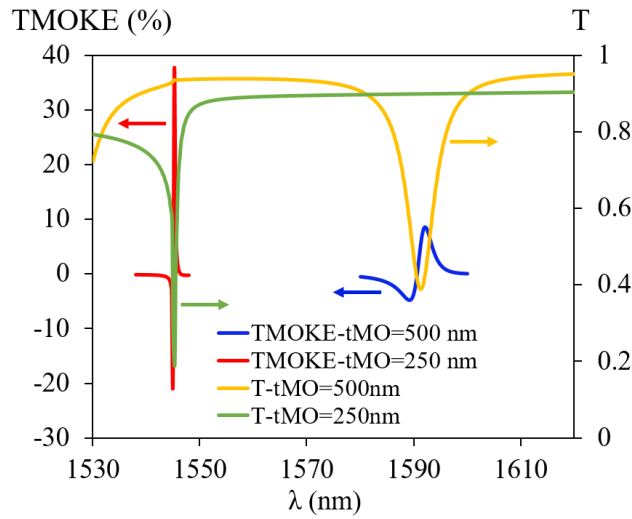


FIGURE III.13: Calculated transmittance and TMOKE in transmission spectra for two different MO film thicknesses with MO refractive index equal to 1.74, for TM polarization and at AOI=2°. The other structure opto-geometrical parameters are the same than Fig.III.11a. ϵ_{xz} was fixed to a value of $-0.0064+i0.0044$.

matching condition was lost which will be close to the case of the fabricated structure.

Finally, the TMOKE was numerically studied and we concluded that it increases with the AOI. And, for a high TMOKE value the thickness should be close to the cut-off value and the refractive index contrast between the PR grating and the MO film should be high. However, as demonstrated in Chap.II, the highest measured n_{MO} can reach a value around 1.64 at $\lambda = 1550$ nm for NPs concentration of 26%. If we want a higher index ϕ should be higher. However, by increasing the concentration more than 26%, there is a risk of having NPs aggregation in the MO-sol resulting in a bad quality of MO thin film (cracks, optical diffusion, etc.). Another way to increase the MO film index is by working with a precursor owing higher refractive index than the TEOS, for example Titanium dioxide TiO_2 . This latter has an index of 2.2 in the near IR region but it needs film annealing at a high temperature (500°C). The increase of the refractive index of the MO composite is therefore feasible but requires a complete study which is not part of the objectives of this thesis.

In the rest of this chapter, the different MO effects will be studied through the presentation of the experimental measurements carried out on the fabricated PR-MO structure. Backward-simulations will be done to insure the agreement between the calculations and the measurements. In order to demonstrate experimentally the enhancement of the MO effects through the fabricated structures, MO setups dedicated to resonant structures were developed in the presented work. They will be detailed in the next section.

III.2 Description of Magneto-Optical Setups for Resonant Structures

Two different MO setups were developed for MO characterization of resonant structures. The first one is for polarization rotation measurements (especially Faraday and LMOKE in

transmission) and the second one is for intensity modulation measurements (especially for TMOKE).

III.2.1 Polarization Rotation Measurements Setup

In section II.3.2.1, the traditional Faraday setup was explained in details. This MO setup can be used to measure FR of thin films or ferrofluid with high sensitivity (0.001°). However, for the resonant structures whose produce a resonant MO effect of FWHM less than 5 nm, the combination of Xenon Arc source and monochromator will limit the MO measurements since its FWHM is larger (12 nm for the minimum width of the input and output slits of the monochromator). Fig. III.14 illustrates an example of the FR spectra for a resonant structure, measured with an Xenon Arc (red curve) or a laser (blue curve) as light sources. The green curve illustrates the transmittance of the resonant structure. It is clear that higher MO

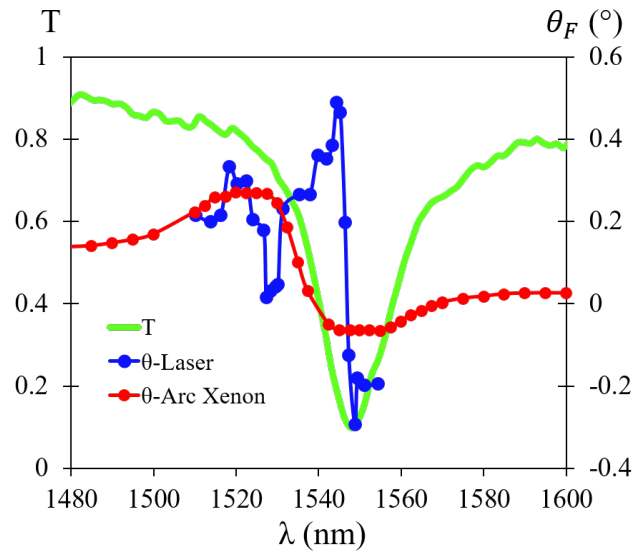


FIGURE III.14: Example of measurements spectra of the transmittance (green curve), and the FR measured through a laser (blue curve) and an Xenon Arc lamp (red curve), for a GMR structure.

resonance was measured through the laser than the combination of Xenon Arc source and monochromator. This behavior is related first to the large FWHM of the combination of Xenon Arc source and monochromator compared to that of the MO resonance, second to the weak signal intensity resulting from the transmittance dip which limit the measurements precision. However, the laser signal intensity is much higher than that of the lamp and its FWHM is less than that of the MO resonance.

Therefore, a special MO setup for resonant structures has been developed. The main elements and the measurements methods of the traditional MO setup are conserved except the lamp that was replaced by a tunable laser DL pro TOPTICA photonics [1490 nm-1630 nm]. Therefore, the monochromator, the optical fiber, the diaphragm and the spherical mirrors are no longer needed (see Fig. III.15). The wavelength of the laser can be tuned manually and analyzed through an Optical Spectrum Analyzer (OSA-HP 70950B).

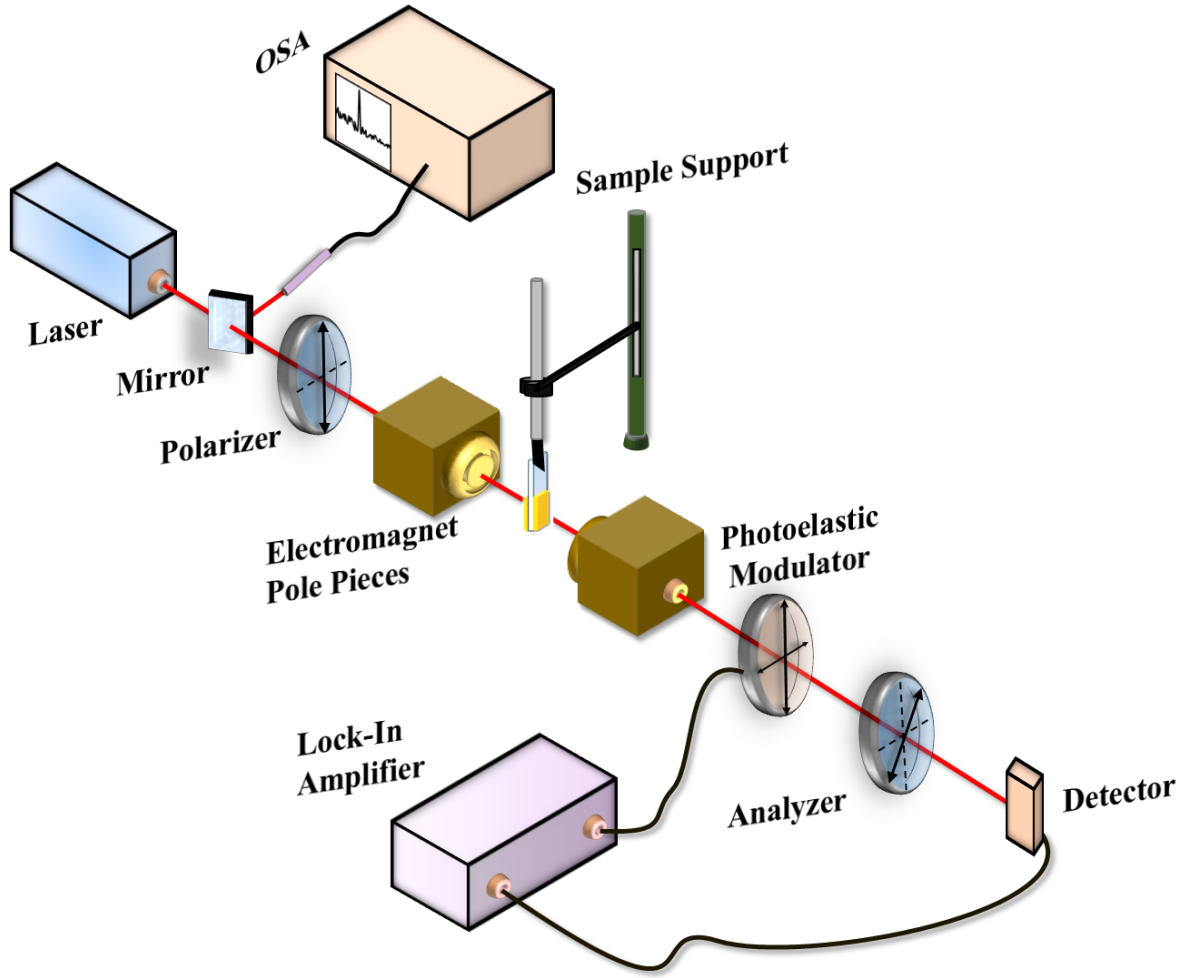


FIGURE III.15: Representation of the essential elements of the MO polarization rotation homemade setup, dedicated to resonant structures.

The LMOKE setup is similar to the new Faraday setup but with a longitudinal configuration of the magnetic field (parallel to the sample and incident planes). Here, due to the geometry of the electromagnet, the amplitude of the magnetic field can be varied only in the range of $[-400 \text{ mT}; +400 \text{ mT}]$. The structure is fixed between the pole pieces of the electromagnet by a vacuum sample holder, mounted on a motorized rotating (PRMTZ8/M THORLABS) support with five axes. Hence, a precise AOI is insured with the possibility to do a wide sweep (longitudinal and vertical) on the structure surface, to optimize the position of the incident light on the grating. The normal incidence is adjusted as follows:

- Superimposing the reflected and the incident light via an IR camera.
- Superimposing the two transmittance resonances resulting from orders $m = \pm 1$ at oblique incidence through a spectrometer.
- Disappearance of the LMOKE polarization rotation since this latter is zero at normal incidence.

The transmittance of the resonant structure was measured through a NIRQuest spectrometer, using a Laser-Driven Light Source (LDLSTM).

III.2.2 TMOKE Measurements Setup

The TMOKE measurements setup is based on the intensity measurements of the transmitted or reflected light of the structure under study. This can be done by a photodetector or by a spectrometer. Hence, no LIA is needed here as for the polarization rotation measurements setup, in other words the photoelastic modulator and the analyzer are not necessary for the TMOKE setup.

Therefore, the TMOKE setup consists of the tunable laser [1490 nm; 1630 nm] followed by the motorized polarizer and the rotating sample's support placed in the air gap of an electromagnet generating a magnetic field oriented perpendicularly to the incident plane. Here, the amplitude of the magnetic field can be varied in the range of [-900 mT; +900 mT] through a HUBERT 1110-16-QE 4 quadrant linear amplifier. The reflected or transmitted light through the sample is then analyzed by a photodetector or an Ibsen spectrometer with 0.25 nm of resolution and a spectral range of [1500 nm; 1600 nm]. The reflected light is directed towards the photodetector by a mirror placed before the sample. Two measurements methods were implemented in this MO setup to obtain the TMOKE signal:

- The first one consists of varying continuously the magnetic field for a fixed wavelength, and the intensity of the light is measured as a function of the magnetic field by the photodetector. As a result, an intensity hysteresis loop (see Fig. III.16) is obtained for each wavelength, and the relative change of the saturated intensity values (using Eq. I.50) is then plotted as a function of the wavelength.
- The second method consists of giving to the magnetic field its saturated values (-900 mT and +900 mT). Using a broader spectral source, the transmitted intensity spectra is measured through the Ibsen spectrometer at these values, and the TMOKE spectra is then extracted from Eq. I.50.

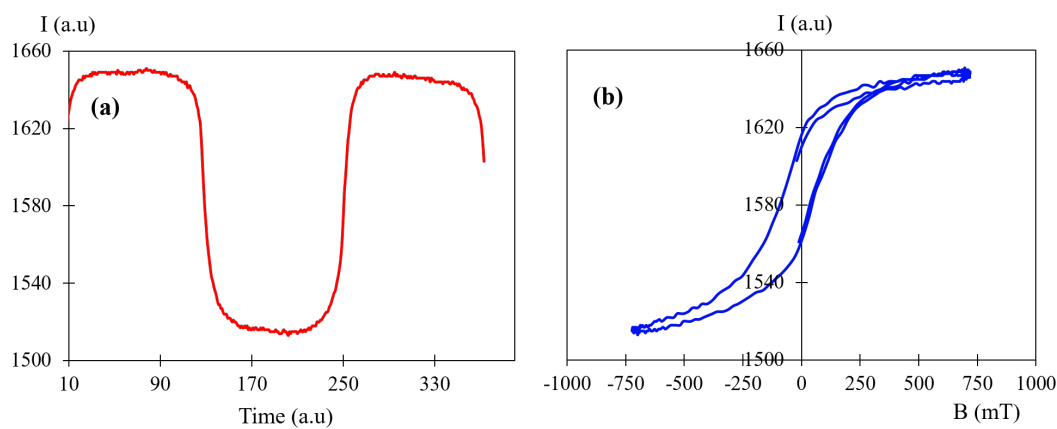


FIGURE III.16: (a) Example of measurements of the intensity as a function of the time under sinus variation of an applied magnetic field. (b) Intensity hysteresis loop.

An important feature of the used light source is that at low lasing intensity, its spectrum presents a large FWHM (see Fig. III.17) and it behaves as an Amplified Spontaneous Emission (ASE) source. Therefore, the second TMOKE measurements method was done with low lasing intensity in order to measure the transmitted intensity spectrum of the structure. However, the first method was done with high intensity where the laser spectrum presents one peak with FWHM less than 0.5 nm.

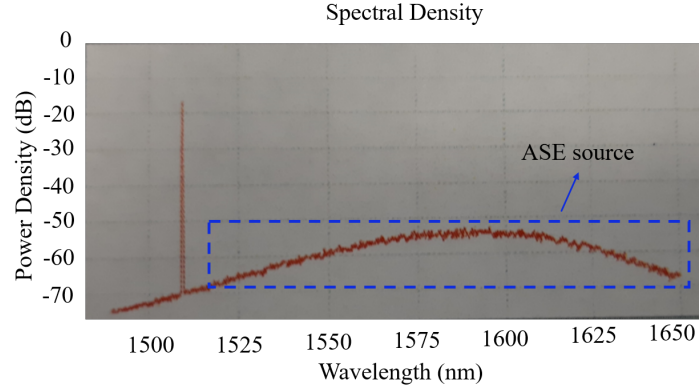


FIGURE III.17: Laser spectral density.

The normal incidence was adjusted by the superposition of the incident and reflected light through an IR camera. The oblique AOI was defined manually and measured on a graduated sample support. An uncertainty of 0.3° can affect the AOI value.

After describing the main elements and the measurements methods of the different MO setups, the experimental measurements of MO enhancement of the all-dielectric GMR structures will be presented in the next section.

III.3 Enhancement of Polarization Rotation Effects

With the same fabrication parameters of PR 3 (see Tab. II.2), different PR gratings were structured on top of MO composite films. The grating parameters are: $h_{PR} = 300$ nm and $f = 0.4$. The grating was not dug to the bottom and presents a thin layer of PR ($t_{PR} = 130$ nm, see Fig. III.18a). The MO film refractive index and thickness are respectively: $n_{MO} = 1.64$ and $t_{MO} = 460$ nm corresponding to $\phi = 26\%$. n_{MO} was chosen to have the highest possible index contrast from PR ($n_{PR} = 1.59$). t_{MO} was chosen to be close to the cut-off value.

The optical response of this structure is plotted in Fig. III.18b as a function of the wavelength, for TE (y direction) and TM (x direction) incident light at normal incidence. One can see dips in transmittance revealing the guided-mode resonance for both polarizations. The TE-TM resonance wavelengths shift ($\Delta\lambda$) is 10 nm, hence the optimized condition where the two resonances should overlap is not satisfied. This shift was expected, since we mentioned before that the gratings parameters are not the optimized ones.

III.3.1 Enhancement of Faraday Effect

III.3.1.1 Photoresist Grating

A magnetic field perpendicular to the MO film plane (z direction according to Fig. III.18a) is applied to the structure during the measurements. The FR was measured for the wavelength range [1500-1560 nm] with the Faraday setup described in previous section and the results are plotted in Fig. III.18c. The yellow curve illustrates the FR for a single MO film. One can

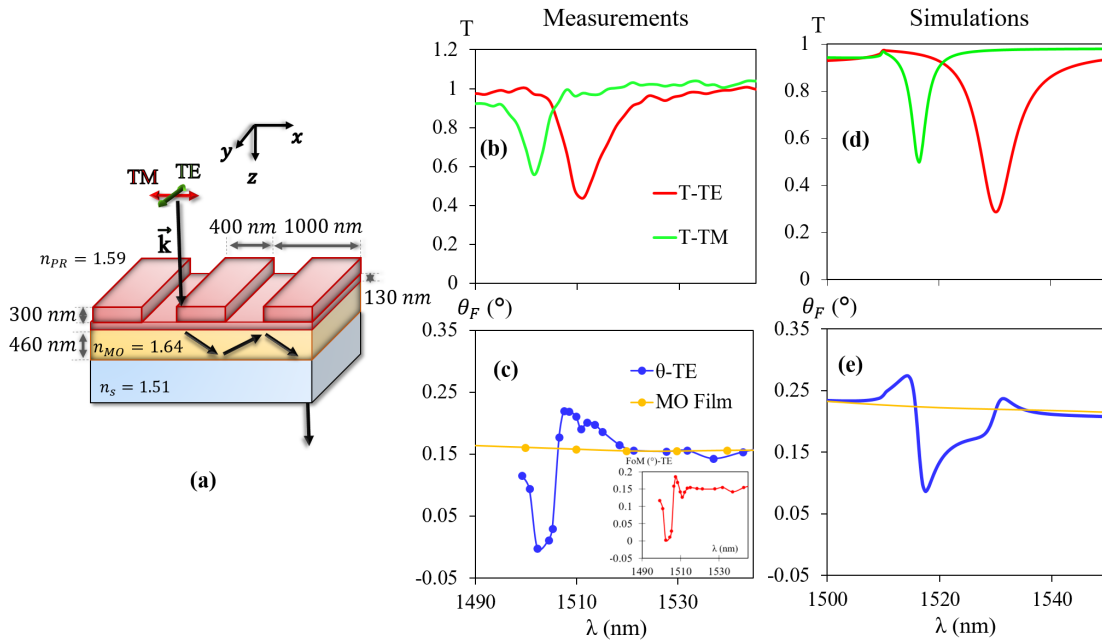


FIGURE III.18: (a) Schematic illustration of the fabricated structure with its opto-geometrical parameters. The left-hand column displays (b) the transmittance measurements for TE and TM polarizations at normal incidence, (c) the FR measurements for TE. Inset (c): measured figure of merit spectrum for TE polarization. (d),(e) display the numerical simulations. The yellow curves illustrate the FR for a single layer of MO composite.

see two opposite MO resonances related to the transmission resonances for both polarizations TE and TM. The measured FR reaches 0.22° as a highest value at $\lambda = 1507.5$ nm with $T=70\%$, which gives an enhancement by a factor of 1.4 compared to the reference film and a FoM value around 0.18° (see inset Fig. III.18c). This small reached FR value is in the same order of that obtained by Lei et al. [Lei+16], who numerically demonstrated a maximum value of 0.35° with a more complex structure and with a MO material owing off-diagonal elements in one order of magnitude higher than the MO composite ($\epsilon_{xy} = -0.0064 + i0.0044$). The structure is a tri-layer structure consisting of a metallic film, periodically perforated with rectangular annular arrays, which is deposited on thin nonmagnetic and magnetic dielectric films. Caballero et al. [CGMC15] have demonstrated values less than 0.25° through a 2D-MP structure (see Fig. I.31).

Furthermore, a good agreement can be observed between the numerical simulations (Figure III.18d-e) and the measurements (Fig. III.18b-c). The small difference is related to the thickness measurements uncertainty or to the imperfections of the fabricated structure.

The measured TE-TM resonance shift (10 nm) is smaller than the simulated one (14 nm), which can be related to stress induced anisotropy in the thin film that cannot be properly simulated. This slight difference explains the difference in the FR curve shape between the simulations and the measurements.

Under Magnetic Field Samples The fabricated structure is not the optimized one, in other words the phase matching condition at normal incidence was not achieved. Therefore, in order to control the phase shift $\Delta\beta$ and try to achieve higher FR values, different PR structures with MO waveguides deposited under magnetic field \vec{B}_{gel} with different orientations, were fabricated and presented in Tab.II.3.

Fig.III.19 depicts the transmittance measurements for TE and TM-polarized incident light at normal incidence, for the four types of PR-MO structures. As seen in this figure, the wavelength shift between TE and TM resonances is not the same for the different structures: the smallest shift (6 nm, see Fig.III.19b) is for the out of-plane gelation field sample and the largest one (14 nm, see Fig.III.19d) is for the sample of in-plane field with grooves parallel to this latter.

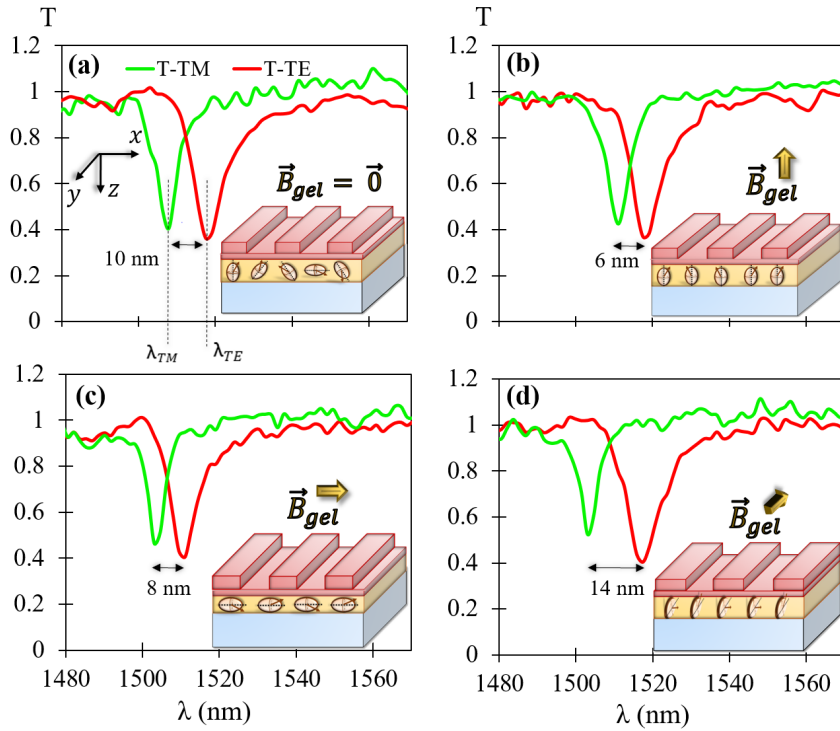


FIGURE III.19: Transmittance measurements at normal incidence, for TE and TM-polarized incident light as a function of the wavelength, for the different types of PR-MO structures (described in Tab.II.3) with schematic geometries illustrated in inset.

As explained in section I.1.2.1, inside the MO waveguide the electric field of the TE mode is along y direction, while that of the TM mode has a component following z direction and a small one following x direction. Therefore, the behavior of $\Delta\lambda$ for the different gelation magnetic field orientations is explained as follows:

- $\vec{B}_{gel} = \vec{0}$ (Fig.III.19a): in this case, there is not a created anisotropy but there is an intrinsic property of the planar dielectric waveguide, where the effective indices of TE and TM modes are not equal and a difference in resonance wavelengths ($\Delta\lambda=10$ nm) is obtained.
- Out of-plane \vec{B}_{gel} (Fig.III.19b): the NPs optical anisotropy axis is oriented along z direction which increases the refractive index in this direction (n_z) and decreases n_x and n_y as compared to the first case ($\vec{B}_{gel} = \vec{0}$). Therefore, the refractive index related to the small component of TM mode following x direction is decreased, while that of the component following z direction is increased giving a rise of the resonance wavelength of TM (λ_{TM}) according to Eq.(I.46), as compared to the first type of structure (Fig.III.19a). However, the resonance wavelength of TE (λ_{TE}) is decreased due to the decreasing of n_y . This behavior explains the decreasing of $\Delta\lambda$ to a value of 6 nm as compared to that of zero field sample.
- Grating grooves perpendicular to the in-plane \vec{B}_{gel} (Fig.III.19c): the refractive index related to the small TM component is increased while that of the component following z direction and the refractive index of TE mode are decreased according to the case without applied \vec{B}_{gel} , which explains the slight decreasing of $\Delta\lambda$ to 8 nm.
- Grating grooves parallel to the in-plane \vec{B}_{gel} (Fig.III.19d): n_{TE} is increased and n_{TM} is decreased explaining the increasing of $\Delta\lambda$ to 14 nm as compared to the zero gelation field sample (Fig.III.19a).

Hence, an important feature of the magnetic field assisted deposition process is that the TE-TM phase shift can be controlled by the NPs orientation in the MO film.

The experimental measurements of the FR for TE polarization and the transmittance for TE and TM polarizations as a function of the wavelength are plotted in Fig.III.20, for the different PR-MO structures.

As seen in this figure and due to a decreasing of $\Delta\beta$, the Faraday resonance is higher for structures with out of-plane gelation field (Fig.III.20b) and in-plane field with grooves perpendicular to this latter (Fig.III.20c), compared to the other cases. As a result, the FR is varied but only by a value of 0.1° .

Fig.III.21 illustrates the calculated FR spectra for two cases: (a) $\Delta\lambda = 10$ nm as zero field sample and (b) $\Delta\lambda = 6$ nm as out of-plane field sample. As seen in this figure, the FR is increased only by a value of 0.2° for the case of $\Delta\lambda = 6$ nm compared to zero field sample, which is not so far from the experimental demonstration (Fig.III.20a-b).

We have to remember that the four samples are not perfectly the same, small differences in grating height and MO thickness can exist resulting in differences in coupling efficiency and resonance wavelength shift. These differences make difficult to compare well the MO effects between the four samples especially that the MO change is not very remarkable. Hence, in the rest of this chapter the zero gelation field sample will be the most studied structure for the MO effects enhancements.

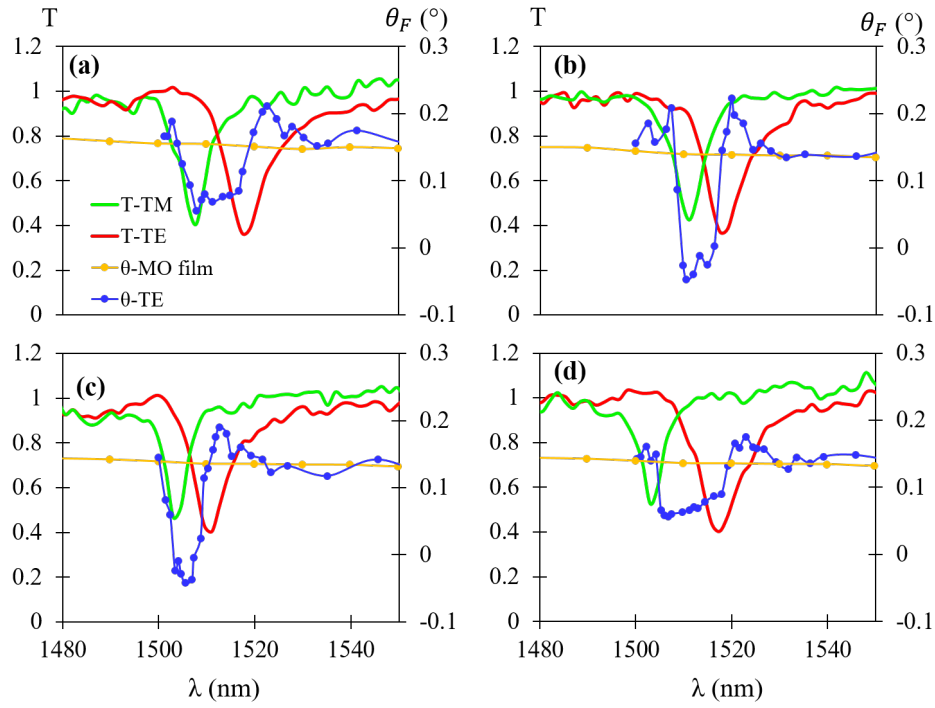


FIGURE III.20: Measurements of the transmittance for TE and TM polarizations and FR spectra for TE polarization, for the different types of PR-MO structures (described in Tab.II.3 with schematic geometries illustrated in inset Fig.III.19). The yellow curves correspond to the FR of the MO thin film.

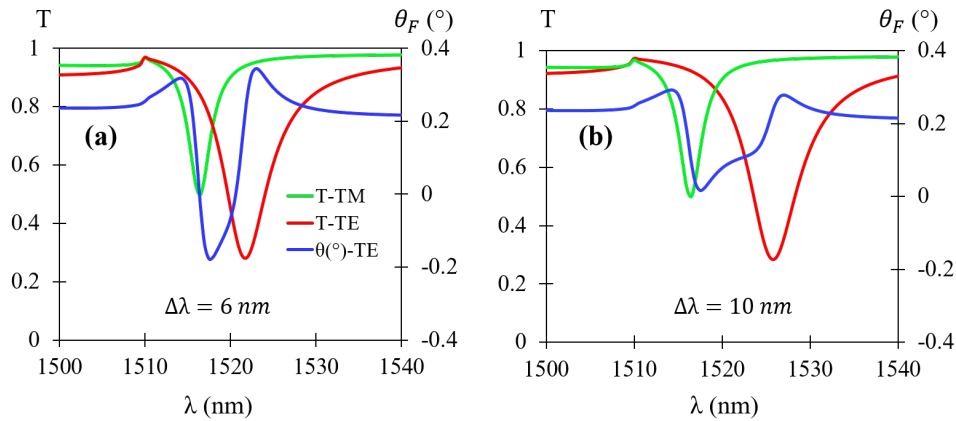


FIGURE III.21: Calculated transmittance spectrum for TE and TM modes, and FR spectrum for TE mode in case of: (a) $\Delta\lambda = 6$ nm and (b) $\Delta\lambda = 10$ nm.

In this section, an enhancement of the Faraday effect was demonstrated experimentally and numerically through the all-dielectric structure based on PR grating. In addition to that, a permanent optical linear anisotropy was created in the MO films coated under magnetic field, allowing the control of the TE-TM phase shift.

As mentioned before, another all-dielectric structure was studied in this work and it is based on a Si_3N_4 grating. The numerical and experimental evidence of the Faraday effect enhancement through this structure will be presented in the next section.

III.3.1.2 Comparison with Silicon Nitride Grating

The structure under study consists of alternating Si_3N_4 and MO composite grating on top of a BK7 substrate (see Fig. III.22a). The refractive indices of BK7 and Si_3N_4 were measured by ellipsometry and they are equal to 1.50 and 1.97 respectively, in the [1480 - 1630 nm] wavelength range.

Fig. III.22b-c illustrates a simulated 2D scan of the transmittance of the resonant structure with parameters described in Fig. III.22a, as a function of the wavelength and the MO composite refractive index, for TE and TM polarizations. The black and white lines corresponds to TM and TE dispersion curves, respectively. As seen in this figure, the resonance wavelengths of TE and TM modes evolves with the MO refractive index and the phase matching is reached for $n_{MO} = 1.49$ at $\lambda = 1552$ nm.

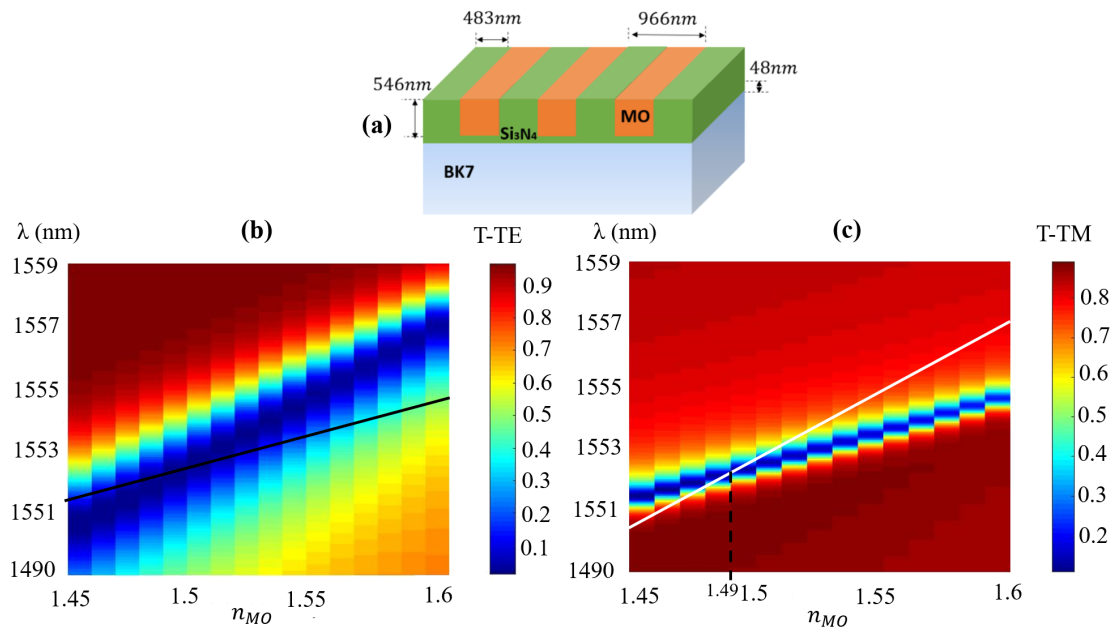


FIGURE III.22: (a) Schematic illustration of the fabricated structure with its geometrical parameters. Simulated 2D diagrams of the transmittance at normal incidence for (b) TE and (c) TM polarizations, as a function of the MO composite refractive index and the wavelength. The black and white lines describe the TM and TE dispersion curves, respectively.

Thus, the Si_3N_4 grating template has been impregnated with a MO composite which NPs volume fraction should be $\phi = 8\%$. This volume fraction corresponds to the optimal refractive index of 1.49 around 1550 nm.

The measured transmittance spectra of TE and TM polarizations at normal incidence are illustrated on Fig.III.23a for the fabricated Si_3N_4 -MO structure. As seen in this figure, the phase matching condition is almost achieved ($\Delta\lambda = 5$ nm). This small TE-TM spectral shift can be linked to the fabrication imperfections where the refractive index of the MO composite is 1.47 instead of the optimal refractive index (1.49).

One can notice on Fig.III.23a, a small dip beside the large one, and this can be linked also to the imperfections of the fabricated structure.

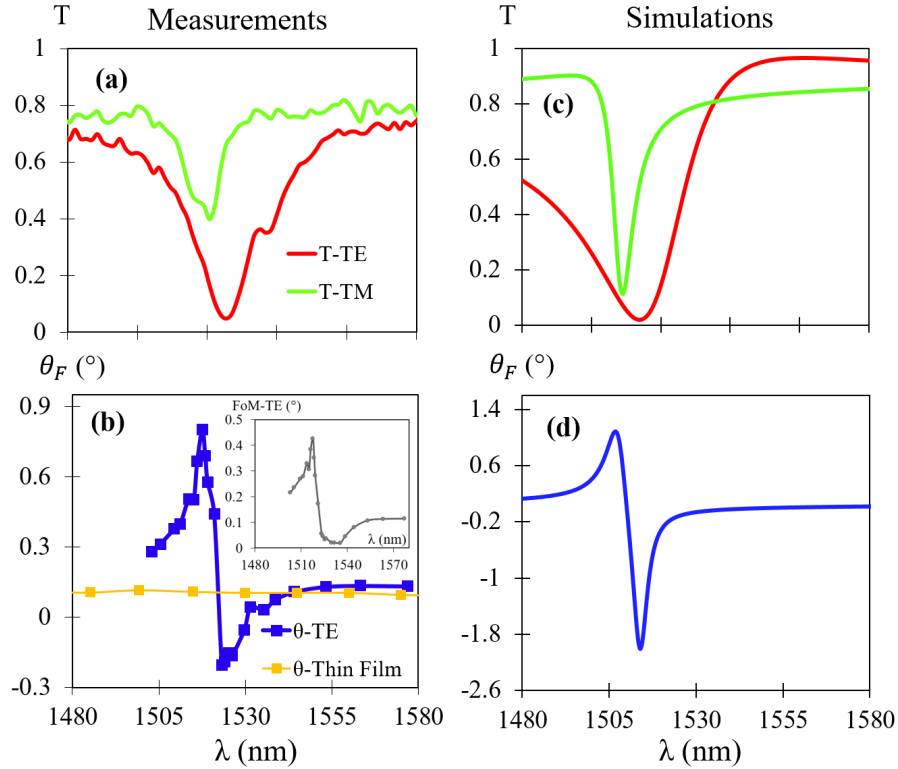


FIGURE III.23: Measured (a) transmittance spectra for TE and TM polarizations at normal incidence and (b) FR spectrum for TE polarization, for the Si_3N_4 -MO structure. The yellow curve corresponds to a continuous film of MO composite. Inset (b): Measured figure of merit for TE polarization. Calculated (c) transmittance and (d) FR spectra.

Transmittance dips with amplitude around 70% and 40% for TE and TM polarizations respectively, were measured. These dips (especially for TE) are higher in amplitude than those demonstrated with the PR grating (amplitude around 60%), since the effective index of this latter (1.34 at $\lambda = 1550$ nm) is less than the Si_3N_4 -MO grating (1.80).

Highest value of 0.8° for the FR was achieved at $\lambda = 1518$ nm with $T=29\%$ as seen in Fig.III.23b, giving a value of FoM equal to 0.43° (see inset Fig.III.23b). Due to the small TE-TM shift, this FR value is higher than that demonstrated in the previous work (0.45°) [Var17], taking into account that the concentration of NPs here ($\phi = 5\%$ for $n_{MO} = 1.47$) is one third compared to the previous work ($\phi = 15\%$). The FR for a continuous MO composite film is 0.1° as seen on the yellow curve of Fig.III.23b, hence an enhancement by a factor of 8 was achieved for the FR, with the fabricated all-dielectric structure.

Comparing the measurements with the numerical simulations illustrated on Fig.III.23c-d, a difference in the rotation spectrum is obvious. One can notice that for the measured spectrum (Fig.III.23b), the first FR peak (the positive one corresponding to TM transmittance dip) is more important than the second FR peak (the negative one corresponding to TE transmittance dip), contrary to the FR simulated spectrum (Fig.III.23d).

The measured FR value through the Si_3N_4 -MO structure are higher by a factor of 4 compared to that measured through the PR-MO structure ($\theta_F = 0.22^\circ$). This difference is obviously linked: first to the transmittance resonance amplitude which is higher for Si_3N_4 -MO structure, second to the small TE-TM phase shift ($\Delta\lambda = 5$ nm). However, the fabrication process of the Si_3N_4 gratings is more complicated and expensive than the simple fabrication of the PR grating, limiting their industrial applications.

The measured FoM values demonstrated through Si_3N_4 -MO and PR-MO structures are compared through Fig.III.24 to others selected in the literature. As seen in this figure, the achieved values (red dots) are higher than that obtained by Caballero et al. [CGMC15] and Lei et al. [Lei+16] who numerically demonstrated respectively values of 0.04° and 0.23° with more complex MP structures. In addition to that, they are in the same order of magnitude than that

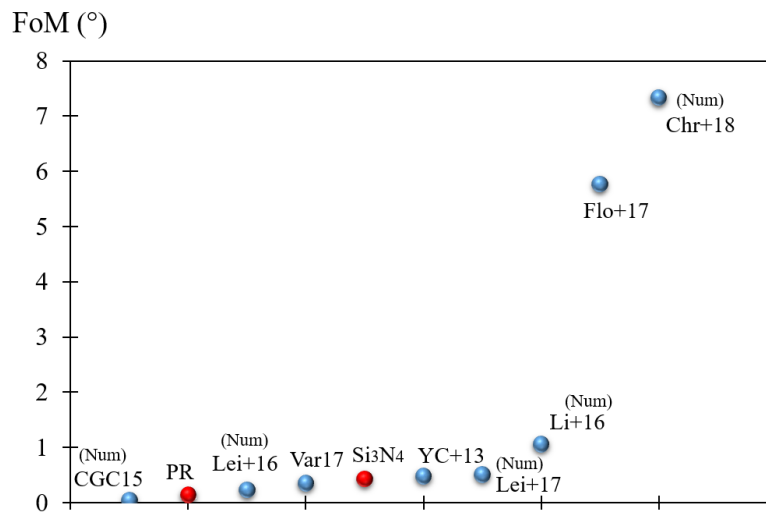


FIGURE III.24: Comparison spectrum of the FoM in Faraday configuration between this work (red dots: PR and Si_3N_4 structures) and the different works done in the literature. Num relates to numerical simulation works.

demonstrated experimentally by Chin et al. [YC+13], where a value of 0.48° was achieved through a gold grating deposited on BIG film. Floess et al. [Flo+17] have experimentally demonstrated, values of 5.77° and 2.26° for TE and TM polarized incident light respectively, with 1D MP structure made by gold nanowires embedded in EuS film (see Fig.I.35). However, the measurements were done at very low temperature of 20K. Finally, Christophi et al. [Chr+18] demonstrated theoretically FoM value up to 7.34° with a structure made by BIG nanodisk arrays embedded into a low-index matrix (see Fig.I.25). However, the fabrication difficulties of such a structure limit its practical application.

After presenting the Faraday enhancement through the two types of all-dielectric

structures, the next section is dedicated to demonstrate the LMOKE enhancement in transmission.

III.3.2 Enhancement of LMOKE in Transmission

III.3.2.1 Photoresist Grating

As demonstrated in section III.1.3.1, the PR-MO structure also allows the LMOKE enhancement at small AOI. For this reason, the LMOKE is studied in this section and in transmission due to the good transmissivity of the PR-MO structure. Hence, the magnetic field \vec{B} is applied in x direction referring to Fig. III.18 and the incident angle is varied from 0° to 5° .

The numerical simulations and experimental measurements of the transmittance for TE and TM polarizations and the polarization rotation $\theta_{LMOKE} (^\circ)$ in transmission for TE polarization are plotted in Fig. III.25, for the structure with zero gelation field ($\vec{B}_{gel} = \vec{0}$) and for different AOI. The LMOKE was also studied for the structures under magnetic field, resulting in no significant difference between them as for the FR.

One can see on Fig. III.25 dips in transmittance of amplitude 25% for TM and 40% for the TE. By increasing the AOI the resonance wavelength increases, which is consistent with the coupling Eq. I.46. The measured polarization rotations reach 0.5° and -0.85° as highest values for the different AOI. These values are very close to numerical simulations of the optimized structure presented in Fig. III.8, since the TE-TM phase shifts for oblique incidence is around 13 nm for the fabricated (Fig. III.25a-b) and optimized structure (Fig. III.5).

As a result, large enhancement of the polarization rotation for LMOKE in transmission and for small AOI was achieved through the all-dielectric GMR structure as compared to the single MO composite film (the rotation is around $\theta_{LMOKE} = 0.01^\circ$ as seen in inset Fig. III.25g).

A good agreement can be seen between the measurements (Fig. III.25a-b-c-d) and the simulations (Fig. III.25e-f-g-h).

Fig. III.25d-h illustrates the experimental measurements and the numerical simulations of the ellipticity spectra for different AOI. The measured values of the ellipticity are not the real ones, they are proportional to them, because the MO setup was not calibrated for ellipticity measurements. Nevertheless, an enhancement is achieved for the different AOI and that is confirmed by the numerical simulations, where a maximum value of 1.1° is reached for AOI = 5° . For a single MO layer the ellipticity is in order of 0.001° , hence a large enhancement is achieved also for the ellipticity with the PR resonant structure.

The decrement (increment) of the amplitude of the rotation (ellipticity) spectra as a function of the AOI is related to the dispersion of the real (imaginary) part of the off-diagonal element presented in Fig. III.11c-d, which decreases (increases) in the wavelength range of [1500-1630 nm].

Also, for TM-polarized incident light (in x direction), the same order of enhancement of polarization rotation was achieved. This can be seen on Fig. III.26, where the polarization rotation of LMOKE in transmission for TM mode are plotted for AOI = 2° as a function of the wavelength. The ellipticity also was enhanced for TM mode but not shown here.

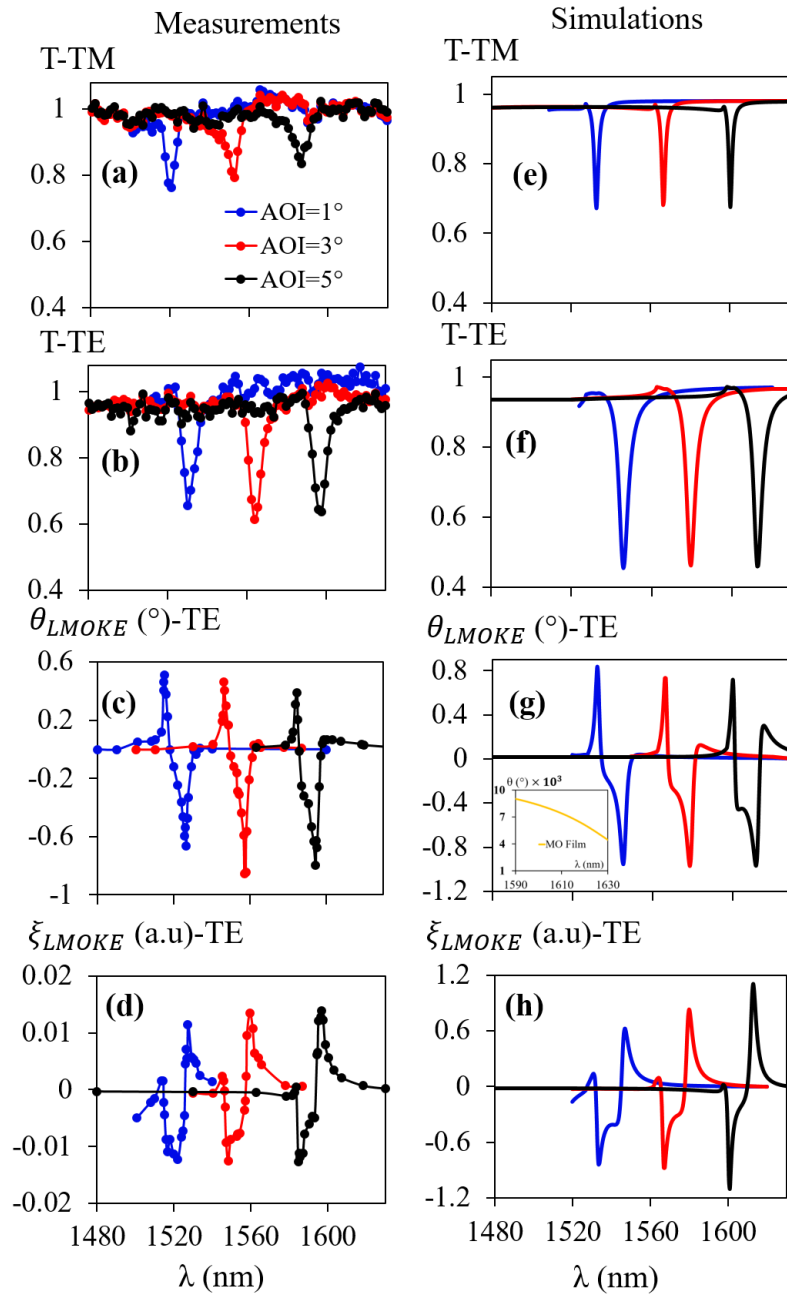


FIGURE III.25: The left-hand column displays the measured transmittance for (a) TM and (b) TE, and the measured (c) LMOKE polarization rotation and (d) ellipticity for TE polarization. The different colored spectra are for different AOI and the studied structure is without gelation field. The simulations of the fabricated structure are illustrated in the right-hand column (e),(f),(g),(h). Inset (g): calculated LMOKE rotation for a single MO film at AOI=5°.

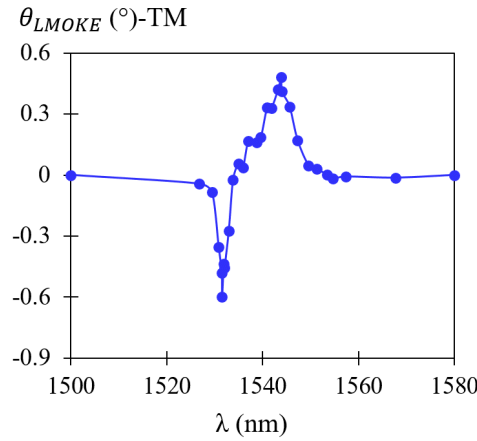


FIGURE III.26: Experimental measurements of polarization rotation of LMOKE in transmission for TM polarization and at AOI=2°.

Fig.III.27a-b illustrates examples of the hysteresis loops of the measured polarization rotation and ellipticity for the LMOKE at fixed wavelengths. As explained in section III.2.1, the magnetic field is varied from -360 mT to +360 mT and the polarization rotation and the ellipticity are measured. The saturated polarization is then plotted as a function of the wavelength giving the spectra of Fig.III.25 and Fig.III.26.

As seen in Fig.III.27, the hysteresis loops are very smooth proving the reliability of the measurements.

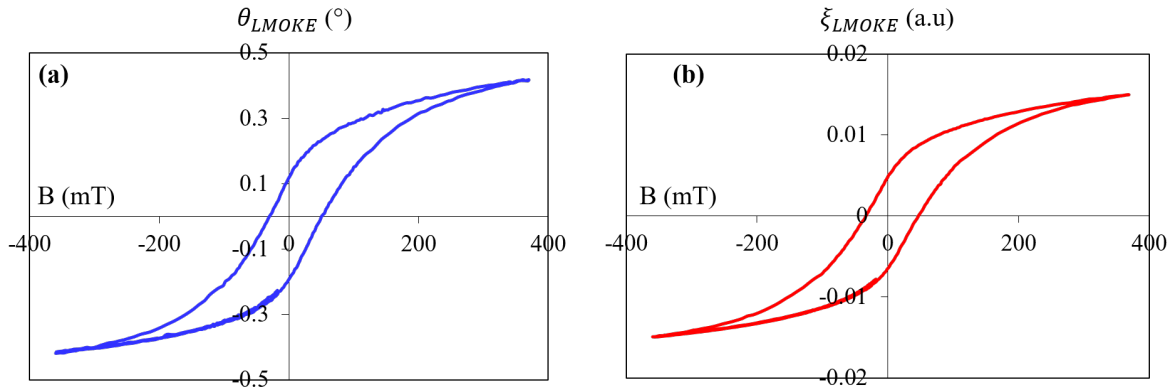


FIGURE III.27: Examples of measured hysteresis loops of (a) polarization rotation at $\lambda = 1544$ nm and (b) ellipticity at $\lambda = 1534$ nm for LMOKE in transmission.

As mentioned before, the resonance wavelengths of TE and TM modes are not overlapped for the different oblique incident angles. However, a simple way to achieve this overlap is by modifying the incident angle. Fig.III.28a depicts the measurements of T for TE and TM polarized incident light and the measurements of $\theta_{LMOKE} (^{\circ})$ for TE polarization at AOI=0.4° as a function of the wavelength. As seen in this figure, the TE and TM transmittance curves resulting from opposite diffraction order (+1st and -1st), are almost overlapped. According to Eq.I.46 it is not a phase matching: the TE and TM modes have different propagation constants.

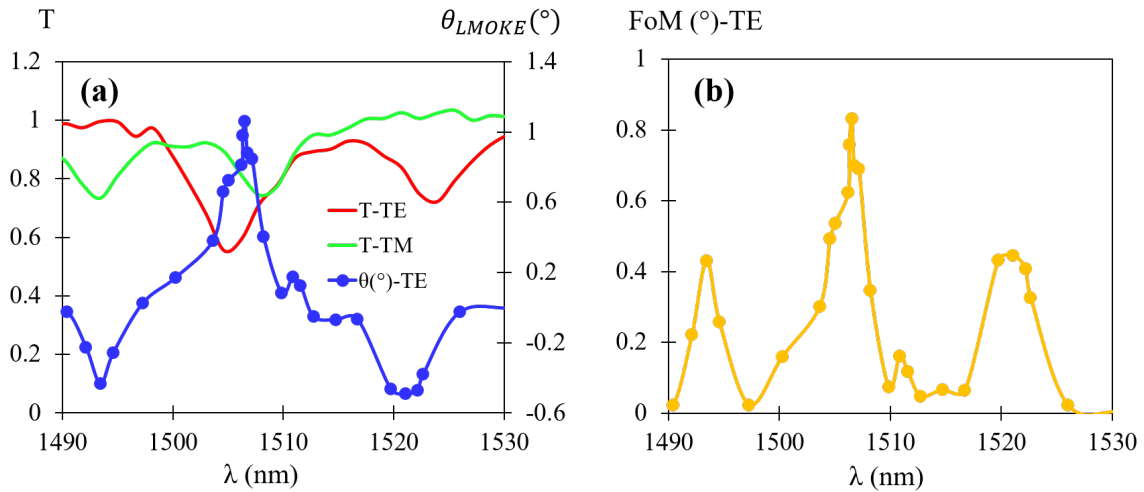


FIGURE III.28: (a) Measurements of transmittance spectra for TE and TM-polarized incident light and measurements of polarization rotation spectrum for TE polarization at AOI=0.4°. (b) Calculated values of figure of merit for the experimental measurements of (a) for TE polarization.

However, the two modes are excited simultaneously in the MO waveguide resulting in a higher rotation ($\theta_{LMOKE} = 1.1^{\circ}$ at $\lambda = 1506$ nm, with $T=60\%$) compared to the values reached with the other AOI ($\theta = 0.85^{\circ}$ presented in Fig. III.25c). As well as, two smaller rotations of -0.43° and -0.5° were detected at $\lambda = 1493$ nm and $\lambda = 1521$ nm respectively as seen in Fig. III.28a.

The calculated values of FoM for experimental measurements are plotted in Fig. III.28b for TE polarization and for AOI=0.4°. One can see three peaks in the FoM curve corresponding to the three MO resonances in Fig. III.28a. High values of FoM are reached and the more important one is 0.85° at $\lambda = 1506$ nm. This value is the same than that presented by the simulations in Fig. III.9b, for the structure satisfying the phase matching condition at normal incidence. This similarity is linked to the fact that for oblique incidence the phase matching condition is lost and for small AOI the TE-TM resonances with opposite diffraction order are very close (Fig. III.5), which is the case of Fig. III.28.

The reached FoM value is higher than that obtained by Chetvertukhin et al. [Che+12], who experimentally demonstrated a value of 0.018° for the LMOKE but in reflection. The work was done with a MP structure consisting of a 2D array of nickel nanodisks arranged into hexagonal lattice. The off-diagonal element of the tensor permittivity of the nickel is around: $Re(\epsilon_{yz}) = 0.24$ [Viš+93]. Kalish et al. [KB16], have numerically demonstrated a value of FoM equal to 2.53° for the LMOKE in transmission with a MP structure formed by a gold grating on top of a magnetic layer of rare-earth iron garnet containing bismuth. The permittivity tensor of the magnetic material, has an off-diagonal $Re(\epsilon_{yz})$ element around 0.016 [YC+13]. Hence, same order of FoM was demonstrated in the presented thesis for the LMOKE in transmission with a MO material owing a value of $Re(\epsilon_{yz}) = -0.0064$, with one and two orders of magnitude smaller compared to the literature.

The next section is dedicated to the LMOKE enhancement in Si_3N_4 -MO structure.

III.3.2.2 Comparison with Silicon Nitride Grating

The LMOKE in transmission was also studied for the Si_3N_4 -MO structure. Since the LMOKE is for oblique incidence, Si_3N_4 -MO structure with $n_{MO}=1.54$ ($\phi = 15\%$) was fabricated, in order to have an overlap of TE and TM resonances at oblique incidence rather than normal incidence. For this latter case n_{MO} is equal to 1.49 as demonstrated in Fig.III.22b-c.

Fig.III.29a illustrates the transmittance measurements for TE and TM polarizations and the LMOKE rotation in transmission for TE polarization at AOI= 0.88° . As seen in this figure, high values of rotation were demonstrated with a maximum equal to 1.5° with $T=20\%$ at $\lambda = 1535$ nm, where the two resonances (TE and TM) with opposite diffraction orders overlap.

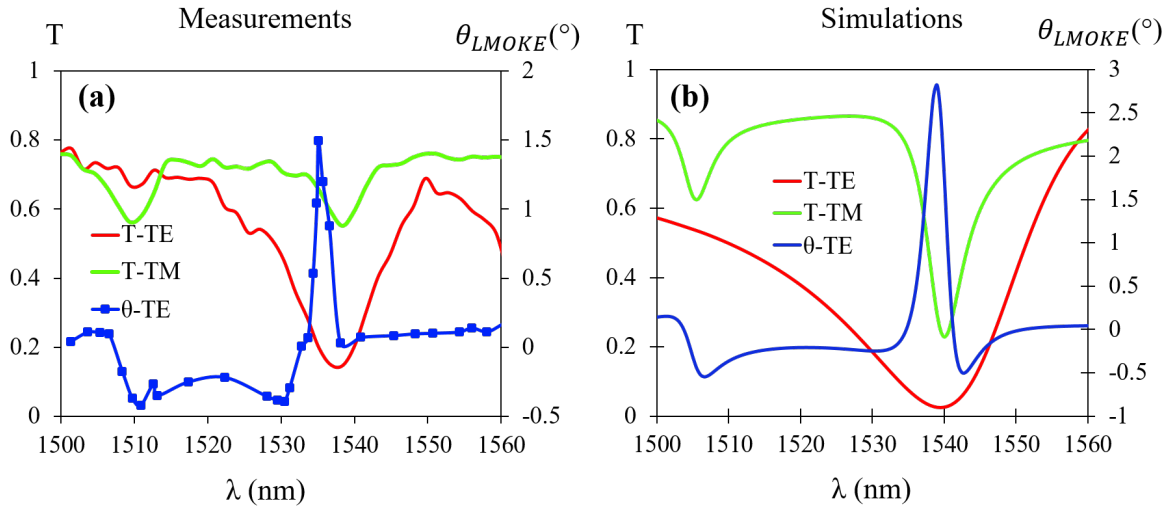


FIGURE III.29: (a) Measured and (b) calculated transmittance spectrum for TE and TM polarizations and LMOKE in transmission for TE polarization, for Si_3N_4 -MO structure at AOI= 0.88° .

As can be deduced from Fig.III.29a, a value of FoM equal to 0.67° can be reached at $\lambda = 1535$ nm. This value is lower than that demonstrated through the PR-MO structure (FoM= 0.83°) due to the more transmissivity of this latter.

The measurements of T and LMOKE rotations are in a good agreement with the numerical simulations (Fig.III.29b).

This section was dedicated to present the experimental evidence of the polarization rotation effects enhancements, through the simple PR-MO structure and compare the results to those obtained through Si_3N_4 -MO structure. As a result, the PR-MO structure is promising for detecting two magnetic field components: z component (Faraday effect) and x component (LMOKE). Tab.III.1 summarizes the measured rotations through the PR-MO structure, with the corresponding optical parameters.

Therefore, in order to achieve the long term objective of this work, which is to find a structure capable to measure with high precision the magnetic field components for sensing applications, the detection of the third component (y direction) should be demonstrated. Hence, the TMOKE in transmission and in reflection, will be studied in the next section.

TABLE III.1: Measured rotations in Faraday and LMOKE configurations through the PR-MO structure, with the corresponding optical parameters.

Non-Reciprocal Effects	$\theta(^{\circ})$	T	FoM ($^{\circ}$)	AOI ($^{\circ}$)	Mode
Faraday	0.22	70	0.18	0	TE
LMOKE	1.1	60	0.85	0.4	TE

III.4 Enhancement of TMOKE

The magnetic field is oriented in y direction according to Fig.III.18a and the incident light is polarized in x direction (TM polarization).

III.4.1 Transmission Geometry

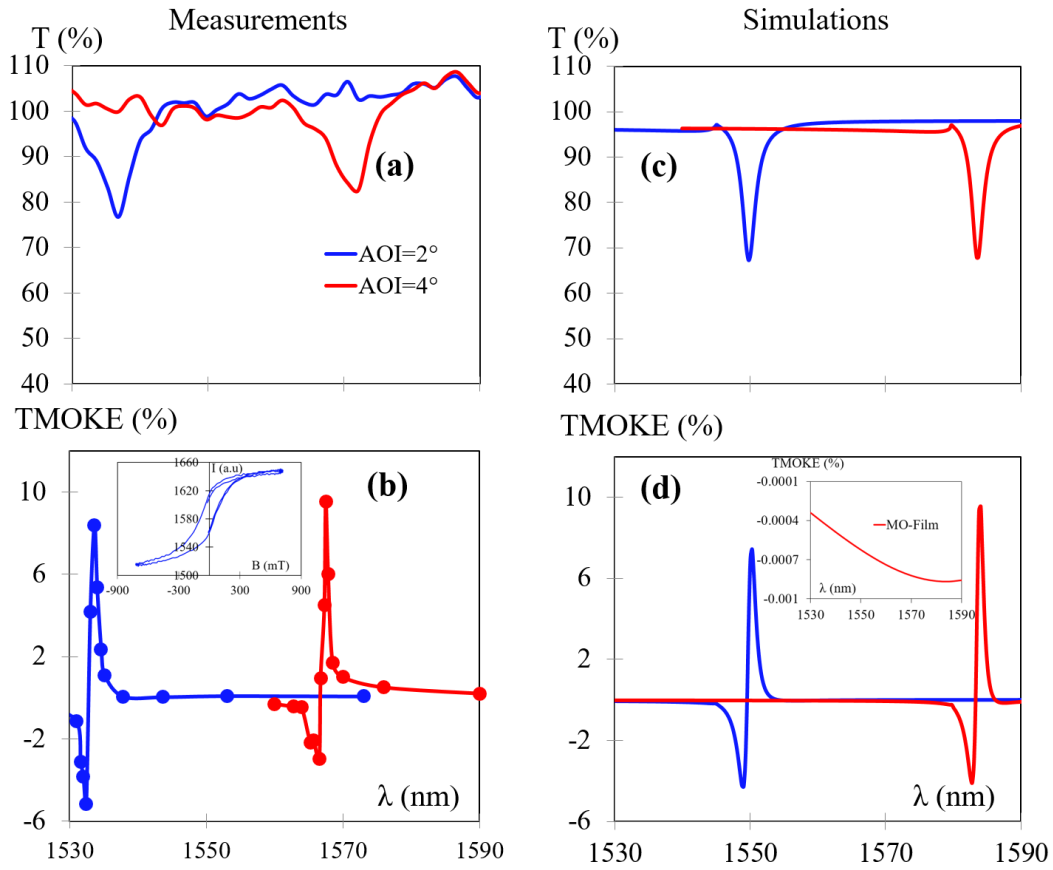


FIGURE III.30: Measurements of (a) transmittance for TM polarization and (b) TMOKE in transmission at AOI=2° and 4°. Inset (b): measured intensity loop at $\lambda = 1533.6$ nm for AOI=2°. (c), (d): calculated transmittance and TMOKE spectra for the zero gelation field PR-MO structure. Inset (d): calculated TMOKE spectrum for a single MO film at AOI=4°.

Fig.III.30 illustrates the measurements (a-b) and the numerical simulations (c-d) of the transmittance and the TMOKE signal for AOI=2° and 4°, for the PR-MO structure without gelation field. Here, the measurements were done by using the first method explained

in section III.2.2. Therefore, the hysteresis loop of the intensity was measured for every wavelength (see inset Fig.III.30b), and the TMOKE was deduced from Eq.I.50.

One can notice on Fig.III.30a-b, that the transmittance resonance is slightly shifted from the TMOKE resonance which is not the case in the simulations (Fig.III.30c-d). This behavior can be linked to the fact that the transmittance and the TMOKE were not measured at the same time, and due to the AOI uncertainty a small shift can be found.

As seen in Fig.III.30b-d, the TMOKE signal is higher for $\text{AOI}=4^\circ$ and its spectrum is more asymmetric, compared to $\text{AOI}=2^\circ$. This behavior can be linked to the dispersion of the MO term ϵ_{xz} as explained in section III.1.3.2.

The measured TMOKE reached 9.5% as highest value at $\lambda = 1567.5$ nm for $\text{AOI}=4^\circ$, with a transmittance higher than 80%. The TMOKE signal for a single MO composite film is very small (maximum 0.001%, see inset Fig.III.30d), hence giant enhancement of the TMOKE in transmission was achieved with the all-dielectric fabricated structure.

In order to study precisely the angular behavior of the TMOKE by the experimental measurements, TMOKE spectra were measured in transmission for different AOI by the second measurements method described in section III.2.2 because it is easier for spectral measurements. The results are plotted on Fig.III.31.

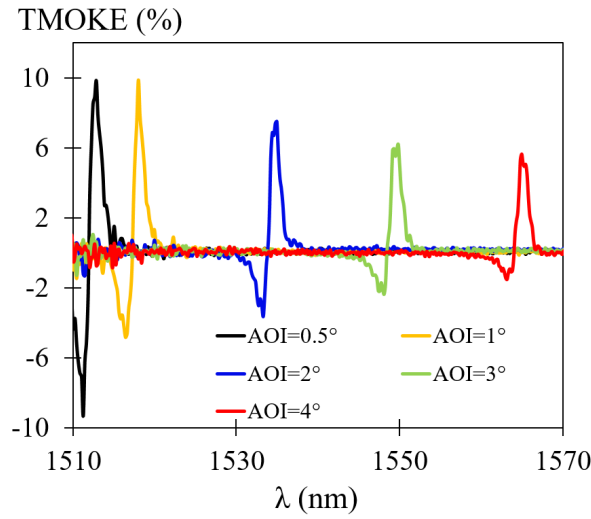


FIGURE III.31: Measurements of TMOKE spectra in transmission for different AOI done by the second measurements method explained in section III.2.2.

As seen in Fig.III.31, by increasing the AOI the symmetric shape of the TMOKE spectra gradually disappears. However, the increase of the TMOKE signal with the AOI was not achieved as predicted by the numerical simulations on Fig.III.11b and as demonstrated for $\text{AOI}=2^\circ$ and 4° on Fig.III.30b-d. But, by increasing the AOI the TMOKE resonance becomes narrower (see Fig.III.30b-d). Hence, if the resolution of the Ibsen spectrometer is not enough, the wavelength corresponding to the maximum peak will be missed resulting in lower TMOKE signal.

The PR-MO structure being a GMR device, it produces a resonant peak of intensity in reflection, simultaneously to the transmittance dip. Thus, in the next section, the

TMOKE will be studied in reflection, and with the first measurement method, for different AOI.

III.4.2 Reflexion Geometry

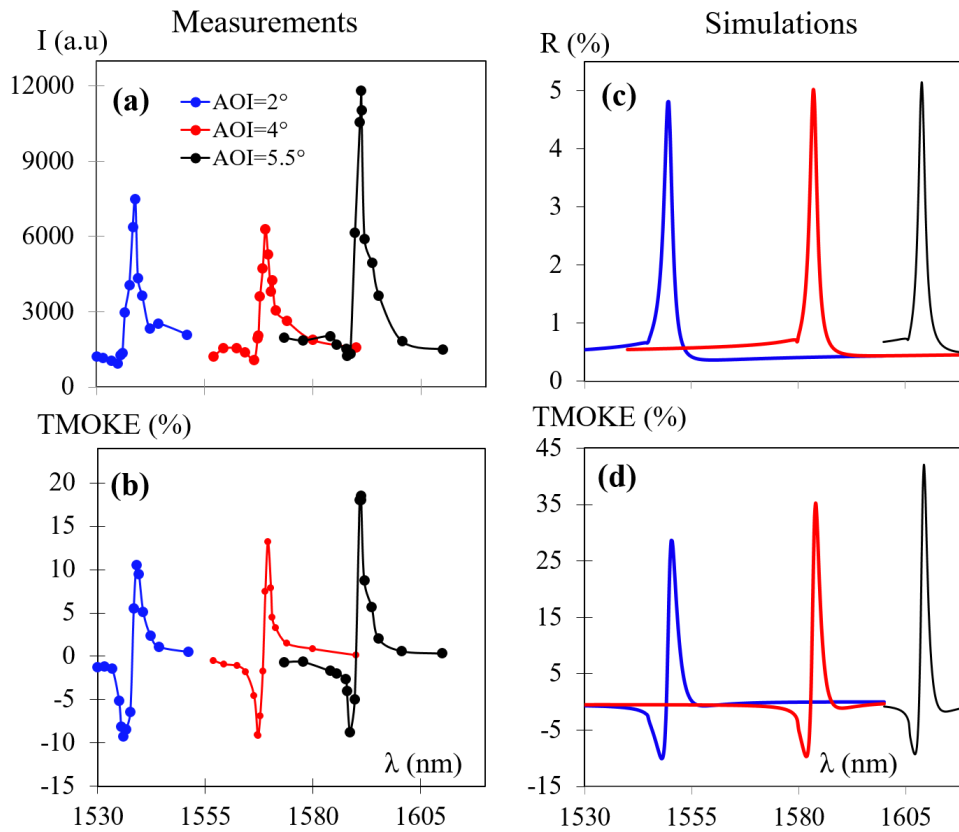


FIGURE III.32: Measured (a) reflected light intensity and (b) TMOKE in reflection spectra for TM polarization and for different AOI. Simulated (c) reflectance and (d) TMOKE spectra.

Fig.III.32a-b illustrates the measurements of the reflected intensity and the TMOKE in reflection spectra for zero gelation field sample, for TM polarization and for different AOI (2°, 4° and 5.5°). As seen in Fig.III.32b, the TMOKE signal increases with the AOI and reaches a maximum value equal to 18.5% at $\lambda = 1591.25$ nm. Similar angular behavior is mentioned for the numerical simulations (Fig.III.32d). One can also notice on Fig.III.32b-d, that the TMOKE spectra is gradually asymmetric by increasing the AOI as for the TMOKE in transmission (Fig.III.30).

Indeed, the reflectance resonances are narrower for higher AOI as seen in Fig.III.32a-c, increasing then the TMOKE signal. Also, the dispersion of ϵ_{xz} plays a role in the increment of the TMOKE with the AOI and for the asymmetric behavior, as described in Fig.III.11.

The TMOKE signal in reflection for a single MO film is around 0.01%, hence giant enhancement of this effect was achieved through the PR-MO structure.

One can notice that, the TMOKE in reflection (18.5%) is higher than in transmission (9.5%), contrary to MP structures [Poh+13].

As a summary, significant values of TMOKE signal in transmission and in reflection were experimentally and numerically demonstrated in the presented work, in addition to the enhancement achievements of the LMOKE in transmission and the FR, through a simple PR-MO structure. Hence, this structure offers the possibility to measure different components of the magnetic field, what qualifies it to be promising for magnetic field sensing or in NDT.

The Si_3N_4 -MO structure can demonstrate also the enhancement of the different MO effects. The enhancement of Faraday and LMOKE were demonstrated in previous sections and the TMOKE in transmission will be presented in the next section.

III.4.3 Comparison with Silicon Nitride Grating

As illustrated on Fig.I.27, the Si_3N_4 -MO structure is also promising for TMOKE enhancement. Hence, due to the development of the TMOKE setup in this work, the TMOKE signal can be now properly measured.

The measurements and the numerical simulations of the TMOKE signal and the transmittance for TM polarization, are illustrated on Fig.III.33a-b respectively, for AOI=1.5° and for the same structure used for LMOKE.

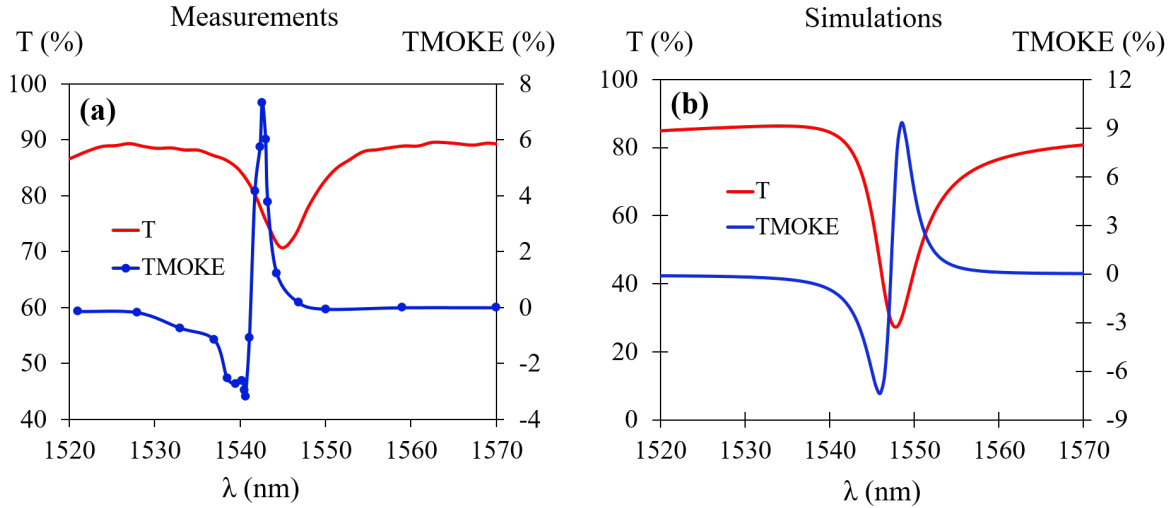


FIGURE III.33: (a) Measured and (b) simulated transmittance and TMOKE spectra in transmission for TM polarization, for Si_3N_4 -MO structure at AOI=1.5°.

As seen in Fig.III.33a, high values of TMOKE were achieved and the highest one is equal to 7.3% at $\lambda = 1543$ nm, accompanied with high transmittance of 70%. The numerical simulations (Fig.III.33b) are in good agreement with the measurements.

Therefore, large values of the different MO effects were experimentally and numerically demonstrated through the Si_3N_4 -MO structure. However, as mentioned before, the fabrication process of this structure is more complex, expensive and longer than the simple PR-MO structure. Therefore, for industrial applications this latter is more competitive.

In Fig.III.34, the TMOKE values demonstrated in this work in transmission (a) and reflection (b), are compared to others selected in the literature and obtained with

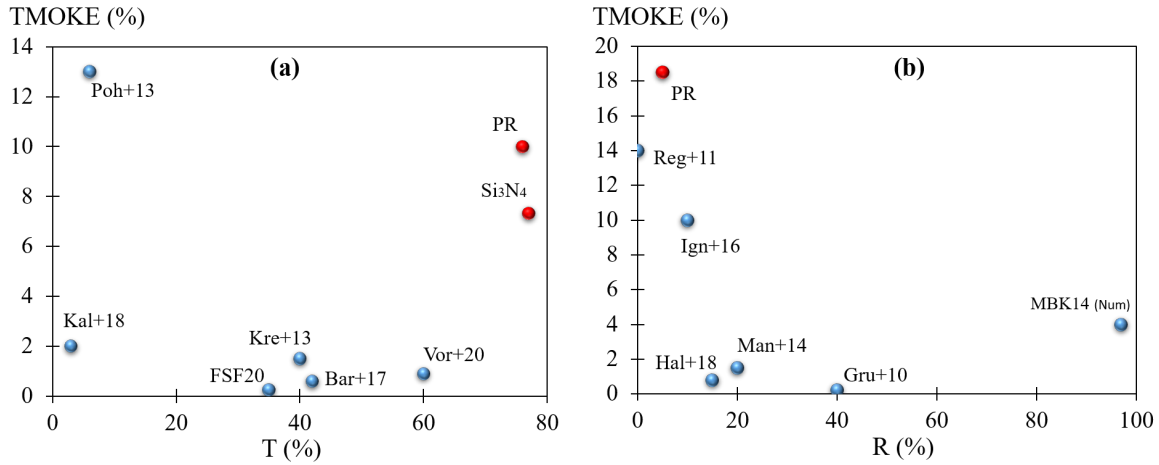


FIGURE III.34: Comparison spectrum of TMOKE values and optical responses, between this work (red dots) and the different works done in the literature. (a) TMOKE in transmission and (b) TMOKE in reflection.

all-dielectric and MP structures (these structures are mainly summarized in Tab.I.3). Hence, as seen in Fig.III.34a the reached TMOKE values (red dots) accompanied with high transmittances, are highly competitive with the values obtained through the 1D MP structure formed by gold nanowires deposited on top of a BIG layer [Kre+13; Poh+13; Kal+18] or on top of Bi-substituted gadolinium iron garnet (Bi:GIG) layer [Hal+18]. In addition to that, the achieved TMOKE values are several times higher than those obtained by Frolov et al. [FSF20] through a structure formed by multilayer Au/Ni/ Au nanowires, or than that demonstrated by Barsukova et al. [Bar+17] through Ni nanodisks.

Moreover, the achieved TMOKE in reflection through the PR-MO structure (see III.34b), is more important than that obtained through MP structures formed by Au/Co multilayers [Man+14; Reg+11; Ign+16]. However, these structures are very promising for biosensing applications (as explained in section I.1.4.2) but accompanied mostly with low reflectance due to the SPPs resonance. Finally, the measured TMOKE in transmission and in reflection are the highest values demonstrated experimentally through all-dielectric structures. To our knowledge, maximum TMOKE value equal to 1% in transmission was demonstrated experimentally in the literature [Vor+20], with a Bi:YIG grating on top of GGG substrate. The fabrication process of this latter is more complex and longer than the simple PR grating.

We have to mention that if we compare the MO term (ϵ_{xz}) of the MO composite adapted in this work, to those of the most MO materials used in the literature (such as Co [Ign+16], Ni [FSF20] and Bi:YIG [Vor+20]), ϵ_{xz} is in one, two and even three orders of magnitude smaller.

Therefore, the simple PR-MO structure can demonstrate experimentally and numerically the enhancement of the different MO effects. The measured Faraday and LMOKE rotations as well as the measured TMOKE in transmission and in reflection are summarized in Tab.III.2 with the corresponding optical parameters. These achieved values are at the state of the art or even beyond for the TMOKE.

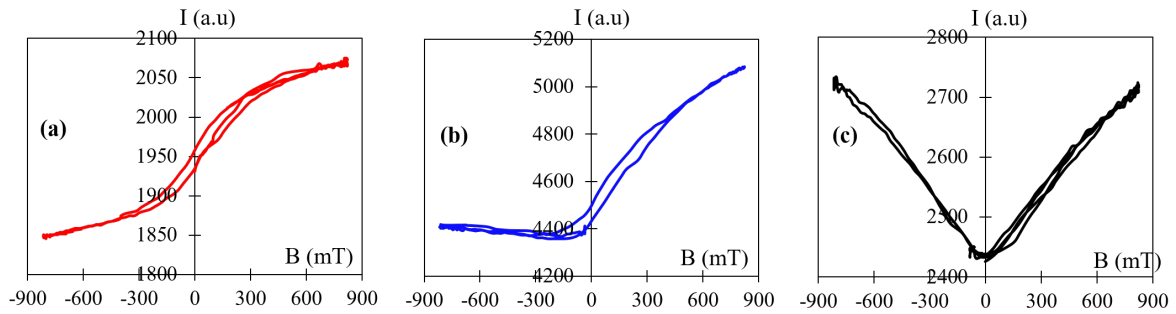
TABLE III.2: Measured Faraday and LMOKE rotations and TMOKE in transmission and in reflection through the PR-MO structure, with the corresponding optical parameters.

Non-Reciprocal Effects	MO Response	Optical Response (%)	AOI (°)	Mode
Faraday	0.22°	T=70	0	TE
LMOKE	1.1°	T=60	0.4	TE
TMOKE	9.5%	T=80	4	TM
	18.5%	R=5	5.5	TM

During the TMOKE measurements, we observed that at some wavelengths the intensity loop was not totally asymmetric. Fig.III.35 illustrates different intensity hysteresis loops at different wavelengths, for transverse configuration and for the PR-MO structure. As seen in Fig.III.35a the curve is antisymmetric, however at $\lambda = 1538$ nm (Fig.III.35b) the cycle starts to have a symmetric behavior before transforming into a fully symmetric curve (Fig.III.35c, $\lambda = 1535$ nm). Hence, in addition to the non-reciprocal effect (TMOKE) a reciprocal effect (RE) clearly appears: the curve is no more odd as a function of the field. We should say that this RE does not add any doubt to the measurements of TMOKE presented before since this latter was deduced from the relative difference of the saturated intensities (Eq.I.50), hence the RE was removed.

Moreover, at some wavelengths, the beginning of symmetric intensity loops were also observed in Faraday and LMOKE configurations.

The next section is dedicated to present these RE in different magnetic field configurations. We should say that in the LabHC, this RE was also observed in MO composite waveguides for transverse and longitudinal magnetic fields [Gar17], and in fiber optics doped with the MO composite material in transverse configuration.

FIGURE III.35: Example of intensity loops measured in transverse configuration for TM polarization with the fabricated PR-MO structure, at (a) $\lambda = 1540$ nm, (b) $\lambda = 1538$ nm and (c) $\lambda = 1535$ nm

III.5 Reciprocal Effects

When a transverse magnetic field is applied to a MO waveguide, in addition to the non-reciprocal effect (TMOKE), a reciprocal effect named Cotton Mouton can be observed as in bulk material. This RE is explained by the fact that the propagation constant of the TM mode changes quadratically with respect to the MO term: β is a function of ϵ_{xz}^2 . Therefore,

the propagation constant is modified when a magnetic field is applied ($\epsilon_{xz} \neq 0$). However, for two opposite magnetic field directions, β is constant. Hence, the RE effect is defined as: $\Delta\beta_{0M} = \beta(0) - \beta(M)$.

This effect is linked to the ϵ_{xz}^2 term in the TM propagation equation, whereas TMOKE is linked to linear ϵ_{xz} term, see Eq.I.43. However, compared to the non-reciprocal effect ($\Delta\beta_{\pm M}$), the Cotton Mouton is very weak. Fig.III.36 illustrates the Cotton Mouton ($\Delta\beta_{0M}$) and the TMOKE ($\Delta\beta_{\pm M}$) effect as a function of the magnetic field, for a MO waveguide with $t_{MO} = 600$ nm and $n_{MO} = 1.64$ at $\lambda = 1550$ nm. As seen in this figure, the non-reciprocal effect ($\Delta\beta_{\pm M} = 0.0012 \mu m^{-1}$) is higher by a factor of 1000 compared to the RE ($\Delta\beta_{0M} = 4.4 \times 10^{-6} \mu m^{-1}$). Thus, the Cotton Mouton effect cannot explain what is observed on Fig.III.35.

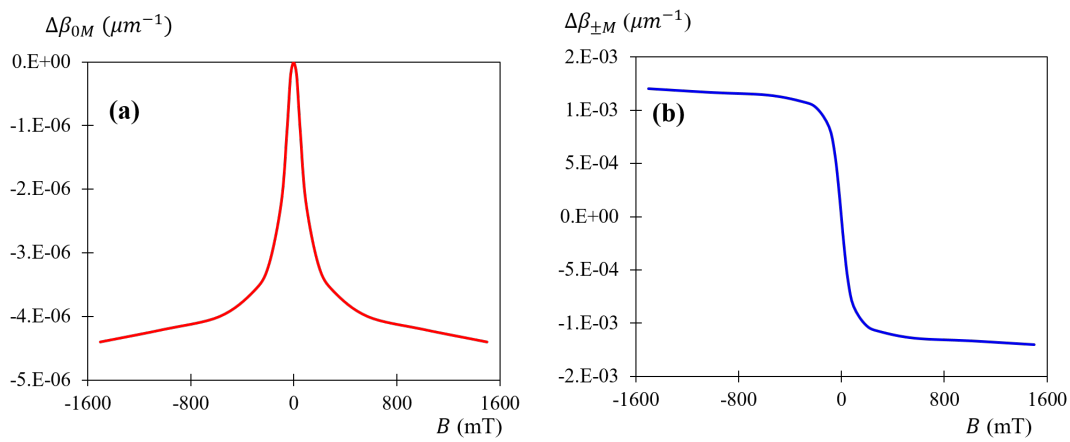


FIGURE III.36: Calculated (a) reciprocal effect $\Delta\beta_{0M}$ and (b) non-reciprocal effect $\Delta\beta_{\pm M}$, for TM guided-mode as a function of the applied magnetic field amplitude. The considered MO waveguide has the following parameters: $n_c = 1$, $n_{MO} = 1.64$ and $n_s = 1.51$ at $\lambda = 1550$ nm. $t_{MO} = 600$ nm and $\epsilon_{xz} = 0.0064$.

However, as illustrated on Fig.I.39, Belotelov et al. [Bel+13] measured a significant reciprocal intensity modulation effect in longitudinal configuration (LMPIE = 24%) at normal incidence, for TM polarization through a MP structure. This latter consists of a gold grating deposited on top of a Bi:YIG film. The origin of LMPIE is explained as follows: due to the longitudinal applied magnetic field, the guided-modes (TE or TM) excited in the MO layer transform into quasi-modes. The mode wave number of these quasi-modes changes quadratically with respect to the MO term ϵ_{yz} , resulting in a spectral shift or shape modification of the transmittance spectrum.

In the presented work, a reciprocal modulation intensity was observed through the PR-MO structure, in the different magnetic field configurations: Faraday, longitudinal and transverse, in addition to the non-reciprocal effects (polarization rotation and TMOKE). The following sections deal with the presentation of these observations, with a systematic comparison with numerical simulations. In each case, the RE is defined as the relative change of the transmitted (or reflected) intensity I , between the magnetized ($\frac{I(M)+I(-M)}{2}$) and demagnetized ($I(0)$) structure:

$$RE(\%) = 100 \times \left(\frac{I(+M) + I(-M)}{2I(0)} - 1 \right) \quad (\text{III.2})$$

III.5.1 Faraday Configuration

Fig.III.37 illustrates the spectral behavior of Faraday reciprocal effect named FRE (\vec{B} following z direction) and defined as Eq.III.2, accompanied with the transmittance at normal incidence for TE polarization, for the zero gelation field structure. As seen in this figure, a value down to -1.3% is measured at $\lambda = 1506.6$ nm. The FRE and θ_F resonance wavelengths are very close as seen in inset Fig.III.37b.

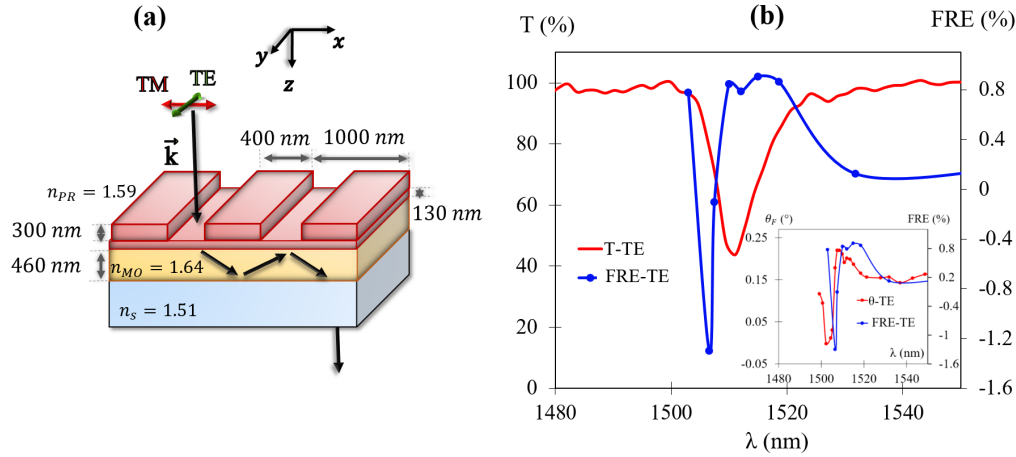


FIGURE III.37: (a) Fabricated PR-MO structure. (b) Measured transmittance and FRE spectra for TE polarization at normal incidence, Inset (b): measured θ_F and FRE spectra.

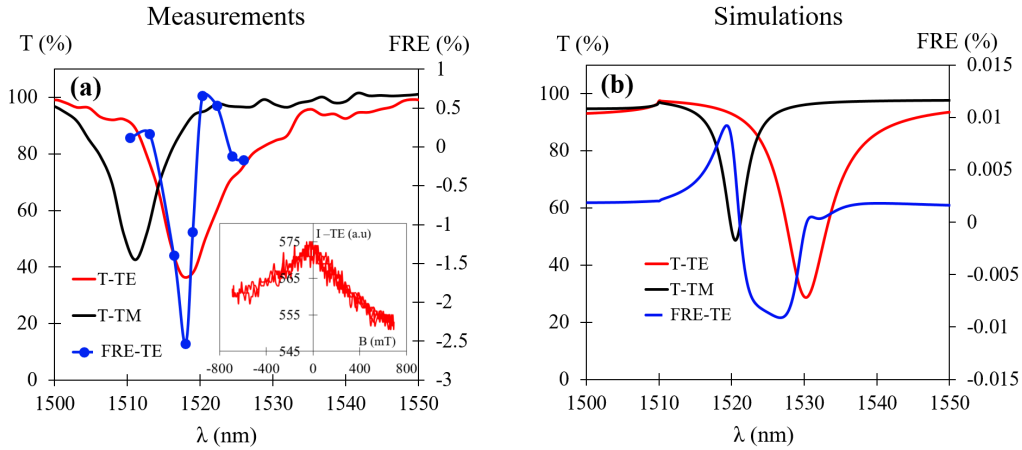


FIGURE III.38: (a) Measured and (b) simulated transmittance for TE and TM polarizations and FRE spectra for TE polarization, for out of-plane gelation field sample and at normal incidence. Inset (a): example of measured transmitted intensity loop at $\lambda = 1518$ nm for TE polarization.

Higher FRE values were measured for the out of-plane gelation field sample (schematic illustration in Fig.III.19b). Indeed, as demonstrated in Fig.III.19b, this structure demonstrates the smallest phase shift $\Delta\beta$ between TE and TM modes. Fig.III.38a illustrates the measured (a) and simulated (b) FRE spectrum for TE polarization accompanied with the transmittance

spectra for TE and TM polarizations, at normal incidence and for out of-plane \vec{B}_{gel} sample. As seen in this figure, the calculated FRE value (-0.01%) are in two orders of magnitude smaller than the measured one (-2.5%). Hence, in the measurements we have the effect considered by the simulations that can be attributed to Cotton Mouton effects since they are very weak, plus another effect whose origin is not defined yet.

III.5.2 Longitudinal Configuration

In this section, the longitudinal reciprocal effect (\vec{B} following x direction referring to Fig.III.37a) named LRE (LMPIE elsewhere [Bel+13]), is studied. Fig.III.39a-b illustrates the measured (a) and calculated (b) LRE for TE polarization and the transmittance for TE and TM polarizations of zero field sample, at normal incidence. As seen in this figure (more obvious in Fig.III.39b), the LRE spectrum presents two resonances corresponding spectrally to the TE and TM resonances. Here, the measurements (Fig.III.39a) and the simulations (Fig.III.39b) are in good agreement and a value of LRE up to 1.5% is reached.

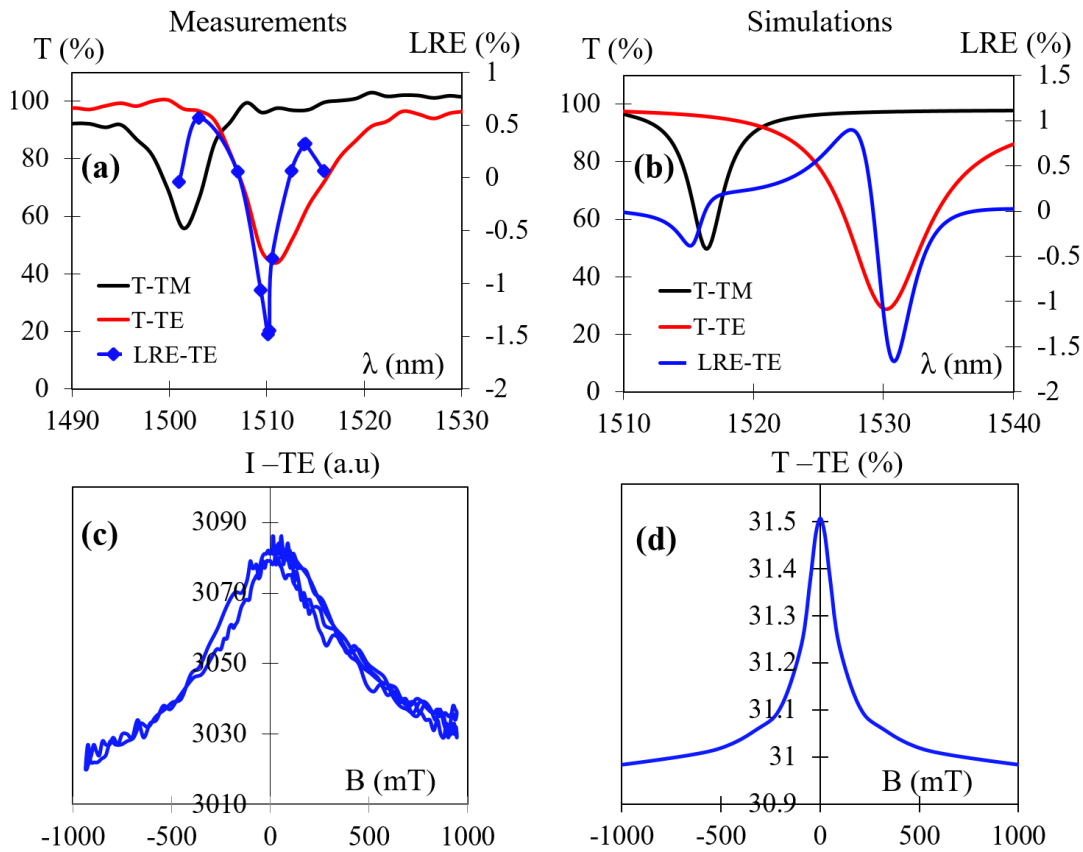


FIGURE III.39: (a) Measured and (b) simulated: transmittance spectra for TE and TM polarizations and LRE spectra for TE polarization at normal incidence, for zero field sample. (c) Measured transmitted intensity loop at $\lambda = 1511$ nm. (d) Simulated transmittance loop at $\lambda = 1531$ nm.

Fig.III.39c-d illustrates the transmitted intensity (measurements) and the transmittance (simulations) as a function of the magnetic field, at spectral positions corresponding to the maximum of the LRE spectra. It is obvious from this figure, that the LRE is a reciprocal effect.

Here, the loops are perfectly reciprocal since there is no polarization rotation effect at normal incidence for the longitudinal configuration as explained before (see Fig.I.7b).

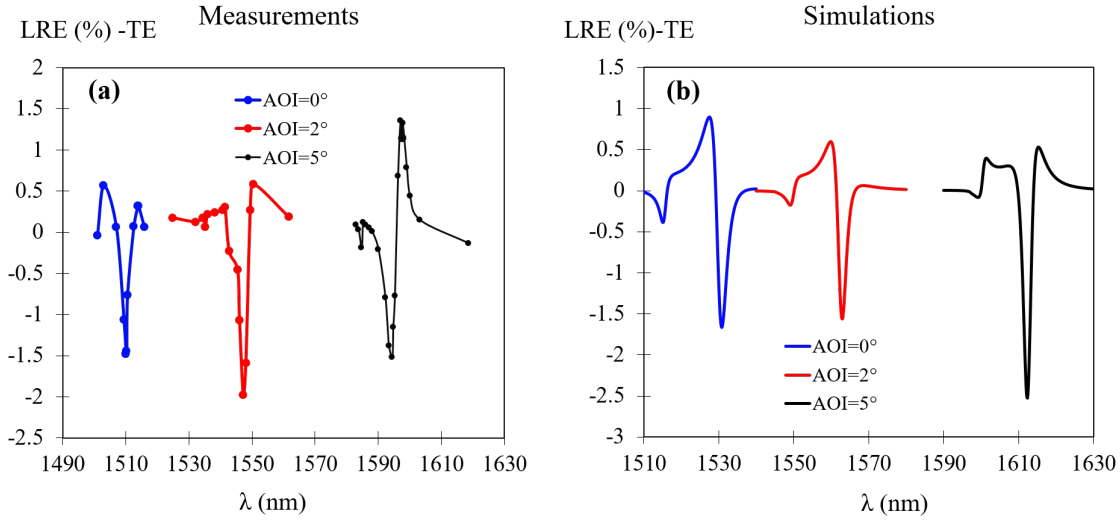


FIGURE III.40: (a) Measured and (b) simulated: LRE spectra in transmission for different AOI, for TE polarization and for zero gelation magnetic field sample.

The measured (a) and calculated (b) LRE spectra for different AOI (0°, 2° and 5°) are plotted on Fig.III.40, for TE polarization and for zero gelation field sample. As seen in this figure, the angular behavior of the LRE is not the same in the measurements and the simulations. The highest measured value is -2% at $\lambda = 1547.3$ nm for AOI=2°.

III.5.3 Transverse Configuration

During the TMOKE measurements (\vec{B} following y direction), we mentioned also that at some wavelengths the intensity loop was not totally asymmetric. Therefore, an effect named TRE (transverse reciprocal effect) defined as in Eq.III.2 is presented in addition to the non-reciprocal effect (TMOKE).

Fig.III.41 illustrates the TRE in transmission (a) and in reflection (b) as a function of the wavelength for TM polarization, at AOI=2° for zero \vec{B}_{gel} sample. As seen in this figure, the TRE in reflection is higher than in transmission (as for the TMOKE). Large TRE values were measured and the highest ones are -1.25% in transmission at $\lambda = 1533$ nm and 3.55% in reflection at $\lambda = 1538.4$ nm. The slight spectral shift between Fig.III.41a and Fig.III.41b is due to the AOI uncertainty, since the two measurements were not done simultaneously.

The measured and calculated TRE spectra in reflection for out of-plane \vec{B}_{gel} sample are illustrated on Fig.III.42a-b, for TM polarization and for different AOI. As seen in this figure, the TRE amplitudes for different AOI are higher than that measured for zero \vec{B}_{gel} structure and presented on Fig.III.41b. One can notice that the measured TRE signals are also higher than the calculated ones (see Fig.III.42b). In addition to that, by increasing the AOI the calculated TRE increases however, the measured TRE values tend to decrease. Moreover, the symmetric shape of the simulated TRE spectra gradually disappear with the AOI, contrary to the measurements. Hence, the angular behavior of the calculated TRE is similar to that of the TMOKE.

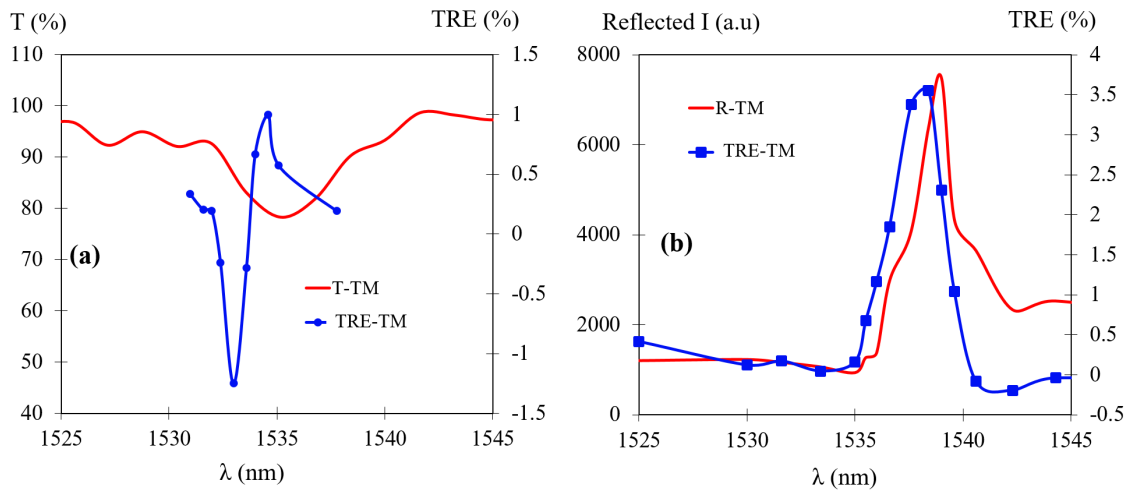


FIGURE III.41: Measured (a) transmittance and TRE in transmission spectra, (b) reflected intensity and TRE in reflection spectra for TM polarization and at $\text{AOI}=2^\circ$, for the zero gelation field sample.

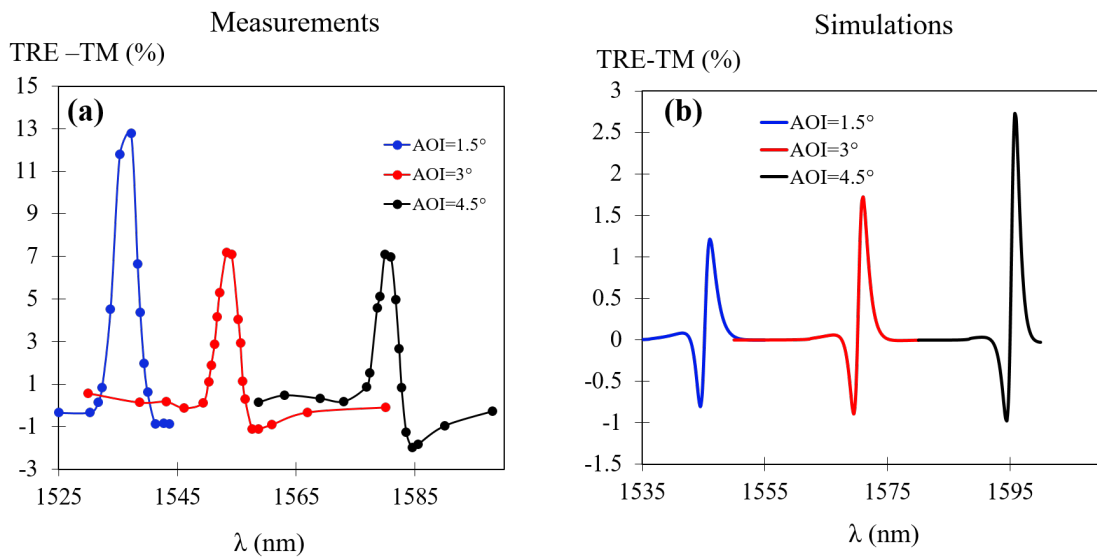


FIGURE III.42: (a) Measured and (b) calculated TRE in reflection spectra for the out of plane gelation field sample, for TM polarization and for different AOI.

The TRE cannot be only the Cotton Mouton effect since we demonstrated on Fig.III.36 that the non-reciprocal effect is higher by a factor of 1000 as compared to the RE. Here both effects are in the same order of magnitude as can be seen on Fig.III.43a.

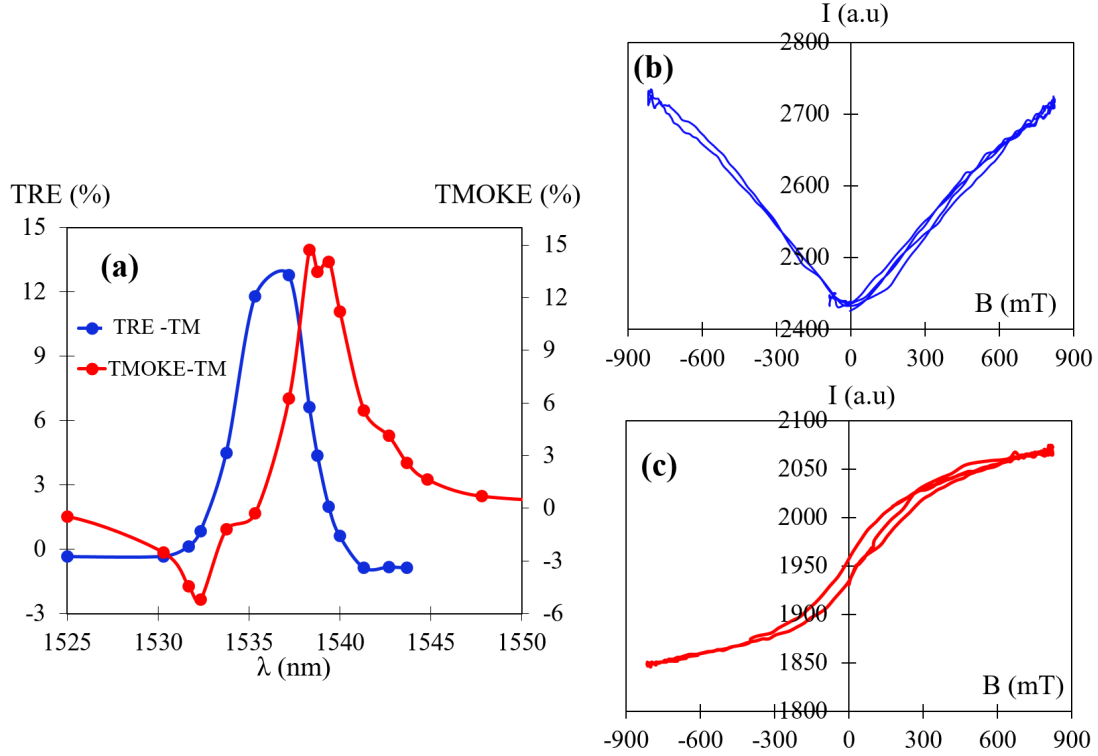


FIGURE III.43: (a) Measured TMOKE and TRE in reflection spectra for TM polarization at AOI=1.5°, for out-of-plane gelation field sample. Examples of measured reflected intensity loops at (b) $\lambda = 1535.33$ nm and (c) $\lambda = 1540$ nm.

Examples of measured intensity hysteresis loops are illustrated on Fig.III.43b-c. As seen in Fig.III.43b, the curve corresponding to $\lambda = 1535.33$ nm is totally symmetric due to the fact that the TMOKE at this wavelength is very weak ($\delta = -0.3\%$, see Fig.III.43a) and the TRE is very high (TRE=12%). However, at $\lambda = 1540$ nm (Fig.III.43c), the TMOKE is very high (11%) compared to the TRE (0.6%), resulting in an antisymmetric curve. We should say that there is no doubt or confusion about the measurements method of each effect (TRE and TMOKE) since this latter is deduced from a formula removing the influence of the other (TRE from Eq.III.2 and TMOKE from Eq.I.50).

The TRE in reflection was also measured for TE polarization. In this case, the intensity loop will be totally symmetric (Fig.III.44a) since there is no TMOKE for TE polarization. The spectral behavior of the TRE, for out-of-plane \vec{B}_{gel} structure and for TE polarization, is plotted on Fig.III.44b with the reflected intensity. As seen in this figure, the TRE peak is shifted from the reflectance peak and the highest measured value is 12% at $\lambda = 1593.5$ nm. However, for the numerical simulation the TRE for TE polarization is zero (see inset Fig.III.44b).

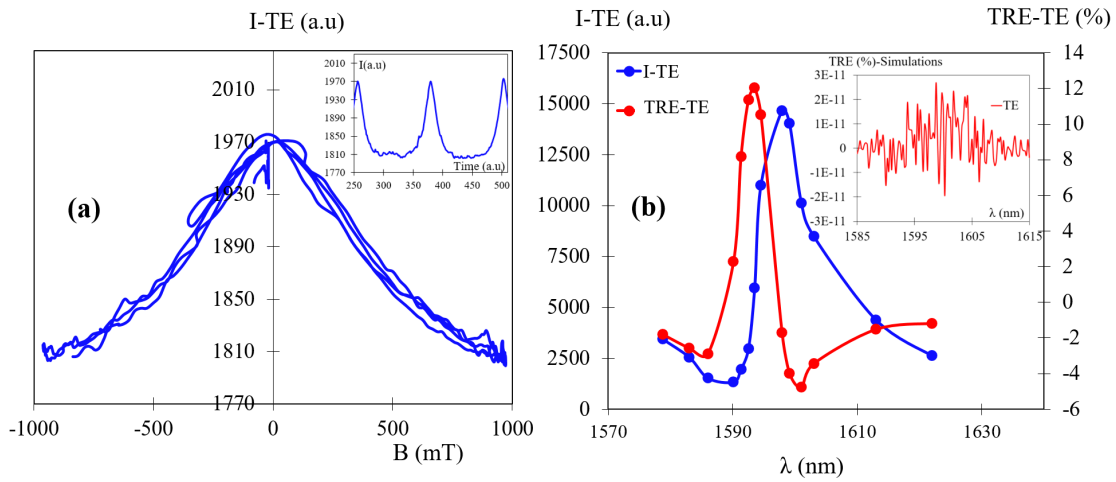


FIGURE III.44: (a): Measurements of reflected intensity loop at $\lambda = 1591$ nm. Inset (a): measured intensity as a function of the time under sinus varying applied magnetic field. (b) Measurements of TRE and reflected intensity spectra for out of-plane gelation field sample. Inset (b): simulated TRE spectrum. The incident polarization is TE and the AOI is equal to 4.5° .

In order to demonstrate that the TRE is a magnetic effect linked to the magnetic NPs, the intensity loop of the pure TRE should present a coercive magnetic field, which is not very obvious on Fig. III.44a. However, as demonstrated in Fig. II.33, the coercive field is maximum for a sample deposited under a gelation field with an orientation parallel to the measurement magnetic field. Therefore, in transverse configuration, this corresponds to the structure with in-plane \vec{B}_{gel} and grating grooves parallel to this latter (Type 4 in Tab. II.3). The schematic illustration of this structure and the measurement field \vec{B}_{meas} orientation (transverse configuration) are illustrated on Fig. III.45a.

Fig. III.45b illustrates the intensity loops in reflection for TE polarization at $\lambda = 1587$ nm (red curve) and for TM polarization at $\lambda = 1567$ nm (blue curve), for the structure of Fig. III.45a and at AOI = 3.5° . One can obviously notice, the coercive field on the reciprocal effect loop (pure TRE, red curve) which overlaps with that of the non-reciprocal effect loop (TMOKE, blue curve). Hence, the TRE is a magnetic effect linked to the ferrite cobalt NPs.

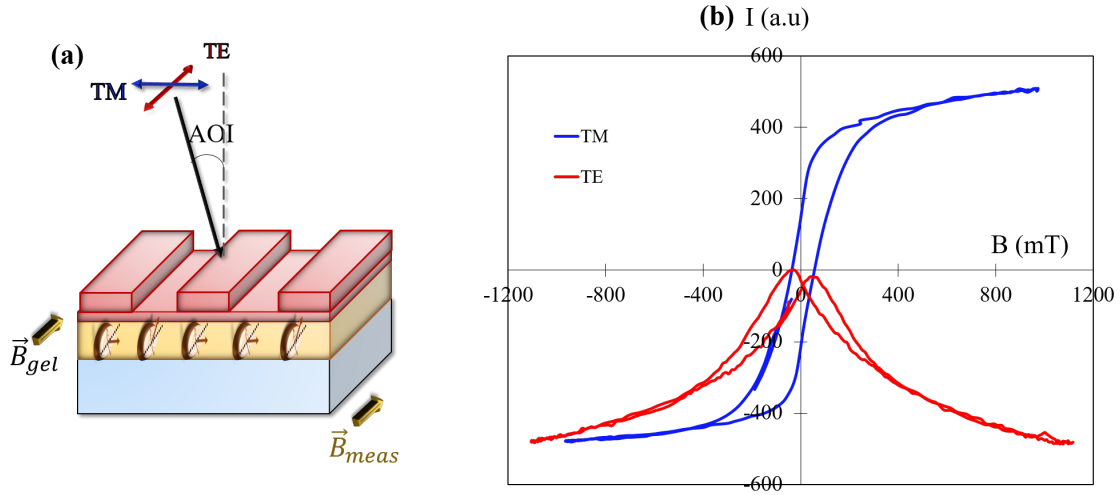


FIGURE III.45: (a) Schematic illustration of the structure under study in transverse configuration. (b) Measured intensity loops in reflection for TM polarization at $\lambda = 1567$ nm (blue curve) and TE polarization at $\lambda = 1587$ nm (red curve), for $AOI=3.5^\circ$.

As a summary, large values of reciprocal intensity modulation were demonstrated in different magnetic field configurations through the PR-MO structure, for TE and TM polarizations and summarized in Tab.III.3. Apart from the longitudinal configuration, numerical simulations do not evidence such magnitude of RE. As first assumption, the demonstrated reciprocal effects can be attributed to the magneto-refractive effect [Cai+10], which is explained by a reciprocal modulation of the refractive index of the MO material under the influence of an applied magnetic field. This index modulation can be translated as a reciprocal shift of the transmittance or reflectance resonance resulting in reciprocal intensity modulation effects.

TABLE III.3: Measured reciprocal intensity modulation effects in Faraday, LMOKE and TMOKE configurations through the PR-MO structure, with the corresponding optical parameters.

RE	Intensity Modulation (%)	Optical Response (%)	AOI (°)	Mode	Structure Type	Numerical Value
FRE	-1.3	T=80	0	TE	$\vec{B}_{gel} = \vec{0}$	-0.01
	-2.53	T=37	0	TE	Out of-plane \vec{B}_{gel}	-0.01
LRE	-1.5	T=45	0	TE	$\vec{B}_{gel} = \vec{0}$	-1.67
	-2	T=64	2	TE	$\vec{B}_{gel} = \vec{0}$	-1.56
	-0.45	T=60	2	TE	Out of-plane \vec{B}_{gel}	-1.5
TRE	-1.25	T=80	2	TM	$\vec{B}_{gel} = \vec{0}$	0.52
	3.55	R=4	2	TM	$\vec{B}_{gel} = \vec{0}$	1.57
	13	R=4	1.5	TM	Out of-plane \vec{B}_{gel}	1.17
	12	R=7	4.5	TE	Out of-plane \vec{B}_{gel}	0

III.6 Conclusion

In the first part of this chapter, numerical simulations were presented in order to understand the behavior of optical and MO responses, as functions of the opto-geometric parameters of the PR grating and the MO film. As a result, the phase matching condition required for higher Faraday effect was achieved at normal incidence, but with grating parameters difficult to achieve ($h_{PR} = 500$ nm and $f = 0.69$). However, the phase matching condition disappears at oblique incidence where the LMOKE was studied since this latter is zero at normal incidence.

The TMOKE was also numerically studied and we concluded that by increasing the AOI, the TMOKE signal is higher and its spectrum is gradually asymmetric, due to the dispersion of the MO term. In addition to that, to maximize the TMOKE values, the MO film thickness should be close to the cut-off value in order to have the minimum transmittance resonance width. Moreover, the refractive index difference between the PR grating and the MO film should be high in order to have a good resonance amplitude.

The second part of the chapter was devoted to the experimental measurements of the different MO effects carried out on the fabricated PR-MO structure: $h_{PR} = 300$ nm and $f = 0.4$. The MO film refractive index and thickness are respectively: $n_{MO} = 1.64$, and $t_{MO} = 460$ nm. This latter is close to the cut-off value (380 nm) and the refractive index corresponds to the highest NPs concentration ($\phi = 26\%$). The MO measurements were done with homemade MO setups which description was presented in this chapter.

FR equal to 0.22° was measured through the PM-MO structure, resulting in an enhancement by a factor of 1.4 compared to the reference film. The reached FoM is equal to 0.18° , which is in the same order of magnitude compared to more complex structures mentioned in the literature [CGMC15; Lei+16].

Maximum LMOKE rotation (1.1°) was measured in transmission at small AOI where TE and TM modes resonances with different diffraction orders ($\pm 1st$) overlap. The reached FoM is equal to 0.83° which is also competitive with other works [Che+12; KB16], taking into account that the used MO composite has off-diagonal elements with one and two orders of magnitude smaller compared to these works.

The main results belong to the TMOKE effect. Large TMOKE values were achieved in transmission (9.5% with $T=80\%$) and in reflection (18.5% with $R=5\%$) with a MO waveguide thickness close to the cut-off value. These measured values are highly competitive with the literature where, to our knowledge, maximum value of 15% [Reg+11] was experimentally demonstrated through MP structure and a value of 1.5% [Vor+20] through all-dielectric structure.

The measurements are in very good agreement with the simulations. However, due to fabrication and measurements imperfections, the simulated MO effects are higher than the measured ones (mainly noted for TMOKE). Therefore, some optimizations could be efficient to achieve larger MO effects.

Another all-dielectric structure studied in this work consists of a Si_3N_4 -MO grating deposited on a BK7 substrate. Large non-reciprocal MO effects were also demonstrated numerically and experimentally through this structure.

FR up to 0.8° was measured with $T=29\%$ ($\text{FoM}=0.43^\circ$), which results in an enhancement by a factor of 8 compared to the FR of a continuous MO film. The reached FR is higher than that demonstrated through the PR-MO structure, because the Si_3N_4 -MO structure is phase-matched.

LMOKE rotation up to 1.5° with $T=20\%$ were measured, resulting in a FoM value equal to 0.67° . This latter is smaller than that demonstrated through PR-MO structure due to the highest transmissivity of this latter.

And, TMOKE value up to 7.5% was measured in transmission with $T=70\%$ which is close to that measured with PR-MO structure.

Hence, we can say that the Si_3N_4 -MO structure is more efficient only for the Faraday effect compared to the PR-MO structure. The fabrication process of Si_3N_4 being complex and more expensive than the simple PR grating, this latter is more suitable for practical applications.

Therefore, the PR-MO structure is a simple all-dielectric MO device, able to enhance every MO effects with high optical response, especially the TMOKE due to the small FWHM of the transmittance dip (or reflectance peak), which is not the case of MP structures (large FWHM due to the plasmonic feature). The process of fabrication of the PR-MO structure is simpler than the structures presented in the literature [Vor+20; Poh+13]. For example, most of the works are based on the Bi:YIG, but due to its high crystallization temperature (higher than 700°) and lattice parameter mismatch, it is complex to deposit on common substrates (such as glass) with simple deposition processes.

In the final part of this chapter, we presented reciprocal intensity modulation effects which were evidenced during the measurements of the MO effects. They have been measured through the PR-MO structure, in different magnetic field configurations. It was demonstrated that these effects are related to the NPs since a coercive field in the intensity loop is present. However, the measurements and the simulations are not in agreement (except for the LRE at normal incidence): the measured values are higher than the simulated ones. Thus, the RE are not linked to the classical terms of the permittivity of the MO material. These effects are still under exploitation but as a first assumption we attribute them to magneto-refractive effects.

Conclusion and Future Works

From several years, the enhancement of the MO effects is taking lots of attention due to the wide applications of the MO activity in controlling light and sensing technologies. As mentioned in section I.3, different planar structures have been implemented to reach this objective. These structures can be divided into two main groups: magneto-plasmonic and all-dielectric structures. In MP structures, the excitation of eigenmodes of this latter, such as SPPs, LSPs, cavity modes and dielectric guided-modes, is responsible of the resonant enhancement of the MO response. However, in all-dielectric structures, the plasmon oscillations are not excited anymore, only TE and pure TM guided-mode are present. Furthermore, for maximum polarization rotation effects the phase matching condition should be achieved between dielectric TE and TM modes, by optimizing the opto-geometric parameters of the structures.

Some selected works from the literature are summarized in Tab.I.2 and Tab.I.3. They show that the best MO enhancements are obtained through simulations, underlying the difficulty of structures fabrication. Furthermore, due to the high absorption of the metal, the MO enhancements through MP structures are generally accompanied with lower optical response compared to all-dielectric structures.

The structures under study in this work are 1D-all dielectric guided mode resonance gratings. The basic principles of these structures were detailed in section I.2. For its simplicity, the adapted structure consists of a photoresist grating deposited on top of a MO film which is deposited on a glass substrate. A more complex all-dielectric structure was studied also in this work as a reference, consisting of alternating Si_3N_4 and MO material deposited on a BK7 substrate.

The MO composite consists of cobalt ferrite NPs embedded in a solid silica matrix, using a sol-gel approach. A major advantage of the MO composite is its ability to be deposited as uniform thin layers on large scale conventional substrates (glass, silicon, etc.), with simple coating processes (spin, dip coating, etc.), and with a 100°C thermal treatment, which is not the case of the ferrimagnet garnet family (YIG, Bi:YIG, etc.).

In Chap.II before GMR gratings elaboration, a special study of the MO composite

has been carried out in order to control well all its opto-geometrical and MO properties, and deduce the whole permittivity tensor of this material. Hence, the thickness, the complex refractive index and the MO activity of the composite were studied as a function of the NPs concentration. Then, the volume fraction and the refractive index of the own NPs were deduced. As a result, for a certain quantity of ferrofluid added in the MO-sol, the whole characteristics of the final MO film can be predicted before elaboration, and used therefore in the simulations for the structure design.

The numerical and experimental evidence of MO enhancements through the fabricated 1D-all dielectric GMR structures, were presented in Chap.III. First, numerical simulations were done in order to understand the behavior of the optical and MO responses of the PR-MO device, as a function of its opto-geometric parameters. As a result, the Faraday effect is maximum ($\theta_F = -0.7^\circ$ and $+0.4^\circ$) at the phase matching condition but with complex grating parameters. However, the phase matching condition disappears at oblique incidence where the LMOKE appears since this latter is zero at normal incidence.

The TMOKE is higher by increasing the AOI, by working close to the MO waveguide thickness cut-off value, and by increasing the refractive index shift between the grating and the MO film. This latter condition increases the transmittance (reflectance) resonance amplitude, and can be useful not only to increase the TMOKE signal but also the Faraday effect and LMOKE.

Significant enhancement of Faraday effect, LMOKE and especially TMOKE were experimentally achieved and verified by backward simulations. For PR-MO structure, the phase matching condition at normal incidence was not achieved due to fabrication limits decreasing hence the FR value. But, a FR equal to 0.22° was measured, resulting in an enhancement by a factor of 1.4 compared to the reference film. The reached FoM value is equal to 0.18° which is in the same order of magnitude compared to more complex structures used in the literature, taking into account that the used MO composite has off-diagonal elements with one and two orders of magnitude smaller compared to other works [CGMC15; Lei+16].

LMOKE rotation value up to 1.1° was reached in transmission at small AOI where TE and TM modes resonances with different diffraction orders (± 1 st) overlap. The reached FoM is equal to 0.83° , which is also competitive with the literature (experimentally 0.018° [Che+12] and numerically 2.53° [KB16]).

The main results of this work concern the TMOKE effect, for which the PR grating seems perfectly suited. Indeed, TMOKE values up to 9.5% and 18.5% were measured respectively in transmission ($T=80\%$) and in reflection ($R=5\%$), with a MO waveguide thickness close to the cut-off value. These measured values are highly competitive with the literature where, to our knowledge, maximum value of 1.5% [Vor+20] and 15% [Reg+11] were experimentally demonstrated respectively through all-dielectric and MP structures.

Moreover, reciprocal effects were observed through the PR-MO structure, in the three magnetic field configurations. High values of these effects were measured but do not agree with the simulations. In these latter, the RE are very weak compared to the measurements. Until now, we have no clear explanation about the origin of these effects. They are still under exploitation. As a first assumption, we attribute them to magneto-refractive effects.

Therefore, with a very simple PR-MO structure, different MO effects have been enhanced especially the TMOKE due to the small FWHM of the transmittance dip (or reflectance peak), with amplitudes at the state of the art or even beyond.

For the Si_3N_4 -MO structure, the phase matching condition was achieved at normal incidence. Large non-reciprocal MO effects were demonstrated numerically and experimentally through this structure ($\theta_F = 0.8^\circ$, $\theta_{LMOKE} = 1.5^\circ$ and $\delta = 7.3\%$). However, the fabrication process of Si_3N_4 -MO is longer, more complex and more expensive than the simple PR-MO structure. Hence, this latter is much more suitable for practical applications. It is a low cost device able to measure the different components of the magnetic field through polarization rotation and intensity modulation measurements. Hence, the PR-MO structure is promising for magnetic field sensing and in NDT, for large inspected areas since this structure can be fabricated on large scale substrates.

The significant results of this work enable us to open the field of new research works for the future:

- The RE should be further studied in order to understand well their origin. We observed in section III.5 that the RE can depend on the orientation of the NPs inside the MO film. Indeed, we mentioned that FRE and TRE are higher for the sample with out of plane \vec{B}_{gel} , compared to zero field sample. Hence, the first track to begin understanding the RE is to study properly the effects of the NPs orientations, by measuring the RE in different configurations for the different samples under gelation field.
- The refractive index shift between the grating and the MO film should be higher for larger transmittance resonance amplitude, hence higher MO effects. We mentioned in section III.1.3.2, that a value of TMOKE in transmission up to 37% was simulated for $n_{MO} = 1.74$ and $d_{MO} = 250$ nm (cut-off value). This is feasible by developing a new MO composite material with solid matrix owing higher refractive index than the silica, such as TiO_2 . Another approach is to keep the traditional MO composite but to work with grating material with refractive index higher than the PR, also such as TiO_2 . The advantage of this latter proposition is the possibility to excite cavity modes in the waveguide, increasing even more the light/MO material interaction.
- As mentioned in section II.1.2, NPs with median diameter of $D_0 = 9.2$ nm were used in the presented work. However, for magnetic field sensing applications, NPs with smaller diameters must be used in order to have a linear behavior between the MO effects (rotation and intensity), and the magnetic field at small values. Indeed, we mentioned in section II.1.5.4 that the width of the hysteresis loop is smaller by decreasing the $CoFe_2O_4$ NPs diameters. Hence, for the future work, the required diameter for the disappearance of the hysteresis loop must be identified.
- Instead of doing a spectral measurement for the MO effects, in other words changing each time the incident wavelength through a tunable laser, a simpler and faster measurement method can be implemented. It is based on the variation of the angle of incidence for a fixed wavelength by injecting an incident light with a certain angle aperture. The

reflected or transmitted signal can be then analyzed through a CCD detector to collect the angle dependence. Thanks to the coupling effect, this resonance analysis through the angle dependence is equivalent to the spectral one. This proposal can be a way of research for the future.

- As explained in section I.1.4.2, the biosensors are used to detect and identify dielectric media (such as gas, fluids, etc.). The MO-SPR biosensors are based on the TMOKE signal shift when the optical property of the dielectric media changes.

An interesting feature of the PR-MO structure is its sensitivity to the external medium (superstrate) refractive index. Fig. III.46a illustrates the TMOKE signal shift in reflection ($\Delta\delta$) upon superstrate refractive index (n_c) change. As seen in this figure, a TMOKE variation up to 48% is reached for a variation of 0.01 of the superstrate refractive index. This could be very interesting for a future field of research concerning a biosensing application.

Furthermore, in order to suppress the electromagnet employed to magnetize the device with reversible directions, we propose to use the remanent magnetization (M_r) of the MO composite. Its magnitude can be controlled by NPs orientation with MO films deposited under in-plane gelation magnetic field (see Fig. III.46b), and by employing larger NPs [Cho08; Nan16].

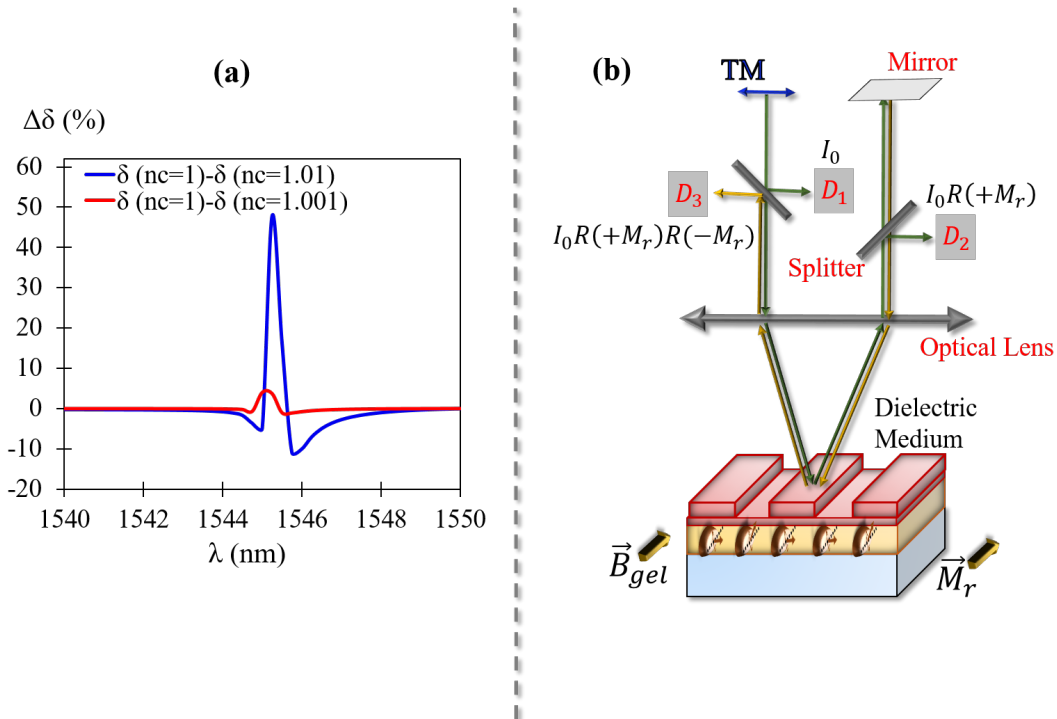


FIGURE III.46: Simulated spectrum of the TMOKE signal shift in reflection ($\Delta\delta(\%)$) upon superstrate refractive index (n_c) change, for TM polarization at AOI=2°. The structure under study have the same parameters than Fig. III.18 with $d_{MO} = 380$ nm (cut-off value). (b) A proposition of a simplified measurement setup for biosensing application. D is referred to detectors.

Then, to obtain both magnetization directions required for TMOKE, we propose the measurement setup illustrated on Fig.III.46b. It is described as follows: part of the TM-polarized incident light is directed towards the detector D_1 by a splitter. Hence, D_1 is referred to the incident intensity I_0 . The other part of the TM incident light is directed towards the PR-MO structure with oblique incidence, through an optical lens. After that, part of the reflected light by the GMR structure is analyzed by the detector D_2 which gives $I_0 R(+M_r)$. Hence, D_2 is referred to the reflected intensity I_+ subjected to a magnetization $+\vec{M}_r$. Then, a mirror is placed in order to redirect the other part of the reflected light towards the structure with an opposite AOI (in other words $-\vec{M}_r$). The detector D_3 gives $I_0 R(+M_r) R(-M_r)$. The TMOKE signal can be directly thus deduced from D_1 , D_2 and D_3 .

- Finally, for magnetic field sensing applications, one experimental setup should be implemented in the future for measuring different components of the magnetic field simultaneously. In the presented work, three MO setups were developed for detecting each magnetic field component.

Hence, a proposition for in-plane magnetic field sensing ($\vec{B}_{in} = \vec{B}_x + \vec{B}_y$) is illustrated on Fig.III.47. This setup is based on TMOKE measurements since this effect is very high especially in reflection, through the PR-MO structure. The strategy is to fabricate two perpendicular gratings on the same MO film. For each grating, the incidence plane is not the same in order to remain in TMOKE configuration. Thus, on each grating the magnetic field parallel to grating grooves and perpendicular to the incident plane can be measured (\vec{B}_x and \vec{B}_y). We should say that the TMOKE is very high compared to the LRE, neglecting the effect of this latter.

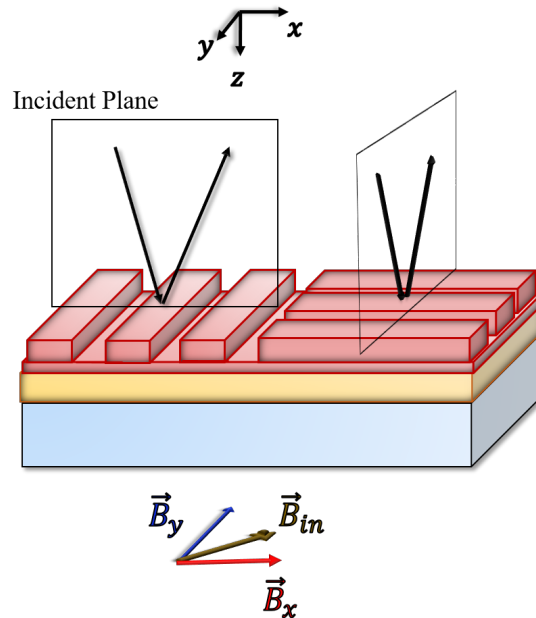


FIGURE III.47: A proposition of a simplified measurement setup for sensing the in-plane magnetic field ($\vec{B}_{in} = \vec{B}_x + \vec{B}_y$).

Bibliography

- [AB78] G. C. Aers and A. D. Boardman. “The theory of semiconductor magneto-plasmon polariton surface modes: Voigt geometry”. In: *Journal of Physics C: Solid State Physics* 11.5 (Mar. 1978), pp. 945–959. ISSN: 0022-3719. DOI: [10.1088/0022-3719/11/5/015](https://doi.org/10.1088/0022-3719/11/5/015).
- [AD+16] E. Abou Diwan et al. “Large spectral modification of the Faraday effect of 3D SiO₂/CoFe₂O₄ magneto-photonic crystals”. In: *Journal of Nanoscience and Nanotechnology* 16.9 (Sept. 2016), pp. 10160–10165. DOI: [10.1166/jnn.2016.12844](https://doi.org/10.1166/jnn.2016.12844).
- [Aic+03] T. Aichele et al. “Garnet layers prepared by liquid phase epitaxy for microwave and magneto-optical applications – a review”. In: *Crystal Research and Technology* 38.7-8 (2003), pp. 575–587. ISSN: 1521-4079. DOI: [10.1002/crat.200310071](https://doi.org/10.1002/crat.200310071).
- [Ala+11] T. Alasaarela et al. “Single-layer one-dimensional nonpolarizing guided-mode resonance filters under normal incidence”. In: *Optics Letters* 36.13 (July 2011), pp. 2411–2413. ISSN: 1539-4794. DOI: [10.1364/OL.36.002411](https://doi.org/10.1364/OL.36.002411).
- [Alb71] W. Albers, ed. *The Physics of Opto-Electronic Materials*. Springer US, 1971. ISBN: 978-1-4684-1949-8. DOI: [10.1007/978-1-4684-1947-4](https://doi.org/10.1007/978-1-4684-1947-4).
- [Ami+18] B. Amirsolaimani et al. “High sensitivity magnetometer using nanocomposite polymers with large magneto-optic response”. In: *Optics Letters* 43.19 (Oct. 2018), pp. 4615–4618. ISSN: 1539-4794. DOI: [10.1364/OL.43.004615](https://doi.org/10.1364/OL.43.004615).
- [And+07] W. Andrä et al. “Application of Magnetic Particles in Medicine and Biology”. In: *Handbook of Magnetism and Advanced Magnetic Materials*. American Cancer Society, 2007. ISBN: 978-0-470-02218-4.
- [Aos+10] K. Aoshima et al. “Submicron Magneto-Optical Spatial Light Modulation Device for Holographic Displays Driven by Spin-Polarized Electrons”. In: *Journal of Display Technology* 6.9 (Sept. 2010), pp. 374–380. ISSN: 1558-9323. DOI: [10.1109/JDT.2010.2058998](https://doi.org/10.1109/JDT.2010.2058998).

- [Arm+08] G. Armelles et al. "Localized surface plasmon resonance effects on the magneto-optical activity of continuous Au/Co/Au trilayers". In: *Optics Express* 16.20 (Sept. 2008), pp. 16104–16112. ISSN: 1094-4087. DOI: [10.1364/OE.16.016104](https://doi.org/10.1364/OE.16.016104).
- [Arm+09] G. Armelles et al. "Magnetoplasmonic nanostructures: systems supporting both plasmonic and magnetic properties". In: *Journal of Optics A: Pure and Applied Optics* 11.11 (Sept. 2009), p. 114023. ISSN: 1464-4258. DOI: [10.1088/1464-4258/11/11/114023](https://doi.org/10.1088/1464-4258/11/11/114023).
- [Bai+20] C. Bai et al. "Inductive Magnetic Nanoparticle Sensor Based on Microfluidic Chip Oil Detection Technology". In: *Micromachines* 11.2 (Feb. 2020). ISSN: 2072-666X. DOI: [10.3390/mi11020183](https://doi.org/10.3390/mi11020183).
- [Bar+17] M. G. Barsukova et al. "Magneto-Optical Response Enhanced by Mie Resonances in Nanoantennas". In: *ACS Photonics* 4.10 (Oct. 2017), pp. 2390–2395. DOI: [10.1021/acsphotonics.7b00783](https://doi.org/10.1021/acsphotonics.7b00783).
- [BB96] B. Berkovski and V. G. Bashtovoi. *Magnetic fluids and applications handbook*. New York; Wallingford: Begell House, Inc., 1996. ISBN: 978-1-56700-062-7.
- [BC03] C. C. Berry and A. S. Curtis. "Functionalisation of magnetic nanoparticles for applications in biomedicine". In: *Journal of Physics D: Applied Physics* 36.13 (June 2003), R198–R206. ISSN: 0022-3727. DOI: [10.1088/0022-3727/36/13/203](https://doi.org/10.1088/0022-3727/36/13/203).
- [BDZ07] V. I. Belotelov, L. L. Doskolovich, and A. K. Zvezdin. "Extraordinary magneto-optical effects and transmission through metal-dielectric plasmonic systems". In: *Physical Review Letters* 98.7 (Feb. 2007), p. 077401. DOI: [10.1103/PhysRevLett.98.077401](https://doi.org/10.1103/PhysRevLett.98.077401).
- [Bed+13] S. Bedanta et al. "Magnetic Nanoparticles: A Subject for Both Fundamental Research and Applications". In: *Journal of Nanomaterials* 2013 (Dec. 2013), p. 952540. DOI: [10.1155/2013/952540](https://doi.org/10.1155/2013/952540).
- [Bel+11] V. I. Belotelov et al. "Enhanced magneto-optical effects in magnetoplasmonic crystals". In: *Nature Nanotechnology* 6.6 (June 2011), pp. 370–376. ISSN: 1748-3395. DOI: [10.1038/nnano.2011.54](https://doi.org/10.1038/nnano.2011.54).
- [Bel+13] V. I. Belotelov et al. "Plasmon-mediated magneto-optical transparency". In: *Nature Communications* 4.1 (July 2013), pp. 1–7. ISSN: 2041-1723. DOI: [10.1038/ncomms3128](https://doi.org/10.1038/ncomms3128).
- [BFL16] V. N. Berzhansky, D. M. Filippov, and N. V. Lugovskoy. "Magneto-optical Visualization of Eddy Current Magnetic Fields". In: *Physics Procedia*. International Baltic Conference on Magnetism 82 (Jan. 2016) 82 (Jan. 2016), pp. 27–31. ISSN: 1875-3892. DOI: [10.1016/j.phpro.2016.05.006](https://doi.org/10.1016/j.phpro.2016.05.006).
- [BKB16] O. Borovkova, A. Kalish, and V. Belotelov. "Transverse magneto-optical Kerr effect in active magneto-plasmonic structures". In: *Optics Letters* 41.19 (Oct. 2016), pp. 4593–4596. ISSN: 1539-4794. DOI: [10.1364/OL.41.004593](https://doi.org/10.1364/OL.41.004593).

- [BQG86] G. Binnig, C. F. Quate, and Ch. Gerber. "Atomic force microscope". In: *Physical Review Letters* 56 (Mar. 1986), pp. 930–933. ISSN: 0031-9007. DOI: [10.1103/PhysRevLett.56.930](https://doi.org/10.1103/PhysRevLett.56.930). URL: <http://adsabs.harvard.edu/abs/1986PhRvL.56..930B> (visited on 08/13/2020).
- [Bra15] W. H. Bragg. "The Structure of Magnetite and the Spinel". In: *Nature* 95.2386 (July 1915), pp. 561–561. ISSN: 1476-4687. DOI: [10.1038/095561a0](https://doi.org/10.1038/095561a0).
- [Bri+92] C. J. Brinker et al. "Review of sol-gel thin film formation". In: *Journal of Non-Crystalline Solids*. Advanced Materials from Gels 147-148 (Jan. 1992), pp. 424–436. ISSN: 0022-3093. DOI: [10.1016/S0022-3093\(05\)80653-2](https://doi.org/10.1016/S0022-3093(05)80653-2).
- [BS13] C. J. Brinker and G. W. Scherer. *Sol-Gel Science: The Physics and Chemistry of Sol-Gel Processing*. 1 edition. Academic Press, Oct. 2013.
- [BTT06] B. Bai, J. Tervo, and J. Turunen. "Polarization conversion in resonant magneto-optic gratings". In: *New Journal of Physics* 8.9 (2006), p. 205. ISSN: 1367-2630. DOI: [10.1088/1367-2630/8/9/205](https://doi.org/10.1088/1367-2630/8/9/205).
- [Cai+10] J. M. Caicedo et al. "Large magnetorefractive effect in magnetite". In: *New Journal of Physics* 12.10 (Oct. 2010), p. 103023. ISSN: 1367-2630. DOI: [10.1088/1367-2630/12/10/103023](https://doi.org/10.1088/1367-2630/12/10/103023).
- [CGMC15] B. Caballero, A. García-Martín, and J.C. Cuevas. "Faraday effect in hybrid magneto plasmonic photonic crystals". In: *Optics Express* 23.17 (Aug. 2015), pp. 22238–22249. ISSN: 1094-4087. DOI: [10.1364/OE.23.022238](https://doi.org/10.1364/OE.23.022238).
- [CGMC16] B. Caballero, A. García-Martín, and J. C. Cuevas. "Hybrid Magnetoplasmonic Crystals Boost the Performance of Nanohole Arrays as Plasmonic Sensors". In: *ACS Photonics* 3.2 (Feb. 2016), pp. 203–208. DOI: [10.1021/acsphotonics.5b00658](https://doi.org/10.1021/acsphotonics.5b00658).
- [Cha+09] W. L. Chan et al. "A spatial light modulator for terahertz beams". In: *Applied Physics Letters* 94.21 (May 2009), p. 213511. ISSN: 0003-6951. DOI: [10.1063/1.3147221](https://doi.org/10.1063/1.3147221).
- [Cha+82] J. Chandezon et al. "Multicoated gratings: a differential formalism applicable in the entire optical region". In: *JOSA* 72.7 (July 1982), pp. 839–846. DOI: [10.1364/JOSA.72.000839](https://doi.org/10.1364/JOSA.72.000839).
- [Che+12] A. V. Chetvertukhin et al. "Magneto-optical Kerr effect enhancement at the Wood's anomaly in magnetoplasmonic crystals". In: *Journal of Magnetism and Magnetic Materials*. Fifth Moscow international symposium on magnetism 324.21 (Oct. 2012), pp. 3516–3518. ISSN: 0304-8853. DOI: [10.1016/j.jmmm.2012.02.079](https://doi.org/10.1016/j.jmmm.2012.02.079).
- [Che+20] A. M. Chernyak et al. "Bound States in the Continuum in Magnetophotonic Metasurfaces". In: *JETP Letters* 111.1 (Jan. 2020), pp. 46–49. ISSN: 1090-6487. DOI: [10.1134/S0021364020010105](https://doi.org/10.1134/S0021364020010105).

- [Cho08] F. Choueikani. “Étude des potentialités de couches minces sol-gel dopées par des nanoparticules magnétiques pour la réalisation de composants magnéto-optiques intégrés”. PhD thesis. Université Jean Monnet - Saint-Etienne, May 2008.
- [Cho15] T. C. Choy. *Effective Medium Theory: Principles and Applications*. Oxford University Press, Dec. 2015. ISBN: 978-0-19-101518-2.
- [Chr+18] A. Christofi et al. “Giant enhancement of Faraday rotation due to electromagnetically induced transparency in all-dielectric magneto-optical metasurfaces”. In: *Optics Letters* 43.8 (Apr. 2018), pp. 1838–1841. ISSN: 1539-4794. DOI: [10.1364/OL.43.001838](https://doi.org/10.1364/OL.43.001838).
- [Dec03] J. M. Decitre. “Modélisation électromagnétique et réalisation d’un dispositif d’imagerie magnéto-optique quantitatif pour la caractérisation des endommagements des structures aéronautiques en alliage léger”. PhD thesis. École normale supérieure Paris-Saclay, 2003.
- [Den+06] Y. Deng et al. “Characterization of Magneto-Optic Imaging Data for Aircraft Inspection”. In: *IEEE Transactions on Magnetics* 42.10 (Oct. 2006). Conference Name: IEEE Transactions on Magnetics, pp. 3228–3230. ISSN: 1941-0069. DOI: [10.1109/TMAG.2006.878419](https://doi.org/10.1109/TMAG.2006.878419).
- [DF08] P. Drexler and P. Fiala. “Utilization of Faraday Mirror in Fiber Optic Current Sensors”. In: *Radioengineering* 17.4 (Dec. 2008). ISSN: 1210-2512.
- [Dir08] Y. L. Diraison. “Imagerie à courants de Foucault pour l’évaluation non-destructive de structures rivetées aéronautiques”. PhD thesis. École normale supérieure de Cachan - ENS Cachan, Nov. 2008.
- [DRD90] M. N. Deeter, A. H. Rose, and G. W. Day. “Fast, sensitive magnetic-field sensors based on the Faraday effect in YIG”. In: *Journal of Lightwave Technology* 8.12 (Dec. 1990), pp. 1838–1842. ISSN: 0733-8724. DOI: [10.1109/50.62880](https://doi.org/10.1109/50.62880).
- [DSN18] V. Dmitriev, C. M. Santos, and C. Nascimento. “Extremely high Faraday and Kerr rotations and extraordinary optical transmission in four-layer dielectric-metal strips-dielectric-Bi:YIG planar structure”. In: *Journal of Microwaves, Optoelectronics and Electromagnetic Applications* 17.1 (Mar. 2018), pp. 44–52. ISSN: 2179-1074. DOI: [10.1590/2179-10742018v17i111107](https://doi.org/10.1590/2179-10742018v17i111107).
- [DV+17] B. F. Diaz-Valencia et al. “Enhanced Transverse Magneto-Optical Kerr Effect in Magnetoplasmonic Crystals for the Design of Highly Sensitive Plasmonic (Bio)sensing Platforms”. In: *ACS Omega* 2.11 (Nov. 2017), pp. 7682–7685. ISSN: 2470-1343. DOI: [10.1021/acsomega.7b01458](https://doi.org/10.1021/acsomega.7b01458).
- [Dya+19] S. Dyakov et al. “Wide band enhancement of the transverse magneto-optical Kerr effect in magnetite-based plasmonic crystals”. In: *Physical review. B, Condensed matter* 100 (Dec. 2019), p. 214411. DOI: [10.1103/PhysRevB.100.214411](https://doi.org/10.1103/PhysRevB.100.214411).
- [Ebb+98] T. W. Ebbesen et al. “Extraordinary optical transmission through subwavelength hole arrays”. In: *Nature* 391.6668 (Feb. 1998), pp. 667–669. ISSN: 1476-4687. DOI: [10.1038/35570](https://doi.org/10.1038/35570).

- [Fan+11] K. Fang et al. "Ultracompact nonreciprocal optical isolator based on guided resonance in a magneto-optical photonic crystal slab". In: *Optics Letters* 36.21 (Nov. 2011), pp. 4254–4256. ISSN: 1539-4794. DOI: [10.1364/OL.36.004254](https://doi.org/10.1364/OL.36.004254).
- [Fed+04] A. A. Fedyanin et al. "Phase-matched magnetization-induced second-harmonic generation in yttrium-iron-garnet magnetophotonic crystals". In: *IEEE Transactions on Magnetics* 40.4 (July 2004). Conference Name: IEEE Transactions on Magnetics, pp. 2850–2852. ISSN: 1941-0069. DOI: [10.1109/TMAG.2004.832805](https://doi.org/10.1109/TMAG.2004.832805).
- [Fit+93] G. L. Fitzpatrick et al. "Magneto-optic/eddy current imaging of aging aircraft: A new NDI technique". In: *Materials Evaluation* 51:12 (Dec. 1993). ISSN: 0025-5327.
- [Fit+96] G. L. Fitzpatrick et al. "Magneto-Optic/Eddy Current Imaging of Subsurface Corrosion and Fatigue Cracks in Aging Aircraft". In: *Review of Progress in Quantitative Nondestructive Evaluation: Volume 15A*. Ed. by Donald O. Thompson and Dale E. Chimenti. Boston, MA: Springer US, 1996, pp. 1159–1166. ISBN: 978-1-4613-0383-1. DOI: [10.1007/978-1-4613-0383-1_151](https://doi.org/10.1007/978-1-4613-0383-1_151).
- [Flo+15] D. Floess et al. "Tunable and switchable polarization rotation with non-reciprocal plasmonic thin films at designated wavelengths". In: *Light: Science & Applications* 4.5 (May 2015), e284. ISSN: 2047-7538. DOI: [10.1038/lsa.2015.57](https://doi.org/10.1038/lsa.2015.57).
- [Flo+17] D. Floess et al. "Plasmonic analog of electromagnetically induced absorption leads to giant thin film Faraday rotation of 14°". In: *Physical Review X* 7.2 (June 2017), p. 021048. DOI: [10.1103/PhysRevX.7.021048](https://doi.org/10.1103/PhysRevX.7.021048).
- [Fre68] M. Freiser. "A survey of magneto-optic effects". In: *IEEE Transactions on Magnetics* 4.2 (June 1968). Conference Name: IEEE Transactions on Magnetics, pp. 152–161. ISSN: 1941-0069. DOI: [10.1109/TMAG.1968.1066210](https://doi.org/10.1109/TMAG.1968.1066210).
- [FSF20] A. Yu. Frolov, M. R. Shcherbakov, and A. A. Fedyanin. "Dark mode enhancing magneto-optical Kerr effect in multilayer magnetoplasmonic crystals". In: *Physical Review B* 101.4 (Jan. 2020), p. 045409. DOI: [10.1103/PhysRevB.101.045409](https://doi.org/10.1103/PhysRevB.101.045409).
- [FSW77] P. E. Ferguson, O. M. Stafsudd, and R. F. Wallis. "Surface magnetoplasma waves in nickel". In: *Physica B+C* 86-88 (Jan. 1977), pp. 1403–1405. ISSN: 0378-4363. DOI: [10.1016/0378-4363\(77\)90930-5](https://doi.org/10.1016/0378-4363(77)90930-5).
- [Fuj+99] J. Fujita et al. "Observation of optical isolation based on nonreciprocal phase shift in a Mach-Zehnder interferometer". In: *Applied Physics Letters* 75.7 (Aug. 1999), pp. 998–1000. ISSN: 0003-6951. DOI: [10.1063/1.124949](https://doi.org/10.1063/1.124949).
- [Gar17] J. P. Garayt. "Etude de la réalisation d'un isolateur optique intégré sur verre". PhD thesis. Université Jean Monnet - Saint-Etienne, Oct. 2017.
- [GD+07] J. B. González-Díaz et al. "Surface-magnetoplasmon nonreciprocity effects in noble-metal/ferromagnetic heterostructures". In: *Physical Review B* 76.15 (Oct. 2007), p. 153402. DOI: [10.1103/PhysRevB.76.153402](https://doi.org/10.1103/PhysRevB.76.153402).

- [GD+10] J. B. González-Díaz et al. "Cobalt dependence of the magneto-optical response in magnetoplasmonic nanodisks". In: *Applied Physics Letters* 97.4 (July 2010), p. 043114. ISSN: 0003-6951. DOI: [10.1063/1.3474617](https://doi.org/10.1063/1.3474617).
- [GMGGVS11] J. García-Martín, J. Gomez-Gil, and E. Vázquez-Sánchez. "Non-Destructive Techniques Based on Eddy Current Testing". In: *Sensors (Basel, Switzerland)* 11 (Dec. 2011), pp. 2525–65. DOI: [10.3390/s110302525](https://doi.org/10.3390/s110302525).
- [Gru+10] A. A. Grunin et al. "Surface-plasmon-induced enhancement of magneto-optical Kerr effect in all-nickel subwavelength nanogratings". In: *Applied Physics Letters* 97.26 (Dec. 2010), p. 261908. ISSN: 0003-6951. DOI: [10.1063/1.3533260](https://doi.org/10.1063/1.3533260).
- [Gru+12] A. A. Grunin et al. "Magnetoplasmonic nanostructures based on nickel inverse opal slabs". In: *Journal of Applied Physics* 111.7 (Mar. 2012), 07A948. ISSN: 0021-8979. DOI: [10.1063/1.3680175](https://doi.org/10.1063/1.3680175).
- [GTA85] M. Gomi, T. Tanida, and M. Abe. "rf sputtering of highly Bi-substituted garnet films on glass substrates for magneto-optic memory". In: *Journal of Applied Physics* 57.8 (Apr. 1985), pp. 3888–3890. ISSN: 0021-8979. DOI: [10.1063/1.334905](https://doi.org/10.1063/1.334905).
- [Hal+13] L. Halagačka et al. "Coupled mode enhanced giant magnetoplasmonics transverse Kerr effect". In: *Optics Express* 21.19 (Sept. 2013), pp. 21741–21755. ISSN: 1094-4087. DOI: [10.1364/OE.21.021741](https://doi.org/10.1364/OE.21.021741).
- [Hal+18] L. Halagačka et al. "Magnetoplasmonic nanograting geometry enables optical nonreciprocity sign control". In: *Optics Express* 26.24 (Nov. 2018), pp. 31554–31566. ISSN: 1094-4087. DOI: [10.1364/OE.26.031554](https://doi.org/10.1364/OE.26.031554).
- [Has+01] E. Hasmonay et al. "Alternating magneto-birefringence of ionic ferrofluids in crossed fields". In: *The European Physical Journal B* 21.1 (May 2001), pp. 19–29. ISSN: 1434-6028, 1434-6036. DOI: [10.1007/s100510170208](https://doi.org/10.1007/s100510170208).
- [Has+98] E. Hasmonay et al. "Static magneto-optical birefringence of size-sorted γ -Fe₂O₃ nanoparticles". In: *The European Physical Journal B - Condensed Matter and Complex Systems* 5.4 (Nov. 1998), pp. 859–867. ISSN: 1434-6036. DOI: [10.1007/s100510050512](https://doi.org/10.1007/s100510050512).
- [Ign+16] D. O. Ignatyeva et al. "Magneto-optical plasmonic heterostructure with ultra-narrow resonance for sensing applications". In: *Scientific Reports* 6 (June 2016). ISSN: 2045-2322. DOI: [10.1038/srep28077](https://doi.org/10.1038/srep28077).
- [Ino+06] M. Inoue et al. "Magnetophotonic crystals". In: *Journal of Physics D: Applied Physics* 39.8 (Mar. 2006), R151. ISSN: 0022-3727. DOI: [10.1088/0022-3727/39/8/R01](https://doi.org/10.1088/0022-3727/39/8/R01).
- [Jam+01] D. Jamon et al. "Optical investigation of γ -Fe₂O₃ nanoparticle-doped silica gel matrix for birefringent components". In: *Magnetics, IEEE Transactions on* 37 (Oct. 2001), pp. 3803–3806. DOI: [10.1109/20.952748](https://doi.org/10.1109/20.952748).

- [Jam+09] D. Jamon et al. "Experimental investigation on the magneto-optic effects of ferrofluids via dynamic measurements". In: *Journal of Magnetism and Magnetic Materials* (Jan. 2009), pp. 1148–1154. DOI: [10.1016/j.jmmm.2008.10.038](https://doi.org/10.1016/j.jmmm.2008.10.038).
- [Jou+08] A. L. Joudrier et al. "Direct bonding conditions of ferrite garnet layer on ion-exchanged glass waveguides". In: *physica status solidi (a)* 205.10 (2008), pp. 2313–2316. ISSN: 1862-6319. DOI: [10.1002/pssa.200778801](https://doi.org/10.1002/pssa.200778801).
- [JP06] P. Y. Joubert and J. Pinassaud. "Linear magneto-optic imager for non-destructive evaluation". In: *Sensors and Actuators A: Physical*. EMSA 2004 129.1 (May 2006), pp. 126–130. ISSN: 0924-4247. DOI: [10.1016/j.sna.2005.11.028](https://doi.org/10.1016/j.sna.2005.11.028).
- [Kal+18] A. N. Kalish et al. "Magnetoplasmonic quasicrystals: an approach for multi-band magneto-optical response". In: *Optica* 5.5 (May 2018), pp. 617–623. ISSN: 2334-2536. DOI: [10.1364/OPTICA.5.000617](https://doi.org/10.1364/OPTICA.5.000617).
- [KB16] A. Kalish and V. Belotelov. "Magneto-Optical Effects for Detection of In-Plane Magnetization in Plasmonic Crystals". In: *Physics of the Solid State* 58 (Aug. 2016), pp. 1563–1572. DOI: [10.1134/S1063783416080163](https://doi.org/10.1134/S1063783416080163).
- [KDG10] V. V. Kruglyak, S. O. Demokritov, and D. Grundler. "Magnonics". In: *Journal of Physics D: Applied Physics* 43.26 (June 2010), p. 264001. ISSN: 0022-3727. DOI: [10.1088/0022-3727/43/26/264001](https://doi.org/10.1088/0022-3727/43/26/264001).
- [Kek+13] R. Kekesi et al. "3D magneto-photon crystal made with cobalt ferrite nanoparticles silica composite structured as inverse opal". In: *Optical Materials Express* 3.7 (July 2013), pp. 935–947. ISSN: 2159-3930. DOI: [10.1364/OME.3.000935](https://doi.org/10.1364/OME.3.000935).
- [Kha+07] A. B. Khanikaev et al. "Anomalous Faraday Effect of a system with extraordinary optical transmittance". In: *Optics Express* 15.11 (May 2007), pp. 6612–6622. ISSN: 1094-4087. DOI: [10.1364/OE.15.006612](https://doi.org/10.1364/OE.15.006612).
- [Khr+19] A. E. Khramova et al. "Resonances of the magneto-optical intensity effect mediated by interaction of different modes in a hybrid magnetoplasmonic heterostructure with gold nanoparticles". In: *Optics Express* 27.23 (Nov. 2019), pp. 33170–33179. ISSN: 1094-4087. DOI: [10.1364/OE.27.033170](https://doi.org/10.1364/OE.27.033170).
- [KJL01] A. Koudriavtsev, R. F. Jameson, and W. Linert. "Maxwell - Boltzmann Statistics". In: *The Law of Mass Action*. Ed. by Andrei Koudriavtsev, Reginald F. Jameson, and Wolfgang Linert. Berlin, Heidelberg: Springer, 2001, pp. 1–42. ISBN: 978-3-642-56770-4. DOI: [10.1007/978-3-642-56770-4_1](https://doi.org/10.1007/978-3-642-56770-4_1).
- [Kny+18] G. A. Knyazev et al. "Magnetoplasmonic Crystals for Highly Sensitive Magnetometry". In: *ACS Photonics* 5.12 (Dec. 2018), pp. 4951–4959. DOI: [10.1021/acsp Photonics.8b01135](https://doi.org/10.1021/acsp Photonics.8b01135).
- [Kos+13] N. Kostylev et al. "Plasmon-assisted high reflectivity and strong magneto-optical Kerr effect in permalloy gratings". In: *Applied Physics Letters* 102.12 (Mar. 2013), p. 121907. ISSN: 0003-6951. DOI: [10.1063/1.4798657](https://doi.org/10.1063/1.4798657).

- [Kre+13] L. E. Kreilkamp et al. "Waveguide-Plasmon Polaritons Enhance Transverse Magneto-Optical Kerr Effect". In: *Physical Review X* 3.4 (Nov. 2013), p. 041019. DOI: [10.1103/PhysRevX.3.041019](https://doi.org/10.1103/PhysRevX.3.041019).
- [Kuh13] E. Kuhn. "Contrôle non destructif d'un matériau excité par une onde acoustique ou thermique, observation par thermographie". PhD thesis. Paris 10, Dec. 2013.
- [Lac99] E. T. Lacheisserie. *Magnétisme. : Volume 2, Matériaux et applications*. Grenoble: Presses Universitaires de Grenoble, Aug. 1999. ISBN: 978-2-7061-0832-7.
- [Lan05] P. Langevin. "Sur la théorie du magnétisme". In: *Journal de Physique Théorique et Appliquée* 4.1 (1905), pp. 678–693. ISSN: 0368-3893. DOI: [10.1051/jphysap:019050040067800](https://doi.org/10.1051/jphysap:019050040067800).
- [Lei+08] S. Leitenmeier et al. "Studies on the growth of epitaxial bismuth-substituted iron garnet on gadolinium gallium garnet single crystals by pulsed laser deposition". In: *Journal of Crystal Growth* 310.24 (Dec. 2008), pp. 5392–5401. ISSN: 0022-0248. DOI: [10.1016/j.jcrysgro.2008.08.058](https://doi.org/10.1016/j.jcrysgro.2008.08.058).
- [Lei+16] C. Lei et al. "Enhancement of magneto-optical Faraday effects and extraordinary optical transmission in a tri-layer structure with rectangular annular arrays". In: *Optics Letters* 41.4 (Feb. 2016), pp. 729–732. ISSN: 1539-4794. DOI: [10.1364/OL.41.000729](https://doi.org/10.1364/OL.41.000729).
- [Len96] J. Lenglet. "Generation de second harmonique et diffusion rayleigh forcee dans les colloides magnetiques". PhD thesis. Paris 7, Jan. 1996.
- [Li+16] D. Li et al. "Plasmon-enhanced magneto-optical activity in a nanostructure with circle annular arrays". In: *JOSA B* 33.5 (May 2016), pp. 922–927. ISSN: 1520-8540. DOI: [10.1364/JOSAB.33.000922](https://doi.org/10.1364/JOSAB.33.000922).
- [Li+18] D. Li et al. "Plasmonics Resonance Enhance Magneto-Optical Effects Through Metallic Sub-wavelength Grating with Bismuth Iron Garnet Slab". In: *Plasmonics* 13.1 (Feb. 2018), pp. 55–62. ISSN: 1557-1963. DOI: [10.1007/s11468-016-0483-z](https://doi.org/10.1007/s11468-016-0483-z).
- [Li98] L. Li. "Reformulation of the fourier modal method for surface-relief gratings made with anisotropic materials". In: *Journal of Modern Optics* 45.7 (July 1998), pp. 1313–1334. ISSN: 0950-0340. DOI: [10.1080/09500349808230632](https://doi.org/10.1080/09500349808230632).
- [Liu+09] J. P. Liu et al., eds. *Nanoscale Magnetic Materials and Applications*. Springer US, 2009. ISBN: 978-0-387-85598-1. DOI: [10.1007/978-0-387-85600-1](https://doi.org/10.1007/978-0-387-85600-1).
- [Liu05] J. M. Liu. *Photonic Devices*. Cambridge ; New York: Cambridge University Press, Apr. 2005. ISBN: 978-0-521-55195-3.
- [Lux+06] R. Lux et al. "Pulsed-laser deposition and growth studies of Bi₃Fe₅O₁₂ thin films". In: *Journal of Applied Physics* 100.11 (Dec. 2006), p. 113511. ISSN: 0021-8979. DOI: [10.1063/1.2399322](https://doi.org/10.1063/1.2399322).
- [Mai07] S. Maier. *Plasmonics: fundamentals and applications*. Springer, 2007. ISBN: 978-0-387-37825-1.

- [Man+14] M. G. Manera et al. "Enhanced antibody recognition with a magneto-optic surface plasmon resonance (MO-SPR) sensor". In: *Biosensors & Bioelectronics* 58 (Aug. 2014), pp. 114–120. ISSN: 1873-4235. DOI: [10.1016/j.bios.2014.02.003](https://doi.org/10.1016/j.bios.2014.02.003).
- [Man+17] M. G. Manera et al. "Functional magneto-plasmonic biosensors transducers: Modelling and nanoscale analysis". In: *Sensors and Actuators B: Chemical* 239 (Feb. 2017), pp. 100–112. ISSN: 0925-4005. DOI: [10.1016/j.snb.2016.07.128](https://doi.org/10.1016/j.snb.2016.07.128).
- [Mar+14] H. Marinchio et al. "Magneto-optical Kerr effect in resonant subwavelength nanowire gratings". In: *New Journal of Physics* 16.1 (Jan. 2014), p. 015007. ISSN: 1367-2630. DOI: [10.1088/1367-2630/16/1/015007](https://doi.org/10.1088/1367-2630/16/1/015007).
- [Mas81] R. Massart. "Preparation of aqueous magnetic liquids in alkaline and acidic media". In: *IEEE Transactions on Magnetics* 17.2 (Mar. 1981). Conference Name: IEEE Transactions on Magnetics, pp. 1247–1248. ISSN: 1941-0069. DOI: [10.1109/TMAG.1981.1061188](https://doi.org/10.1109/TMAG.1981.1061188).
- [MBK14] I. S. Maksymov, J. Bacri, and M. Kostylev. "Transverse magneto-optical Kerr effect in subwavelength dielectric gratings". In: *Optics Express* 22.7 (Apr. 2014), pp. 8720–8725. ISSN: 1094-4087. DOI: [10.1364/OE.22.008720](https://doi.org/10.1364/OE.22.008720).
- [MCB01] T. Malvin Carl and S. Bahaa. *Fundamentals of Photonics*. Hoboken, N.J.: Wiley-Interscience, 2001. ISBN: 978-0-471-35832-9.
- [MG81] M. G. Moharam and T. K. Gaylord. "Rigorous coupled-wave analysis of planar-grating diffraction". EN. In: *JOSA* 71.7 (July 1981), pp. 811–818. DOI: [10.1364/JOSA.71.000811](https://doi.org/10.1364/JOSA.71.000811).
- [MJ07] D. S. Mathew and R. S. Juang. "An overview of the structure and magnetism of spinel ferrite nanoparticles and their synthesis in microemulsions". In: *Chemical Engineering Journal* 129.1 (May 2007), pp. 51–65. ISSN: 1385-8947. DOI: [10.1016/j.cej.2006.11.001](https://doi.org/10.1016/j.cej.2006.11.001).
- [MMH04] A. F. Michels, T. Menegotto, and F. Horowitz. "Interferometric monitoring of dip coating". In: *Applied Optics* 43.4 (Feb. 2004), pp. 820–823. ISSN: 2155-3165. DOI: [10.1364/AO.43.000820](https://doi.org/10.1364/AO.43.000820).
- [MS09] T. Mizumoto and Y. Shoji. "Optical Isolator with SOI Waveguide". In: *Optical Fiber Communication Conference and National Fiber Optic Engineers Conference* (2009), paper OWV3. Optical Society of America, Mar. 2009, OWV3. DOI: [10.1364/OFC.2009.0WV3](https://doi.org/10.1364/OFC.2009.0WV3).
- [Nad+19] I. Nadinov et al. "Limits of the magneto-optical properties of Bi: YIG films prepared on silica by metal organic decomposition". In: *Ceramics International* 45.17, Part A (Dec. 2019), pp. 21409–21412. ISSN: 0272-8842. DOI: [10.1016/j.ceramint.2019.07.129](https://doi.org/10.1016/j.ceramint.2019.07.129).
- [Nad19] I. Nadinov. "Fonctionnalisation de fibres optiques par des grenats pour les applications magnéto-optiques". PhD thesis. Strasbourg, Dec. 2019.

- [Nan16] L. Nandiguim. "Etude du comportement magnétique et spectral de l'effet Faraday dans des oxydes métalliques dopés par des nanoparticules magnétiques de ferrite de cobalt". PhD thesis. Université Jean Monnet - Saint-Etienne, May 2016.
- [NCJ91] Y. N. Ning, B. C. B. Chu, and D. A. Jackson. "Miniature Faraday current sensor based on multiple critical angle reflections in a bulk-optic ring". In: *Optics Letters* 16.24 (Dec. 1991), pp. 1996–1998. ISSN: 1539-4794. DOI: [10.1364/OL.16.001996](https://doi.org/10.1364/OL.16.001996).
- [Nev+02] S. Neveu et al. "Size-Selective Chemical Synthesis of Tartrate Stabilized Cobalt Ferrite Ionic Magnetic Fluid". In: *Journal of Colloid and Interface Science* 255.2 (Nov. 2002), pp. 293–298. ISSN: 0021-9797. DOI: [10.1006/jcis.2002.8679](https://doi.org/10.1006/jcis.2002.8679).
- [New+08] D. M. Newman et al. "Magneto-optic behaviour in the presence of surface plasmons". In: *Journal of Physics: Condensed Matter* 20.34 (Aug. 2008), p. 345230. ISSN: 0953-8984. DOI: [10.1088/0953-8984/20/34/345230](https://doi.org/10.1088/0953-8984/20/34/345230).
- [Nis15] S. Nishikawa. "Structure of Some Crystals of Spinel Group". In: *Tokyo Sugaku-Buturigakkwai Kizi Dai 2 Ki* 8.7 (1915), 199–209_1. DOI: [10.11429/ptmps1907.8.7_199](https://doi.org/10.11429/ptmps1907.8.7_199).
- [NSM04] P. Novotný, P. Sajdl, and P. Macháč. "A magneto-optic imager for NDT applications". In: *NDT & E International* 37.8 (Dec. 2004), pp. 645–649. ISSN: 0963-8695. DOI: [10.1016/j.ndteint.2004.05.002](https://doi.org/10.1016/j.ndteint.2004.05.002).
- [Onb+16] M. C. Onbasli et al. "Optical and magneto-optical behavior of Cerium Yttrium Iron Garnet thin films at wavelengths of 200–1770 nm". In: *Scientific Reports* 6 (Mar. 2016), p. 23640. ISSN: 2045-2322. DOI: [10.1038/srep23640](https://doi.org/10.1038/srep23640).
- [Pet08] D. S. Peterson. "Sol–Gel Technique". In: *Encyclopedia of Microfluidics and Nanofluidics*. Ed. by D. Li. Boston, MA: Springer US, 2008, pp. 1870–1874. ISBN: 978-0-387-48998-8. DOI: [10.1007/978-0-387-48998-8_1432](https://doi.org/10.1007/978-0-387-48998-8_1432).
- [Poh+13] M. Pohl et al. "Tuning of the transverse magneto-optical Kerr effect in magneto-plasmonic crystals". In: *New Journal of Physics* 15.7 (July 2013), p. 075024. ISSN: 1367-2630. DOI: [10.1088/1367-2630/15/7/075024](https://doi.org/10.1088/1367-2630/15/7/075024).
- [Rad+01] U. Radtke et al. "Application of magneto-optical method for real-time visualization of eddy currents with high spatial resolution for nondestructive testing". In: *Optics and Lasers in Engineering* 36.3 (Sept. 2001), pp. 251–268. ISSN: 0143-8166. DOI: [10.1016/S0143-8166\(01\)00052-5](https://doi.org/10.1016/S0143-8166(01)00052-5).
- [Reg+11] D. Regatos et al. "Suitable combination of noble/ferromagnetic metal multilayers for enhanced magneto-plasmonic biosensing". In: *Optics Express* 19.9 (Apr. 2011), pp. 8336–8346. ISSN: 1094-4087. DOI: [10.1364/OE.19.008336](https://doi.org/10.1364/OE.19.008336).
- [Riz+19] C. Rizal et al. "Surface Plasmon Resonance (SPR) to Magneto-Optic SPR". In: *Condensed Matter* 4.2 (June 2019), p. 50. DOI: [10.3390/condmat4020050](https://doi.org/10.3390/condmat4020050).

- [Roy+04] F. Royer et al. "New technological approach in phase-matched magneto-optic planar waveguide realization". In: *Advances in Optical Thin Films*. Vol. 5250. International Society for Optics and Photonics, Feb. 2004, pp. 72–80. DOI: [10.1117/12.512915](https://doi.org/10.1117/12.512915).
- [Roy+20] F. Royer et al. "Enhancement of Both Faraday and Kerr Effects with an All-Dielectric Grating Based on a Magneto-Optical Nanocomposite Material". In: *ACS Omega* 5.6 (Feb. 2020), pp. 2886–2892. ISSN: 2470-1343. DOI: [10.1021/acsomega.9b03728](https://doi.org/10.1021/acsomega.9b03728).
- [Roy04] F. Royer. "Etude et application des effets magnéto-optiques dans des couches minces sol-gel dopées à l'aide de nanoparticules magnétiques". PhD thesis. Grenoble INPG, Jan. 2004.
- [RPH18] C. Rizal, S. Pisana, and I. Hrvoic. "Improved Magneto-Optic Surface Plasmon Resonance Biosensors". In: *Photonics* 5.3 (Sept. 2018), p. 15. DOI: [10.3390/photonics5030015](https://doi.org/10.3390/photonics5030015).
- [RR+19] R. M. Rowan-Robinson et al. "Thickness dependent enhancement of the polar Kerr rotation in Co magnetoplasmonic nanostructures". In: *AIP Advances* 9.2 (Feb. 2019), p. 025317. DOI: [10.1063/1.5079713](https://doi.org/10.1063/1.5079713).
- [RSF97] D. Rosenblatt, A. Sharon, and A. A. Friesem. "Resonant grating waveguide structures". In: *IEEE Journal of Quantum Electronics* 33.11 (Nov. 1997), pp. 2038–2059. ISSN: 0018-9197. DOI: [10.1109/3.641320](https://doi.org/10.1109/3.641320).
- [San+06] T. Sang et al. "Resonant excitation analysis of sub-wavelength dielectric grating". In: *Journal of Optics A: Pure and Applied Optics* 8.1 (2006), p. 62. ISSN: 1464-4258. DOI: [10.1088/1464-4258/8/1/009](https://doi.org/10.1088/1464-4258/8/1/009).
- [Sch03] U. Schubert. "7.10 - Sol-Gel Processing of Metal Compounds". In: *Comprehensive Coordination Chemistry II*. Ed. by J. A. McCleverty and T. J. Meyer. Oxford: Pergamon, Jan. 2003, pp. 629–656. ISBN: 978-0-08-043748-4. DOI: [10.1016/B0-08-043748-6/06213-7](https://doi.org/10.1016/B0-08-043748-6/06213-7).
- [SCH10] A. A. Serga, A. V. Chumak, and B. Hillebrands. "YIG magnonics". In: *Journal of Physics D: Applied Physics* 43.26 (June 2010), p. 264002. ISSN: 0022-3727. DOI: [10.1088/0022-3727/43/26/264002](https://doi.org/10.1088/0022-3727/43/26/264002).
- [Scr88] L. E. Scriven. "Physics and Applications of DIP Coating and Spin Coating". In: *MRS Online Proceedings Library Archive* 121 (1988). ISSN: 0272-9172, 1946-4274. DOI: [10.1557/PROC-121-717](https://doi.org/10.1557/PROC-121-717).
- [Sek+99] T. Sekijima et al. "Optical Faraday rotator using Ce-substituted fibrous YIG single crystal grown by floating-zone method with YAG laser heating". In: *IEEE Transactions on Microwave Theory and Techniques* 47.12 (Dec. 1999). Conference Name: IEEE Transactions on Microwave Theory and Techniques, pp. 2294–2298. ISSN: 1557-9670. DOI: [10.1109/22.808973](https://doi.org/10.1109/22.808973).
- [Sep+06] B. Sepúlveda et al. "Highly sensitive detection of biomolecules with the magneto-optic surface-plasmon-resonance sensor". In: *Optics Letters* 31.8 (Apr. 2006), pp. 1085–1087. ISSN: 1539-4794. DOI: [10.1364/OL.31.001085](https://doi.org/10.1364/OL.31.001085).

- [SH18] S. Sadeghi and S. M. Hamidi. “Enhanced Faraday rotation in one dimensional magneto-plasmonic structure due to Fano resonance”. In: *Journal of Magnetism and Magnetic Materials* 451 (Apr. 2018), pp. 305–310. ISSN: 0304-8853. DOI: [10.1016/j.jmmm.2017.11.080](https://doi.org/10.1016/j.jmmm.2017.11.080).
- [Sha+13] M. Shalaby et al. “A magnetic non-reciprocal isolator for broadband terahertz operation”. In: *Nature Communications* 4 (Mar. 2013), p. 1558. ISSN: 2041-1723. DOI: [10.1038/ncomms2572](https://doi.org/10.1038/ncomms2572).
- [SJM10] L. Sun, S. Jiang, and J. R. Marciante. “All-fiber optical magnetic-field sensor based on Faraday rotation in highly terbium-doped fiber”. In: *Optics Express* 18.6 (Mar. 2010), pp. 5407–5412. ISSN: 1094-4087. DOI: [10.1364/OE.18.005407](https://doi.org/10.1364/OE.18.005407).
- [SRF97] A. Sharon, D. Rosenblatt, and A. A. Friesem. “Resonant grating-waveguide structures for visible and near-infrared radiation”. In: *JOSA A* 14.11 (Nov. 1997), pp. 2985–2993. ISSN: 1520-8532. DOI: [10.1364/JOSAA.14.002985](https://doi.org/10.1364/JOSAA.14.002985).
- [SS91] H. B. Sohlstrom and K. G. Svantesson. “Waveguide-based fiber optic magnetic field sensor with directional sensitivity”. In: *Fiber Optic Sensors: Engineering and Applications*. Vol. 1511. International Society for Optics and Photonics, Aug. 1991, pp. 142–148. DOI: [10.1117/12.45986](https://doi.org/10.1117/12.45986).
- [SSH90] K. G. Svantesson, H. B. Sohlstrom, and U. Holm. “Magneto-optical garnet materials in fiber optic sensor systems for magnetic field sensing”. In: *Electro-Optic and Magneto-Optic Materials II*. Vol. 1274. International Society for Optics and Photonics, Aug. 1990, pp. 260–269. DOI: [10.1117/12.20503](https://doi.org/10.1117/12.20503).
- [SSW74] R. P. Spiers, C. V. Subbaraman, and W. L. Wilkinson. “Free coating of a Newtonian liquid onto a vertical surface”. In: *Chemical Engineering Science* 29.2 (Feb. 1974), pp. 389–396. ISSN: 0009-2509. DOI: [10.1016/0009-2509\(74\)80048-5](https://doi.org/10.1016/0009-2509(74)80048-5).
- [Sti94] L. Stichauer. “Étude des propriétés optiques et magnéto-optiques de films nanocristallins de ferrite de cobalt”. PhD thesis. Nancy 1, Jan. 1994.
- [Tar+03] P. Tartaj et al. “The preparation of magnetic nanoparticles for applications in biomedicine”. In: *Journal of Physics D: Applied Physics* 36.13 (June 2003), R182–R197. ISSN: 0022-3727. DOI: [10.1088/0022-3727/36/13/202](https://doi.org/10.1088/0022-3727/36/13/202).
- [Tat+17] T. Tatarchuk et al. “Spinel Ferrite Nanoparticles: Synthesis, Crystal Structure, Properties, and Perspective Applications”. In: *Nanophysics, Nanomaterials, Interface Studies, and Applications*. Ed. by Olena Fesenko and Leonid Yatsenko. Springer Proceedings in Physics. Cham: Springer International Publishing, 2017, pp. 305–325. ISBN: 978-3-319-56422-7. DOI: [10.1007/978-3-319-56422-7_22](https://doi.org/10.1007/978-3-319-56422-7_22).
- [Var17] B. Varghese. “Resonant enhancement of magneto-optical effects using 1-D planar micro-structuration”. PhD thesis. Université Jean Monnet, Saint-Etienne, Dec. 2017.

- [Vas+09] M. Vasiliev et al. "Microstructural characterization of sputtered garnet materials and all-garnet magnetic heterostructures: establishing the technology for magnetic photonic crystal fabrication". In: *Journal of Physics D: Applied Physics* 42.13 (June 2009), p. 135003. ISSN: 0022-3727. DOI: [10.1088/0022-3727/42/13/135003](https://doi.org/10.1088/0022-3727/42/13/135003).
- [Vas+11] M. Vasiliev et al. "Annealing behaviour and crystal structure of RF-sputtered Bi-substituted dysprosium iron-garnet films having excess co-sputtered Bi-oxide content". In: *Journal of Physics D: Applied Physics* 44.7 (Feb. 2011), p. 075002. ISSN: 0022-3727. DOI: [10.1088/0022-3727/44/7/075002](https://doi.org/10.1088/0022-3727/44/7/075002).
- [Viš+93] Š. Višňovský et al. "Magneto-optical Kerr spectra of nickel". In: *Journal of Magnetism and Magnetic Materials* 127.1 (Oct. 1993), pp. 135–139. ISSN: 0304-8853. DOI: [10.1016/0304-8853\(93\)90206-H](https://doi.org/10.1016/0304-8853(93)90206-H).
- [VKP80] A. S. Vaingankar, B. V. Khasbardar, and R. N. Patil. "X-ray spectroscopic study of cobalt ferrite". In: *Journal of Physics F: Metal Physics* 10.7 (July 1980), pp. 1615–1619. ISSN: 0305-4608. DOI: [10.1088/0305-4608/10/7/027](https://doi.org/10.1088/0305-4608/10/7/027).
- [Vor+20] A. A. Voronov et al. "Magneto-optics of subwavelength all-dielectric gratings". In: *Optics Express* 28.12 (June 2020), pp. 17988–17996. ISSN: 1094-4087. DOI: [10.1364/OE.394722](https://doi.org/10.1364/OE.394722).
- [Weh+11] T. Wehlius et al. "Magneto-optical garnets for integrated optoelectronic devices". In: *physica status solidi (a)* 208.2 (2011), pp. 252–263. ISSN: 1862-6319. DOI: [10.1002/pssa.201026672](https://doi.org/10.1002/pssa.201026672).
- [WF05] Z. Wang and S. Fan. "Optical circulators in two-dimensional magneto-optical photonic crystals". In: *Optics Letters* 30.15 (Aug. 2005), pp. 1989–1991. ISSN: 1539-4794. DOI: [10.1364/OL.30.001989](https://doi.org/10.1364/OL.30.001989).
- [Woh86] E. P. Wohlfarth, ed. *Ferromagnetic Materials: A Handbook on the Properties of Magnetically Ordered Substances, Vol. 2*. Amsterdam: North Holland, Aug. 1986. ISBN: 978-0-444-85312-7.
- [Yan+07] Q. H. Yang et al. "Effect of Post-Annealing on the Magnetic Properties of Bi:YIG Film by RF Magnetron Sputtering on Si Substrates". In: *IEEE Transactions on Magnetics* 43.9 (Sept. 2007). Conference Name: IEEE Transactions on Magnetics, pp. 3652–3655. ISSN: 1941-0069. DOI: [10.1109/TMAG.2007.900979](https://doi.org/10.1109/TMAG.2007.900979).
- [Yan+15] M. Yanaga et al. "Compact magneto-optical isolator with cobalt ferrite on silicon photonic circuits". In: *Applied Physics Express* 8.8 (July 2015), p. 082201. ISSN: 1882-0786. DOI: [10.7567/APEX.8.082201](https://doi.org/10.7567/APEX.8.082201).
- [Yar73] A. Yariv. "Coupled-mode theory for guided-wave optics". In: *IEEE Journal of Quantum Electronics* 9.9 (Sept. 1973). Conference Name: IEEE Journal of Quantum Electronics, pp. 919–933. ISSN: 1558-1713. DOI: [10.1109/JQE.1973.1077767](https://doi.org/10.1109/JQE.1973.1077767).
- [YC+13] J. Yao Chin et al. "Nonreciprocal plasmonics enables giant enhancement of thin-film Faraday rotation". In: *Nature Communications* 4 (Mar. 2013), p. 1599. ISSN: 2041-1723. DOI: [10.1038/ncomms2609](https://doi.org/10.1038/ncomms2609).

- [Yos+16] T. Yoshimoto et al. "Magnetophotonic crystal with cerium substituted yttrium iron garnet and enhanced Faraday rotation angle". In: *Optics Express* 24.8 (Apr. 2016), pp. 8746–8753. ISSN: 1094-4087. DOI: [10.1364/OE.24.008746](https://doi.org/10.1364/OE.24.008746).
- [YWF07] Z. Yu, Z. Wang, and S. Fan. "One-way total reflection with one-dimensional magneto-optical photonic crystals". In: *Applied Physics Letters* 90.12 (Mar. 2007), p. 121133. ISSN: 0003-6951. DOI: [10.1063/1.2716359](https://doi.org/10.1063/1.2716359).
- [Zha01] W. Zhao. "Magneto-optic properties and sensing performance of garnet YbBi:YIG". In: *Sensors and Actuators A: Physical* 89.3 (Apr. 2001), pp. 250–254. ISSN: 0924-4247. DOI: [10.1016/S0924-4247\(00\)00560-4](https://doi.org/10.1016/S0924-4247(00)00560-4).
- [ZK97] A.K. Zvezdin and V.A. Kotov. *Modern magneto-optics and magneto-optical materials*. IOP Publishing : Bristol and Philadelphia, Jan. 1997. ISBN: 978-1-4200-5084-4. DOI: [10.1201/9781420050844](https://doi.org/10.1201/9781420050844).
- [Śmi+10] W. Śmigaj et al. "Magneto-optical circulator designed for operation in a uniform external magnetic field". In: *Optics Letters* 35.4 (Feb. 2010), pp. 568–570. ISSN: 1539-4794. DOI: [10.1364/OL.35.000568](https://doi.org/10.1364/OL.35.000568).

Abstract

Enhancement of Every Magneto-Optical Effect with All-Dielectric Guided-Mode Resonant Gratings Based on a Magnetic Sol-Gel Nanocomposite

by Laure BSAWMAII

Magneto-optical (MO) photonic devices are currently highly desirable because of their ability to improve the sensitivity of biosensors or their sensitivity to the magnetic field. However, MO effects being rather small through classical magnetic films, it is relevant to find ways to enhance such effects which can manifest as light polarization rotation or intensity modification under magnetic field. The proposed device in this work to enhance MO effects is an all-dielectric planar structure formed by a 1D photoresist (PR) grating deposited on top of a MO film itself deposited on a glass substrate. Under coupling conditions through the grating, guided-modes (TE and TM) with narrow resonances are excited in the MO film by the incident light, increasing hence the light-matter interaction. Such coupling results as a dip (peak) in the transmittance (reflectance) spectrum. The MO film is a composite formed by magnetic nanoparticles ($CoFe_2O_4$) embedded in a silica matrix and obtained through sol-gel process. This nano-structurable composite can be easily deposited on common substrates with low annealing temperature ($90^\circ C$), which is not the case of the most MO materials used within integrated optics platforms. Large enhancements of the different non-reciprocal polarization rotation effects (such as Faraday and longitudinal MO Kerr) were achieved experimentally and numerically through the all-dielectric resonant structure. The main results of this work concern the transverse MO Kerr effect (TMOKE). This effect induces a non-reciprocal spectral shift of the transmittance (reflectance) resonance upon magnetization reversal, resulting in an intensity modulation effect. TMOKE values up to 9.5% and 18.5% were measured respectively in transmission with $T = 80\%$ and in reflection with $R = 5\%$. These large TMOKE values are mainly due to the high quality factor of TM transmittance (reflectance) resonances. The TMOKE signal for a single MO film is around 0.01%, hence an enhancement with three orders of magnitude was achieved through the fabricated structure. The reached measured TMOKE values are highly competitive with the literature where, to our knowledge, maximum values of 1.5% and 15% were experimentally demonstrated respectively through all-dielectric and magneto-plasmonic structures. Moreover, unexpected reciprocal magnetic effects were experimentally evidenced. Finally, the proposed all-dielectric structure is a low-cost device, which can be fabricated on large scale substrate, and able to enhance all the MO effects. Hence, it is a promising structure for non-destructive testing, magnetic field sensing and even biosensing.

Résumé

Exaltation des Différents Effets Magnéto-Optiques à l'aide de Réseaux Résonants Diélectriques Basés sur un Nano-composite Magnétique Obtenu par Voie Sol-Gel

par Laure BSAWMAII

Les dispositifs photoniques magnéto-optiques (MO) sont l'objet d'une attention particulière pour leur capacité à améliorer la sensibilité des biocapteurs ou leur sensibilité au champ magnétique. Les effets MO, pouvant se manifester par une rotation de polarisation ou une modification d'intensité de la lumière sous champ magnétique, sont cependant plutôt faibles lors d'interactions simples (réflexion ou transmission) avec les films magnétiques classiques. Le dispositif proposé dans le cadre de ce travail permet d'exalter les effets MO. C'est une structure diélectrique planaire simple formée par un réseau 1D de résine photosensible (PR) déposé à la surface d'un film MO lui-même déposé sur un substrat de verre. Selon les conditions de couplage imposées par le réseau, des modes guidés (TE et TM) sont excités dans le film MO par la lumière incidente, augmentant ainsi l'interaction lumière-matière. Un tel couplage produit ainsi une résonance étroite qui se traduit par un creux (pic) dans le spectre de la transmittance (réflectance). Le film MO est un composite formé par des nanoparticules magnétiques (CoFe_2O_4) insérés dans une matrice de silice par un procédé sol-gel. Ce composite nano-structurable peut être facilement déposé sur des substrats classiques à faible température de recuit (90°C), ce qui n'est pas le cas de la plupart des matériaux MO utilisés dans les plates-formes d'optiques intégrées. Des exaltations importantes des différents effets de rotation de polarisation (Faraday et Kerr longitudinal) ont été atteintes par les mesures et les simulations grâce à cette structure résonnante toute diélectrique. Les principaux résultats de ce travail concernent cependant l'effet Kerr MO transverse (TMOKE). Cet effet induit un décalage spectral non réciproque de la résonance de transmittance (réflectance) lors de l'inversion de l'aimantation, résultant en une modulation d'intensité. Des valeurs de TMOKE atteignant 9,5% et 18,5% ont été mesurées respectivement en transmission avec $T = 80\%$, et en réflexion avec $R = 5\%$. Ces valeurs très significatives de TMOKE sont principalement dues au facteur de qualité élevé des résonances de transmittance (réflectance) du mode TM. La valeur de TMOKE pour un film MO sans réseau étant d'environ 0,01%, une exaltation de trois ordres de grandeur a ainsi été obtenue grâce à la structure fabriquée. Les valeurs mesurées de TMOKE sont bien positionnées par rapport à la littérature où, à notre connaissance, des valeurs maximales de 1,5% et 15% ont été démontrées expérimentalement par des structures respectivement diélectriques et magnéto-plasmoniques. De plus, des effets magnétiques réciproques inattendus ont été démontrés expérimentalement. Enfin, la structure proposée est un dispositif à faible coût, qui peut être fabriqué sur des substrats à grande échelle, est capable d'exalter tous les effets MO. Cela en fait une structure à fort potentiel pour des applications comme le contrôle non destructif, les capteurs de champ magnétique et même les biocapteurs.